TU Delft

Delft University of Technology

ADR

The use of Advanced Dry Recovery in recycling fine moist granular materials

de Vries, Walter

DOI
10.4233/uuid:c3c8578d-fd2c-493f-b4c5-79e63bc6d70c

Publication date
2017

Document Version
Final published version

Citation (APA)
de Vries, W. (2017). *ADR: The use of Advanced Dry Recovery in recycling fine moist granular materials*. [Dissertation (TU Delft), Delft University of Technology]. https://doi.org/10.4233/uuid:c3c8578d-fd2c-493f-b4c5-79e63bc6d70c

Important note
To cite this publication, please use the final published version (if applicable).
Please check the document version above.

Copyright
Other than for strictly personal use, it is not permitted to download, forward or distribute the text or part of it, without the consent of the author(s) and/or copyright holder(s), unless the work is under an open content license such as Creative Commons.

Takedown policy
Please contact us and provide details if you believe this document breaches copyrights.
We will remove access to the work immediately and investigate your claim.

This work is downloaded from Delft University of Technology.
For technical reasons the number of authors shown on this cover page is limited to a maximum of 10.

ADR

The use of Advanced Dry Recovery in recycling fine moist granular materials

Walter de Vries

ADR

The use of Advanced Dry Recovery in recycling fine moist granular materials

Proefschrift

ter verkrijging van de graad van doctor
aan de Technische Universiteit Delft,
op gezag van de Rector Magnificus prof.ir. K.C.A.M. Luyben,
voorzitter van het College voor Promoties,
in het openbaar te verdedigen op
14 november 2017 om 12:30 uur

door

Walter DE VRIES

Master of Science, Civil Engineering,
Technische Universiteit Delft, Nederland
geboren te Purmerend, Nederland

This dissertation has been approved by the
promotor: Prof.dr. P.C. Rem

Composition of the doctoral committee:

Rector Magnificus	Chairman
Prof.dr. P.C. Rem	Delft University of Technology

Independent members:

Prof.dr.ir. E. Schlangen	Delft University of Technology
Prof.dr. G.J. Witkamp	Delft University of Technology
Prof.dr.ing. T. Pretz	Rheinisch-Westfälische Technische Hochschule Aachen, Germany
Prof.dr. J.P. van der Weele	University of Patras, Greece
Dr. F. Di Maio	Delft University of Technology

Copyright © 2017 by W. de Vries

ISBN 978-94-6233-802-9

An electronic version of this dissertation is available at: http://repository.tudelft.nl/

Summary

Effective recycling of municipal solid waste incinerator bottom ashes (MSWI-BA) and construction and demolition wastes (CDW) has proven to be a challenge, despite the high potential for recovering valuable metals in MSWI-BA and reducing the carbon footprint of the construction industry. The fundamental problem is caused by the combined presence of fines (-1 mm) and moisture. This combination forms agglomerates and fouls screens and other separation equipment, making it notoriously difficult to recover value from these waste-streams.

Focusing on recovering value from waste streams is the next step in using recycling in an effective way to fulfill societies' needs. Recycling originated from the need to minimize waste volumes and simultaneously reduce the dependency on raw resources. This led to an evaluation of recycling in terms of recycled mass. Optimizing the total mass of a waste flow that is recycled often leads to undesirable or suboptimal solutions and to a waste of resources and money. A transition to an evaluation based on the recovered value realigns the evaluation with the real objective and allows for effective steering via subsidies and taxes.

Recycling value out of a waste flow is achieved by separating and concentrating the valuable constituents. This is typically done via liberation, classification and separation of the material at various levels of complexity, using different techniques at each level. As stated, problems occur when processing materials such as MSWI-BA and CDW because of the combined presence of moisture and fines.

Dimensional analysis shows that these moisture bonds can only be liberated with dispersive accelerations far beyond the level of conventional technology. In an ADR, a rotating rotor provides such acceleration through perpendicular blades impacting the material at 25 m/s. This liberates and disperses the moist particles, allowing a particle classification based on size and density via the air-drag in ballistic trajectory.

To understand the break-up of a moist poly-dispersed cluster, its complex structure is investigated. A model is developed by scanning a sample of a randomly deposited particle mixture using X-ray tomography. The results are analyzed to obtain the kiss-matrix, which quantifies the number of contacts between particle groups.

A new model to predict the kiss-matrix is constructed based on the observation that each pair of spheres has a so-called kissing surface on which a track is formed when particles come into contact and move along each other. By the ergodic assumption that the number of kisses, or the length of kissing track per unit area of the kissing surface, will be uniform over the total of all kissing surfaces, a kiss matrix can be derived. The experimental scan results compare well with the results of this new ergodic model.

The model is expanded by adding a description of the liquid bridge between particles. Analysis shows that the acceleration required to liberate particles depends more on particle size than on moisture content. Also, it follows that liberation is dominated by the size of the smaller particle rather than the size of the larger particle to which it is attached. Furthermore, it shows that the degree of liberation will increase sharply with an increase of the smaller particle size.

The validity and conclusions of this model are confirmed by an experiment in which the residual adhesion after impact with the rotor is studied in isolation. The data also suggest that liberation will be complete in the limit of zero throughput, suggesting that moist particle clusters are transformed into pancakes at the rotor blade.

Further experimental study with an ADR shows the classification achieved over distance from the rotor and special features herein. Basic ballistic classification dominates in the size fractions between 1 mm and 8 mm. Secondary effects like residual adhesion and air movements in the ADR affect the finer particles. For coarser fractions, differences in air-drag are smaller, reducing classification between them. The coarse fractions are also affected by a boundary effect of the rotor blade, causing them to follow aberrant trajectories. Despite the deviations of the smallest and biggest particles, a very effective separation can be achieved for a cut-point at 1 or 2 mm. Influences of important operational parameters like throughput, moisture content and material type are studied by experimental variations on a base case. Comparison of all results shows that the overall classification result is very robust.

An industrial pilot ADR was tested to process MSWI bottom-ash, demonstrating the ballistic classification between different material types like organics, minerals and heavy non-ferrous metals (HNF). When the ADR is used to effectively remove the <2mm minerals, organics are removed up to 4 mm, while HNF will be recovered down to 0.5 mm. This combination results in a very effective pre-concentration of non-ferrous metals prior to eddy current separators, which further concentrate the metals. Using the ADR, an overall NF-metals recovery rate of 89% was achieved, doubling the state of art value. Similarly, positive results have been obtained for CDW. In that application the ADR can be used to significantly increase the quality of crushed concrete, making it suitable to replace natural aggregates in making new concrete. By using the ADR on sifting sand, almost a quarter of the very complex waste stream is saved from landfilling and can be applied as a useful aggregate.

A model of the ADR process is developed by combining a description of the mutual interaction of an air-flow and a ballistic trajectory with drag with a description of collisions of particles with static and dynamic surfaces. In this basic model, effects of residual adhesion, air-drag, air-movement and collisions are taken into account using elementary descriptions, and the results are interpreted statistically. The model can be used to quickly quantify impacts, visualize the classification process and give more general insight.

In a follow up comprehensive model, more fundamental process descriptions are used. The refinements allow detailed study of collisions, showing that the formation of the particle jet at the rotor is determined mainly by the randomizing effect of the collisions. The diverging jet is converged upon collision with the roof because of the limited restitution coefficient. And the bouncing of a particle on an inclined high velocity conveyor belt can be sustained because of the constant influx of energy into a rotating ellipsoidal particle. The detailed air-profile description, combined with the calculation of a high number of ballistic trajectories can be used to see the effects of a change in throughput, particle size distribution (PSD) and size of the encasing. Despite the complex interaction between particles, air flow and moving and static solid surfaces, the classification of particles in the ADR process can be predicted fairly accurately from first principles using the presented models.

Samenvatting

Het effectief recyclen van de bodemassen uit een afvalverbrandingsinstallatie (AVI-as) en bouw- en sloopafval (BSA) blijkt uitdagend, ondanks de hoge potentie in de vorm van het terugwinnen van waardevolle metalen in AVI-as en het verminderen van de CO_2-uitstoot van de bouwsector. Het fundamentele probleem wordt veroorzaakt door de gecombineerde aanwezigheid van fijne delen (-1 mm) en vocht. Deze combinatie vormt agglomeraten welke zeven en andere scheidingsinstallaties vervuilen, waardoor het erg zeer lastig is om de waarde uit deze afvalstoffen terug te winnen.

Een focus op het terugwinnen van waarde uit afvalstromen is de volgende stap om recycling op een effectieve wijze te gebruiken om de behoeften van de samenleving te vervullen. Recycling is begonnen met de noodzaak om het afvalvolume te reduceren en tegelijk de afhankelijkheid van grondstoffen te verminderen. Dit leidde ertoe dat recycling werd beoordeeld massa. Door te optimaliseren op de totale gerecyclede massa die van een afvalstof, ontstond vaak een ongewenste of suboptimale oplossing en het leidde bovendien tot verspilling van geld en middelen. Een overgang naar een beoordeling op basis van teruggewonnen waarde zorgt voor een zuiverdere nastreving van de doelstelling en biedt de mogelijkheid om effectief te sturen via subsidies en belastingen.

Het terugwinnen van waarde uit een afvalstroom wordt bereikt door het afscheiden en concentreren van waardevolle bestanddelen. De primaire stappen in dit proces zijn vrijmaking, classificatie en scheiding van het materiaal op verschillende complexiteits-niveaus met verschillende technieken op elk niveau. Zoals gezegd, ontstaan er problemen bij het verwerken van materialen zoals AVI-as en BSA door de gecombineerde aanwezigheid van vocht en fijne delen.

Dimensie-analyse toont aan dat de binding via vocht alleen kan worden verbroken via dispersieve versnellingen ver boven die van conventionele technologie. In een ADR wordt de benodigde versnelling geleverd via een roterende rotor met loodrechte bladen welke het materiaal raakt met 25 m/s. De klap maakt de deeltjes vrij uit vochtige clusters vrij en verspreidt deze waardoor de deeltjes kunnen worden geclassificeerd op grootte en dichtheid via de luchtweerstand op een ballistische baan.

Om het opbreken van de vochtige deeltjesclusters te begrijpen, is de complexe structuur hiervan bestudeerd. De structuur van een monster van een mengsel willekeurig gedeponeerde deeltjes is bepaald door deze te scannen met behulp van röntgenstralen. De scan-resultaten zijn geanalyseerd om de zogenaamde raak-matrix te bepalen. Deze raak-matrix geeft het aantal contacten tussen de verschillende groepen deeltjes.

Een nieuw model om de raak-matrix te voorspellen is ontwikkeld gebaseerd op de observatie dat elk paar bollen een zogenaamd raakoppervlak vormen, waarop een spoor wordt gevormd wanneer deeltjes elkaar passeren of raken. Door gebruik te maken van de ergodische aanname dat het aantal raakpunten, of de lengte van het raak-spoor per oppervlakte-eenheid van het raakoppervlak, uniform verdeeld is over het gehele raakoppervlak, kan een raak-matrix worden bepaald. De analyseresultaten van de scan komen goed overeen met de resultaten van dit nieuwe ergodische model.

Het model wordt uitgebreid met een beschrijving van de vloeistofbrug tussen twee deeltjes. Uit de analyse volgt dat de versnelling die nodig is om deeltjes vrij te maken meer afhangt van deeltjesgrootte dan van het vochtgehalte. Tevens blijkt dat de vrijmaking meer wordt gedomineerd door de grootte van het kleinste deeltje dan de grootte van het grotere deeltje waaraan het verbonden is. Bovendien blijkt dat de mate van vrijmaking sterk toeneemt als het kleinste deeltje groter wordt.

De geldigheid en conclusies van dit model worden bevestigd via een experiment waarin de vrijmaking van deeltjes door de impact met de rotor is geïsoleerd. De resultaten suggereren ook dat de vrijmaking volledig wordt als de doorzet naar nul gaat. Dit suggereert dat vochtige deeltjes clusters in elkaar worden gedrukt tot een pannenkoek op het rotorblad.

Vervolgexperimenten met de ADR tonen de scheiding over de afstand van de rotor en de afwijkingen hierin. Het ballistische scheidingsgedrag domineert in de korrelgroottefracties tussen 1 en 8 mm. Secundaire effecten zoals onvolledige vrijmaking en luchtbewegingen in de ADR beïnvloeden de fijnere deeltjes. Bij de grovere fracties worden de verschillen in de luchtweerstand kleiner, waardoor de onderlinge scheiding minder wordt. De grove fracties worden ook beïnvloed door een randeffect van het rotorblad, waardoor grove deeltjes een afwijkende baan volgen. Ondanks de verstoringen van de kleinste en grootste deeltjes, kan een zeer effectieve separatie worden bereikt voor een scheiding op 1 of 2 mm. De invloed van belangrijke operationele parameters zoals doorzet, vochtgehalte en het type materiaal zijn bestudeerd via experimentele variaties op een base case. Het totaal aan resultaten laat zien dat het scheidingsresultaat zeer robuust is.

Een industriele pilot van de ADR is getest om AVI-bodemassen te verwerken en toont de ballistische scheiding tussen verschillende soorten materiaal, zoals organische stoffen, mineralen en zware non-ferrometalen (HNF). Wanneer de ADR wordt gebruikt om effectief de <2mm mineralen te verwijderen, worden organische stoffen verwijderd tot 4 mm, terwijl HNF wordt teruggewonnen tot 0,5 mm. Deze combinatie zorgt voor een zeer effectieve voor-concentrering van non-ferro metalen voorafgaand aan wervelstroomscheiders, welke de metalen verder concentreren. Met behulp van de ADR wordt een terugwinning van NF-metalen van 89% bereikt, een verdubbeling ten opzichte van de huidig best beschikbare techniek. Vergelijkbaar positieve resultaten werden verkregen voor BSA. Hier kan de ADR worden gebruikt om de kwaliteit van betonpuin sterk te verhogen, waardoor deze geschikt wordt om grind in nieuw beton te vervangen. Het gebruik van de ADR op sorteerzeefzand zorgt ervoor dat bijna een kwart van deze zeer complexe afvalstroom niet meer gestort hoeft te worden en kan worden toegepast als een nuttige toeslagstof.

Het ADR-proces is gemodelleerd door een beschrijving van de wisselwerking van een luchtstroom en een ballistische baan met luchtweerstand te combineren met die van botsingen van deeltjes met statische en dynamische oppervlakken. In een basismodel worden de effecten van vrijmaking, luchtweerstand, luchtbewegingen en botsingen meegenomen via simpele beschrijvingen en de verkregen resultaten worden statistisch geïnterpreteerd. Het model kan worden gebruikt om verschillende invloeden snel te kwantificeren en te visualiseren.

In een uitgebreider model worden meer fundamentele procesbeschrijvingen gebruikt. Hierdoor kunnen botsingen in detail worden bestudeerd. Hieruit blijkt dat de vorming van de deeltjes-jet bij de rotor vooral wordt bepaald door het stochastische effect van de botsingen. De divergerende jet wordt geconvergeerd via botsingen met het dak vanwege de beperkte restitutiecoëfficiënt. En het stuiteren van een deeltje op een schuine snellopende transportband kan lang aanhouden omdat er voortdurend energie in het roterende ellipsoïde deeltje wordt gebracht. De gedetailleerde beschrijving van het luchtprofiel, in combinatie met het bepalen van een groot aantal ballistische banen kan worden gebruikt om de effecten van een verandering in doorzet, de deeltjesgrootte-verdeling (PSD) en de maat van de omkasting te zien. Ondanks de complexe interactie tussen deeltjes, luchtstroom en bewegende en statische oppervlakken, kan de scheiding van de deeltjes in de ADR via de gegeven modellen vrij nauwkeurig worden voorspeld vanuit eerste beginselen.

Table of Contents

Outline

This thesis discusses the development of a novel recycling technology called ADR: Advanced Dry Recovery. The technology was developed to enforce a break-through in the recycling of some large waste flows, particularly municipal solid waste incineration bottom ash and construction and demolition wastes.

To understand the need for the ADR within the wider context of recycling, the thesis starts with a rather broad introduction. Hereafter, the ADR concept is explained by analyzing the problem of classification of fine moist granular materials. The details of this problem are investigated in Chapter 3, where the structure of moist particle clusters is analyzed and modelled.

In the experimental Chapter 4, a base case experiment shows the fundamentals of classification with the ADR. Variations on this base are used to show the influence of key parameters. Industrial pilot experiments performed with bottom-ash and construction waste show the practical implications of using the ADR and how this type of classification leads to a significant improvement upon the state of art.

The final chapter discusses a basic and a comprehensive model of the ADR. For the basic model, elementary models are combined to obtain insight into the processes determining the classification performance of the ADR. The key parts of this model are extended in the comprehensive model, which gives a detailed insight in the main processes of collisions and the ballistic trajectory in a drag induced airflow.

1 Introduction

To properly understand the *why* and *how* of recycling, this thesis starts with a rather general introduction, answering the question why society desired recycling initially and how this formed the way we choose our recycling objectives. After a correction of the current way of thinking, the methodology for recycling is presented. In this section a framework of effectively characterizing a waste stream is introduced, the basic recycling scheme is explained and terms and methodologies are presented to objectively and effectively optimize a recycling process. The introduction is finalized by presenting the three fine grained (0-16mm) solid granular waste streams that are considered in this thesis.

1.1 Recycling philosophy

In the sixties, society started to develop objectives for recycling to reduce the footprint of waste. Society's initial motivation for recycling introduced an assessment of recycling in terms of mass. In the following sections it will be demonstrated why this is not the best unit. After establishing a better unit for assessment, current recycling trends in Europe are evaluated and the presented framework of thinking is summarized and completed with additional considerations.

Origin of recycling

Recycling originated from the desire to no longer bring waste material to landfills. Mainly because these landfills were filling up, but also because of the growing awareness that it was a waste to literally throw resources away. Legislation was designed starting from about the turn of the century to prevent materials ending up at landfills [1]. This legislation always focused on mass and volume, since these are the most important units of measurement when regarding landfills. Under this legislation, recycling rates of materials have grown tremendously, to up to 90% [kg/kg] [1].

However, recycling aimed at mass or volume can lead to dubious situations. Is it really recycling to support a road by a layer of MSWI bottom ash? Can we increase recycling by increasing the height of the road even if there is no functional gain in this elevation? More generally; is it recycling if a material is reused in a way that brings no functional advantage?

From mass oriented to value oriented

In recent times, attention is increasingly focusing on sustainability and strategic availability of resources. It is becoming clear that looking at recycling in terms of mass no longer fulfills the objectives of society since the type of resources associated with largest mass flows are typically not problematic from the point of view of sustainability or strategic availability. A transition is occurring, where the unit of recycling is changing from mass or volume to value (i.e. €).

The value (or price) of a material can be determined by two things, depending on its availability. When a material is abundantly available, competition among suppliers forces the price to be determined by production costs. However, when a material becomes scarce, its value will be determined by demand and will therefore be coupled to added value it has in the product or component. If the component manufacturer has the option to use alternative materials, the prices of these materials may get linked to each other. As scarcity is expected for many materials within the near future, their values will come to be directly linked to their functionality. This effect can be seen in Figure 1.1, which shows the price development of three very different commodities over the last ten years (normalized for inflation to its price in 2003). It can be seen that the price of the commodities started at a relative stable level (the cost of production), then became unstable, and finally stabilized at a new level (the value of its functionality).

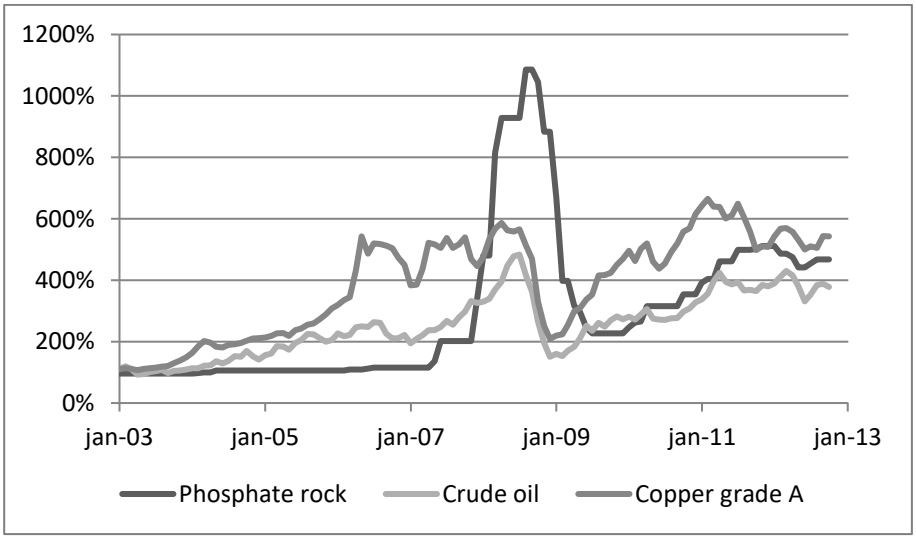

Figure 1.1: Price development of three very different commodities over the last ten years (normalized for inflation to its price in 2003).

The mechanism that couples value to functionality causes the transition for the unit of recycling from mass or volume to value, to effectively be a transition to functionality, but made quantitative. Therefore, the new unit of recycling rate can be seen as the functionality of the recycled material in its new application relative to its original function in the primary product. In this framework, optimization of recycling rates will result in optimum recycling of the functionality of materials, which is in line with current societal demands.

Figure 1.2 shows the new life cycle of materials. Within this diagram two new definitions are introduced to distinguish waste streams before processing (End of Life, EOL) from those after processing (End of Waste, EOW). Material or products will flow through the diagram and in every step value is either added or subtracted from the material, corresponding to its (potential) functionality. The loop can only be closed when the value/functionality of EOW material is as high as that of the primary resource. At this point the waste-stream has become a fully sustainable secondary resource.

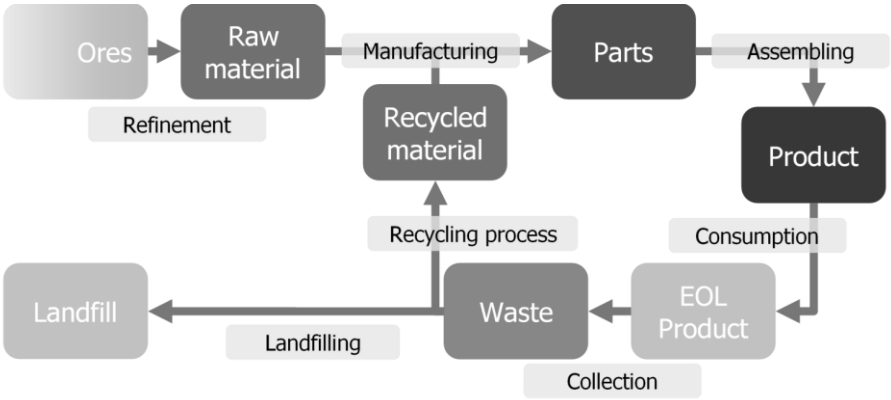

Figure 1.2: The new life cycle of materials

When the example of MSWI bottom ash is revisited, it becomes clear that the recycling rate is not as high as first thought. MSW, consisting of household appliances made from high value raw materials (10^3 €/ton), is used to heighten a road, at a value of **-** 10^1 €/ton. The consequences in this example are valid for many more 'recycling' routes; even though 80% of the mass is recycled, none (or little) of its original value is recovered.

To further attune the framework of thinking to society's desire to be sustainable, it is important to change focus from the outlet of waste streams to the influx of materials into the economy. The ambition should be to fully fulfill the raw material demand with a secondary resource supply. Because of economic growth it will not be possible to achieve the 100% level, but the remainder should then be obtained solely from other renewable resources.

Recycling in Europe: the mass point of view

The European Union has defined a European Waste Hierarchy, which sets the preference of waste treatment methods. It is described in Article 4 of the Waste Framework Directive [2] and sets the order of preference as follows:

1. Prevention;
2. Preparing for re-use;
3. Recycling;
4. Other recovery, e.g. energy recovery; and
5. Disposal (landfill)

This hierarchy, originally known by the name 'Ladder of Lansink' (1979), aims to minimize waste production and maximize the extraction of benefits from waste. The

usage of waste treatment methods in Europe over time is shown in Figure 1.3. In the graph countries are subdivided over three groups as shown in Figure 1.4. The composition of the groups is determined by a country's share of incineration and material recovery (represented as the sum of recycling and composting), group 1 having the highest rates. The graph shows a clear development over time, following the direction of the waste hierarchy, for each group of countries. Furthermore, the apparent connection between groups suggests that within a 15-year period, countries within a group have moved into the next level.

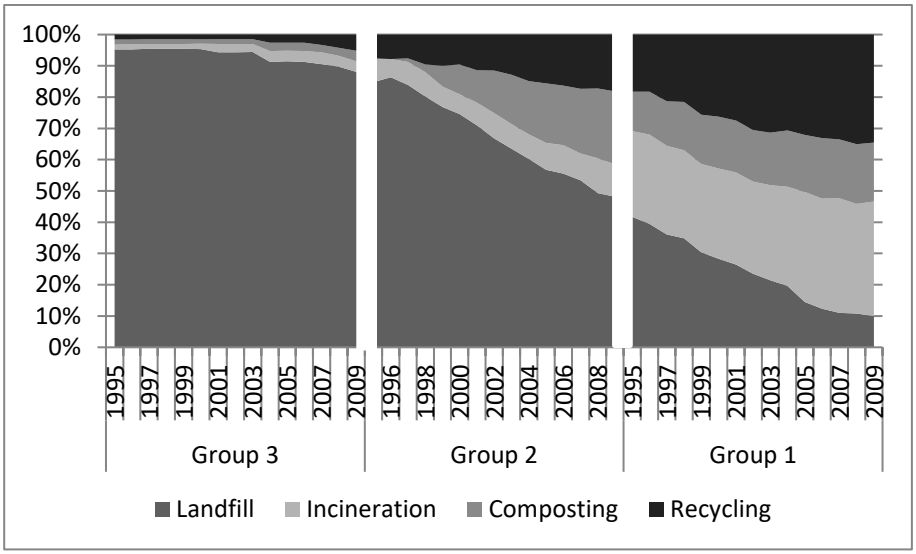

Figure 1.3: The usage of waste treatment methods by country groups in Europe over time

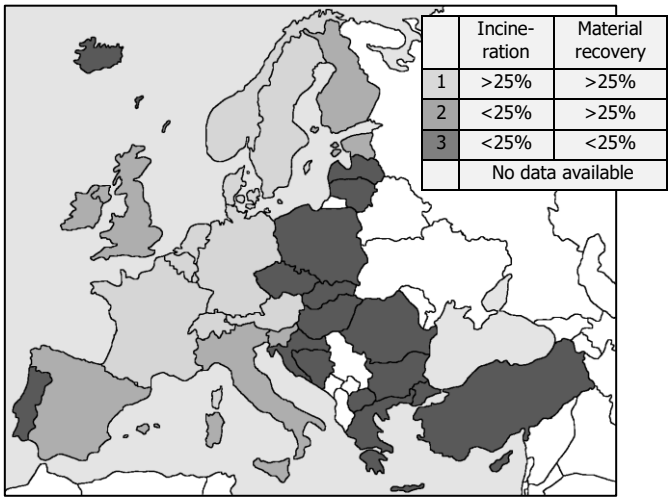

Figure 1.4: Country groups for waste treatment [1]

These data show us that there is a general decline of landfilling. The first objective of recycling, reducing the total mass of our waste is almost achieved. But how does Europe perform in terms of value?

Recycling in Europe: the value point of view

The data of the previous paragraph still assess recycling in term of mass and from the outlet point of view. However, as mentioned before, focus should no longer lie on the management of waste, but on turning waste into resources and reviewing them as such. Unlike other continents, Europe has very little natural resources left and should reduce its dependencies on other continents for its raw material supply. The goal of resource management should therefore be to fully supply the European Union's raw material demand by secondary resources to obtain a sustainable society.

In order to evaluate the progress on successfully turning waste into raw material, the total recycled value should be assessed. However, market effects such as scarcity or changes in functionality of a commodity cause prices to fluctuate. To eliminate this influence the value of secondary resources is normalized with the total value of raw material use in the economy.

Over the last decade, Europa has started to develop a framework directive to increase the secondary resource value influx into the economy of Western Europe [2]. The result of this can be seen in Figure 1.5, which shows the total recycled materials value as a percentage of all non-energy raw materials used in manufacturing and construction in Germany. It can be seen that there is a steady increase from less than 5% in 1999 to almost 14% in 2009. Here it must be mentioned that Germany is a leading country of Group 1. Europe's overall value influx from recycling into the economy will be lower.

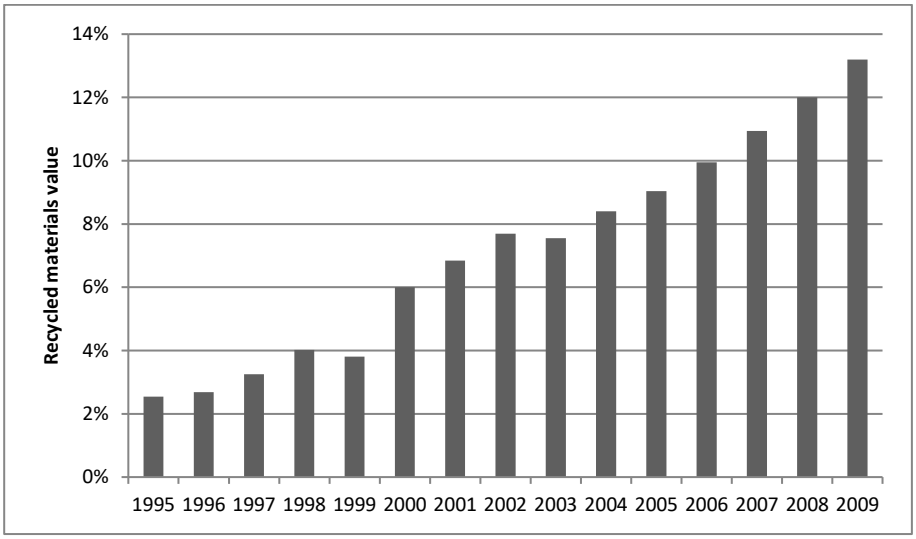

Figure 1.5: Recycled materials value as a percentage of all non-energy raw materials used in manufacturing and construction (Germany) [3]

Objectives and constraints: economy, ecology, quality and legislation

Below the framework of thinking about recycling in terms of value is summarized and completed by giving some additional considerations.

To create a strategic raw material supply for Europe, the legislative framework of Europe should promote independence for our raw material supply. This should be done by supporting the development of economically and ecologically viable recycling technologies. This is effectively done by generating an economically useful outlet for our waste products. The usefulness of the outlet is represented by its value. By comparing this value to the value of the original raw material used for the EOL product which resulted in the waste product, an objective evaluation of the recycling rate can be obtained. The benefit of a recycling (sub-) process can be directly assessed by comparing the value added to the integral costs of the (sub-) process.

Recycling processes should be implemented with minimum environmental impact. This means that upon evaluating the value of the secondary raw material, all cost of externalities (e.g. environment, society, health, energy, safety) should be considered. This will prevent excessive negative environmental impact. This mechanism can become automatic by making proper use of taxes (turning externalities into internalities). CO_2 is an interesting example of this. When we consider CO_2 to be worth money (as we will do in the global trading of it), then it is valid to say that money is also worth CO_2. This means that if a process is costing more than its worth, you actually produce CO_2 in a sense. The money (value) needed to finance the process had to be created somewhere, and in this somewhere there is probably CO_2 being produced (or other externalities created), and therefore these externalities (of the value creating process) should be directly linked to the subsidized process, making it more likely to be unsustainable.

Furthermore, in recycling the safeguarding of the quality of the products by means of process consistency, guarantees and certification is extremely important to generate the highest value. This is because the value of a secondary raw material is only as high as the lowest guaranteed quality. Quality can be defined in an appropriate sense by making full use of experts in the relevant fields. The users of secondary raw materials have great knowledge of material science. Normally this knowledge only flows down the material chain (towards the end-product), where it gets detached from the product in the usage-stage. Knowledge should also flow backwards towards the EOL-stage in order to bridge the gap between EOL product characteristics and primary resource characteristics.

Finally, this all needs to be anchored in properly designed long-term legislation to control the development and societal impact. This is especially so when making use of subsidies because of two reasons. First, if a technology is only profitable by subsidies, it will not be sustainable for reasons stated before. Therefore, the objective of development should always be an unsubsidized process. Second, if the continuation of subsidies is uncertain, no long-term investments will be done in sustainable developments. Similarly, a system of taxing undesired technology to fund subsidized (desired) technology is also not sustainable, simply because if the intended objective is obtained (only the desired technology is used) there is no funding. Since legislation is subject to a four-year horizon at most, companies will not change their long term business strategy to governmental obligations since long term stability is not guaranteed.

1.2 Recycling methodology

After establishing why recycling is desired and in which framework it should be assessed, a framework of evaluating the actual processes of recycling is introduced. For this, a method of effectively characterizing a waste stream is proposed and the basic recycling scheme is introduced. Hereafter, the terms grade and recovery are explained, as a necessary step for describing a method to objectively optimize a recycling operation in an economic sense.

1.2.1 Description of a waste stream

To professionalize recycling, it is essential to set a framework in which all relevant properties of a solid granular waste stream can be expressed, with as few parameters as possible. The data resulting from such a description must form an exhaustive set of information to objectively, quantitatively and accurately describe a predefined list of properties and the effect of relevant recycling processes on the waste stream. An example, with the most important items which should be on such an assessment list, is given below:

- Quality assessment of EOL/EOW material
    - Purity and performance in the application
    - Value
    - Risks
- Assessment of a recycling process
    - Liberation rates
    - Recovery rates
    - Economics
- Description of a recycling process by scientific models
    - Physical properties of a material
    - Physical properties of a particle

To get such a general description, the framework of Kuilman, Rem and Leeftink [4] is used which involves a description on a categorical level and one on a particle level.

The category is defined by a number of descriptors that break the complexity of a waste stream down to a selection in which a random set of an acceptably small number of particles ($10<N<100$) will form a statistically sound sample to significantly describe the properties (for assessment parameters) and behavior (for models) of all particles within that category. An example of such a set of descriptors (as it will be used in this study), is given in the following category list:

- EOL product flow (e.g. bottom ash, CDW or sifting sand)
- Envelop size, i.e. sieve fraction (e.g. retained on 4, but passing 8mm sieve)
- EOW material (e.g. heavy non-ferrous metals)
- Set of analysis techniques to isolate material from this category (e.g. sieving, not breakable by crushing, density >3 kg/l)

The particles within a category sample are described by an as short as possible list of parameters that is still adequate in fulfilling all demands set by the predefined list (i.e. assessment and description).

An example of such a set of parameters describing a particle (as it will be used in this study), is given in the following list:

- Dry mass
- Envelop dimensions (bounding box length, width, height)
- Compositional build up (mono-material parts and their connections)
- Mono-material dimensions (layer thickness, unfolded envelope dimensions)

By defining an exhaustive set of categories and describing the set of particles within each category, a complex waste stream can be fully defined. In essence: the set of particles represent the category, the set of categories represent the waste stream. An effective quantitative description of the whole waste stream is obtained by determining the relative weight percentages of each category.

An expert in the relevant field should lay the blueprint for the actual definition of this framework (the assessment, categorical and particle lists), based on the anticipated list of properties, recycling processes, products and models that will be of relevance. This expert should determine the level of detail used in the description. For example, a soda bottle can be generically described as plastic, or a division can be made between the polyethylene (PE) cap and the polyethylene terephthalate (PET) bottle depending on the product quality assessments required.

1.2.2 The basic recycling scheme

To enable high grade recycling, an efficient process must be designed that transforms a complex EOL (waste) stream comprising of a multitude of constituents into EOW secondary resources which fulfill the requirements of manufacturing and construction. These requirements set limits to properties of the product (e.g. particle size distribution and grades in composition) and prices are a function of the degree of fulfillment of these requirements.

Figure 1.6 shows the basic recycling scheme to transform a waste streams into a secondary resource in an efficient way.

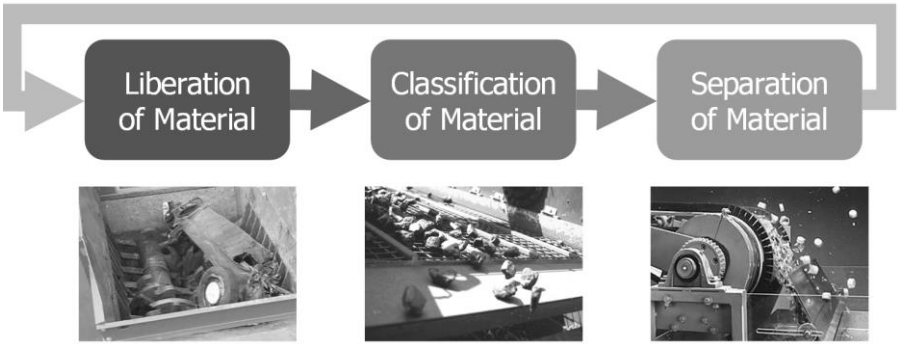

Figure 1.6: Basic recycling scheme

Liberation

A typical waste stream is complex and comprises a multitude of constituents. These constituents can be bonded together on various levels. Depending on the desired end products of the recycling process, the bonds need to be broken in order to be able to

separate the two constituents in a later stage. The various levels of binding and examples of appropriate liberation techniques are given in Table 1.1.

Table 1.1: Binding between constituents and liberation techniques

Binding level	Bonds	Liberation techniques
Molecular level	Chemical	Metallurgy, solvent
Material level	Ore in gangue, composites	Milling, shredding
Particle level	Moisture, electrostatic	Drying, physical separation

Classification

After liberation, efficient classification according to particle size is generally necessary for two reasons. First, mechanical separation techniques utilize differences in physical properties of the constituents such as terminal velocity in water (proportional to both density and size). When material is classified into narrow size fractions (a particle property) the influence of a material property increases and a more efficient separation can be achieved. Secondly, the concentration of a constituent is often a function of particle size. For example; weak and brittle constituents will concentrate into the fine fraction, while strong and ductile materials remain in the coarser fraction. As a result, classification can be a means for concentration.

Separation

When a mono size-fraction is liberated from the rest of the material, a separation of different materials can be performed effectively. In this process, the difference in physical properties between the materials to be separated is utilized, examples are given in Table 1.2.

Table 1.2: Separation techniques and their operational parameter

Technique	Physical parameter
Ballistic	Density
Wind sifter	Density
Flotation	Density, hydrophobicity
Magnets	Magnetic susceptibility
Eddy current	Conductivity
Sensor	Color, X-ray absorption

Note: processes performing classification often incorporate a form of liberation and separation. A high impact flat sieve can serve as an example. On impact with the sieve deck, moisture bonds are broken, the sieve mesh classifies on particle size, and gravity separates particles passing the mesh from particle that do not pass.

1.2.1 Effective optimization of recycling processes

The performance of an industrial recycling process is often determined by the settings of certain parameters of the process. These parameters can be items such as the throughput, the position of a splitter, or the order of operations. To be able to optimize the economy of such a recycling operation, three types of information are required:

- A definition of grade and recovery
- Characteristics of the constituent materials of the input and outputs of a process
- Quantitative relations between the recovery of each constituent in each output of a process and the process settings parameters

Once an analytical quantitative description can be given for this information, the recycling operation can be economically optimized.

Grade and recovery

Within recycling, the terms grade and recovery are often used to describe the effectiveness of a classification or separation process, where an input is separated into one or more outputs. The grade represents the amount of a certain constituent within a stream (input or output). Recovery represents the mass distribution of one constituent of the input over the different outputs. In essence, grade reflects the quality of a flow (input or output), while recoveries reflect the quality of a process. Grade and recovery are determined by the following formulas:

$$G_{x,y} = \frac{M_{x,y}}{\sum_{i=\text{all constituents}} M_{i,y}}$$

$$R_{x,y} = \frac{M_{x,y}}{\sum_{i=\text{all inputs}} M_{x,i}}$$

In which $M_{x,y}$ is the mass of constituent x in flow y, $G_{x,y}$ is the grade of constituent x in flow y and $R_{x,y}$ is the recovery of constituent x in output y. The two formulas are linked via the common term $M_{x,y}$.

Models

By modeling a classification or separation process (either empirically or theory-based), the recovery (and grade) can be expressed as a function of the operational parameters (e.g. sieve mesh size, splitter position, moisture level, throughput). The optimum operation can then be found by linking grade and recovery to revenue.

Revenues

When determining the value of a certain output, it is not possible to simply add the values of the individual constituents. The output will be sold to a certain buyer which will have an intended use for the product. Therefore, for this buyer, some constituents of the output will have a positive impact on the price, while others have a negative impact on the price. For example, lead and copper normally will both have a positive value as a pure material, but when selling a copper concentrate with a minor component of lead, the lead will represent a negative value. Therefore, the value of a constituent is a function of the constituent itself in combination with the flow in which it appears.

By defining:

$$P_{x,y} = \text{Price for constituent } x \text{ in output } y$$

The formula determining the total revenue per ton of a flow can often be rewritten to take the form:

$$I_y = \sum_{i=all\ constituents} G_{i,y} \cdot P_{i,y} \qquad (1.1)$$

Where each of the grades $G_{i,y}$ is bounded to some interval that is characteristic for the use or further processing route of the product. The total revenue of a process, per ton of input, can then be expressed as:

$$I_T = \sum_{i=\text{all constituents}} \sum_{j=\text{all products}} G_{i,\text{Input}} \cdot R_{i,j} \cdot P_{i,j}$$

This formula is a function of specific prices of buyers (given by the market), recovery relations (given by the model) and the composition of the input. The optimum operational parameters can be found by maximizing the total revenue per ton of input. In the following section an example is given to illustrate the practical implications.

Optimizing an operation: an example of an eddy current separator

In operating an eddy current separator (ECS), a splitter is set to a certain position (p) to divide an input (I), consisting of minerals (M) and non-ferrous metals (NF), into a mineral (M) and a non-ferrous (NF) product, see Figure 1.7. The input for the example is described in Table 1.3.

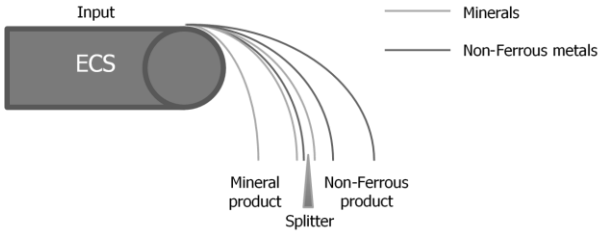

Figure 1.7: Schematic of an ECS

Table 1.3: Characteristics of example ECS Input

EOL material	Size class	EOW material	Distribution [kg/kg]
WI BA	8-12mm	Mineral	98%
		Non-Ferrous metal	2%

For this example the workings of the ECS are modeled by a cumulative normal distribution giving each constituent's recovery in the mineral product as a function of the splitter position (p). Since there are only two products, the recoveries in the non-ferrous product are also determined, see the following formula.

$$R_{M,M}(p) = \Phi\left(\frac{p-\mu_M}{\sigma_M}\right)$$
$$R_{MF,M}(p) = \Phi\left(\frac{p-\mu_{NF}}{\sigma_{NF}}\right)$$
$$R_{M,NF}(p) = 1 - R_{M,M}(p)$$
$$R_{NF,NF}(p) = 1 - R_{NF,M}(p)$$

The non-ferrous product of the ECS is usually sold to a sink-floater, which processes it into raw metal products for manufacturing and construction. The mineral residue is usually sold as a foundation layer material, requiring no further upgrading.

Sink-floaters typically base their prices on a formula that includes the (modified) LME prices for the pure metals, a disposal fee for the minerals and handling costs for the total mass (e.g. transport, sink-floating, smelting) [5]. The formula in the reference paper can be rewritten to take the form of formula (1.1) to get:

$$I_{NF} = G_{NF,NF} \cdot P_{NF,NF} - G_{M,NF} \cdot P_{M,NF}$$

With:

I_{NF} = Total revenue non-ferrous product in €/(ton of non-ferrous product)
$G_{NF,NF}$ = Grade of non-ferrous metals in non-ferrous product
$P_{NF,NF}$ = Modified LME price in €/(ton of non-ferrous metals in non-ferrous product)
$G_{M,NF}$ = Grade of minerals in non-ferrous product
$P_{M,NF}$ = Modified fee for minerals in €/(ton of minerals in non-ferrous product)

The price for the mineral product is typically based on a fixed price per ton of product with the understanding that the material satisfies a number of engineering and environmental limits.

The optimum splitter position is found by maximizing the combined revenues of the mineral and non-ferrous. The total revenue per ton of ECS input as a function of the splitter position is given by:

$$I_T = I_{NF} + I_M$$
$$I_T = G_{NF,Input} \cdot \left[R_{NF,NF}(p) \cdot P_{NF,NF} - \left(1 - R_{NF,NF}(p)\right) \cdot P_{NF,M}\right]$$
$$+ G_{M,Input} \cdot \left[R_{M,M}(p) \cdot P_{M,M} - \left(1 - R_{M,M}(p)\right) \cdot P_{M,NF}\right]$$

This formula can be interpreted as giving a certain reward for the recovery of a constituent in the right product, minus a penalty for its recovery in the wrong product. The results of above given formulas are given in Figure 1.8. A clear optimum in the total revenue can be seen at 0.55 m.

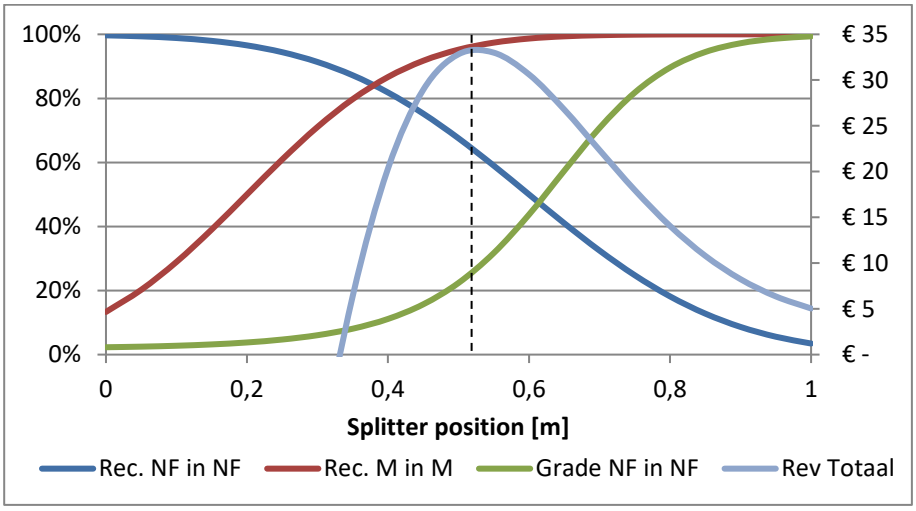

Figure 1.8: Influence of splitter position on recoveries, grade and revenue

Figure 1.9 and Figure 1.10 show the difference between the NF revenue and the total revenue as well as the difference between the dependence of revenue on grade vs dependence on recovery. In the first graph, both lines show the NF revenue, but the first line is a function of grade and the second is a function of recovery. The trivial result is that at a high grade the value of the NF product is high, and at a high recovery (all minerals are also collected into the NF-product) the value is low. In the second

graph the same two series are given but now for the *total* revenue. This shows a counter intuitive result: the *total* optimum can be at a relatively low grade (and a relatively high recovery). So, in order to optimize value recovery, the splitter should be set for high non-ferrous recovery and not for high non-ferrous grade.

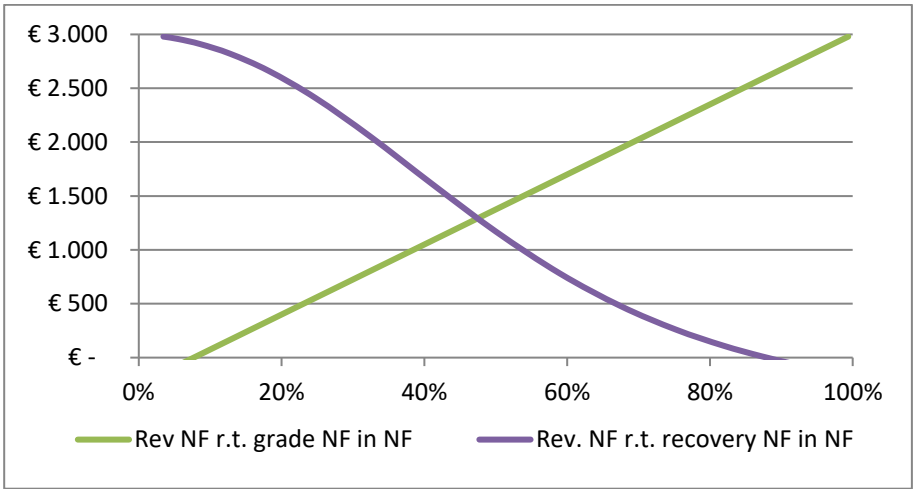

Figure 1.9: Revenue per ton ECS Output as a function of grade and recovery

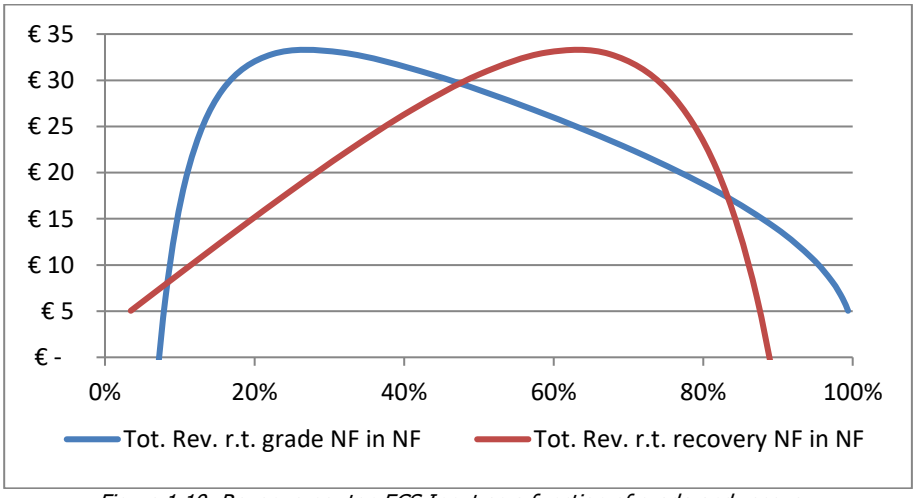

Figure 1.10: Revenue per ton ECS Input as a function of grade and recovery

For a real world example, reference is made to [5], in which an extensive evaluation of a Dutch incineration plant is given.

1.3 Waste streams

Important waste streams in Europe (in terms of value, mass and ecological impact) are [6]:

- Municipal solid waste incineration bottom ash (MSWI-bottom ash)
- Construction and demolition waste (CDW)
- Packaging (plastics)
- Cars
- WEEE
- Hazardous wastes

Of these waste streams, the first two (MSWI-bottom ash and CDW) are discussed in this thesis. They have in common that they are solid granular wastes, of which the current processing of the 0-16mm size range is problematic. This thesis will present a novel technology that will enable high grade recycling. Here, the waste streams will be further introduced.

The total magnitude of the MSWI-bottom ash flow in Europe is significant at 20 million tons (2014) and is expected to increase in the future (see Figure 1.3). It is especially of interest because of its economic potential. Currently this waste stream is mainly landfilled due to its high complexity.

Construction and demolition waste is one of the heaviest and most voluminous waste streams generated in the EU [7]. It accounts for approximately 25% - 30% of all waste generated in the EU and consists of numerous materials, including concrete, bricks, gypsum, wood, glass, metals, plastic, solvents, asbestos and excavated soil, many of which can be potentially recycled. Two streams of CDW are of interest in this thesis, crushed concrete and sifting sand, for different reasons. Crushed concrete has a large share in the total CDW stream, and a large potential for reducing CO_2 emissions. Sifting sand is the most complex waste stream within CDW. All components that cannot be processed by present technology are collected into this stream. Currently it can only be landfilled, causing an ecological burden.

1.3.1 Municipal solid waste incinerator bottom ash

The public debate about the incineration of municipal solid waste has been the topic for a lot of scientific papers. [8, 9, 10]. It is not the objective of this thesis to add to this debate. Nevertheless, there are two main reasons why incineration is considered a beneficial recycling process. First of all, household waste is an extremely complex waste stream in terms of the variety of its constituents and the interlinked state of materials (particles are mainly composites). Incineration decreases the weight of MSW by 90%. Therefore, the relative amount of valuable (non-combustible) constituents increases substantially, making them easier to recover in an economically viable manner. Second, during incineration the caloric value of the waste is directly recovered and is transformed into useful forms of energy (e.g. electrically, steam). For the best available incineration technology, 30% of the heat is converted to electricity, almost as efficiently as in modern power plants [11].

The incineration process

To better understand the properties of incinerator bottom ash, a brief outline of the incineration process is given. Figure 1.11, shows an overview of the most common type of facility. Five principle stages can be distinguished:

- Waste preparation and stoking (screening, mixing, and feeding into the incinerator)
- Waste incineration and emissions mitigation via efficient combustion
- Energy extraction
- Emissions mitigation via neutralization and/or capture in control devices
- Ash handling

During incineration, the waste is gradually run down a grate where the material is dried, combustibles are burned and the ashes are cooled. The fine parts of this ash will rise with the fumes to the off-gas systems, forming the boiler ash and fly-ash. The bigger and heavier parts of the ash remain on the grate and form the bottom ash. This ash is deposited into a water slot, quenching and cooling the ash and reducing dust and NOx emissions. The moist ash is then transported to a landfill where it can be processed further.

Even though the main objective of incineration is to extract caloric value, the bottom ashes often still contain 1-5% of unburnt material. This results from the optimization of economics for the incinerator in terms of total received gate fees and energy production. The total energy produced is a multiplication of the energy extracted per ton of waste and the throughput. Maximizing energy production often favors higher throughput.

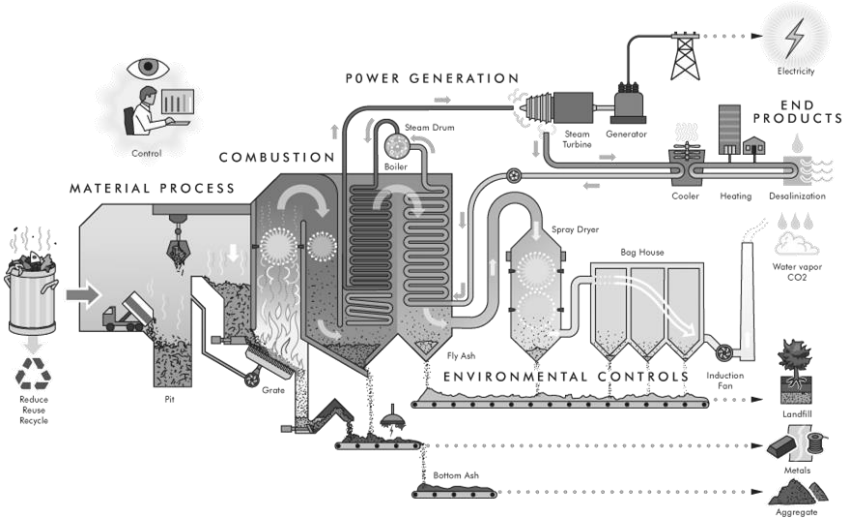

Figure 1.11: Overview of an incinerator facility [12]

Magnitudes and potentials

In Europe, the total amount of municipal solid waste is approximately 200 million tons per year, 50% of this is incinerated in waste-to-energy facilities. In Western European countries like the Netherlands this percentage can be as high as 90% [1].

The main output of incineration, bottom ash, is a moist granular material with 90% of the mass having particles sizes between 0-40 mm. Table 1.4 shows its typical composition. This table also shows approximate prices for each constituent and the total potential value for the 20 million tons of incinerator bottom ash (IBA) in Europe. It can be seen that the current total amount of IBA in Europe has a potential value of more than a billion euros. Despite this high potential value, most of Europe's bottom ash is currently still being landfilled [1] at a cost of around 50€/ton (depending strongly on local legislation), causing its current value to be a negative one billion euros. The full recovery of valuable constituents could result in an overall benefit of almost two billion euros for Europe.

Table 1.4: Typical composition of MSWI bottom ash

Constituent	Concentration	Price	Potential value
Minerals	75%	4 €/t	60 M€
Fine minerals	15%	-50 €/t	-150 M€
Ferrous metals	7.5%	100 €/t	150 M€
Non-ferrous metals	2.5%	1000 €/t	500 M€

An important part of the potential value of IBA resides in the metals, especially non-ferrous metals. Here aluminum is particularly interesting because of its high scrap value and large carbon footprint. The production of aluminum from scrap results in a 90% CO2 reduction in comparison to production from raw (bauxite) ore [13, 14].

The recovery of heavy non-ferrous metals increases the overall recycling rate of these metals, resulting in less depletion of scarce natural resources, and less metal content in the IBA, that may be a problem in the long term because of its possible leaching to the groundwater [15, 16].

State of art

Currently, the standard technology for treating IBA is to remove all non-ferrous (NF) and ferrous metals above 12 mm using magnets and eddy current separators. The fine fraction is either land-filled or aged with the rest of the mineral product for 6 weeks to induce carbonation and reduce leaching. After acceptable leaching values are reached, the material can be used in road foundations. Depending on the local legislation, the material may need to be carbonated, sealed, stored in a recoverable way and monitored for its entire lifespan [17].

Table 1.5 and Table 1.6 present reference data for the processing of one ton of raw IBA by a Dutch state-of-the-art bottom ash processing facility operated at maximum aluminum recovery (and a relatively high slag content of the NF mix of 57%) [5]. Within the reference facility, three streams are produced. Table 1.5 shows the wet amount and moisture content of these three streams. The size distribution and aluminum content of the dry IBA-rest and NF metal concentrate are shown in Table 1.6.

Table 1.5: Properties of main product streams

	Weight (kg)	Moisture (%)
IBA-rest	875	13.3
NF	41	6.1
Ferrous	84	-
Total	1,000	-

Table 1.6: PSD and aluminum contents/recovery

Size class	Size distribution (%)		Al grade (%)		Al recovery (kg/ton)		Total recovery
(mm)	Rest	NF-Conc.	Rest	NF-Conc.	Rest	NF-Conc.	(%)
>20	7.8	44.3	0.1	27.6	0.08	4.69	98.4
6-20	16.3	29.5	0.5	49.7	0.57	5.62	90.8
2-6	30.0	11.8	1.3	39.8	3.06	1.80	37.1
<2	45.9	14.4	0.7	0.6	2.61	0.03	1.27
Total	100	100	0.8	31.6	6.32	12.14	65.8

The data show an excellent aluminum recovery for the +6 mm class. However, the recovery for the 2-6 mm is significantly lower. One ton of wet IBA contained about 18.5 kg of aluminum. Almost 3.1 kg remains in the 2-6 mm fraction of the IBA-rest and is not recovered. Separation of this fine aluminum using eddy current separators is theoretically possible; however, properties of the fine material cause it to be uneconomic.

Separation objectives and challenges

The main separation objective for MSWI-bottom ash is to recover the valuable constituents into a form of output that can be valorized. Since the main proportion of the potential value of bottom ash lies in the nonferrous metals content, this means the objective should be to separate and concentrate the nonferrous metals.

The most cost-efficient process to achieve this separation is to use an eddy current separator. For this process to be efficient, prior strict size classification is essential. However, the high content of fines (0-1mm) in the 0-12mm fraction combined with the moisture present from quenching, makes classification by conventional techniques uneconomic.

In order to enable economic nonferrous metal recovery, a novel classification technique is required.

1.3.2 Crushed concrete

Crushed concrete is the biggest contributor to construction and demolition waste (CDW). It originates mainly from the demolition of buildings, which contain a large variety of constituents strongly interconnected to each other. Even though an effort is made to extract constituents separately, mutual pollution of the separate streams within CDW is unavoidable and the problems associated with this must be solved in the recycling process.

However, the challenge for an economic recycling of crushed concrete is not posed by the pollution problems only. Difficulties also arise from other factors. These factors include its relatively low price/ton, the magnitude of the total waste stream and complex market situations. However, anticipated changes in the future will force a different way of handling this waste stream, which can bring big advantages, but require some fundamental changes.

Magnitudes and potentials

Dutch government projects an increase of the amount of crushed concrete (CC) in the Netherlands from 10Mton in 2005 to 22Mton in 2025 [18]. This strong increase is caused by the construction boom in the 1950's from which now a lot of buildings enter

their end of life, increased application of concrete in buildings due to higher quality demands and the overall shortening lifespan of buildings. With the current recession this increase has slowed down, however the fundamental reasons for the increase are not eliminated, so the increase will still come.

Currently CC are primarily used as a sub base for road construction. This low-level application provides a surprisingly good end-of-life (EOL) solution in terms of ecology and economy. It replaces high quality (primary) material, reduces transport costs and creates interesting revenues for the demolition companies. The current demand for CC in this sector is in equilibrium with the supply of 10Mton, but due to stagnation in road construction, it is unlikely that it will follow the trend of supply. It is expected that the demand will stay constant or even diminish, resulting in a surplus of over 12Mton of CC in 2025. Prices of CDW will decrease if this surplus is not absorbed by an alternative market, resulting in a bigger need for land filling and threatening the established high level of recycling (i.e. dismantling instead of bulk demolishment).

Crushed concrete is a main component of CDW, and CDW is a main ecological component in the building industry. The IPCC has evaluated seven industries on the possibility to reduce the CO_2 (equivalent) output by 2030 at a certain price, see Figure 1.12 [19]. Within this diagram the building industry stands out for three reasons: overall rate of potential reduction is high (compared to other industries), reduction is cheap (for the lowest price already 90% of all potential reduction can be realized) and the potential is evenly spread over OECD (Organization for Economic Co-operation and Development), EIT (Economies in transition) and Non OECD/EIT. This means that even in societies with high technological development, potential is high.

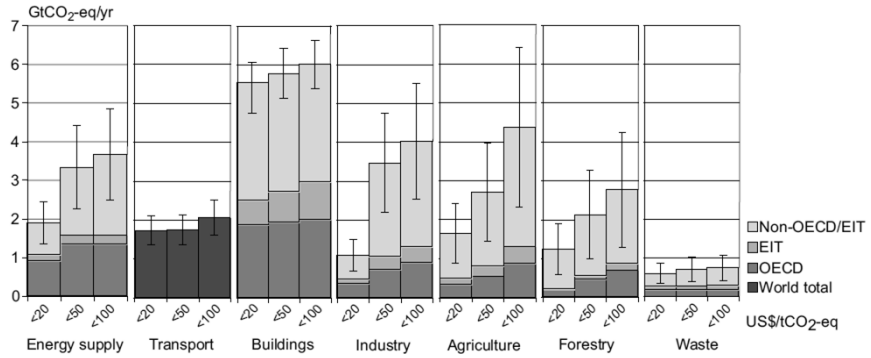

Figure 1.12: Potential CO2 reduction dollar spend, specified per industrial sector. Estimated economic mitigation potential by sector and region using technologies and practices expected to be available in 2030.

Utilization of the surplus as an aggregate for new concrete will not only have economic and ecological benefits for the CDW recycling industry but also for the mortar producers. The mortar industry feels the increasing societal pressure to become more 'green'. As primary aggregates are becoming scarce an alternative is desirable, both to reduce the burden on the environment, as to avoid increased prices. In addition, (coupled with the scarcity) supply of primary material will become more centralized, resulting in high transport costs and CO_2 emissions. Contrary to primary sources, demolition companies have a geographical distribution that is similar to that of concrete plants.

The above show a considerable incentive for the use of crushed concrete as concrete aggregate. To enable this, the crushed concrete needs to meet certain quality requirements. The most critical of these requirements are the amount of fines (0-1 mm) and the level of contamination. The fines enable bridge forming due to hydroscopic and hydraulic effects; making storage of aggregates in silos impossible. Furthermore, the fines decrease the workability of a concrete mixture made with CDW-aggregates because of their high water absorption and high specific surface area. Contamination decreases structural performance and durability because of intrinsic weakness and possible expansions and can cause aesthetical problems in surface finishing [20, 21]. Untreated crushed concrete does not usually meet the quality criteria, so processing is necessary. However, the low value of aggregates requires cost-efficient processing, which is currently not available. So far, however, even simple contaminants like wood and steel are not being removed from the -12 mm fraction, since this is difficult to achieve without complete drying or using an expensive wet processes [22].

State of art

In the current Dutch situation, the primary use of construction and demolition waste is in road foundations. Only about 5% of the crushed concrete is recycled into concrete [18]. In short, this is because of three reasons. First, the market of CDW is in equilibrium, resulting in lack of incentive to recycle the material in innovative ways. Second, prices for primary material are still low. Third, conventional processing of granulates into suitable concrete aggregate is still too expensive.

Traditional processing involves screening and washing, which are expensive, in part due to operating costs but mainly because of the high disposal costs of sludge. Furthermore, the processed crushed concrete only contains the fraction larger than 4mm, which leaves a big volume unused.

In the Closed-Cycle-Construction-project a novel approach was investigated [23], which used heat to separate aggregates and cement to make them suitable for concrete manufacturing. The organic content of CDW was burned to save energy, but because the thermal treatment was carried out on almost the entire CDW stream, the process was found to be economically not viable because of the high energy consumption.

Separation objectives and challenges

At present only crushed concrete larger than 4mm can be recycled as aggregate due to technological reasons. Since this >4mm fraction is less than 50% of the total 0-16mmm concrete granulate, it is desirable to lower the split point to optimize the amount of recycled material. Limiting factors are the processability and storage in upgrading processes, workability of the product in a fresh concrete and the quality of the recycled aggregates (i.e. contamination).

These problems relate mainly to the specific surface area of particles or to the fine particles in general. In a 0-16mm granular material, more than 75% of the surface area is concentrated in the 0-1mm particles. The removal of these particles will also eliminate all its associated problems, making 1mm an ideal cut-point in the trade off in economics and product requirements.

Another interesting aspect of a 1mm split point concerns the cement content of crushed concrete, which can be considered to be a valuable constituent. Current

breaking techniques focus on efficient breaking while minimizing the amount of fines produced and often produce chunks of concrete instead of de-agglomerating the concrete into aggregates and cementitious fines. With growing environmental awareness, it is very likely that the importance of cement recovery will steer the breaking processes towards de-agglomeration techniques.

In this situation, the cement will be present in one of two forms: either as cementitious powder or as a small layer on the surface of aggregates. For the latter, surface area will be the dominating factor for cement presence in a size fraction. Therefore, a cut on 1mm will be effective on both sides: the coarse product will become a fraction with optimized properties and volume while the fines will have an optimized amount of cementitious material. The fine product can be further processed by using selective milling processing to concentrate the cementitious material. Reusing this material in a cement kiln could have an enormous impact of the recovery of CO_2 production in the concrete production cycle [24].

The above suggest the separation objective for crushed concrete to be a classification at a particle size of 1mm, while removing all contamination (according to the code NEN-EN12620 only contamination >4mm is of concern). Since the crushed concrete is moist (due to dust prevention and outdoor storage), classification down to 1mm is not economically viable. Because this classification is unobtainable, wind sifting is also not possible. Therefore, a novel technology is needed that removes the 0-1mm fraction prior to removing the contaminations.

1.3.3 Sifting sand

Sifting sand is another flow within construction and demolition waste (CDW). Even though it is closely related to crushed concrete, the problems concerning sifting sand are more similar to those of municipal solid waste.

Sifting sand originates as the residue stream of the first separation process of the main CDW flows. When crushed concrete or mixed granulates are collected at a construction or demolition site, the fine material (<16mm-40mm) of the material is sifted off before the first processing step (e.g. a crusher). This finer fraction is called sifting sand and contains an extremely large variety of materials, since it can contain almost anything that is present on a construction site.

This large variety of constituents makes the waste stream extremely complex to process. Furthermore, it also contains high amounts of soil residues, foils, wires, and foams which make it highly unsuited for conventional sieving techniques.

Magnitudes and potentials

In Europe the total amount of sifting sand is approximately 25 million tons. This material is now mainly landfilled at a cost of around 50€/ton (depending strongly on local legislation) [1].

The biggest potential for the complex waste stream of sifting sand is to reduce the amount of it that needs to be landfilled. If the product can be separated into isolated groups of constituents, a large portion can be reused in a useful application. Since the costs of landfilling are high, a reduction of the flow that needs to be landfilled quickly increases the value of the whole flow. E.g. when 20% of the flow can be extracted

and used in a useful application against 0€/t, it will effectively generate a value increase of 10€/t on the whole flow.

An interesting sub-division of the flow for separation is:

- Minerals
  - This flow can be mixed in with mixed granulate and used in foundation layers: requires gypsum needs to be removed
- Ferrous and Non-Ferrous metals
  - Is only a very minor component but interesting for its high potential value: requires fines to be removed
- Sand fraction(+gypsum)
  - Can be used for stabilizing layers, but requires organics to be removed
- Burnable materials
  - Recover caloric value, but requires fine moist fraction to be removed

Table 1.7 shows the typical composition, the approximate values of the main components and the total potential value for the 25 million tons of sifting sand in Europe. If separation into these four groups is completely achieved a value surplus of 100 million euros per year could be generated.

Table 1.7: Composition and potential value of sifting sand (data from Van Vliet)

Constituent	Concentration	Price	Potential value
Fines (0-1mm)	40%	1 €/t	10 M€
Minerals (natural stone, ceramics, porous stones)	30%	4 €/t	30 M€
Glass	5%	0 €/t	0 M€
Gypsum	10%	1 €/t	2.5 M€
Ferrous and non-ferrous metals	0.5%	150 €/t	19 M€
Burnable material (e.g. plastics, wood, bitumen, Styrofoam, Insulation material)	4.5%	-10 €/t	-11 M€

Separation objectives and challenges

The main objective for processing and recycling sifting sand is to reduce its complexity. For this, the material needs to be classified both to size as to volumetric weight.

The most efficient way to achieve this, would be to first perform a size classification prior to a volumetric weight classification. However, conventional size classification techniques are unsuitable for this material. The problems are caused by the high amount of fines and the moisture associated with these fines.

In order to reduce the complexity and recover value from this flow, a novel classification technique is required.

2
The ADR concept

With current technology it seems economically unfeasible to process moist granular material smaller than 16mm. Due to the fact that the potential to upgrade is so large, it is clear that the problem is fundamental of nature and will not be solved by adapting current technology. New technology must be developed to enable recycling.

In this chapter, the root cause is identified and quantified. After understanding the origin of the problem it is demonstrated why current technology falls short and what needs to be changed to solve the problem. This change is transformed into a new recycling concept. The concept of the new technology is then converted into practical form and the value of the key-parameters is determined.

2.1 Problems in recycling

Effective recycling starts by liberation of the materials that need to be separated. With the waste streams of interest (moist granular 0-16mm material) this proves problematic. However, from practice it can be observed that coarse material, as well as dry material pose no problems. The problem is caused by the combined presence of fines and moisture.

2.1.1 Source of the problem

A microscopic image of fine moist granular material is shown in Figure 2.1. It can be seen that fine particles, with a size <1 mm, are formed into a network connected by high tensile strength water bonds, as a result of surface tension. These networks of fines interconnect large particles, promoting agglomeration. Table 2.1 shows empirical data found in mineral processing literature [24] on the typical limiting moisture content for conventional classification techniques (flat screens). Figure 2.2 shows experimental recovery curves of flip-flow screens at a classification size of 4, 8 and 12 mm. Flip-flow screens can handle moist material better than conventional flat screens, since the stretching motion of the deck reduces clogging. The data shows that for typical free moisture levels of waste streams (>5%), efficient classical classification below 8 mm becomes impossible when using existing techniques.

Table 2.1: Literature table on limiting moisture level in mechanical classification [24]

Opening size [mm]	**1**	**2.5**	**5**	**10**	**20**	**>25**
Moisture threshold [kg/kg]	0%	1%	2%	4%	6%	No limit

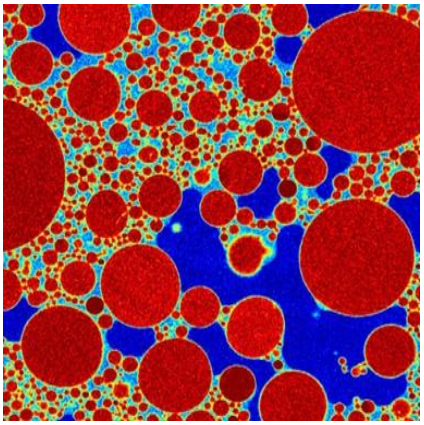

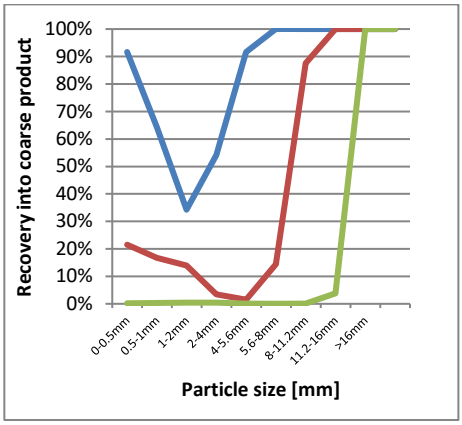

Figure 2.1: CT image of fines with associated moisture (largest particle is 1mm in diameter)
Figure 2.2: Experimental recovery curves of moist feed particles into the coarse product for three screens, with 4, 8 and 12 mm holes, respectively.

The root cause of the problem is the combined presence of fines and surface moisture. Surface moisture is adhered to the outside of the particle in contrast to absorbed moisture which is present inside the particle and has no binding effect. The moisture on the surface of the particles, will be distributed according to specific surface area of the particle size fractions. The surface area of a specific size fraction is inversely proportional to the diameter; therefore, the vast majority of the moisture is directly associated with the fines. Hence, the removal of fines will also result in the removal of moisture. This reduces agglomeration of the whole material dramatically since the adhesive element is removed, the void filling fraction (fines) is removed, and the inter-particle distance is increased.

2.1.2 Available solutions

In conventional recycling and mineral processing, problems caused by moisture and fines are eliminated either by complete drying or complete wetting of the material.

By completely drying the material, the effect of surface tension is eliminated. However, such processes consume large amounts of energy. Completely drying granular materials may also introduce health risks by the formation of airborne dust and fibers. Measures such as water spraying, ventilation, the use of respirators, or even pressurized working areas, are necessary to guarantee a safe working environment and can make operations with dry fine materials very expensive and impractical.

In complete wetting techniques, the effect of surface tension is broken by saturating the voids between particles. When all particles are in suspension, they can be classified efficiently. However, after classification the water needs to be removed from the products. This proves to be difficult for the fine fraction, which results in the formation of a sludge waste stream which is expensive to dispose in urban environments.

Both methods seem disadvantageous, primarily because of their high costs and environmental impact. This argument weighs heavy when processing waste streams. The potential of recycling waste streams lies mainly in the large volumes available. The total value contained is high, but the processing costs per ton must remain low in order for the processes to remain economically viable. Therefore, a novel method needs to be developed to recover the potential value. In order to obtain such a method, the problem is studied to a deeper level.

2.1.3 Physics of the problem

In typical classification processes, such as a vibrating screen, particles of different sizes are liberated from moist clusters due to the repeated accelerations imposed by the sieve deck. Directly following this liberation, some particles will pass the mesh and some particles will not, see Figure 2.3. If the acceleration of the screen is not high enough, fine particles will remain attached to a coarser particle or to the screen itself, due to the bonding force exerted by the water, and cannot pass the sieve.

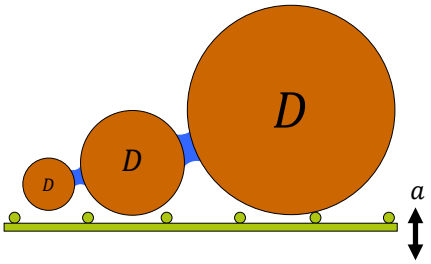

Figure 2.3: Schematic of a sieve deck with moist particles

To estimate the acceleration needed to liberate fines from a particle as a function of the diameter of the finer particle, a simple analysis is performed. Large particles will be accelerated by the deck and liberation of fines will occur if this acceleration cannot be transferred to the small particle via the adhesive force. The adhesive force is developed via the liquid pressure in the moisture present.

The situation can be described by three elements: the inertia force, adhesive force and liquid pressure. The inertia force required to accelerate the fine particle is given by:

$$F_{inertia} = \rho_p \frac{1}{6} \pi D_i^3 a$$

In which ρ_p is the density of the particle (2500kg/m^3), D_i the diameter of the fine particle and a the acceleration imposed by the deck of the screen.

This force must break the water bond and so must be bigger than the adhesive force given by:

$$F_{adhesive} = \sigma \, D_i^2$$

In which σ is the liquid pressure caused by surface tension and the cube of the particle diameter D_i is the estimated wetted surface which is in contact with other particles. The liquid pressure is assumed to be equal throughout the mixture and can be estimated to be equal to:

$$\sigma = \frac{\gamma}{d}$$

In which γ is the surface tension of water ($75 mN/m$) and d is the diameter of particles which contribute most to the total surface area within the mixture. In this first simple estimation it is assumed that the curvature of the water surface is roughly equal to the radius of the particles which has the most wetted surface.

The required acceleration (normalized by g) for liberation can thus be given by:

$$a = \frac{\gamma}{g\rho_p \frac{1}{6}\pi D_i d}$$

Figure 2.4 shows some results of this calculation. The first graph is for a mixture in which the surface area is dominated by 250µm particles. In the other graph the surface area is dominated by 1mm particles, which can be interpreted as the same mixture where the fines are removed.

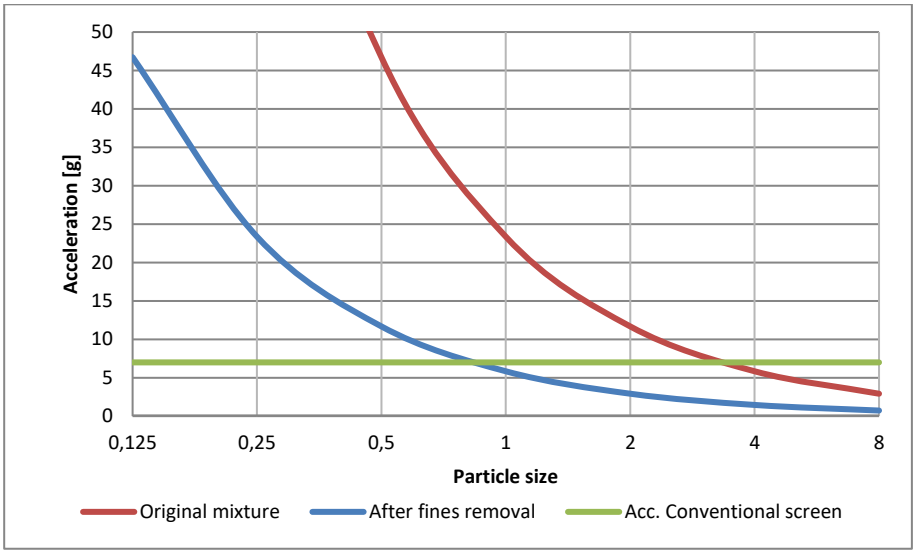

Figure 2.4: Range of required acceleration for liberation, for a mixture

The figure shows two important features. First, the acceleration needed for liberation increases rapidly for smaller particles. To liberate a 250µm particle, the acceleration needed is impossible for a conventional screen. Therefore, a radically new technology is required to overcome this problem. Second, it shows that once the fines particles have been removed from the mixture, much lower accelerations are required for further classification and thus conventional techniques become applicable again.

2.2 ADR

2.2.1 Main principle

To directly classify fine moist materials down to the sub-millimeter region, extreme accelerations are required. These accelerations cannot be imposed by a sieve deck,

therefore, the medium imposing the acceleration and the one performing the separation have to be disconnected. This new approach is called ADR (Advanced Dry Recovery).

In an ADR unit the acceleration is imposed by a solid flat surface moving at high speed. A thin layer of agglomerates collides with this surface, the inter-particle water-bonds are broken and a particle-jet is formed. This particle jet interacts with air, causing a de-acceleration inversely proportional to the size and density of the particle, effectively creating a classification mechanism.

2.2.2 Practical implementation

A practical way of obtaining a high velocity surface that can be fed by a thin layer of material is shown in Figure 2.5. In this setup a drum with blades rotates at high speed of revolution while material is continuously supplied via a feeding plate. The particle jet widens into the enclosing, which imposes secondary impacts and converges the particle jet. Fine and light particles are slowed down by air-friction and will descend onto a first conveyor, while coarse and heavy particles will travel to the far end of the enclosing and will be collected on a second conveyor.

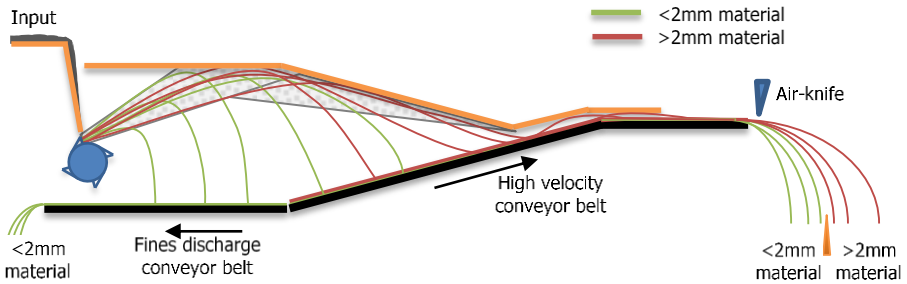

Figure 2.5: Design of an ADR unit

Within this configuration, a number of parameters play a key role in the classification. These are:

- The layer thickness on the blade
- The distance at which the products are divided into fine and coarse
- Rotational velocity of the drum
- Diameter of the drum
- Height of the blades on the rotor
- Maximum grain-size fed
- Number of blades on the drum
- Height of feeding
- Shape of the encasing surrounding the particle jet
- The location of feeding relative to the axis of rotation of the rotor
- The angle of the blade relative to the secant line
- The velocity of the coarse fraction collection conveyor
- The velocity of the air-flow of the air-knife

The layer thickness plays a crucial role in the relation between the capacity of the ADR and the efficiency of water bond break-up. In the collision with the rotor blade, the agglomerate is accelerated to the velocity of the blade. The layer thickness in relation to the particle diameter determines the probability of the mode in which this happens: direct or indirect hit, see Figure 2.6. When a particle is hit directly, it will experience a very high acceleration and try to propel the particles that are attached to it at the same acceleration (via water bonds). When the water bond is not strong enough to accommodate this, it is broken and the particles can be classified effectively. However, when the layer thickness is too thick, particles will be hit indirectly (effectively the transfer-time increases), and accelerations will not be high enough to break the water bonds. The layer-thickness is therefore, a key parameter for the effectiveness of the classification.

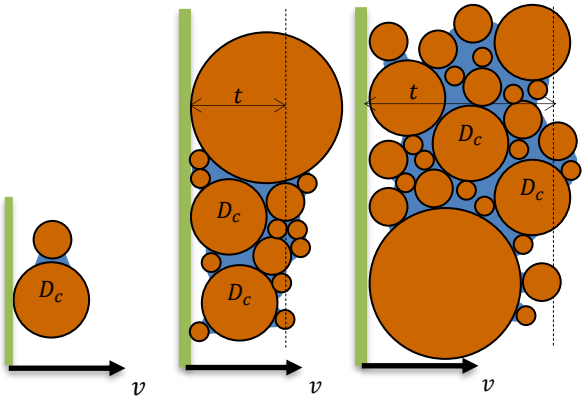

Figure 2.6: Relation between layer thickness and indirect or direct impact

Once the agglomerate of particles has been disintegrated, the fragments follow a ballistic trajectory until they are collected at a certain horizontal level. The horizontal distance traveled till collection is (primarily) a function of the particle's terminal velocity. The distance at which a separation between two products is made will be another very important classification parameter, which primarily determines the quality of the classified products. According to the desired grade and recovery of the products, a distance is chosen where the particles with a lower terminal velocity are separated from the ones with a higher terminal velocity.

The rotational velocity of the drum, together with its diameter, determines the tangential speed. The tangential speed determines the acceleration of the particles when hit by the blade. This acceleration must be balanced between sufficient breaking of water bonds and limiting the crushing of particles. In general, larger particles will break at lower impact velocities. Therefore, when the upper size of the feed is increased, the rate of breakage will also increase. The tangential speed also determines the distance particles will travel and will therefore, be a dominant factor for determining the distance at which the fine and coarse product is separated.

The rotor is fed with a constant layer of material, falling down the feeding plate. The number of blades combined with the rotational velocity determines the amount of time between blades passing the feeding point. Within this time the total height of the blade needs to be filled with material. Therefore, the height of the blade together with the

rotational velocity and the number of blades determine the velocity of the feed. The required velocity determines the required height of the feeding plate.

The height of the blade relative to the particle diameter determines the amount of particles hit partially. Since the total height of the blade is filled with a homogenous layer of material, the chance of a particle being hit partially is directly proportional to its diameter, see Figure 2.7. The larger the particles, the bigger the chance it is hit partially and propelled at an aberrant velocity and angle.

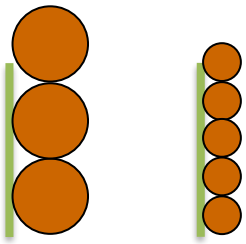

Figure 2.7: Indication of partially hit particles in relation to particle size

In the case that the jet interacts with the confinement, the shape of the confinement determines how the jet is redirected. By using a downward directed confinement, the total length of the ADR can be reduced. However, when the angle of inclination is chosen to sharp, the coarse particles could bounce back onto the fines collection conveyor.

The position of feed relative to the rotational axis of the rotor determines the angle at which the jet is released into the confinement. See Figure 2.8. The shooting angle largely determines the distance particles will travel. As the length of the trajectory increases, so does the effect of air-friction. Therefore, the classification efficiency can be higher when the total trajectory length is increased.

Secondary, the shooting angle will determine how the jet interacts with the confinement. When the angle relative to the confinement is too steep, the jet will not converge and the classification efficiency is reduced. Also, at the moment of impact with the confinement, fines will be released for a second time. When the position of impact is chosen correct, the fines can be collected more effectively.

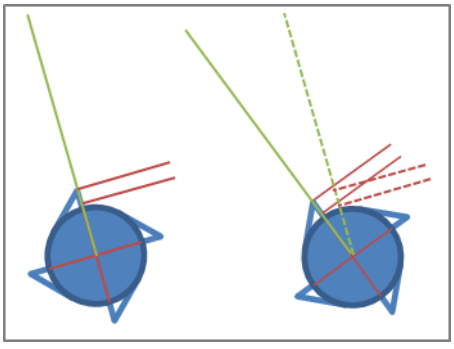

Figure 2.8: Shooting angle as a function of the feed position

Secondary to the statistics of a partial particle collision, the height of the blade also plays a role in the opening angle of the jet. When the line of feeding does not go through the rotational axis, the height of the blade will determine the difference in the shooting angle between the top and bottom of the blade, see Figure 2.9.

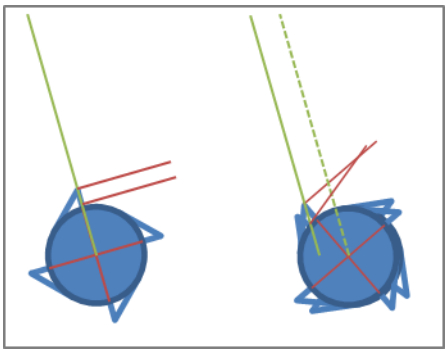

Figure 2.9: Influence of blade height on shooting angle

Secondary to the statistics of direct versus indirect impact, the layer thickness plays another role in the classification. When the layer-thickness increases, in effect the range in feeding position increases, effectively increasing the opening angle of the jet.

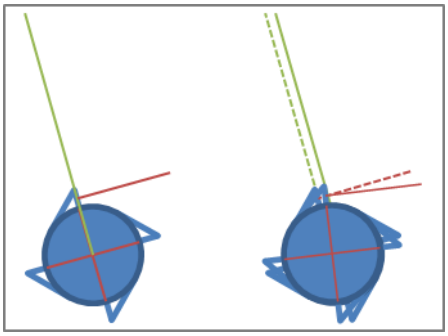

Figure 2.10: Increase of opening angle of the jet due to layer thickness

To further refine this, a distinction must be made between the fed layer thickness and the compacted layer thickness. The material is fed into the ADR out of a relatively thick layer at low speed. During descent along the feeding plate, the layer accelerates and is therefore stretched. Since the feeding plate is at an angle to vertical, the layer will be compacted. However, this will not be a perfect compaction. When the agglomerate is hit by the rotor it will first be compacted, while being accelerated. For the opening of the jet the un-compacted thickness is of importance, while for the breakage of water bonds the compacted thickness is of importance.

Whilst the particles are moving away from the rotor-blade after collision, the rotor-blade will rotate in the same direction. When the velocity after collision is insufficient

(i.e. the restitution factor is low), it can occur that the rotor catches up with the particle and inflicts a secondary hit. To reduce this effect, the rotor blade can be placed at an angle r.t. the normal of the drum, see Figure 2.11.

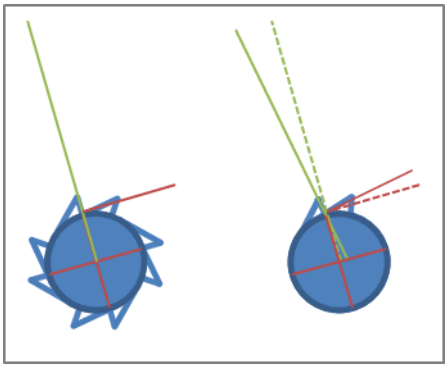

Figure 2.11: Angle of rotor-blade r.t. normal to prevent secondary impact with rotor

Additional to the feeding and rotor configuration, the jet will also open because the particles will not be perfectly round and the surface of the blade will not be perfectly smooth. The impact vector will not be perpendicular to the surface and not coincide with the particles center of gravity. Therefore, the particle will leave the surface at an angle and with a certain rotational velocity.

Finally, classification by the air within the ADR will remove a substantial amount of the fines. However, it may be that the removal of fines is still not sufficient for follow up processes. If so, another feature of the ADR can be made use of. During classification the material is liberated and spread out over a large area. By collecting the material over a large surface area (i.e. a fast moving conveyor belt), re-agglomeration is prevented and the layer thickness of the material will remain limited. These two aspects make the flow very suitable for ballistic classification supported by an air-knife. The air-knife will deflect light and small particles, making the ballistic classification more efficient.

The list discussed above is extensive but not yet complete in describing all relevant parameters. It does, however, demonstrate that careful tuning of a large range of parameters is required to obtain an effective classification.

2.2.3 Classification of a moist granular waste stream 0-16mm at 1mm

For high grade recycling, the waste materials need to be made suitable for conventional upgrading techniques such as sieving, ferrous-metal extraction and eddy current separators. To enable the efficient working of these techniques the fines and their associated moisture must be removed. The removal of the <1mm fines will result in a loose grained material, which is suitable for further upgrading. The specific value of the components of a waste stream and required techniques for their extraction will determine the exact cut-off points for the grade and recovery. Generally, however, to obtain a processable product, the 0-2mm grade of the product must be reduced to less than 15% and to retain an economic process the recovery of the 2-16mm fraction

must be higher than 90%. The following section will discuss the parameters of an ADR that will allow classifying the targeted waste streams to this end.

Since conventional processes are able to liberate and classify at particle sizes larger than 12-16mm, the upper size of the ADR input will be limited to that value.

The economics of the process are largely dominated by the allowable throughput of the ADR. Furthermore, the throughput must be compatible with the throughputs of other, conventional, processes upstream and downstream the ADR. Therefore, the capacity must be in the order of 60-120 t/h.

The boundary conditions for the ADR design can be summarized as follows:

- Classification grain size: 2 mm
- 0-2mm grade: <15%
- 2-16mm recovery: >90%
- Maximum grain size: 12-16 mm
- Throughput: 60-120 t/h

The required parameters in the ADR design:

- Tangential speed: 25 m/s
- Rotor diameter: 0.40 m
- Blade height: 0.08 m
- Rotational velocity: 1000 RPM
- Feed height: 1.6 m
- Rotor/machine width: 1-2 m
- Speed coarse product collection conveyor: 4.5 m/s
- Speed air-flow air-knife: 25 m/s

Based on this basic ADR design an experimental study was conducted to quantify the classification. Furthermore, the data resulting from these experiments form the basis for a 'first principles' model which can be used to further refine the design and optimize the classification. First, the break-up of the moist particle cluster will be investigated in detail. Hereafter the classification of the broken-up cluster is studied.

3

Structure and break up of unsaturated poly-disperse particle mixtures

The ADR enables high grade recycling by breaking up moist particle clusters using high accelerations. To investigate the workings of the ADR, first the break-up of these clusters must be studied. To understand how a cluster breaks up, the structure and forces within the moist particle structure itself must be understood.

3.1 Introduction

The ADR concept is used to liberate particles that are agglomerated into a moist clumpy material and then and classify them according to size and density. It does so by the subsequent actions of freeing the particles from their agglomerates by the impact with a spinning rotor, followed by friction with air during the ballistic trajectory of the liberated particles and the remaining agglomerates through the encased volume of the ADR. The liberation at the rotor is usually incomplete for fine particles, since the ratio of the binding forces between particles as a result of moisture over the inertia forces resulting from the acceleration of the agglomerates quickly increases for smaller particles. As a result, heavier (larger) particles will break away from each other when the agglomerates hit the rotor but lighter (smaller) particles may remain bound to the surface of other particles. This can be a major issue in the further processing of the heavier (larger) particles, and therefore the processes involved need to be understood.

Understanding the structure of partially saturated poly-dispersed mixtures is relevant for a broad range of engineering applications where moist granular materials are being utilized and processed, including granulation [25], mechanical, thermal and electrical properties of packed beds [26, 27], chemical and adsorption processes [28] and multiphase flow [29]. In many cases, interesting macroscopic properties of such packings relate directly to their microscopic geometry. Also, liquid bridges within a

mixture create a structure that plays a key role in describing macroscopic properties like structure stability, strength and workability characteristics. For this reason, a large number of experiments and computer simulations have been executed to provide data and understanding of the structure of packed beds and capture their essence into models [25, 26, 30].

To understand the structure in a way that is relevant for the working of the ADR a number of items must be carefully considered:

- Range in particle sizes
- Amount of moisture
- Method of mixing
- Time-scales of mixing and break-up
- Known and unknown parameters of the system

For many applications in raw material processing, the size distribution of granular flows of particles essentially covers a wide range of sizes. For granular waste flows, and for crushed concrete and incinerator bottom ash in particular, the ratio of coarse and fine particle diameters that needs to be taken into account for a realistic description of the material is typically about 100 [32]. However, experiments or simulations with granular materials with particle size distributions that cover a similarly wide range of particle sizes are difficult, since large size ratios imply both high spatial resolution and very large numbers of the smaller particles. For this reason, studies on packed beds with non-uniform particle size have typically considered several thousands of particles with a factor of 2-5 between the largest and smallest particles [26, 27, 28, 30, 33, 34, 35]. In exceptional cases, data have been generated for larger size ratios, up to a factor of 8 [35, 36].

For granular waste materials such as MSWI bottom ash, the structure of the packing is formed by adding water to a poly-disperse particle system under repeated mixing. Excess water is allowed to run off freely, while dust-formation must be prevented because of health issues. Therefore, the moisture in the system will be low enough to prevent full saturation of the pores, but high enough to form fully interconnected networks (the packing is coherent).

Within the system there is a mutual influence of the position of particles and the characteristics of the liquid bridges, creating the need to solve these two interactions simultaneously. However, the dynamics of the formation processes are such that we can assume an infinite mixing period at infinitely slow rate. Therefore, the shape of a single liquid bridge is dictated by the Young–Laplace equation and the mixture is at thermodynamically equilibrium.

During break-up of the cluster, the time-scale of the deformation (i.e. acceleration) will determine the forces between the particles. These accelerations are determined by how the particles within the cluster move relative to each other, when hit by the rotor.

In many engineering applications only the particle size distribution (PSD) and moisture content of unsaturated poly-disperse particle structures can be assessed. To predict relevant properties of the mixture from the PSD and moisture content alone, two assumptions are made. First, any tendencies of moisture to favour contacts (water bonds) between certain sizes of particles over contacts between other sizes are ignored

in the modelling. Second, the statistics of particle-particle contacts of the system is assumed to follow a simple ergodic principle for spherical particles, regardless of the (complex) dynamic history of the system of sedimentation and shear, and ignoring the fact that the ash particles are granular in shape. Both assumptions are relatively strong, but they are believed to be necessary for making the system tractable to analysis.

In essence the kiss matrix of a random system of spheres is modelled and verified with a lab experiment and the influence of static liquid bridges is then evaluated separately. As a final step, the combination of these elements is compared to a special ADR experiment, in which the liberation of fines is studied in detail, to check the validity of the underlying assumptions.

3.2 Analysis of particle structure

3.2.1 Introduction

Ideally, models for predicting the kiss matrix should be verified against strongly poly-disperse mixtures, so that they can be properly tested on their different physical foundations. Of all the experimental techniques for detecting contacts in a bed of particles [28, 29, 35], X-ray microtomography is the proper tool to generate data in the limit of large particle size ratios. The technology is able to deal with hundreds of thousands of particles, for the monodisperse case [37], as well as polydisperse sizes and shapes [35, 36, 38].

Extending on this work, an experiment was performed that makes use of the high spatial resolution of X-ray microtomography to extend the experimental data to a packing of more than 200,000 particles with a ratio of 18 between the largest and smallest sizes. A packing inside a sample cylinder of 10 mm inner diameter was scanned with a resolution of 11.4 micron. This way, a mixture of glass beads ranging in size from about 100 microns to 2 mm could be studied (a trial image including also 60-micron glass spheres showed too difficult to interpret). The experimental procedures and algorithm for interpreting the tomograph images are reported below. Hereafter, the results are discussed and the experimental kiss matrix is compared to two existing models and a newly developed model.

3.2.2 Materials and methods

Glass beads were obtained from various manufacturers in different size ranges and screened carefully to produce five narrow size fractions: 106-125 micron, 212-250 micron, 500-589 micron, 1000-1168 micron, and 2000-2380 micron. Crushed minerals composed of a single material often have an approximately Rosin-Rammler or lognormal size distribution in terms of mass [26, 27]. Therefore, this was taken as the basis for the PSD of the scanned mixture.

The geometrical structure of the bed is rather determined by the distribution of material volume over size, than by the distribution of mass. Furthermore, the types of glass used by the various manufacturers of the beads differed somewhat in density. Therefore, the average density of the glass spheres of each size fraction was used to create a cumulative particle size distribution in terms of volume that approximated a lognormal distribution (μ=0.053 mm, σ=1.07 mm). This choice led to the numbers of glass beads for the experimental mixture as presented in Table 3.1.

Table 3.1: Input mixture of glass sphere fractions.

Size fraction	Lower size [micron]	Upper size [micron]	Number of spheres	Method
1	106	125	216629	weighed
2	212	250	22795	weighed
3	500	589	2065	weighed
4	1000	1168	374	counted
5	2000	2380	73	counted

This mixture was produced in 73 equal parts by counting individual spheres for the largest two size fractions and by weighing the finer fractions, using cups made of a plastic that showed no tendency to interact electrostatically with the finest glass beads. Since it is difficult to feed glass particles randomly over the surface of a bed by dropping them in air, and because it was aimed to avoid side effects of dislocation of already deposited spheres by new large spheres impinging on the surface of the bed, the mixture was made to settle in a liquid that was later removed by suction and drying.

A transparent PMMA tube machined for the test (Figure 3.1) was filled 60 mm high with de-mineralized water mixed with a few drops of 2-propanol. The 2-propanol was added to minimize air bubbles entering the liquid with the beads, since air bubbles cause the finest glass spheres to stick to the walls of the tube. PMMA, a polymer composed of light elements and without mineral fillers, was chosen because it is nearly transparent for the X-ray tomograph. The height of 60 mm of liquid was found to be sufficient to spread individually settling glass spheres of all sizes homogenously over an area larger than the cross-section of the tube when fed from a single point near the surface of the liquid.

The 73 equal parts of the mixture were fed one by one through a centered glass funnel ending just above the surface of the liquid. Each part was added in several small scoops while rotating the tube, with enough time in between scoops to allow the material to settle down the tube before new material was fed. This highly controlled feeding proved to be essential to avoid serious segregation of the bed according to particle size due to the higher settling speed of larger particles. After feeding the last part, the liquid above the ca 20 mm of packing was extracted with a syringe and the tube was placed in an oven at 60 degrees Celsius for three days to dry away the remaining liquid. The moisture was removed to increase the contrast in the scan.

The middle 10 mm over the height of the dry packing was then scanned in a Phoenix Nanotom X-ray microtomograph with the settings shown in Table 3.2 and the resulting image was exported as a DICOM stack of ca 2.5 GB.

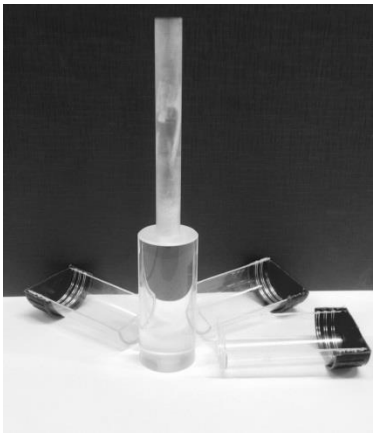

Figure 3.1: Equipment used: cups for handling parts of the mixture and a PMMA tube, inside volume 100 mm high, 10 mm diameter, 1 mm wall thickness.

Table 3.2: Settings for making the X-ray scan

Setting	Value
Scan parameters	500ms, avg 4, skip 1, 1x1 binning, Vsensor 1, shiftV; 2000 Images
	YS = 84, Zs = 35, ZD = 300
	80kV, 260µA, mode 0
	5.7 µm, 121min, 3.39W
Reconstruction	Beam hardening 9.4
	Shifts x = -0.9, y = -0.7; Scale 0; Contrast 10; Calculated calibration value -10.85411
	Resolution ½ (voxel-rib-size from 5.7 to 11.4mu)
3-D image preprocessing	Maximum use of ROI's
	Filter Median 3
Adaptive Gauss filter	Smoothening 4.5; Edge hardening 0.05; Apply opacity mapping

3.2.3 Image interpretation

The pre-processed 3-D image needed to be interpreted into a list of spheres and a collection of kisses between spheres. For this, each sphere was given a serial number, and its diameter and center position were listed. Each kiss was defined by its position and the serial numbers of the two spheres. To obtain this information the image of the glass sphere packing was thresholded, to get a binary field: a 1 at glass voxels and a 0 at air (other) voxels. This field was then first eroded in a special way to obtain centers and sizes, and then a dilated to obtain kisses.

The 2-D cross-sections of the packing showed that some glass spheres had vacuoles of air (Figure 3.2). To eliminate these, the air voxels of the image were divided into connected 3-D regions and small regions were inspected to verify that they were indeed part of a sphere and so could be correctly re-interpreted as 'glass'. Unfortunately, some vacuoles occur so close to the boundary of the glass bead that the image interpretation algorithm connected it to the air outside the bead (see Figure 3.3). The significance of this effect for the statistics was checked and it was found to affect approximately 10% of the beads larger than 500 microns.

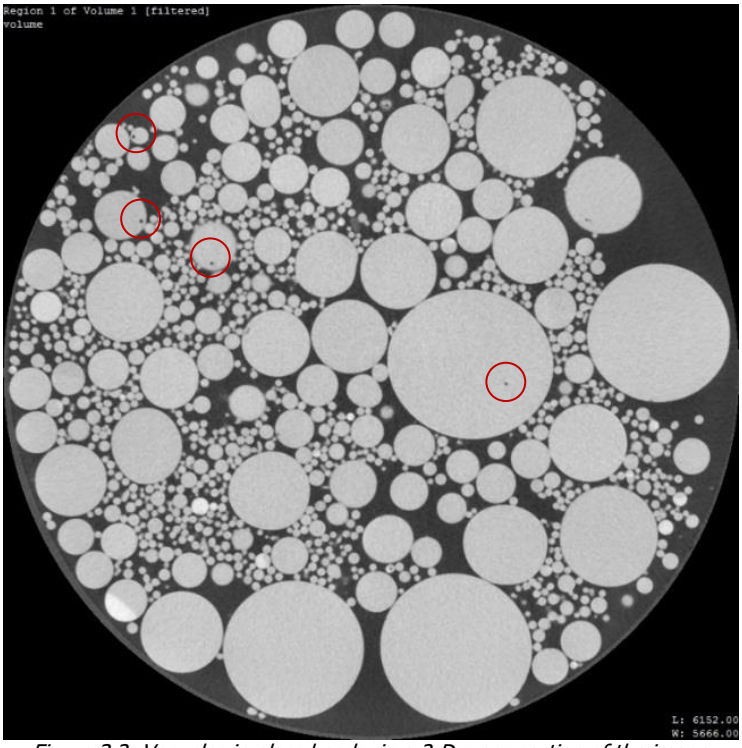

Figure 3.2: Vacuoles in glass beads: in a 2-D cross-section of the image.

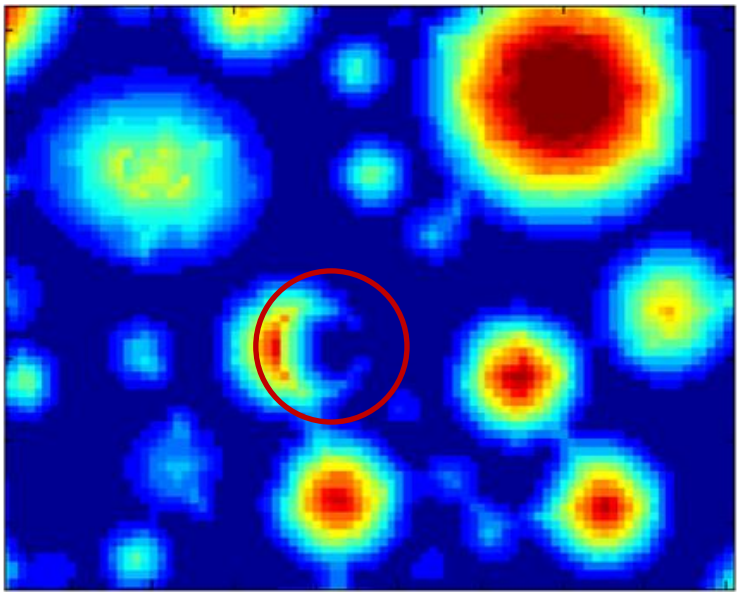

Figure 3.3: Effect on the eroding algorithm of vacuoles near the bead surface

The corrected binary field was then analyzed by an iterative eroding algorithm to determine the minimum distance to the 0-space for each voxel. During each step, the surrounding 26 voxels of all glass voxels are checked to determine if they are void (0). If one or more voxels is a void, the distance of that voxel to the current voxel is determined. If a surrounding voxel has an already identified distance to void, that distance plus the distance of that voxel to the current voxel is determined. The minimum of all determined distances is assigned to the current voxel. If no distances are determined, the voxels value remains 1.

The procedure is described by the following algorithm that runs along all the voxels (i, j, k) of S_1 which is the 3d voxel space of the binary image:

$$S_1 = \text{binary image voxel space (0 for void, 1 for glass)}$$

$$F_{a,b,c} = \sqrt{(a-2)^2 + (b-2)^2 + (c-2)^2} \text{ with } a, b, c = 1, .., 3$$

F gives the distance to the center voxel ($F_{2,2,2}$)

$$S_3 = S_{1\,i\pm1,j\pm1,k\pm1} \quad \text{if } S_1(i, j, k) = 1$$

S_3 is a 3x3x3 subsample of S_1 around a voxel $S_{i,j,k}$ with value 1.

$$T = (S_3 == 0) \odot F + (S_3 > 1) \odot (S_3 + F)$$

T gives the distance of all void voxels or voxels with a known distance to void. ($\odot$ is the elementwise multiplication of the 'binary' (1 for 'true') and 'real-number' matrices)

$$S_{2\,i,j,k} = \min_{>0} T$$

After a full loop along all voxels, the resulting image S_2 is compared to S_1. If these are not equal, the steps are repeated with $S_1 = S_2$. The iterative process stops when S_2 is identical to S_1. The number of steps is equal to the radius in voxels of the largest particle. The value of $S_{1\,i,j,k}$ is a reliable measure for its distance to air, even if parts of the surfaces of spheres are obscured by kisses with other spheres. Sphere centers are identified in the final field as voxels that are local maxima, i.e.:

$$S_{2\,i,j,k} \geq S_{2\,i\pm1,j\pm1,k\pm1}$$

Glass beads from commercial bulk samples are not sufficiently spherical in relation to the resolution of X-ray tomography [38] and so the integer field reaches its maximum in several voxels and so multiple local maxima may be found for each sphere. Elongated islands of local maxima result, of which the centers were interpreted as the centers of spheres and the maximum itself is an approximate measure for its diameter. Multiple centers of the same particle can be combined by setting a threshold on their overlap. The overlap is given by the ratio of the distance between two centers and the sum of each center's distance to void. Centers belonging to the same sphere are given the same ID-number.

The voxel space belonging to a single particle is estimated by assigning the unique ID-number it to its center(s) and expand this value iteratively. At every step it is checked whether a neighboring voxel in the S_2 field has a lower value than the current center voxel and is yet unclaimed. If so, the voxel is claimed by the ID and added to the list of voxels to expand. If not, it is checked whether the neighboring voxels already have

an ID. If so, a kiss is identified, filtered for uniqueness and registered. Once all voxels having the current ID are fully expanded the next ID is expanded. Voxels assigned to a unique particle identifier may be counted to obtain a volume estimate of the particle.

Finally, the kiss matrix is constructed. First all ID's are binned according to their (maximum) radius. Then for every duo of kissing ID's it is determined which two bins are involved. From this the histogram of the kisses according to the size of the particles is determined to obtain the kiss matrix.

3.2.4 Correction for the limited sample size

For the kiss matrix of the packing, only spheres and kisses with centers and coordinates in the sample volume between vertical voxel layers 136 and 829 were taken into account. This guaranteed that all statistics referred to spheres that were completely documented in the image. The selection of the middle section from the bed made sure that the data for spheres and kisses near the bottom and top of the sample volume should present no wall effects.

The choice to include all particles and kisses in the radial direction implied, unfortunately, that spheres near the wall of the tube were not representative for the interior of an infinite packing in two different ways: the statistics of their center positions is affected by the fact that spheres cannot come closer to the wall than their own radius [36, 37], and, spheres near the wall lack kisses with spheres at positions within a radius on either side of the wall.

A correction was applied by determining how many kisses between each two sizes of spheres near the top and bottom surfaces of the sample volume involved a sphere crossing these surfaces (i.e. a wall-effect was artificially created), and these numbers of kisses of each type, multiplied by the ratio of the wall area of the tube segment between vertical voxel layers 136 and 829 and the area of the bottom and top surface of the sample volume, were added to the statistics. In the same way, the numbers of beads were corrected by counting the number of spheres crossing the bottom and top surfaces of which the center was still inside the sample volume. The correction of the wall effect is particularly important for kisses involving larger spheres.

3.2.5 Modeling the particle structure

The determined kiss-matrix is compared to the results of three simple models, one by Ouchiyama and Tanaka [25], another by Suzuki and Oshima [26, 27] and a third model developed below based on an ergodicity-type argument. Below the three models are briefly described.

The Ouchiyama and Tanaka model uses the particle size distribution of the mixture to define an average sphere diameter and an average square sphere diameter:

$$\overline{D} = \frac{1}{N}\sum_i N_i D_i \;;\; \overline{D^2} = \frac{1}{N}\sum_i N_i {D_i}^2.$$

Here D_i is the diameter of spheres of size fraction i (for the present mixture, $i = 1, 2, \ldots, 5$), N_i is the number of spheres in that fraction and N is the total number of spheres. Ouchiyama and Tanaka also define an overall surface porosity ε_A, expressing the degree to which the surfaces of spheres are left, on average, uncovered by kissing

neighbors, and which is related to the model's estimate for the coordination numbers for each size of sphere

$$C(D_i) = 16(1 - \varepsilon_A)\left(\frac{D_i + \overline{D}}{2\overline{D}}\right)^2$$

The surface porosity is a measure for the density of the packing and it relates to the standard volume porosity ε. On the basis of the three numbers $\overline{D}, \overline{D^2}$ and ε_A, the authors propose a formula for the kiss matrix, i.e., the numbers of kisses between all spheres of size i with all spheres of size j in the packing:

$$K_{ij} = \frac{C(D_i)C(D_j)}{4(1 - \varepsilon_A)\left(3 + \frac{\overline{D^2}}{\overline{D}^2}\right)N} N_i N_j$$

The elegance of the formula by Ouchiyama and Tanaka is that it is explicit and has only one parameter ε_A that needs to be fitted to experimental data. A parameter like ε_A is inevitable because the same set of spheres can have random packings of varying porosities depending on the details of its formation. An improved but more complex version of the model proposed by Song et al. [30] introduces an additional fitting parameter m and leads to an implicit form. This model was not used because its physical basis is not as straightforward.

The Suzuki and Oshima model [26] is similar in design to the Ouchiyama and Tanaka model, but it avoids the reference to a sphere of average diameter. Instead, it considers all possible interactions between spheres of different sizes individually. The Suzuki and Oshima model first computes for each size fraction i the fraction of the bed's total particle surface area:

$$S_i = \frac{N_i {D_i}^2}{\sum_j N_j {D_j}^2}$$

From these numbers, the numbers of kisses between all spheres of size i with all spheres of size j in the packing are estimated:

$$K_{ij} = \frac{2\alpha S_i\left(\frac{D_j}{D_i} + 1\right)}{1 + \left(\frac{D_j}{D_i} + 1\right) - \sqrt{\frac{D_j}{D_i}\left(\frac{D_j}{D_i} + 2\right)}} N_j$$

The parameter α relates to the density, or porosity, of the packing.

Another simple model can be derived from the observation that a system of two kissing spheres of diameters D_i, D_j may be defined by a vector $\vec{r}$ running from one sphere center to the other. When any of the two spheres moves over the surface of the other, this vector moves proportionally along the surface of a 'kissing sphere' with diameter $D_i + D_j$ (see Figure 3.4). Many random instances of the binary system could thus be represented by a pattern of dots on this surface, and it may be expected that the number of dots per unit surface area of such a 'kissing sphere' is uniformly distributed.

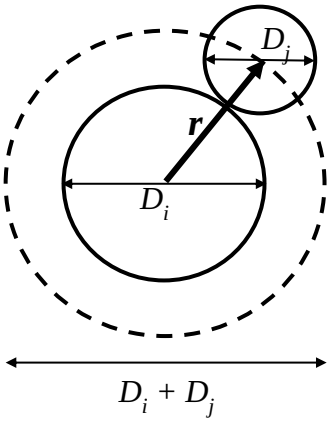

Figure 3.4: 'Kissing sphere' (dashed) defining the set of vectors connecting the positions of two kissing spheres.

If the system of the two spheres would be studied while one of the spheres is alternatingly getting into contact with the other sphere, sliding over the other sphere and losing contact again, as we would expect to happen when the system is part of a packing of spheres which is sheared or stirred, tracks of the vector $\vec{r}$ would appear on the surface of the kissing sphere. Again, supposing the stirring is random, the tracks should be uniformly distributed, in terms of unit length of track per unit surface area, over the surface of the kissing sphere.

If we consider a series of random packings involving the same set of spheres, each pair of spheres would form a system as described above, and the simplest assumption would be that the number of kisses or the length of kissing track per unit surface area of the kissing spheres will be uniform over the total surface of all kissing sphere surfaces. From this ergodicity assumption, it follows immediately that the kiss matrix is given by:

$$K_{ij} = \begin{cases} C \cdot N \dfrac{N_i(N_i - 1)(2D_i)^2}{2K} \; ; j = i \\ C \cdot N \dfrac{N_i N_j \left(D_i + D_j\right)^2}{K}; \; j \neq i \end{cases}$$

Where C is the average coordination number of the packing as a whole, and so $C \cdot N$ is twice the total number of kisses in the packing. This total is distributed according to the ratio of the 'kissing sphere'-surface to the total of 'kissing sphere'-surface. So the normalizing factor K is:

$$K = \sum_i \left\{ N_i(N_i - 1)(2D_i)^2 + 2 \sum_{j<i} N_i N_j \left(D_i + D_j\right)^2 \right\}$$

The model defined above is an extrapolation of a 1D model (string of balls) that is discussed in Appendix 0. For the 1D case, the exact number of states can be derived for any given kiss-matrix, and so the Ergodic solution can be derived rigorously and compared to the model.

Like the Ouchiyama and Tanaka model and the Suzuki and Oshima model, the Ergodic model is a simple explicit model with a single fitted parameter, C, related to the density (or porosity) of the packing. For a perfect sedimentation process, in which spheres come to rest whenever they are supported at three points by earlier deposited spheres, C is expected to be equal to 6.

The kiss numbers calculated by the models described above are to be interpreted as predictions for an infinite packing or for averages over a large number of instances of a finite packing. For a given single finite packing, the kiss matrix is a stochastic variable, in which the realization of an entry $\acute{K}_{ij}$ is the result of a very large number of pairs of spheres of sizes D_i, D_j having a potential kiss with a very small probability. The entry $\acute{K}_{ij}$ of the kiss matrix for an actual packing is therefore approximately Poisson distributed and its variance is approximately equal to its expected value:

$$\acute{K}_{ij} = K_{ij} \pm \sqrt{K_{ij}}$$

3.2.6 Results

As a first check, the statistics of particle sizes and positions identified in the image were checked against the particle size distribution of the input mixture and the expectation of a homogeneous distribution over the vertical coordinate of the packing. It was found that the sphere sizes in the image reflected the screen sizes used in preparation of the mixture (see Table 3.3 and Figure 3.5). Roughly 40% of the particles fed into the tube were found back in the image but particles of the smallest size categories were relatively under-represented. Part of the scan volume was inspected by eye and the results were compared to the computer-generated statistics so as to rule out that the numerical algorithm had missed or misinterpreted some of the small-size particles. The likely cause of the missing fine beads is the haze of fine particles found sticking to the wall of the tube above the surface of the packing after feeding. Since the input to the models is based on the numbers of particles identified in the image, this does not present any problem of interpretation.

Table 3.3: Input and scan results on particle statistics

Size fraction	**Lower size** [µm]	**Upper size** [µm]	**Number of spheres**	**Method**	**Found in scan**	**Ratio**
1	106	125	216629	weighed	63946	29.5%
2	212	250	22795	weighed	8935	39.2%
3	500	589	2065	weighed	863	41.8%
4	1000	1168	374	counted	154	41.2%
5	2000	2380	73	counted	30	41.1%

The homogeneity of the packing in the vertical dimension was inspected by counting the cumulative number of spheres of each size identified below a given level in the scan and comparing this level (expressed as the vertical voxel coordinate) with the level below which this number of spheres would have been expected on the basis of perfect homogeneity. Even though particles are fed in parts of equal composition, the top surface of the packing during feeding is at no time horizontal, so a random few extra 2 mm spheres collecting at a certain level will shift the actual cumulative number of all sizes away from the predicted number. If the biggest spheres would be added

purely randomly, the lower half of the image would be expected to have 15±3 of such spheres, meaning that the shift in voxels would be ca 20% of 450 voxels, or about 90 voxels.

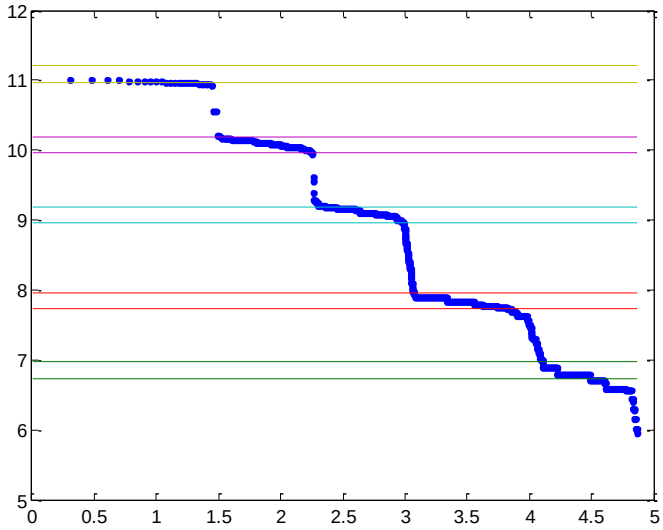

Figure 3.5: Sizes of particles found (log2 of size on vertical axis), sorted from large to small (log10 of the index on horizontal axis). The screen sizes used for creating the input mixture are indicated as horizontal lines.

The actually observed shift in Figure 3.6 is smaller, about 40 voxels. A similar analysis in the radial direction gives an expected shift of 70 voxels around radial voxel 300, whereas the actual shift is about 30 voxels. A larger and expected deviation from homogeneity is clearly visible near the wall, where all cumulative sphere counts stop at 1 radius from the wall and so the shift curves end at minus the radius in voxels.

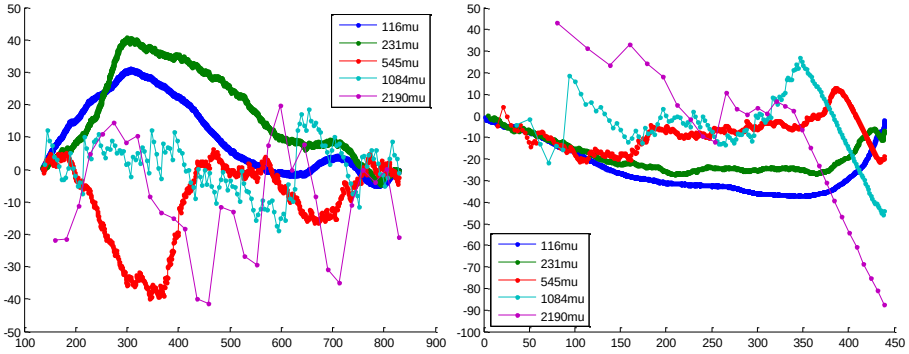

Figure 3.6: Shift in voxels between the actual cumulative fractions of spheres of each size category and the one predicted from the assumption of homogeneity in the vertical (left: from bottom to top) and radial (right: from center to wall) directions.

Table 3.4: Numbers of spheres and kisses found in the sample volume (vertical voxels 136 to 829), not corrected for the wall effect. The corrections for the effect of the tube wall are in brackets.

	N_i	K_{ij}				
		$j=1$	2	3	4	5
i = 1	63946 [1019]	108433 [2671]	63670 [2682]	20249 [2459]	13642 [2316]	8651 [2567]
2	8935 [355]		8945 [439]	4716 [673]	2774 [545]	1444 [496]
3	863 [95]			669 [101]	472 [144]	220 [68]
4	154 [35]				74 [22]	68 [29]
5	30 [10]					11 [3]

Table 3.4 shows the numbers of spheres and kisses identified in the sample volume. The numbers in brackets are corrections for particles and kisses missed due to the presence of the tube wall. They are an extrapolation (on the basis of wall area) of the numbers of particles and kisses in the sample volume for which one of the spheres is partially crossing the bottom or top boundary. The experimental coordination number of the packing is 6.61 (after correction), which is 10% higher than expected from a perfect sedimentation process. Figure 3.7 shows the corrected kiss numbers against the predictions of the simple models described above.

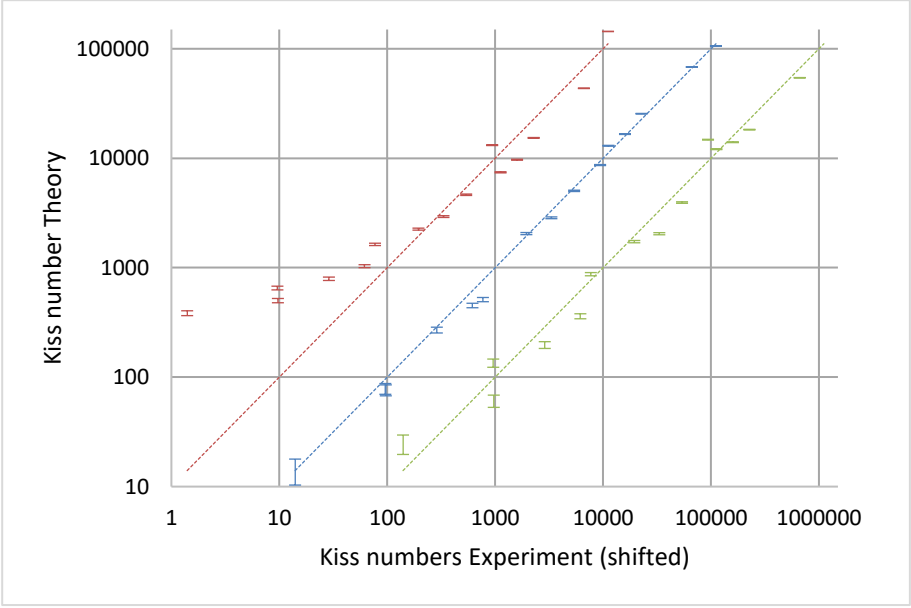

Figure 3.7: Experimentally determined entries of the kiss matrix (horizontal) against predictions of three simple models, the Ouchiyama and Tanaka model (red, shifted one order to left), the Ergodic model (blue, no shift) and the Suzuki and Oshima model (green, shift one order to right)

The error bars reflect only stochastic errors due to the finite size of the packing. The parameter ε_A in the Ouchiyama and Tanaka model and the parameter α in the Suzuki and Oshima model have been chosen so as to match the coordination number found in the experiment. It is clear from the results that the Suzuki and Oshima model and the Ergodic model extend well to larger particle size ratios. In relation to the experimental data, the RMS relative error of the predictions is 39% for the Suzuki and Oshima model and 20% for the Ergodic model.

The expected RMS relative stochastic error due to the finite size of the packing is 8.2%. This shows that the Ergodic model can be confidently used to obtain an estimation of the kiss-matrix for a random packing, from the PSD and the expected average kissing number (i.e. packing density) alone.

3.3 Analysis of liquid bridges

3.3.1 Introduction

In order to obtain macroscopic properties of the unsaturated poly-disperse particle system, the properties of liquid bridges are added to the coordination number matrix.

To this end, the liquid in the mixture is considered to exist between any two particles in the form of a single liquid bridge with the same global liquid pressure, which shape can be described by the Young-Laplace equation. By summation of the properties of the individual bridges over all particle kisses, the wetted surface, liquid pressure and binding force can then be expressed as a function of the moisture content.

Hereafter the dependency of the binding force on moisture content and PSD can be evaluated per size fraction of the mix to assess the ease of particles being liberated from the cluster.

3.3.2 Mathematical framework

The system of two spheres in contact with an axisymmetric liquid bridge is defined as in Figure 3.8.

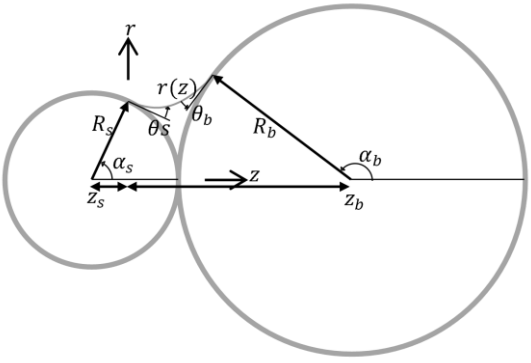

Figure 3.8: Definition of parameters describing the liquid bridge

The axisymmetric surface of the liquid bridge is derived by substituting the general expressions for curvature into the hydrostatic Young–Laplace equation [40], after which the expression is rewritten to a differential equation:

$$\frac{\Delta p}{\sigma} = \frac{1}{R1} + \frac{1}{R2} = \frac{1}{\sqrt{1 + r(z)'^2}}\left[\frac{1}{r(z)} - \frac{r''}{1 + r(z)'^2}\right]$$

$$r'' = (1 + r(z)'^2)\left[\frac{1}{r(z)} - \frac{\Delta p}{\sigma}\sqrt{1 + r(z)'^2}\right]$$

Starting conditions are:

$$z_0 = 0$$
$$r_0 = \sin(\alpha_s) R_s$$
$$r_0' = -\cot(\alpha_s + \theta_s)$$

where, for a given value of Δp, the wetting angle α_s is initially guessed.

The liquid surface that is thus computed connects correctly to the boundary of the sphere with radius R_b if the combination of radius r, derivative r' and contact angle θ_b complies with the (end) boundary condition

$$r_e(z_e) = r = R_b \cos(\tan^{-1}(r') + \theta_b)$$

If this equation is not satisfied, the guess for the wetting angle α_s is revised until it does.

At this point the geometry is fully defined and the distance between the particles can be expressed as below:

$$z_s = -R_s \cos(\alpha_s)\, R_s$$
$$z_b = z_e + r_e \tan(\tan^{-1}(r_e') + \theta_b) r_e$$
$$d = (z_b + z_s) - (R_b + R_s) \geq 0$$

Within this system of equations, a set of independent variables is chosen from the particle and liquid properties, $\sigma, \theta_s, \theta_b, R_s$ and R_b, the wetted particle angle and homogenous pressure differential of the liquid, α and Δp, and the distance d between the spheres. By the restriction $d = 0$, α becomes a function of Δp for given particle and liquid properties, and all properties of the liquid bridge can then be expressed as a function of Δp, as shown by the following equations.

$$\alpha = f(\Delta p; d = 0)$$

$$V_{\text{liquid}} = \int_{z_0}^{z_e} \pi r^2(z)dz - \frac{1}{3}\pi {R_s}^3(2 - 3\cos(\alpha_s) + \cos^3(\alpha_s))$$

$$- \frac{1}{3}\pi {R_b}^3(2 + 3\cos(\alpha_b) - \cos^3(\alpha_b))$$

$$A_{wetted_s} = 2\pi {R_s}^2(1 - \cos(\alpha_s))$$

$$A_{wetted_b} = 2\pi {R_b}^2(1 + \cos(\alpha_b))$$

$$F_\sigma = 2\pi \sin(\alpha_s)\, R_s \sigma \sin(\alpha_s + \theta_s)$$

$$F_{\Delta p} = -\pi \sin^2(\alpha_s)\, {R_s}^2 \Delta p$$

$$F_\Sigma = F_\sigma + F_{\Delta p}$$

Finally, the properties of individual liquid bridges are combined with the coordination matrix K to obtain macroscopic properties of the mixture. Here the assumption is made that the liquid pressure Δp in all bridges is equal. The argument is that moisture has had the time to redistribute and so there is (mechanical and) thermodynamic equilibrium in the mixture. By assuming a homogeneous liquid pressure, the moisture content of the mixture can be expressed as a function of Δp.

$$m = \frac{\rho_l \cdot \sum_{i,j} K_{i,j} \cdot V_{l_{i,j}}(\Delta p)}{\rho_l \cdot \sum_{i,j} K_{i,j} \cdot V_{l_{i,j}}(\Delta p) + \rho_p \cdot \sum_i N_i \cdot V_{p_i}}$$

Here, m is the moisture content defined as the mass of moisture over total moist mass.

By this relation all micro and macroscopic properties and effects of the liquid bridge(s) can be expressed as a function of the moisture content m.

3.3.3 Results

By combination of the kiss matrix with the properties of individual liquid bridges, the liquid pressure within the bridges can be expressed as a function of the moisture content. This relation is given in Figure 3.9. In the graph at right the liquid pressure is normalized via the surface tension and the radius of the smallest particle:

$$\Delta p_{\text{norm}} = \ln\left(\frac{-\Delta p\, R_s}{\sigma}\right)$$

The purpose of the analysis of properties of the liquid bridges, is to assess to which extent the rotor will be able to liberate fine particles. Upon impact with the rotor, the moist clump of particles is accelerated. Only the part of the clump directly in contact with the rotor is accelerated directly. The remainder needs to be accelerated though forces within the clump. In order for a small particle to remain attached only to a directly accelerated (bigger) particle which is moving away from it, the binding force needs to be bigger than the acceleration times the mass of the small particle. This force can be transferred via one or multiple liquid bridges.

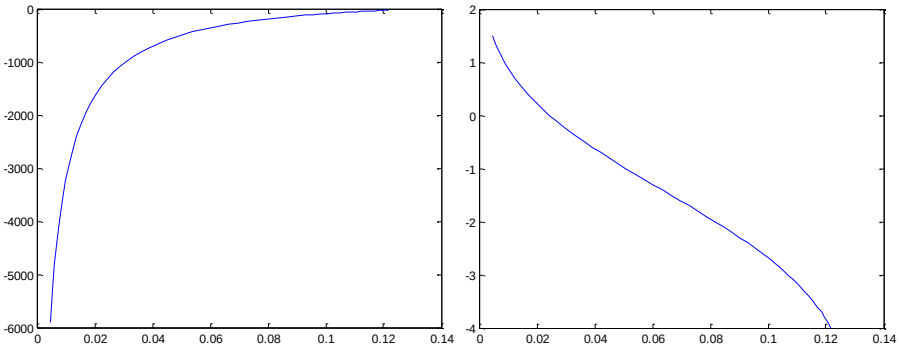

Figure 3.9: Liquid pressure (left), and the log of the normalized liquid pressure (right) as a function of the moisture content.

Table 3.5, shows the binding force of a single liquid bridge between two particles for four different moisture contents (shown in the top-left cell). The number is the log of the force normalized via the force on the particle which size is shown in the first column of the table, at an acceleration of 1 g.

$$F_{norm} = \log\left(\frac{F_{i,j}(\Delta p)}{\rho_p \cdot V_{p_i} \cdot g}\right)$$

Table 3.5: Binding force of a liquid bridge expressed as the log of the acceleration g_n needed to overcome the binding force (normalized via particle with size in first column).

10%	7.5%	62.5mu		125mu		250mu		500mu		1000mu	
5.0%	2.5%										
62.5mu		3.10	3.10	3.22	3.23	3.27	3.29	3.27	3.30	3.26	3.29
		3.11	3.14	3.24	3.27	3.31	3.35	3.33	3.38	3.33	3.39
125mu		2.24	2.25	2.45	2.46	2.59	2.61	2.63	2.66	2.64	2.67
		2.27	2.30	2.48	2.51	2.63	2.67	2.69	2.74	2.71	2.77
250mu		1.08	1.09	1.37	1.39	1.64	1.67	1.77	1.79	1.82	1.86
		1.12	1.17	1.42	1.46	1.70	1.74	1.83	1.87	1.90	1.94
500mu		0.17	0.20	0.51	0.53	0.86	0.89	1.05	1.09	1.17	1.20
		0.24	0.28	0.57	0.62	0.93	0.96	1.12	1.16	1.24	1.28
1000mu		-0.62	-0.59	-0.27	-0.23	0.14	0.18	0.39	0.42	0.55	0.59
		-0.55	-0.47	-0.19	-0.14	0.22	0.26	0.46	0.49	0.62	0.65

In essence, this table gives the log of the minimum acceleration in units of g needed on particles with sizes given in the top row (the accelerated particles) to liberate particles with size given in the first column (the bound particles), at the moisture content given in the top left cell.

The numbers show that the dependence on the size of the bound particle is much stronger than the dependence on moisture content. It is also clear that liberation will be controlled by the size of the particle to be liberated rather than the size of the directly accelerated particle. This means that a certain level of acceleration virtually all particles down to a certain size of will be liberated, and this limiting size is rather independent of the size to which these particles are bonded.

It is also noted that the critical acceleration for small particles is almost three orders of magnitude higher than for the biggest particles. It is therefore anticipated that when a system of particles is accelerated, there is rather sharp transition to the extent that a certain size fraction is still liberated and smaller particles are not.

The above analysis has assumed the moisture to be solely present in single liquid bridges. As the moisture contents increases, single liquid bridges will overlap and merge. Figure 3.10 below shows the average fraction of wetted area of a size fraction i as function of the moisture content as given by the following equation.

$$A_{wetted,i_{norm}} = \frac{\sum_j K_{i,j} \cdot A_{wetted\,i}(\mathrm{m})}{N_i \cdot A_{p_i}}$$

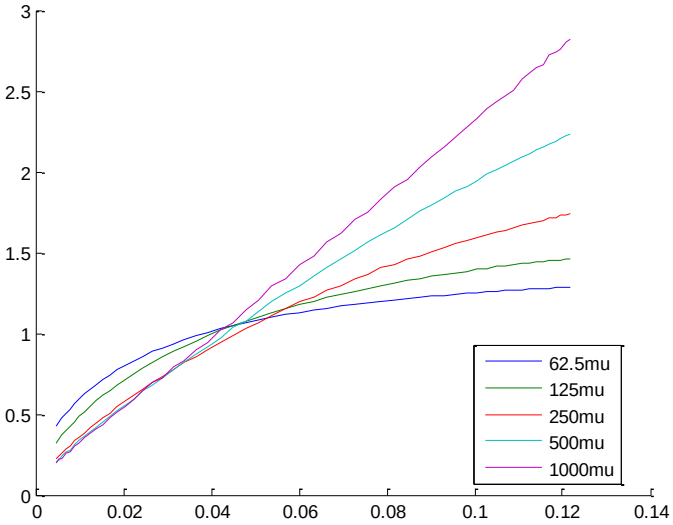

Figure 3.10: Average wetted surface fraction of particles as a function of moisture content.

When this number is bigger than one, the liquid bridges can no longer be single isolated bridges. The graph shows that the assumption of individual bridges may hold up to an adsorbed moisture content of around 4%. Above this threshold, individual bridges will merge and at least some inter-particle voids will completely fill with liquid. At this transition, the relation between moisture content and liquid pressure will change. However, this level of detail is currently not of interest in this first explorative analysis.

3.4 Residual adhesion experiment

3.4.1 Introduction

To understand how moisture-bonds behave statistically during liberation at the rotor, an experiment was conducted in which an ideal air classification was accomplished immediately after the agglomerates hit the rotor. All other influences, which are usually present at industrial conditions, were suppressed as best as possible.

Industrial ADR classification is (negatively or positively) influenced by a variety of factors. These factors include:

- Partial hit of the agglomerate by the (tips of the) rotor blades
- Spread of the initial particle and agglomerate trajectories originating from the rotor: variation of speed and direction of particles and agglomerates leaving the rotor blade
- Collisions of particles and agglomerates with the encasing, interrupting their ballistic trajectory
- Air-flow caused by the jet of (decelerating) particles leaving the rotor

The setup of the experiment was designed to eliminate all of these influences except for the variation of speed of particles and agglomerates leaving the rotor. The aim of this was to collect the particles and agglomerates released by the rotor in different bins according to their size/mass, and so measure how much fines remained bound to coarser particles directly after liberation at the rotor. For this, a structure of slits was made inside the ADR that allowed particles to pass only if they had a narrowly distributed direction of flight. The same slits also rejected particles that had been partially hit and reduced the particle mass flow and therefore the virtually eliminated the driving force for the air flow during ballistic separation to about 1% of normal operation.

3.4.2 Setup

Three panels with letterbox slits were fitted inside the ADR directly after the rotor (see Figure 3.11). These three letterboxes filter particles with a specific flight direction from the wide jet of particles coming from the rotor. The first two letterboxes define a narrow gate, accepting essentially only particles from the jet that were shot from the heart (middle) of the rotor blade with near-zero vertical velocities. This way, particles from agglomerates that hit the tip of the rotor blades are excluded and the particles passing the first two slits must have had initial velocities (after the rotor) varying primarily in horizontal speed and their lateral velocity component. It is inevitable that some of these particles hit the edge of the second slit and thereby obtain a substantially different velocity. To filter out this influence of the letterboxes themselves, a third letterbox was used which has a somewhat wider slit so that all particles that pass the first two slits without hitting their edges will surely pass also the third one without hitting. When a particle hits the edge of a letterbox its trajectory will sharply change and will likely be filtered out by the third slit.

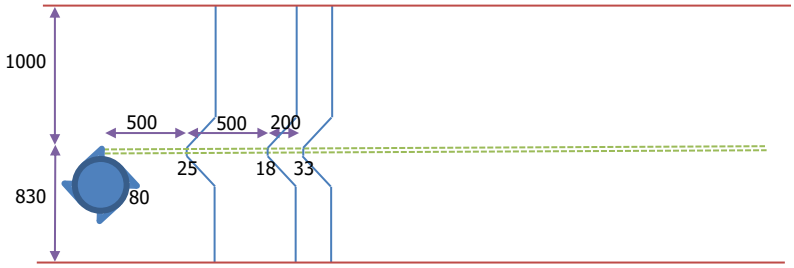

Figure 3.11: Geometry of the set-up (sizes in mm) for converting moist and clumpy granular wastes into a jet, and selecting a small sample of the jet extending from the rotor to the right, for determining the distribution of <250 micron fines bound by moisture to coarser particles.

By filtering the trajectories to a horizontal line, collisions with the roof of the ADR are avoided. Additionally, feeding over a small lateral width, combined with the limited lateral width of the letterboxes, reduced the influence of collisions with the side walls. The maximum angle allowed by the filtering action of the letterboxes is 9°. The side-walls of the ADR enclosing are at 0.5 m away from center, so particles can only collide with the side-wall after about 3 m of ballistic flight.

As a result of the extensive filtering, the total momentum of particles relative to the air-mass is reduced to less than 1% of its normal ratio, while keeping the conditions at the rotor the same as in industrial use. This reduces the air-flow within the ADR to a minimum and therefore eliminates the effect of large-scale air-movement on (small) particles.

In total, four experiments were conducted with the following variations of test parameters:

Table 3.6: Test parameters for the four experiments

	Test 1	**Test 2**	**Test 3**	**Test 4**
Throughput wet [t/h/m]	28.5	42.1	52.9	33.5
Moisture input	5.9%	6.1%	6.1%	9.3%
Moisture throughput [t/h/m]	1.70	2.90	3.52	3.71
Total mass recovery	0.564%	0.629%	0.596%	0.494%
Moisture type	Tap water	Alkaline water with salts	Alkaline water with salts	Alkaline water with salts
Ph	7	11	11	11
NaCl	0%	6.6%	6.6%	6.6%
K2SO4	0%	1.0%	1.0%	1.0%
PSD of input material				
4-5.6 mm	1.0%	0.9%	0.9%	1.1%
2-4 mm	40.6%	38.9%	40.5%	42.2%
1-2 mm	24.1%	25.1%	22.7%	24.4%
0.5-1 mm	16.4%	16.4%	17.8%	14.9%
0.25-0.5 mm	12.2%	12.7%	12.3%	11.5%
125-250 µm	5.7%	5.8%	5.6%	5.6%
0-125 µm	0.2%	0.2%	0.1%	0.2%

PSD of output material				
4-5.6 mm	0.3%	0.5%	0.6%	0.5%
2-4 mm	40.1%	39.4%	41.0%	37.5%
1-2 mm	33.1%	31.9%	29.0%	31.0%
0.5-1 mm	18.0%	17.2%	18.1%	16.8%
0.25-0.5 mm	6.5%	7.6%	7.7%	9.0%
125-250 µm	1.9%	3.2%	3.5%	5.0%
0-125 µm	0.1%	0.2%	0.2%	0.2%

3.4.3 Results

Figure 3.12 shows the distribution of particles per size fraction over the length of the ADR for Test 2.

The classification action can be clearly seen. The distributions follow an expected log-normal distribution as a result of variation of the speed of particles leaving the surface of the rotor. The peaks of the distributions are at larger distance for bigger particles. However, the 125-250 µm curve has a clear second peak, which means that part of the fines have traveled further than would be expected by their ballistic properties. These particles remained attached to bigger particles, and therefore traveled the distance of their bigger 'host' particle.

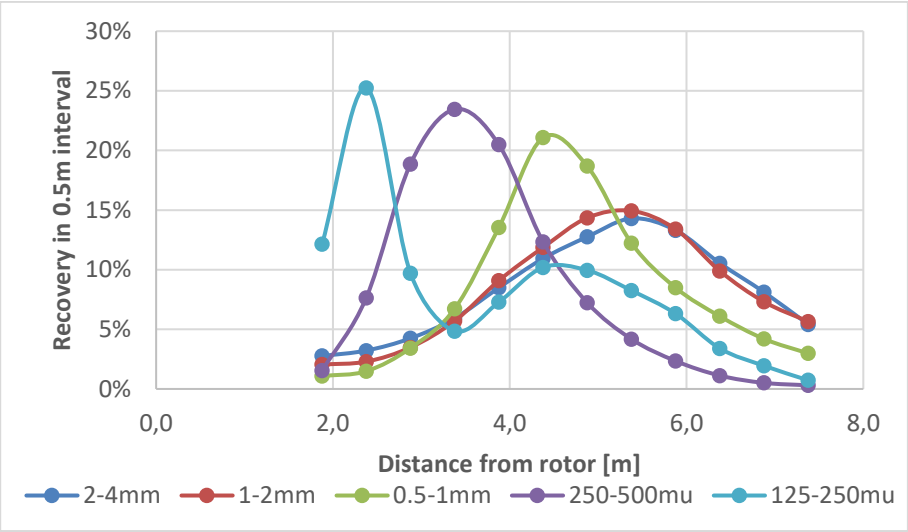

Figure 3.12: The recovery of a size fraction per bin over the length of the ADR

The effects can be seen more clearly when the four tests are compared for only the finest size fraction (125-250 µm), see Figure 3.13.

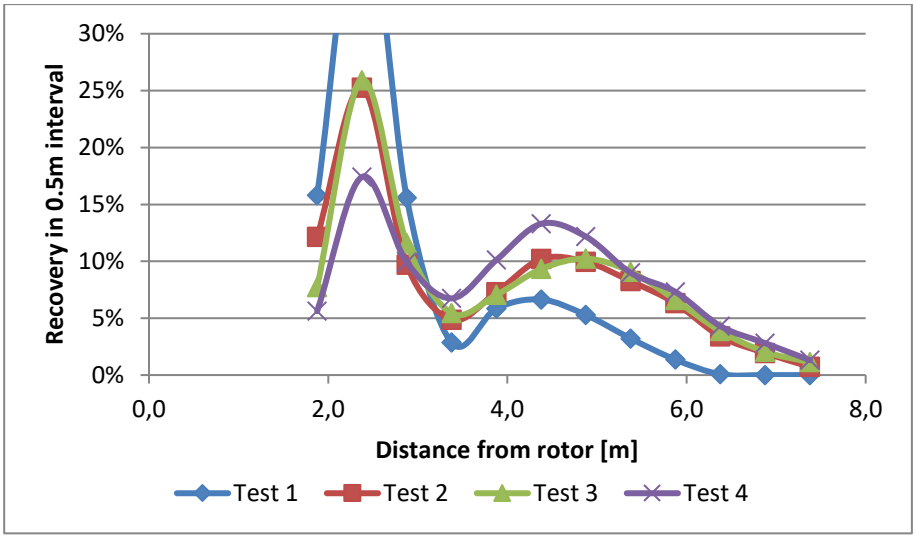

Figure 3.13: Recovery of the 125-250 µm particles in four tests

3.4.4 Interpretation

The goal of the experiment was to determine the amount of free fine particles and the characteristics of the distribution of the non-free particles over their host particles.

To obtain this information, a fitting model is used to describe the experimental results. The model is based on the following components:

- The particle size distribution of the input: M_i,is the input mass-fraction of size fraction i defined by bounds $d_{\text{max},i}$and $d_{\text{min},i}$. d_i is the geometric mean of its bounds.

$$d_i = \sqrt{d_{\text{max},i} d_{\text{min},i}}$$

- A function describing the probability of a particle of a given size fraction i to be free (vs. attached to a 'host' particle) after acceleration by the rotor: F_i is the mass fraction of free particles in size fraction i.

$$F_i = 1 - \frac{1}{1 + \left(\frac{d_i}{d_0}\right)^{\alpha_s}}$$

- A mass distribution function ($M_{i,j}$) that describes how bound 'client' particles i are distributed over bigger 'host' particles j. It is assumed that 'client' particles only attach to 'hosts' that are bigger ($j > i$) and free: mass-fraction $M_j F_j$. Furthermore, it is assumed that the trajectory of the 'host' particle is not affected by the attachment of the 'client' particles.

$$M_{i,j} = M_j F_j d_j^{\alpha_r} \frac{M_i(1 - F_i)}{\sum_{k>i} M_k F_k d_k^{\alpha_r}}$$

- A parameter (P_j) that gives the percentage of particles per size fraction that pass the three letterboxes (M'_P). The parameter only applies to free particles, attached 'client' particles are 'filtered' according to the parameter of the 'host' particle ($M_{i,j}$ is filtered on P_j).

$$M'_{P_{i,j}} = P_j M_{i,j}$$

$$M'_{P_i} = P_i M_i F_i + \sum_{j>i} M'_{P_{i,j}}$$

$$M_{P_i} = \frac{M'_{P_i}}{\sum_i M'_{P_i}}$$

These components model the effects of residual attachment, distribution of fines and filtering by the letterboxes. They can be used to unravel the experimentally found recovery curves into their 'free' and 'attached' parts. The 'free' part has traveled 'on its own' and is therefore fit by a log-normal distribution. The 'attached' or 'client' part has traveled according to its host. Therefore, the following components are added:

- A recovery of 'free' particles (R_{f_i}) is deduced from the recovery of a size fraction (i) given by the experiment (R_i), Starting with the coarsest size fraction, the recovery of 'client' particles is subtracted to obtain the recovery of only the 'free' particles.

$$R_{f_i} = \frac{M'_{P_i} R_i - \sum_{j>i} M'_{P_{i,j}} R_{f_j}}{P_i M_i F_i}$$

- A model description (indicated by $\tilde{R}$) of the recovery of 'free' particles in size fraction (i) between two boundaries (s_1, s_2) is given by a log-normal function ($\tilde{R}_{f_i}$). The function is normalized to the range in which particles were collected.

$$\tilde{R}_{f_i} = \frac{\ln \mathcal{N}(\mu_i, \sigma_i, s_1, s_2)}{\ln \mathcal{N}(\mu_i, \sigma_i, s_{min}, s_{max})}$$

- A reconstruction of the experimental result from the model by combining the log-normal function with the deduced experimental recovery of 'free' particles ($\tilde{R}_i$)

$$\tilde{R}_i = \frac{P_i M_i F_i \tilde{R}_{f_i} + \sum_{j>i} M'_{P_{i,j}} R_{f_j}}{M'_{P_i}}$$

The parameters in these equations are fit to the known experimental data:

- The (dry) mass PSD of the input (M_i)
- The (dry) mass and PSD of the combined output (M_{E_i})
- The recovery of every size fraction over the length of the ADR (R_{f_i})

A least square fit is used to find the best estimates for $d_0, \alpha_s, \alpha_r, P_j, \mu_i$ and σ_i. In this fit the total error between M_{P_i} and M_{E_i} is restricted and the root mean square error between $\tilde{R}_i$ and R_i is minimized.

The results of the fit are shown in the following table:

Table 3.7: Fitted parameters.

	Test1	**Test2**	**Test3**	**Test4**
d_0	0.119	0.154	0.163	0.211
α_s	5.445	3.860	3.593	3.900
α_r	-0.916	-0.916	-0.916	-0.916
$\mu_{250-500\mu m}$	3.20	3.28	3.30	3.52
$\mu_{125-250\mu m}$	2.10	2.03	2.12	2.14
$\sigma_{250-500\mu m}$	1.26	1.28	1.27	1.26
$\sigma_{125-250\mu m}$	1.15	1.15	1.14	1.15
P_{2-4mm}	0.564%	0.636%	0.604%	0.427%
P_{1-2mm}	0.746%	0.801%	0.766%	0.616%
$P_{0.5-1mm}$	0.638%	0.667%	0.611%	0.570%
$P_{250-500\mu m}$	0.309%	0.344%	0.330%	0.380%
$P_{125-250\mu m}$	0.136%	0.212%	0.242%	0.343%
$RMSE(\tilde{R}_{f_i}, R_{f_i})$	1.174%	1.538%	1.396%	1.209%
$RMSE(\tilde{R}_i, R_i)$	1.049%	0.783%	0.708%	0.563%
$RMSE(M_{P_i}, M_{E_i})$	0.010%	0.010%	0.010%	0.010%

As an example, below the experimental results and fit for 125-250 µm of Test 4 is shown:

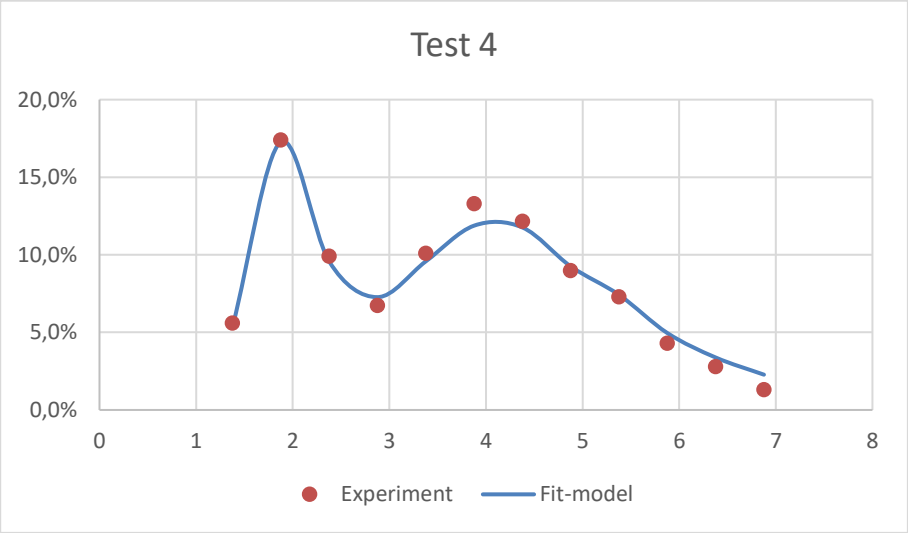

Figure 3.14: Comparison of the experimental result and the model

The parameters d_0 and α_s of the probability function F_i have a relation with the moisture throughput (throughput multiplied by the moisture content), as can be seen in Figure 3.15. The diameter at which the liberation starts (d_0) increases with moisture throughput, though not by orders of magnitude. The sharpness of the transition (α_s) decreases with moisture throughput.

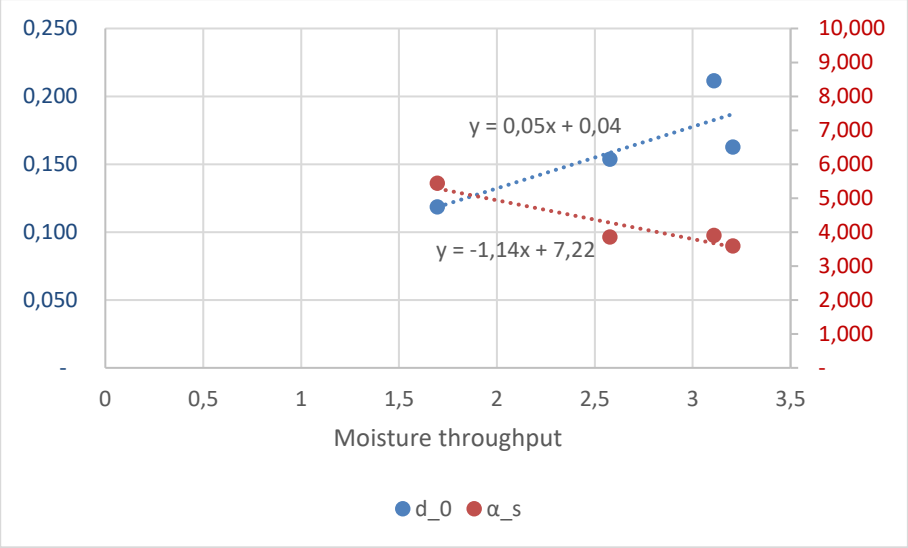

Figure 3.15: Fit parameters d_0 and α_s as a function of the 'Moisture throughput'

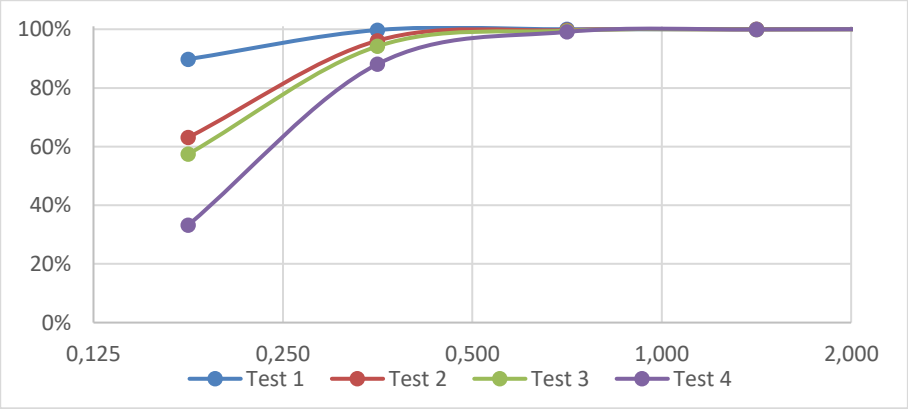

Figure 3.16: Ratio of particles liberated within a size fraction for the four tests

The significance of this can be seen in Figure 3.16, which shows the ratio of liberated particles per fraction. The amount of liberated particles is most likely related to the accelerations inside the moist clump material upon impact. As a general starting point for the physical interpretation of these results, it is noted that the fraction *B* (%) of 125-250 µm fines that remains bound to coarser particles after hitting the rotor blade is a function of the input particle size distribution, the moisture content C_M (%) and the throughput *T* per meter width (ton/h). Since the input particle size distribution to

the rotor was kept the same in all experiments, it seems reasonable to write B as a polynomial in C_M and T:

$$B = A_0 + A_1 C_M + A_2 T + A_3 C_M T + A_4 C_M^2 + A_5 T^2 + \cdots$$

where each of the coefficients A_k is a function of the particle size distribution. Since for zero moisture content, no fines are bound to the coarser grains, regardless of the throughput, the polynomial can be simplified to:

$$B = A_1 C_M + A_3 C_M T + A_4 C_M^2 + \cdots$$

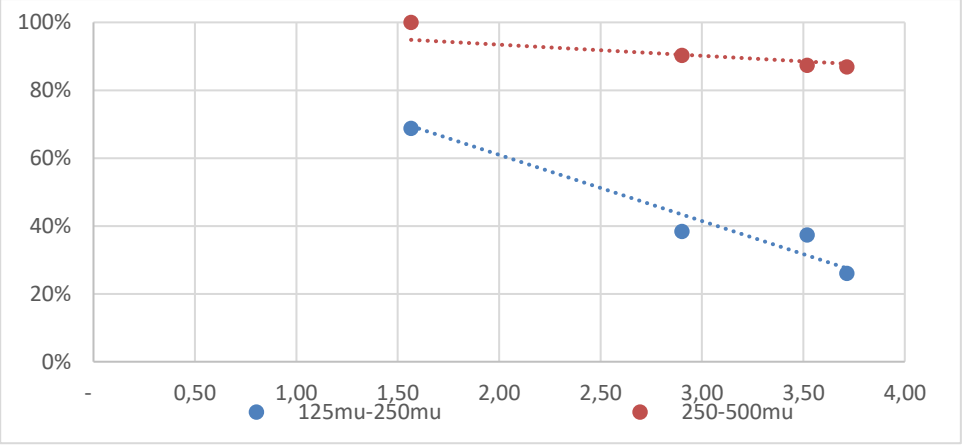

Figure 3.17: Free particles [kg/kg] vs moisture throughput [t/h/m]

The plot of the fraction of free 125-250 µm fines versus $C_M T$ shows that A_1 and A_4 must be much smaller than A_3, because the data fit very well to a straight line passing through the origin (0 ton/h, 100%). In particular, the liberation of fines seems to become complete in the limit of zero throughput, regardless of the moisture content. This observation has implications for the mode of disintegration of the moist clumps at the rotor. If the mechanism of disintegration would be a shock wave running through the clump (Figure below left), one would expect that the level of moisture content would be relevant even at very low capacity (top left), which the data show it is not. If, on the other hand, the mechanism is to compress the clump into a pancake, disintegration could be complete for finite moisture content at very low capacity, as the data suggest.

Figure 3.18: Effect of capacity for disintegration by a shock wave (left) versus disintegration by compression into a pancake (right).

Since the conditions by which the fines adhere to the larger particles are almost independent of the size of these larger particles, it would be reasonable to expect that the distribution of fines over these larger size fractions reflect the original kiss matrix of the clumpy waste.

The Ergodic model predicts that the mass distribution of the finest particles over the coarse particle would relate to the diameters of the particles as follows:

$$M_{ij} \sim N_i d_i^3 \; N_j \left(d_i + d_j\right)^2$$

where N_i is the number of fine particles in the clump and N_j is the number of coarse particles. Since the dry mass fraction of particles of size fraction j is $M_j \sim N_j d_j^3$, we have

$$M_{ij} \sim M_i \; M_j \left(d_i + d_j\right)^2 / d_j^3$$

The experimental data were fit with the correlation

$$M_{ij} \sim M_i \; M_j d_j^{-0.916}$$

which comes very close to the model equation since mostly $d_i \ll d_j$ (see Figure 3.19). So it can be concluded that the correlation of the mass of fines per unit mass of coarse material as a function of (coarse) particle size compares well to the prediction by the Ergodic model.

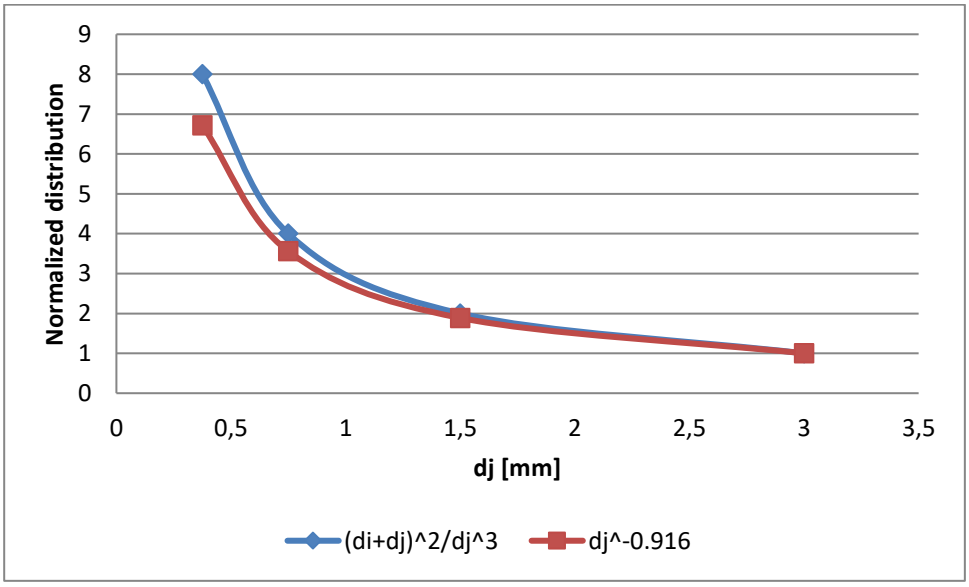

Figure 3.19: Comparison of a correlation (squares) for the experimental distribution of fines bound to coarser particles of different sizes in the jet and the predictions from the Ergodic model (diamonds).

3.5 Conclusion

To understand the residual adhesion of fine particles to coarser particles after high acceleration upon impact with the rotor of the ADR, the moist particle structure of the clumpy feed was studied in detail.

A strongly disperse random packing of over 200,000 glass beads was produced by sedimentation in a water-based medium, with an approximately lognormal size distribution and a ratio of 18 between the maximum and minimum size. It was found that it is possible to determine the kiss matrix of this packing by X-ray micro-tomography and interpretation via an eroding and dilating algorithm. The experimentally found kiss-matrix corresponds well with the model of Suzuki and Oshima and even better with results of a newly developed model based on an ergodicity argument. This last model was then taken as the basis for understanding the structure of moist clumpy material.

The analysis of liquid bonds of kissing particles suggests that liberation sharply transitions over particle size. This was confirmed in an experiment in which the liberation efficiency by the rotor was carefully isolated. The data further suggest full liberation when the throughput goes to zero. This, in turn, suggests that clumps of particles are most likely compressed by the rotor blades into a pancake before liberation, and that the radius of these pancakes and therefore liberation are limited by the throughput. Furthermore, it was found that the distribution of non-liberated fines over coarse particles in the jet is in line with the predictions of the Ergodic model.

Appendix

Modeling the spatial distribution of the microstructure of moist polydispersed granular material via a one dimensional microcanonical ensemble

A.1 Mathematical framework

A.1.1 1D model for clusters of solid particles and water bonds

Consider a linear array of N balls $B_1, \cdots, B_N$ of k different sizes $D_1, \cdots, D_k$, but otherwise indistinguishable (see Figure below: $k = 2$).

Figure A.1: Example of a linear array of balls

If the number of balls of size D_i is $N_i > 0$, so:

$$N = \sum_{i=1,..,k} N_i$$

If a ball of size D_j in the linear array is the right-hand neighbor of another ball of size D_i, we say that the two balls share a bond of type ij. For convenience, ball B_1 is said to be the right-hand neighbour of ball B_N, effectively creating a periodic boundary condition for the array. It follows then that the linear array system has N bonds, the same as the number of balls. Suppose that K_{ij} is the number of bonds of type ij, also known as the kiss matrix. Then the numbers of bonds left and right of the N_i balls of size D_i are the same and equal to N_i:

$$\sum_{j=1,..,k} K_{ij} = \sum_{j=1,..,k} K_{ji} = N_i$$

A realization of the system defining the size D_i, $i = 1,..,k$ for each individual ball in the array $B_1, \cdots, B_N$ is called a microstate of the system. The following set of parameters is called a macrostate:

$$\begin{aligned} &N_i, && i = 1,..,k \\ &K_{ij}, && i = 1,..,k;\ j = 1,..,k \end{aligned}$$

The question arises how many microstates correspond to some given macrostate.

A.1.2 Calculating the number of microstates

In order to answer the question about the number of microstates corresponding to a given macrostate, a second system is defined that allows for easier counting. A microstate of this second system is defined as a combination of the size S ($S = 1, \cdots, k$) of the lead ball and k linear arrays of bonds (ij), organized according to the first index, so that the i^{th} linear array of bonds contains only bonds of types $ij,\ j = 1, \cdots, k$, and satisfying the usual condition

$$\sum_{j=1,..,k} K_{ij} = \sum_{j=1,..,k} K_{ji} > 0$$

The link between the two systems is best explained by an example. Suppose that a linear array of balls is as in Figure A.2. Then the description of the microstate in the first system (top) and in the second system (bottom) is as given in Figure A.3. To the right the description of the macrostate is given.

Figure A.2: Example of a linear array of balls

1st System

Array of balls:	D_1	-	D_1	-	D_2	-	D_1	-	D_2	-	D_2	-	D_1	-	D_1	-
Array of bonds:		11		12		21		12		22		21		11		11

2nd System

$S = 1$								
1st array of bonds:	11	12		12			11	11
2nd array of bonds:			21		22	21		

Macrostate

$k = 2$

$N = 5 \quad 3$

$K = \begin{matrix} 3 & 2 \\ 2 & 1 \end{matrix}$

Figure A.3: Example of a microstate in the first system (top) and second system (bottom) and the description of the macrostate (right)

It is clear (a) that every linear array of balls of the original system projects onto precisely one microstate of the second system, and, (b) that different microstates of the original system project onto different microstates of the second system. There is, in other words, a one-to-one relation between the set of microstates of the original system of linear arrays of balls and the set of their projections into the second system. It is also clear, however, that the second system is bigger than the original system, because it is possible to define a microstate of the second system which does not translate back to the first system. This is illustrated in Figure A.4. Here a first system cannot be constructed from all bonds in the second system. Therefore, the given second system cannot be the projection of any microstate of the original system

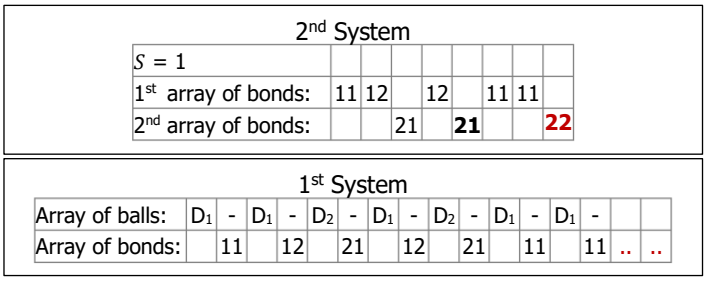

Figure A.4: Example of a microstate in the second system which cannot be translated to the first system

The underlying reason is that the final bond 2-2 of the second array of bonds, on the one hand cannot be the final bond of any linear array of balls (because then it would have to connect to the lead ball, which is of size 1) and, on the other hand, it cannot be followed by a bond of type 1-j (because the second index is 2) or 2-j (because it is the final bond of the bond array of type 2-j).

In order to rule out microstates of the second system that are not a projection of microstates of the first system, we now restrict the set of microstates of the second system to those microstates that satisfy the following additional constraint on the final bonds in the bond arrays:

- The $k-1$ final bonds of all the bond arrays of the microstate except the S^{th} bond array (the one with bonds S-j) form a directed in-tree (i.e., a directed graph in which all points of the graph are connected and there are no cycles, such that all edges point towards the root node) with k nodes $i = 1, \cdots, k$.

Such a directed in-tree consists of k nodes $i = 1, \cdots, k$ and $k-1$ directed edges (arrows between vertices) p-j_p, $p = 1, \cdots, k$ with $p \neq S$ such that for all p, p-j_p is the final bond in the p^{th} array of bonds. S is the root node. Two examples are given in Table A.1.

Table A.1: Example of directed trees for the end bonds in the second system

Microstate of the second system	**Directed graph**	**Corresponding microstate of the original system**
$S = 1$ 1st: 12 13 2nd: 21 **23** 3rd: 32 34 **31** 4th: **43**	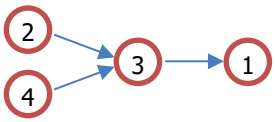	D1 D2 D1 D3 D2 D3 D4 D3
$S = 1$ 1st: 12 13 2nd: 21 **23** 3rd: 31 **32**	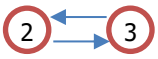	None

It is claimed that this constraint is sufficient and necessary for a microstate of the second system to be a projection of a microstate of the original system.

In order to see that it is sufficient, consider any given state of the second system. We now make available

$$N_i = \sum_{j=1,..,k} K_{ij}$$

balls of each size D_i. The corresponding microstate of the first system should start with a ball of size D_S and therefore the S^{th} array of bonds supplies the first bond, say S-i, of this microstate. Subsequently a ball of size D_i is added (which may be the lead ball if $i = S$ and none other of size D_S is left). For the remaining procedure, we note that, after adding any ball of size D_i (other than the lead ball) after some bond h-i, there must necessarily be a yet-unused bond of type i-j, with $j = 1,.,k$, since

$$\sum_{j=1,..,k} K_{ij} = \sum_{j=1,..,k} K_{ji}$$

Therefore, the only way that the procedure of completing the microstate can end is by adding the lead ball of size D_S. If at this point all the bonds of the microstate of the second system are used, the constructed microstate will have the same macrostate parameters as the microstate of the second system, and will be projected onto it. If, on the other hand, there are any bonds of the state of the second system left unused, these unused bonds must necessarily include a final bond of some bond array. If this final bond is i-j, then the final bond of the j^{th} bond array must also be unused. Since the final bonds form an in-tree with root S, it follows that there is an unused bond h-S. This is impossible, however, since all balls of size D_S have already run out in completing the microstate.

The constraint is also necessary. In order to see this, select a state of the second system for which the final bonds of all the bond arrays of the microstate except the S'^{th} bond array do not form a directed in-tree. Then the graph constructed from the k-1 final bonds includes a cycle. Now suppose that there (nevertheless) exists a microstate of the original system that is projected onto this selected microstate. By definition, the cycle of the directed graph cannot include the node S since the final bond of the S^{th} array of bonds is not part of the graph. While reconstructing the microstate of the original system from the selected microstate, one of the arrays of bonds that correspond to a node in the cycle, say $j \neq S$ will run out first. Consider the node i preceding this vertex in the cycle, and the corresponding array of bonds. Note that $i \neq j$. At some later point in the reconstruction, the final bond i-j of the i^{th} array of bonds will be added to the microstate of the original system. Since $j \neq S$, there must be a corresponding ball with diameter D_j left, but this is impossible because the j^{th} array of bonds is already exhausted.

We conclude that for given

$$\begin{array}{ll} N_i, & i = 1,..,k \\ K_{ij}, & i = 1,..,k;\ j = 1,..,k \end{array}$$

the number of states of the second system satisfying the additional constraint on the final bonds is equal to the number of microstates of the first system. Therefore, we may as well count the number of states of the constrained second system. This number is computed by first considering all possible sizes of the lead ball

$$S = 1, \cdots, k$$

Then for given S, we enumerate all possible directed in-trees constructed from $k-1$ final bonds p-j_p, $p = 1, \cdots, k$ with $p \neq S$.

Finally, for a given in-tree, we count the number of different ways to arrange the first $N_p - 1$ bonds in the p^{th} array of bonds, knowing that the final bond is of type p-j_p,

$$\frac{(N_p - 1)!}{\left(K_{pj_p} - 1\right)! \prod_{j=1,..,k; j \neq j_p} K_{pj}!} = \frac{(N_p - 1)!}{\prod_{j=1,..,k} K_{pj}!} K_{pj_p}$$

For the S^{th} array of bonds, there is no restriction on the final bond, so the number of alternative arrays is:

$$\frac{N_S!}{\prod_{j=1,..,k} K_{Sj}!} = \frac{(N_S - 1)!}{\prod_{j=1,..,k} K_{Sj}!} N_S$$

Therefore, the total number of microstates for the given parameters of the macrostate is given by:

$$\begin{aligned} \Omega = N_{microstates}(k) &= \sum_{S=1,..,k} \left[\sum_{t \in T_{k,S}} \frac{(N_S - 1)!}{\prod_{j=1,..,k} K_{Sj}!} N_S \prod_{(p,j_p) \in t} \frac{(N_p - 1)!}{\prod_{j=1,..,k} K_{pj}!} K_{pj_p} \right] \\ &= \prod_{i=1,..,k} \left[\frac{(N_i - 1)!}{\prod_{j=1,..,k} K_{ij}!} \right] \sum_{S=1,..,k} \left[N_S \sum_{t \in T_{k,S}} \prod_{(p,j_p) \in t} K_{pj_p} \right] \end{aligned}$$

Here $T_{k,S}$ is the collection of directed in-trees with k nodes and $k-1$ directed edges towards root node S. Example of Ω for $k = 2$:

$$N_{microstates} = \left[\frac{(N_1 - 1)!\,(N_2 - 1)!}{K_{11}!\,K_{12}!\,K_{21}!\,K_{22}!} \right] [N_1 K_{21} + N_2 K_{12}]$$

And $k = 3$:

$$N_{microstates} = \left[\frac{(N_1-1)!(N_2-1)!(N_3-1)!}{K_{11}!K_{12}!K_{13}!K_{21}!K_{22}!K_{23}!K_{31}!K_{32}!K_{33}!} \right] \times \begin{bmatrix} N_1(K_{21}K_{31} + K_{23}K_{31} + K_{32}K_{21}) + \\ N_2(K_{12}K_{32} + K_{13}K_{32} + K_{31}K_{12}) + \\ N_3(K_{13}K_{23} + K_{12}K_{23} + K_{21}K_{13}) \end{bmatrix}$$

Table A.2 shows the numbers of different microstates for an example case with $k = 3$, $N = [4 \quad 4 \quad 2]$.

Table A.2: Number of different microstates for $k = 3,\ N = [4 \quad 4 \quad 2]$

Ω	K_{11}	K_{12}	K_{13}	K_{21}	K_{22}	K_{23}	K_{31}	K_{32}	K_{33}
10	3	0	1	0	3	1	1	1	0
10	3	0	1	1	3	0	0	1	1
30	3	0	1	1	2	1	0	2	0
30	2	0	2	1	3	0	1	1	0
45	2	0	2	2	2	0	0	2	0
10	3	1	0	0	3	1	1	0	1
30	3	1	0	0	2	2	1	1	0
30	3	1	0	1	2	1	0	1	1
30	3	1	0	1	1	2	0	2	0
30	2	1	1	0	3	1	2	0	0
30	2	1	1	1	3	0	1	0	1
270	2	1	1	1	2	1	1	1	0
90	2	1	1	2	2	0	0	1	1
180	2	1	1	2	1	1	0	2	0
30	1	1	2	1	3	0	2	0	0
180	1	1	2	2	2	0	1	1	0
90	1	1	2	3	1	0	0	2	0
45	2	2	0	0	2	2	2	0	0
90	2	2	0	1	2	1	1	0	1
180	2	2	0	1	1	2	1	1	0
90	2	2	0	2	1	1	0	1	1
45	2	2	0	2	0	2	0	2	0
180	1	2	1	1	2	1	2	0	0
90	1	2	1	2	2	0	1	0	1
450	1	2	1	2	1	1	1	1	0
90	1	2	1	3	1	0	0	1	1
90	1	2	1	3	0	1	0	2	0
45	0	2	2	2	2	0	2	0	0
90	0	2	2	3	1	0	1	1	0
15	0	2	2	4	0	0	0	2	0
90	1	3	0	1	1	2	2	0	0
90	1	3	0	2	1	1	1	0	1
90	1	3	0	2	0	2	1	1	0
30	1	3	0	3	0	1	0	1	1
90	0	3	1	2	1	1	2	0	0
30	0	3	1	3	1	0	1	0	1
70	0	3	1	3	0	1	1	1	0
10	0	3	1	4	0	0	0	1	1
15	0	4	0	2	0	2	2	0	0
10	0	4	0	3	0	1	1	0	1

In studying models for clusters of particles bound by water, we are interested in large, isotropic systems, where the actual particle size distribution is approximated by a small number of different particle sizes, i.e., $3 \leq k \leq 6; \lim_{N\to\infty}(N); K_{ij} = K_{ji}$. For such cases, the number of microstates is strongly peaked at a specific combination of frequencies of inter-particle bonds (see Figure A.5). In fact, for such systems, it is a reasonable assumption, in line with the standard line of reasoning in thermodynamics, that at any time, the system will be in the most probable macrostate that satisfies the relevant macroscopic constraints (particle size distribution, energy level, etc.), i.e., the macrostate with the maximum number of microstates that satisfy these same constraints. In determining this maximum, the final term in brackets in the equation for the number of microstates can conveniently be ignored, as it introduces only a minor shift (see Figure A.5)

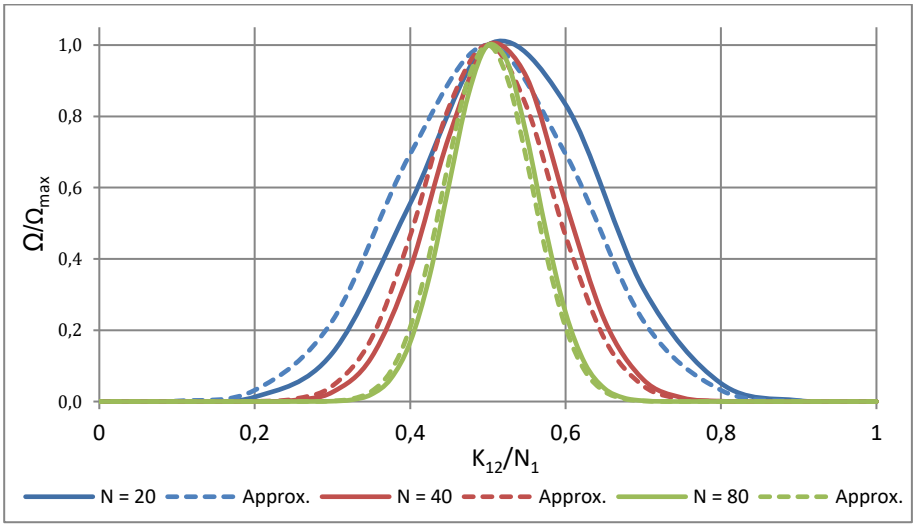

Figure A.5: Relative frequencies of microstates (normalized on the maximum) for $k = 2; N_1 = N_2 = 10{:}20{:}40$ *as a function of the number of bonds of different-sized balls. The approx. curves indicate the relative frequencies calculated by ignoring the final term in brackets*

A.1.3 Solving the microcanonical ensemble

The macrostate of the system is obtained by finding the maximum of Ω under the given constrains. The position of the maximum of Ω corresponds to the position of the maximum in $\log\Omega$:

$$log(\Omega) = \sum_{i=1,..,k}\left[log\big((N_i-1)!\big) - \sum_{i=1,..,k} log\big(K_{ij}!\big)\right] + log\left(\sum_{S=1,..,k}\left[N_S \sum_{t\in T_{k,S}} \prod_{(p,q)\in t} K_{pq}\right]\right)$$

Which can be approximated by:

$$log(\Omega) = \lim_{N\to\infty}\left(\sum_{i=1,..,k}\left[log\big((N_i-1)!\big) - \sum_{i=1,..,k} log\big(K_{ij}!\big)\right]\right)$$

When N and K can be considered large, Stirling's formula can be used to approximate the $\log(n!)$ terms.

$$log(\Omega) = \lim_{N\to\infty}\left(\sum_{i=1,..,k}\left[(N_i - 1)\cdot(log(N_i - 1) - 1) - \sum_{i=1,..,k} K_{ij}\cdot\left(log\left(K_{ij}\right) - 1\right)\right]\right)$$

Since N_i is constant, and $\sum_{i,j=1,..,k} dK_{ij} = dN = 0$ the derivative of $\log\Omega$ is given by:

The systems of equations to be solved is given by:

$$dN_i = \sum_{j=1,..,k} dK_{ij} = 0$$
$$dN_j = \sum_{i=1,..,k} dK_{ij} = 0$$
$$d\log(\Omega) = \sum_{i,j=1,..,k} \log K_{ij}\, dK_{ij} = 0$$

Which can be solved using Lagrange multipliers to obtain the following result:

$$\alpha_0 \log K_{ij} + \alpha_i + \alpha_j = 0$$
$$K_{ij} = e^{-(\alpha_i+\alpha_j)/\alpha_0}$$
$$\sum_{j=1,..,k} K_{ij} = N_i$$
$$\sum_{i=1,..,k} K_{ij} = N_j$$

$$\alpha_0 = 1$$
$$\alpha_i = -\log\frac{N_i}{\sqrt{N}};\ \alpha_j = -\log\frac{N_j}{\sqrt{N}}$$
$$K_{ij} = \frac{N_i N_j}{N}$$

For the simple model in which no distinction is made between the balls of the same size, this result is trivial and as expected. Note that there are N positions for kisses in the system. The number of ways that balls of size i may kiss at their right with balls of size j is equal to $N_i N_j N$ (if $i = j$, it is actually slightly lower, $N_i(N_i - 1)N$, but for N going to infinity, this difference can be neglected). Therefore, the probability that a kiss at any position in the array of balls is of type ij can be estimated as

$$P_{ij} = \frac{N_i N_j N}{\sum_{i,j} N_i N_j N} = \frac{N_i}{N}\frac{N_j}{N}$$

and so

$$K_{ij} = P_{ij} N = \frac{N_i N_j}{N}$$

4
Experiments with ADR

4.1 ADR Prototype

To validate the principle of the ADR concept, a prototype was built in the laboratory of TU Delft. This prototype was used to gain insight in the workings of the ADR, to facilitate modeling and to develop an industrial prototype operating at 120 tons per hour.

In the following sections, first the results of a 'base case' are presented. On the basis of these results a number of characteristic properties of the ADR are demonstrated. Hereafter, the condensed results of a series of experiments are presented that will show the influence of throughput, moisture and material type on the classification results.

4.1.1 Methodology

Figure 4.1 shows the layout of the lab prototype. Material was fed at constant rate by a vibrating feeder that led the material via a smooth, stationary plate to the rotor. The height of the feeding plate was designed in accordance with the blade height and RPM of the rotor, to ensure that the vertical speed of the material was precisely tuned to cover the complete rotor blade height. The position of the feeding plate relative to the rotor determines the angle of the jet, i.e., the initial angle of the particle trajectories. For the experiments reported below, the angle of the jet was such that the jet slightly hit the roof of the construction.

To prevent the rebound of particles hitting the back wall, a flexible fabric cloth was loosely affixed at 11 m from the rotor to slow down fast moving coarse particles and collect them.

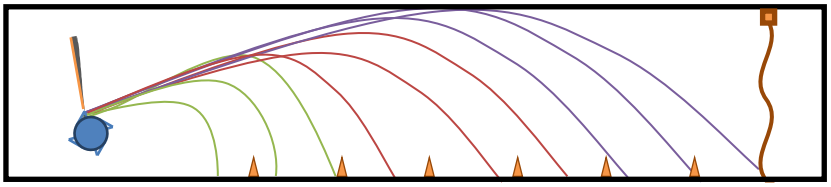

Figure 4.1: Schematic of the laboratory ADR setup

For a single test, an amount of 50 to 250 kg was fed with the vibrating feeder. The processing time was recorded to determine the throughput. After processing, the material was directly collected at fixed distance intervals from the center of the rotor and dried to determine the moisture content and consecutively dry sieved to determine the particle size distribution.

4.1.2 Results

Base case

Figure 4.2 shows the cumulative PSD (sieve passing), per distance category plus the input. Bottom ash consists mainly of mineral-like materials such as slags, glass and ceramics. Since these have roughly the same specific density, the classification by the ADR will be mainly on particle size. This can be seen in the graphs; the PSD's show that the material collected near the rotor has a D_{50} that is roughly ten times as fine as the D_{50} of the material that is collected 11 m away from the rotor.

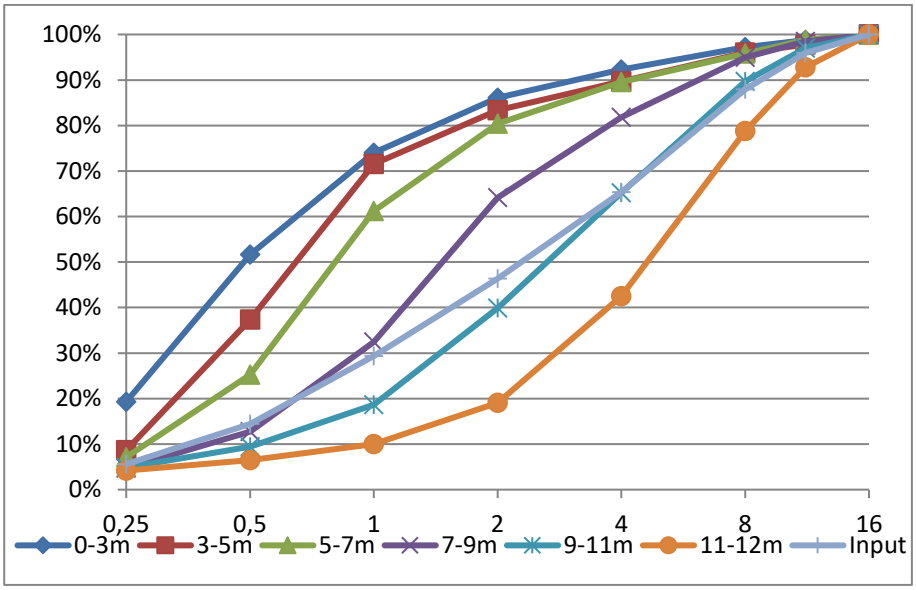

Figure 4.2: Cumulative particle size distribution for every distance category (distance measured from rotor)

To better understand the workings of the ADR, the results are presented in a recovery graph, see Figure 4.3. This graph shows the recovery for every size fraction in the different distance categories. It effectively shows how a certain size fraction distributes over the length of the ADR.

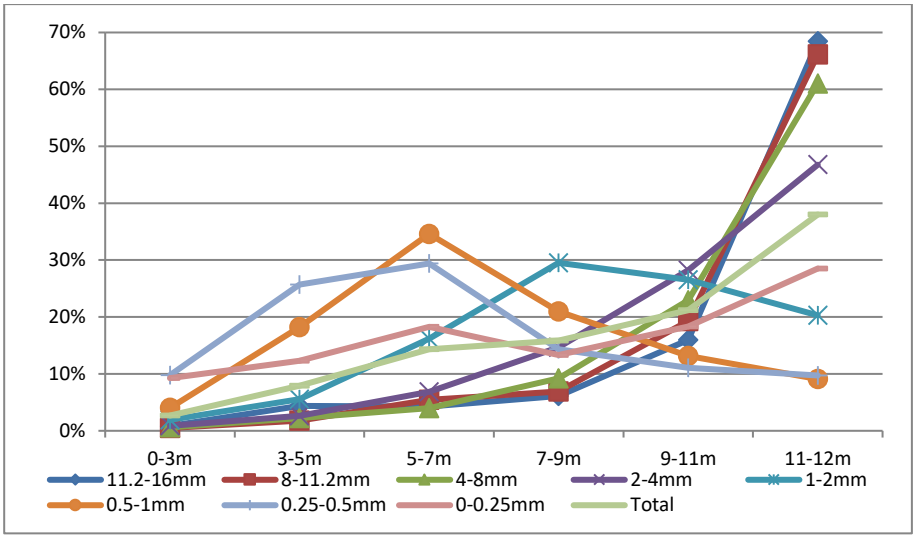

Figure 4.3: Recovery curves of a size fraction over distance intervals from the rotor

In essence, after the water bonds are broken by the high acceleration induced by the rotor, classification within the ADR is much like a ballistic separator. Therefore, the expected recovery pattern for a given size of particles would be a strongly peaked recovery, with an increasing distance for increasing particles sizes. The results show a similar trend, but there are clearly strong deviations, indicating other influences on the classification behavior of the particles than a purely ballistic effect. It can be seen that the behavior of the particles can be subdivided into three different size categories ranging from fine, middle to coarse. For each category there is a different effect dominating the classification behavior (i.e. trajectory distance).

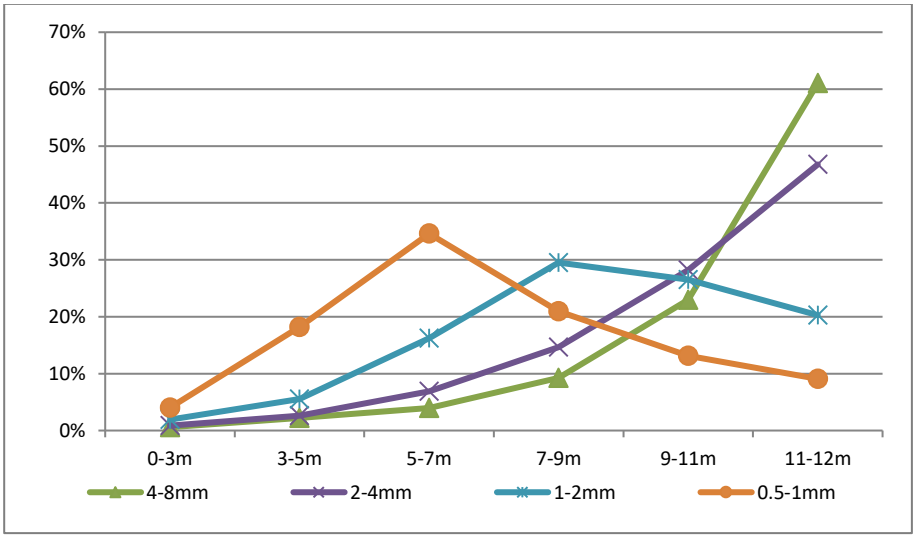

Figure 4.4: Recovery curve of the middle size fractions

Particles between 0.5 mm and 4 mm behave most like expected from a ballistic separator. The landing position is a function of diameter, where fine particles land before coarser ones. However, the recoveries of particles of the same size fraction show a big spread in their final position. The main reasons for this spread are:

- The different hit position on the rotor blade (different starting velocity, starting angle)
- The quasi random influence of collisions with the encasing due to irregular particle shapes
- Spread of particle properties within a size fraction

Aside from these disturbing influence that effect all particles, the very fine and very coarse particles show additional deviations from the ballistic trajectory which cannot be explained by these influences.

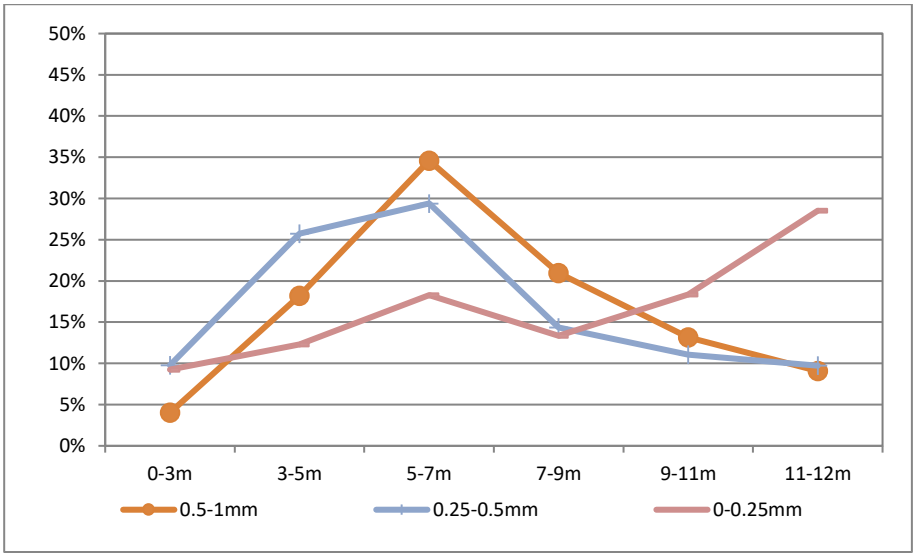

Figure 4.5: Recovery curve of the fine size fractions

In Figure 4.5 it can be seen that particles smaller than 0.5 mm, and particularly the ones smaller than 0.25 mm, land on a position further away than could be expected for a ballistic trajectory of their diameter. Also, as the diameter gets smaller, the spread in landing position increases. This indicates that a simple ballistic trajectory is not the dominant function determining their landing position. Within the ADR there are two mechanisms that have the most influence on why small particles are transported further away:

- Residual adhesion to coarser particles
- Air movement within the ADR

As mentioned in Section 3.3.3, the acceleration needed to break a water bond between a big and small particle is roughly reversely proportional to the cube of the smallest diameter. Even though the ADR applies extremely high acceleration to break water bonds, it still cannot effectively break up water bonds of particles smaller than 250 um.

When these bonds are not broken, smaller particles will follow the trajectory of their host. So the dominant classification parameter of this client particle will be the diameter of the host particle. The recovery curve for the 0-0.25 mm particles in Figure 4.3 clearly shows this effect in that the distribution of these particles as a function of distance to the rotor resembles the average of the distributions of the other particle sizes.

The second effect is caused by the particles' interaction with the air. During the interaction with air, particles are decelerated by drag and the momentum of the particles is transferred to the air, causing a movement of the air. When the air-movement is larger than the terminal velocity of a particle, it will become a dominant force in the trajectory of the particle. The terminal velocity of a 0.5 mm particle with a density of 2000 kg/m^3 is around 3-5 m/s, see equation below. This is a realistic velocity of the air-movement within the ADR. Particles with a diameter smaller than 0.5 mm will follow the air flow until they hit the floor of the separator due to gravity. For these particles, the dominant classification parameter will be the airflow causing them to be widely dispersed.

$$v_t = \sqrt{\frac{2m_p g}{\rho_a A_p C_d}} \xrightarrow{for\ sphere} \sqrt{\frac{4}{3}\frac{D_p \rho_p g}{C_d \rho_a}}$$

$$\sqrt{\frac{4}{3}\frac{0.5 \cdot 10^{-3} \cdot 2000 \cdot 9.81}{0.5 \cdot 1.2}} = 4.7$$

These two effects cause the recovery peaks of fine material to be further away and more spread out than expected

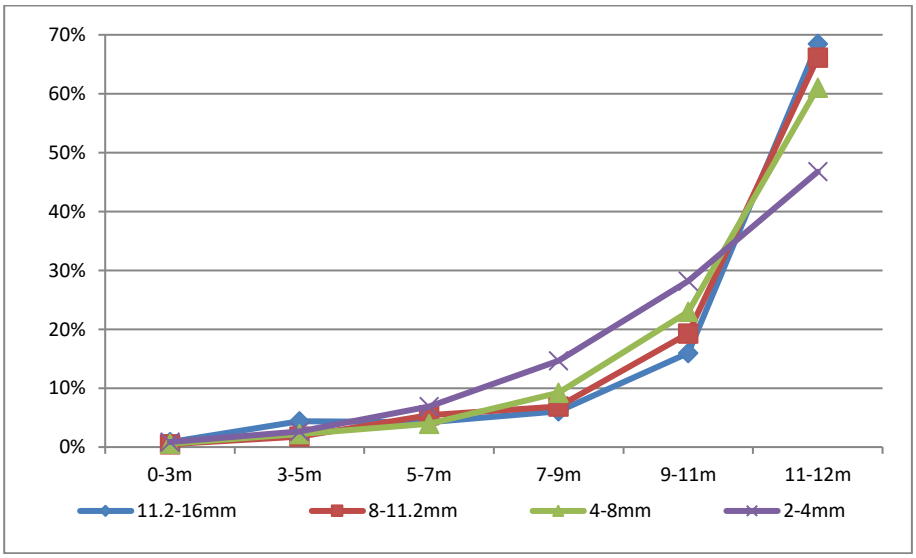

Figure 4.6: Recovery curve of the coarse size fractions

Figure 4.6 shows that the recoveries for the coarsest particles are almost identical. The terminal velocity of these coarse particles is much higher than the initial velocity. Therefore, the drag force is significantly less dominant than gravity and the particles follow almost the same ballistic trajectory. Also, all coarse particles have a deep trajectory and all trajectories crossing the back wall of the ADR are concentrated into the last distance category.

The recovery rates in the 9-11 m category still show a ballistic classification, but the differences between the size fractions are very small. Since the influence of air drag is proportional to the square ratio of the particles velocity to the terminal velocity, discrimination between particle sizes diminishes with increasing size as this ratio goes to zero.

Another, minor effect causing the recovery of coarse particles to deviate, is shown in Figure 4.7. It shows the counter intuitive result that at a smaller distance the recovery for coarser particles increases. This is caused by the boundary (or edge) effect of the rotor blade. The proportion of particles affected by this effect is related to ratio of the size of the particle relative to the size of the rotor-blade. Big particles are hit relatively more often on the edge of the blade, giving them a substantially different trajectory and breaking the regular recovery trend.

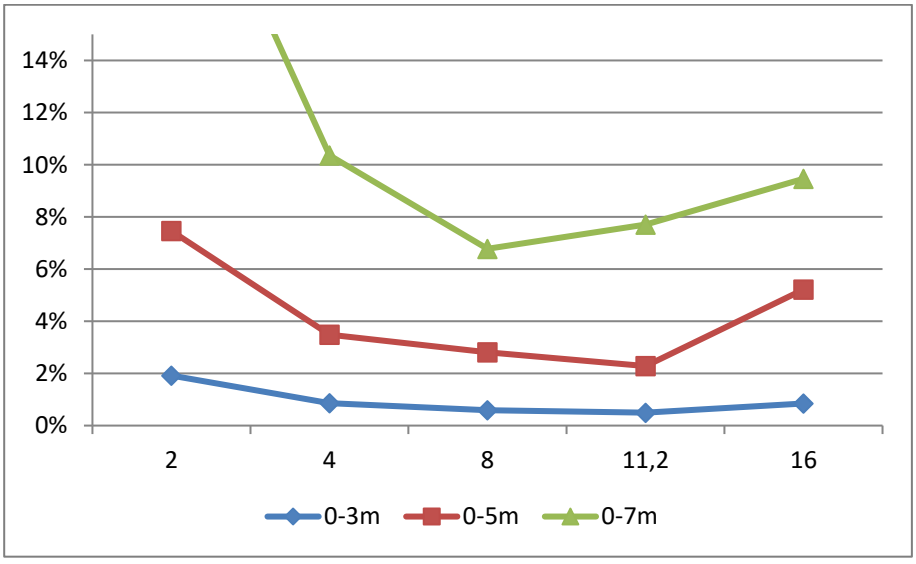

Figure 4.7: Recovery of the coarse size fraction in the first meters

Even though there are deviations on the ballistic classification principle, a good separation between coarse and fine particles can still be obtained. The separation result of this simple ADR unit is determined by the position of a splitter, where the product is divided into two outputs: a fine product (in front of the splitter) and a coarse one (behind the splitter). Figure 4.8 shows the cumulative recovery over the distance for every size fraction (i.e. the recovery in the fine output as function of the splitter position). The (vertical) distance between the lines shows the effectiveness of separation of the two products at that (horizontal) distance.

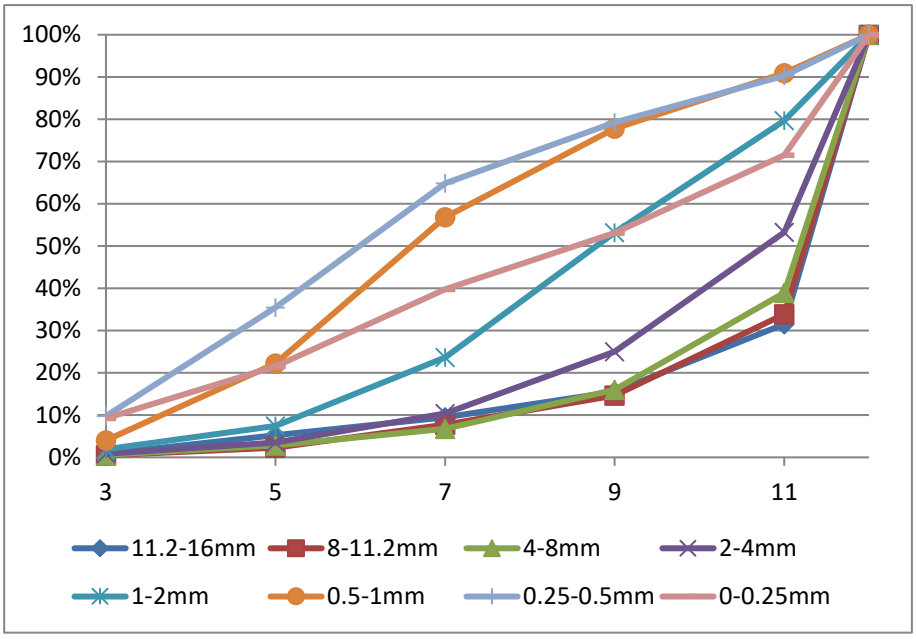

Figure 4.8: Cumulative recovery over the distance from the rotor for every size fraction

The main objective of classification is maximum recovery of fines in the fine output, and maximum recovery of coarse particles in the coarse output. However, as in most classifications a 100% separation cannot be obtained and the optimum position depends on the preference of fines recovery over coarse recovery and the desired classification size.

Figure 4.9 shows a recovery-recovery curve for different classification sizes. The classification is created by separating the product within the ADR at a certain distance. If the classification cut-point is defined as "X mm", the recovery of >X mm in the farthest (coarse) product is plotted on the horizontal axis, and the recovery of particles <X mm in the nearest (fine) product is shown on the vertical axis. A perfect separation would yield 100% recovery for both these outputs. The points in the graph are formed by the different distances at which the two products can be separated within the ADR (the classification distance).

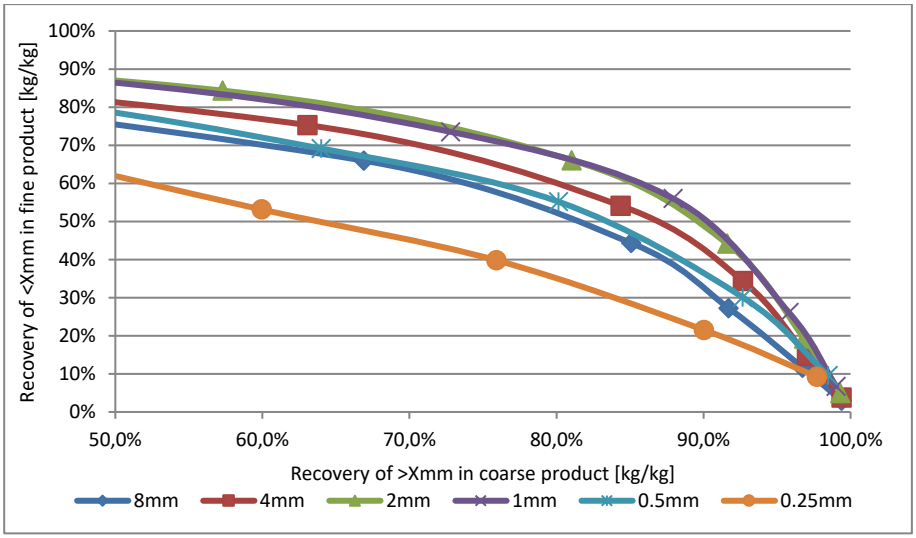

Figure 4.9: Recovery-recovery curve for several cut-sizes

It can be seen that a classification with a cut-point at 1 or 2 mm yields recovery rates which are closest to the optimum. The data points on the graph correspond with splitter distances within the ADR, the lower-right point are close to the rotor, the upper-left points are close to the back of the ADR. Economics and operational constraints determine what the optimum point is within a given operation. When a point most suitable for the targeted waste streams in this study is chosen, recovery rates for coarse and fine are as given in Figure 4.10.

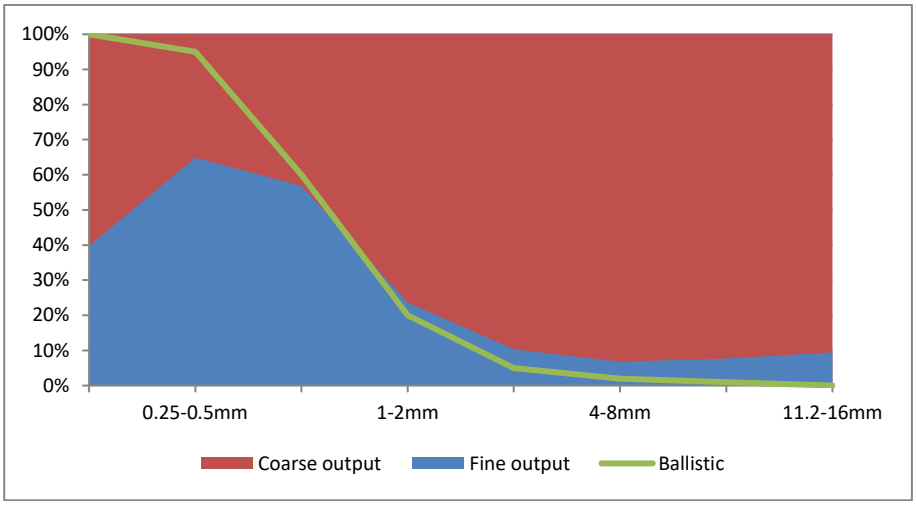

Figure 4.10: Recovery split of size fraction into a coarse and fine product

The effect of the afore mentioned deviations from the ballistic behavior for coarse and fine can clearly be seen in this graph.

Variations on the base case

The results of the base case show the main features of classification with the ADR. A number of additional experiments have been performed with the same experimental setup where a number of key aspects have been varied to see the influence on the classification result. This was done to obtain additional data for modelling and to design an industrial prototype.

The results of these experiments result in large amounts of data. To make the results more insightful the recovery lines are fitted with a simple model. For this, the graphs showing the recovery of a particle size fraction over the distance from the rotor are used. The previous paragraph demonstrated that the majority of the particles in the ADR behave according to a ballistic classification. Additional to this ballistic behavior it can be seen that there are aberrant particles, of which the behavior is dominated by secondary effects. These effects can be subdivided into three groups: residual adhesion, air-movements and blade edge impacts. For a single particle size fraction, only one of these secondary effects is dominant. The effect of the residual adhesion concerns particularly the 0-0.25 mm fraction as was explained above. The behavior of the remaining size fractions is described by the summation of two statistical distributions, forming a fitting model.

The fitting model comprises of two log-normal distributions, defined by a mean and a standard deviation. The first reflect the ballistic behavior of 'normal' particles including the effect of air movement, while the second represents the aberrant particles. A factor determines the ratio between the two distributions. The recovery-line of every size fraction is fitted with the following function:

$$R_{F\,d,s_1,s_2} = (1-\gamma d)\ln N\left(\mu_{d,b},\sigma_{d,b},s_1,s_2\right) + \gamma d\,\ln N\left(\mu_{d,a},\sigma_{d,a},s_1,s_2\right)$$

$$\mathrm{RMSE} = \sqrt{\frac{\left(R_{F\,d,s_1,s_2} - R_{E\,d,s_1,s_2}\right)^2}{n_E}}$$

Where d is the particle diameter of the size fraction and $R_{F\,d,s_1,s_2}$ is the fitted recovery of the size fraction in between distances s_1 and s_2. $\mu_{d,b}, \sigma_{d,b}, \mu_{d,a}, \sigma_{d,a}$ and γ are fitting parameters and $\ln\mathrm{N}(\ldots)$ is the integral of the log-normal probability density function from s_1 to s_2. R_E is the experimental recovery of a size fraction and n_E is the number of distance intervals. The fitting parameters are chosen to minimize the RMSE. For convenience, the contribution of the aberrant term is ignored for particle sizes smaller than 2mm.

Figure 4.11 shows the fit for the base case. The figure presents the recovery curves as a function over particle size and the distances are series. The experimental data is plotted as points, the result of the fit-model as the lines. The RMSE of the fit is 1.83%

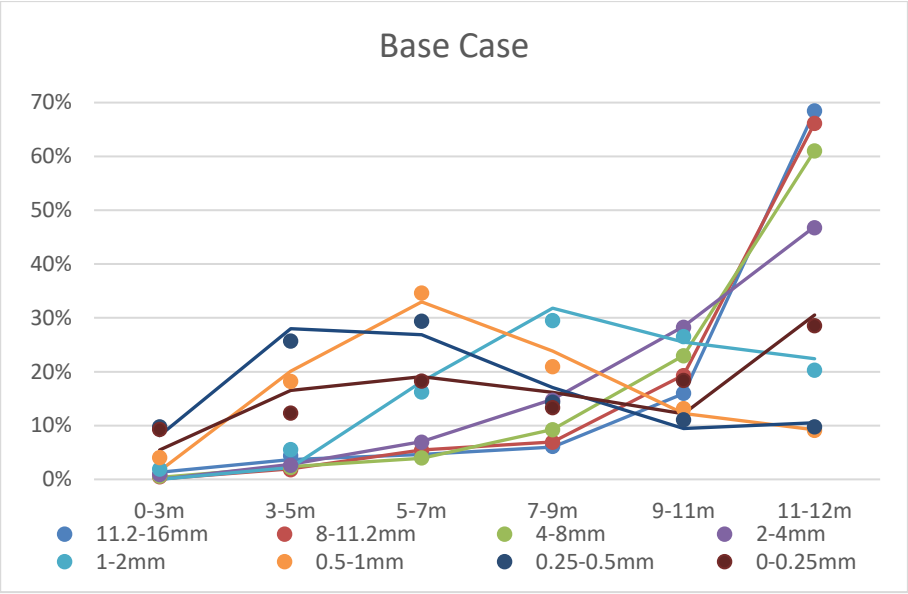

Figure 4.11: Comparison of raw experimental data (points) and the fit model (lines)

The fitting model transforms the data of a single experiment into a set of five lines. The first two lines give the means of the log-normal distributions as a function of the particles diameter. The next two show the standard deviation and the last shows the amount of aberrant behavior (given by the function γd). The fit parameters for the base-case are shown in Figure 4.12.

The figure shows the workings of the ADR. The graph for ballistic mean ($\mu_{d,b}$) shows the basic ballistic separation: coarse particles land further away than fine particles. The slope of the line is not as steep as expected for a ballistic separation because of air-movement effects within the ADR. Secondary, there is a sharp deviation of the finest fraction due to residual adhesion. The distribution of a size fraction (given by $\sigma_{d,b}$) is wider for fine fractions for the ballistic particles because of influences mentioned earlier. For the aberrant particles, the ballistic mean is lower because the initial speed is lower and the intial angle can vary to very steep. This large variation in initial angle also results in the wide distribution ($\sigma_{d,a}$) and coarsest particles are effected more because of size effects.

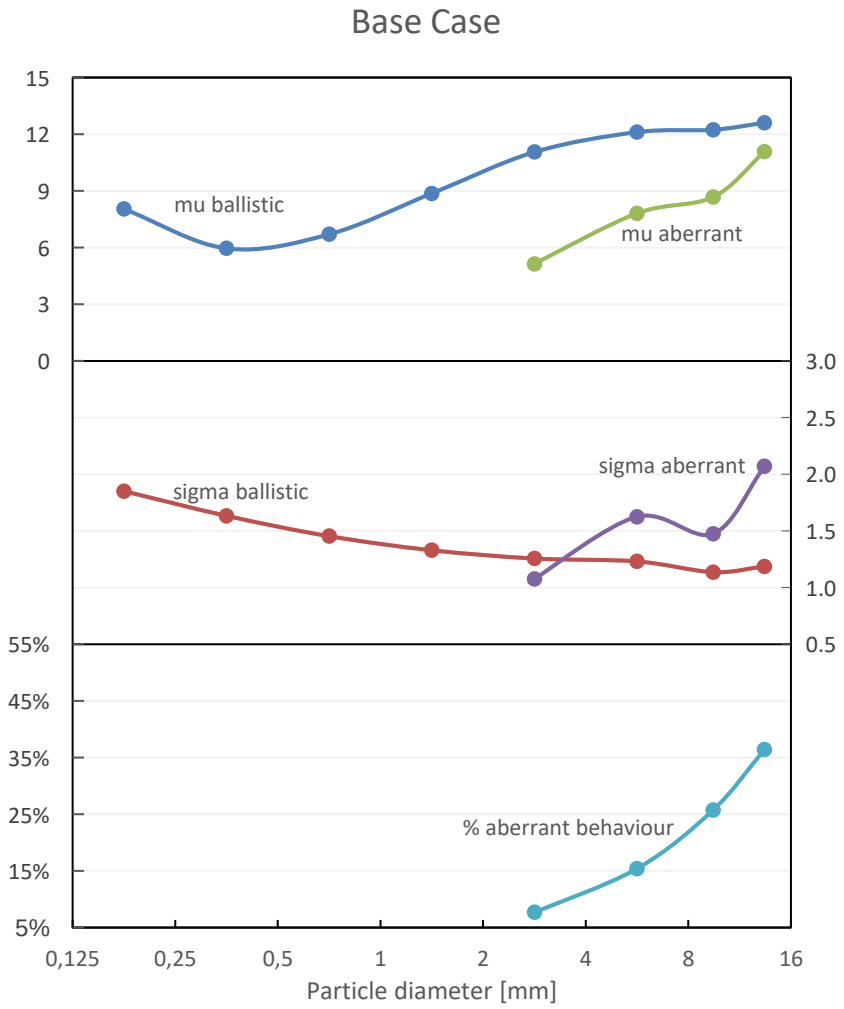

Figure 4.12: Fit parameters for the base-case

The representation of the experimental data by its fit parameters allows for better comparison between experiments. During these experimental sessions a number of key parameters have been changed as follows:

- Throughput from standard to low
- Material from moist to no moisture
- Material from IBA to CC

The changed values can be seen in Table 4.1. The influence of these changes is discussed in the text below.

Table 4.1: Changed parameters for experimental variations on the base case

	Base case	**IBA 30 t/h**	**No moisture**	**CC 76 t/h**
Material	Bottom ash	Bottom ash	Bottom ash	Crushed concrete
Throughput t/h/m	58.4	33.3	59.1	76.2
Moisture content kg/kg	15.0%	12.8%	0.0%	9.4%

Low throughput

Figure 4.13 shows the fitting parameters of the low throughput experiment and the base case is shown in the background. The RMSE of the fit is 1.83%.

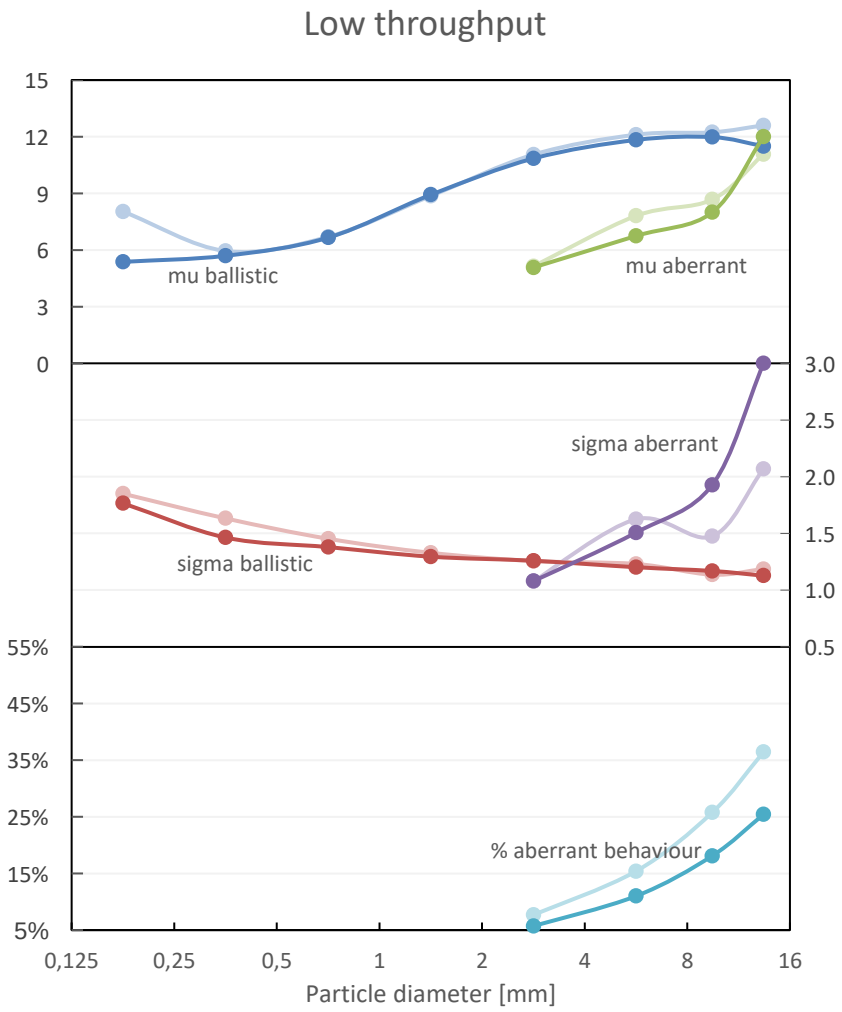

Figure 4.13: Fit parameters for 'Low throughput'

Decreasing the throughput decreases the layer thickness on the rotor blade and so the impact of the rotor on the material is more direct and more fine particles will be liberated. This can be seen in the lower $\mu_{d,b}$ for the <250 µm particles. Furthermore, at a lower throughput, less momentum is transferred to the air, causing there to be less air movement, which can be seen in $\sigma_{d,b}$ which shows a slightly lower value for smaller particles. The aberrant behavior has a large statistical component and it is therefore not possible to draw solid conclusions from single experiments.

No moisture

Figure 4.14 shows the fitting parameters of the no moisture experiment and the base case is shown in the background. The RMSE of the fit is 2.14%.

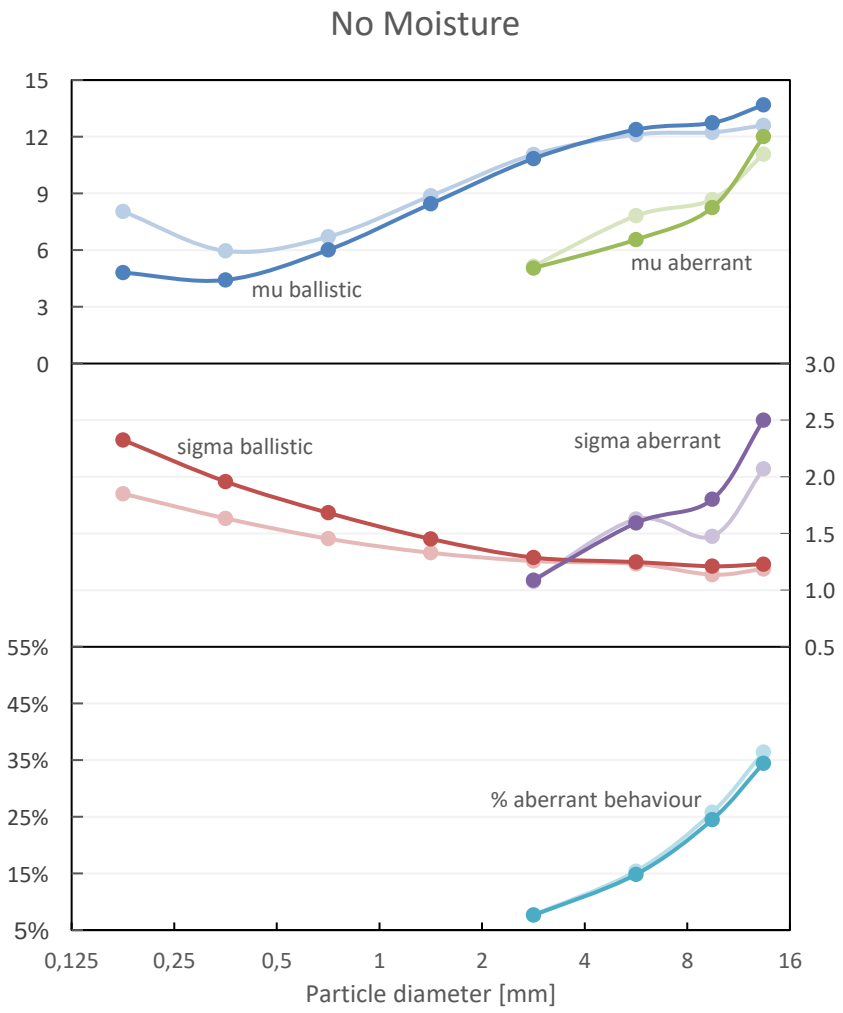

Figure 4.14: Fit parameters for 'No Moisture'

When there is no moisture, all particles are free, so no particles will remain attached to coarser particles. However, the finest particles are decelerated rapidly, increasing the total momentum transfer to the air and therefore increasing the air-movement. This becomes the dominant factor for the finest particles since the terminal velocity of these particles (~2.3 m/s) is much lower than the air velocity. The $\mu_{d,b}$ of the 0-250 µm particles will be much higher than expected in stationary air and spread wider. This also affects the particles up to 1 mm, as can be seen in $\sigma_{d,b}$.

Crushed concrete

Changing the material from incinerator bottom ash (IBA) to crushed concrete (CC), alters the type of material as well as the PSD of the input material. Crushed concrete has a higher density, a higher modulus of elasticity and is more irregularly shaped than bottom ash. Figure 4.15 shows the PSD of both materials.

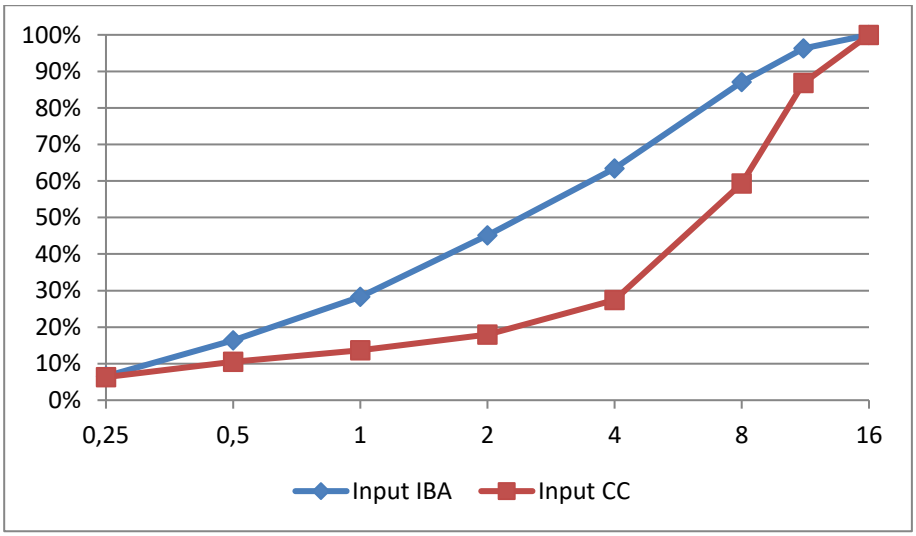

Figure 4.15: PSD of IBA compared to PSD of CC

Figure 4.16 shows the fit parameters of both experiments. The RMSE of the crushed concrete experiment is 0.74%.

It can be seen that the main differences are in $\sigma_{d,b}$. The recovery of a size fraction of crushed concrete has a bigger spread than bottom-ash. This is most probably due to the higher modulus of elasticity. This causes the collision of particles to be more sensitive for the shape of the particles and the orientation of the particle relative to a surface. Therefore, increasing the randomness introduced by this effect.

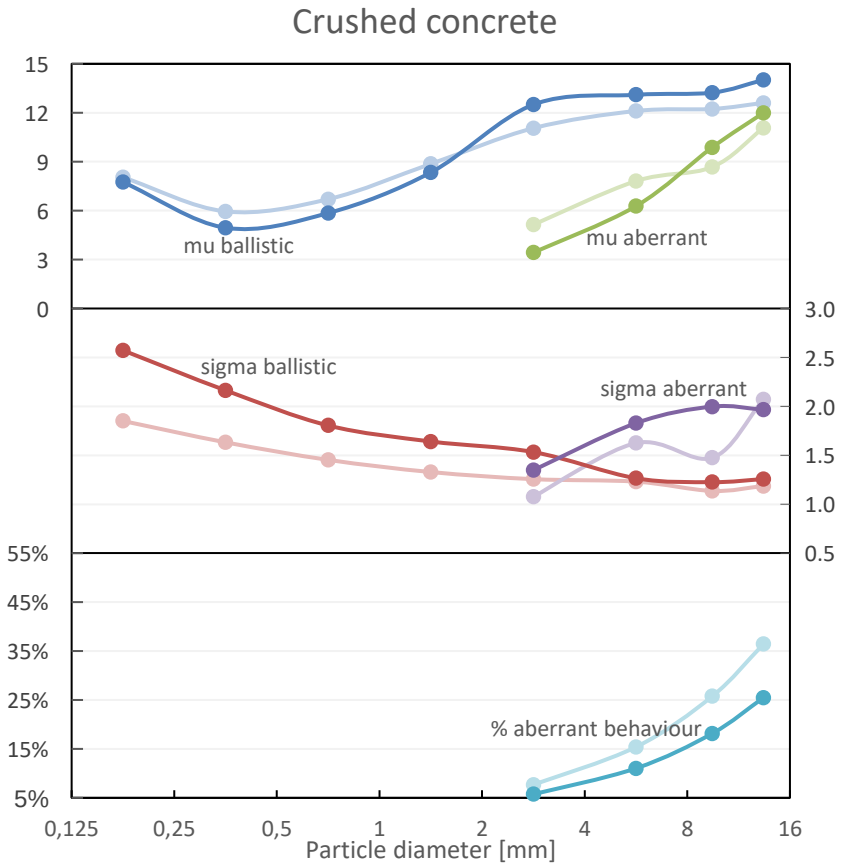

Figure 4.16: Fit parameters for 'Crushed concrete'

General influences on classification efficiency

To create a single point of comparison, a separation distance, $s_{50\%}$ is defined at the 50% recovery point of the 0.5-1 mm fraction. The separation at distance $s_{50\%}$ results in a fine and coarse product, in which the recovery of the <1 mm particles and the >1 mm particles can be assessed. To determine the classification distance and the recoveries, the fit model is used. The results are shown in Table 4.2.

$$(1-\gamma\cdot 0.71)\ln N\left(\mu_{0.5-1mm,b},\sigma_{0.5-1mm,b},0,s_{50\%}\right) = 50\% \rightarrow s_{50\%}$$

$$R_{<1mm} = \frac{\sum_{d_{0.25\mathrm{mm}}}^{d_{1\mathrm{mm}}} P_d R_{d,0,s_{50\%}}}{\sum_{d_{0.25\mathrm{mm}}}^{d_{1\mathrm{mm}}} P_d}$$

$$R_{>1mm} = \frac{\sum_{d_{1\mathrm{mm}}}^{d_{16\mathrm{mm}}} P_d R_{d,s_{50\%},\infty}}{\sum_{d_{1\mathrm{mm}}}^{d_{16\mathrm{mm}}} P_d}$$

Here P_d is the mass particle size distribution.

Table 4.2: Comparison of classification results for the four experiments

	Base case	Low throughput	No Moisture	Crushed concrete
S50 of 0.5-1 mm	6.70	6.66	5.82	5.97
Rec. <1 mm	50.7%	58.8%	57.5%	48.4%
Rec >1 mm	90.5%	91.3%	90.4%	93.2%

The results show the consistent results of the ADR classification.

More general, Figure 4.17 shows the recovery-recovery graph for all four experiments performed. The lines are constructed similarly as the table above, but the experimental $R_{E\,d,s_1,s_2}$ is used at the splitter distances used in the experiment. The graph-points below are labeled by their splitter distance.

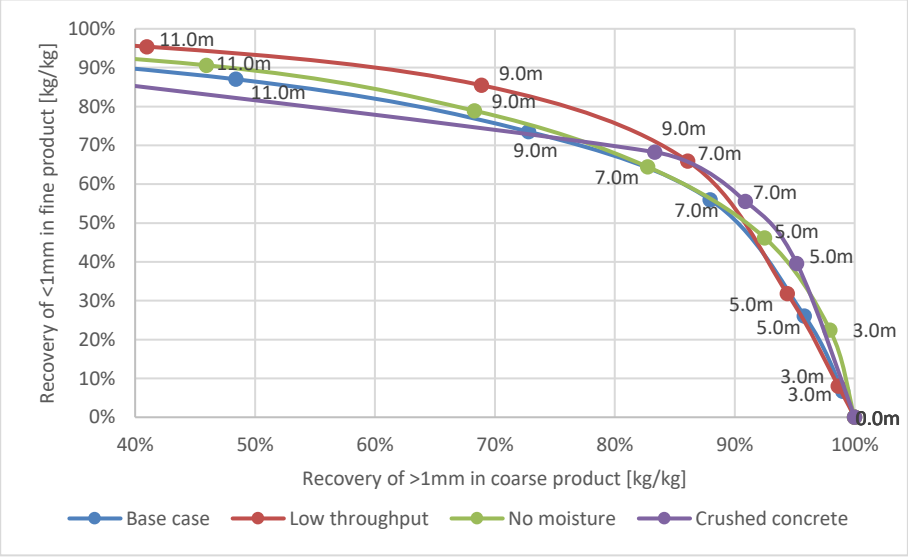

Figure 4.17: Recovery-recovery graph for the four experiments performed

Note that all curves are relatively close to each other, demonstrating the robustness of the ADR. It can be seen that the recovery of <1 mm particles strongly increases only over the first few meters. Beyond this point, recovery of >1 mm particles in the coarse is sacrificed for additional recovery of <1 mm in the fines. Figure 4.18 shows a zoom-in on this region of interest.

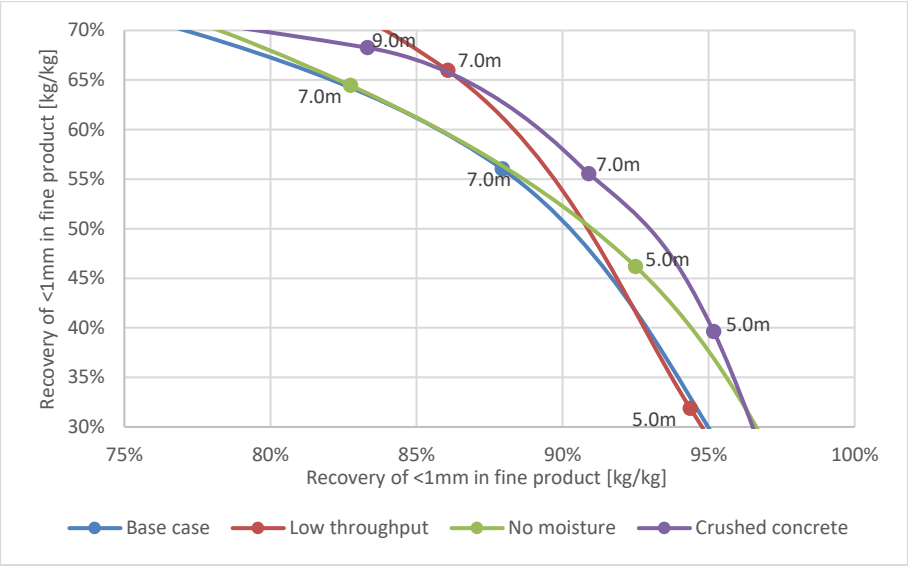

Figure 4.18: Region of interest of the recovery-recovery graph for the four experiments performed

Recovery of <1 mm in fine output is not high enough for this simple ADR process to directly create a high grade coarse product which is suitable for conventional techniques (e.g. to enable screening at 5 mm, or magnetic or ECS separation). However, processing with the ADR enables the use of an air-knife to further clean the coarse product. An air-knife after ADR is highly efficient because of three reasons:

- A significant amount of the <1 mm particles has already been removed
- The <1mm particles are liberated from the >1 mm particles
- All particles are spread out over a large surface

To sustain the properties of the coarse product that enable air-knife classification, the product needs to be collected on a big surface (i.e. in a mono-layer). For this, a conveyor moving at high velocity (>3 m/s) is used. The mono-layer on the conveyor is then classified via a powerful air-stream (>25 m/s) to further remove the <1 mm particles.

4.2 Incinerator bottom ash

4.2.1 Introduction

The results of the ADR prototype were combined with early modelling results to design an industrial ADR for processing municipal solid waste incineration bottom ash at 120 t/h, see Figure 4.19. The input of this ADR comes from a conventional bottom ash upgrading process, where the material is classified with vibrating deck screens and the metal is extracted with magnets and eddy current separators. This pre-process produces a 0-12 mm stream, which used to be unprocessable and would be landfilled or used AS IS in road foundations. This material is now processed with the ADR and the coarse output is treated with ECS to recover non-ferrous metal particles down to 1 mm.

Results of the prototype ADR showed that the recovery of 0-1 mm in the fine output is not high enough for conventional processes (e.g. ECS) to be directly applicable when only classification of the rotor is used. However, because a significant amount of the fines is removed and the 0-1 mm particles are liberated from the >1 mm particles, an air-knife can be used to further clean the coarse output. The industrial ADR uses such an air-knife to further remove the fine fraction from the coarse product. Therefore, this ADR produces three outputs, which will be indicated by 'Coarse', 'Air-knife' and 'Rotor'.

Figure 4.19: Industrial ADR operating at 120 t/h

4.2.2 Methodology

The performance of the industrial ADR on processing different moisture contents and throughputs was assessed via four tests. In these tests the key parameters were as follows:

- Low throughput (base case)
- High throughput
- Wet low throughput
- Wet high throughput

For every experiment, the input and three output streams were sampled (~100kg/per sample) and analyzed. After drying the material, the material was screened at 1, 2, 4 and 8 mm. For the fractions >1 mm the composition in terms of light material (floats), mineral, light non-ferrous and heavy nonferrous (HNF) was determined via the analysis scheme given in Figure 4.20 [39].

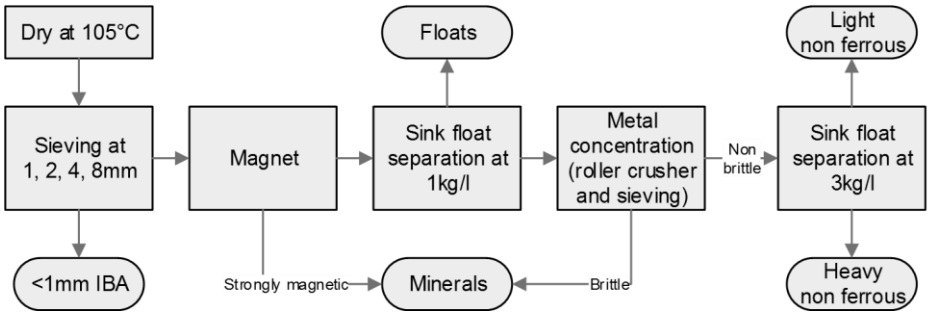

Figure 4.20: Analysis scheme for bottom-ash samples processed with the ADR

4.2.3 Results

Input

Table 4.3 shows the properties of the input streams in the four experiments. The moisture content of the 'wet' experiments is only slightly higher than the base case. However, this slight increase leads to a substantial difference in the appearance and behavior of the bottom ash, because the moisture level is getting close to packing void saturation. The grade of 0-1 mm material decreases with both an increased throughput and an increased moisture level. This is because the sieve efficiencies in the pre-processing of the bottom ash decrease for higher throughputs and moisture contents.

Table 4.3: Parameters for the four experiments with an industrial ADR and bottom ash

	Low throughput	**High throughput**	**Wet low throughput**	**Wet high throughput**
Throughput [t/h]	91	140	64	115
Moisture [%]	16.9%	16.5%	19.8%	19.4%
Grade 0-1mm [%]	30.7%	27.0%	23.9%	23.1%
Grade LNF [%]	1.40%	1.5%	2.0%	1.6%
Grade HNF [%]	0.6%	0.8%	0.9%	0.7%

Output

Figure 4.21 shows the particle size distribution of the input and outputs for the base case. It is also shown the control series, which is the weighted average of the outputs. This control is slightly finer than the input material, because some particles break during processing with the ADR.

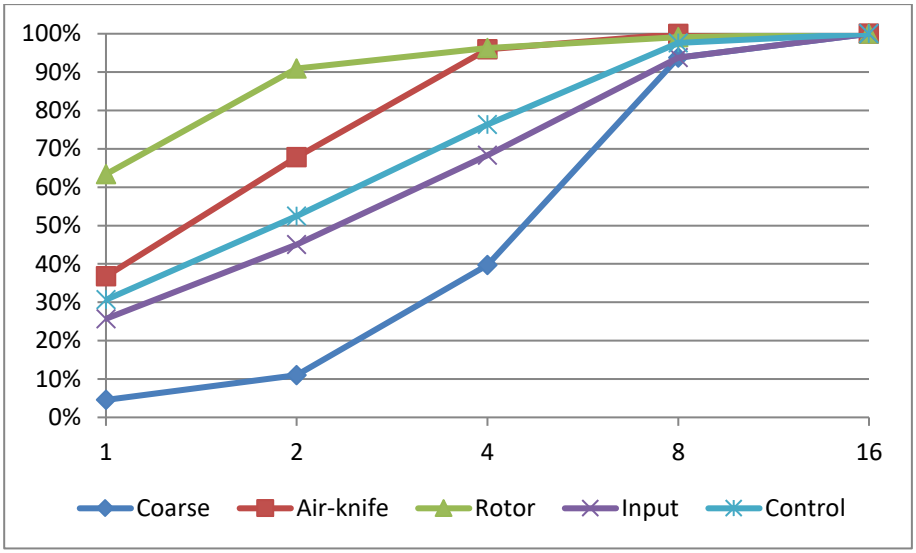

Figure 4.21: Particle size distributions of input and outputs of the base case

It is shown that the coarse output has a substantially lower grade of 0-1 mm particle (5% compared to the 30% of the input). Since moisture is associated with fines, the moisture content of the coarse fraction decreased from 17% to 12%. These two effects (reduction of fines content and moisture content) result in a material that can be well processed using conventional sieves and eddy current separators (ECS).

To better compare the results of the four experiments, recovery rates are shown in the following section. The recovery over the three outputs is given per size class, and the constituents are grouped, based on density (as indicated in Figure 4.20).

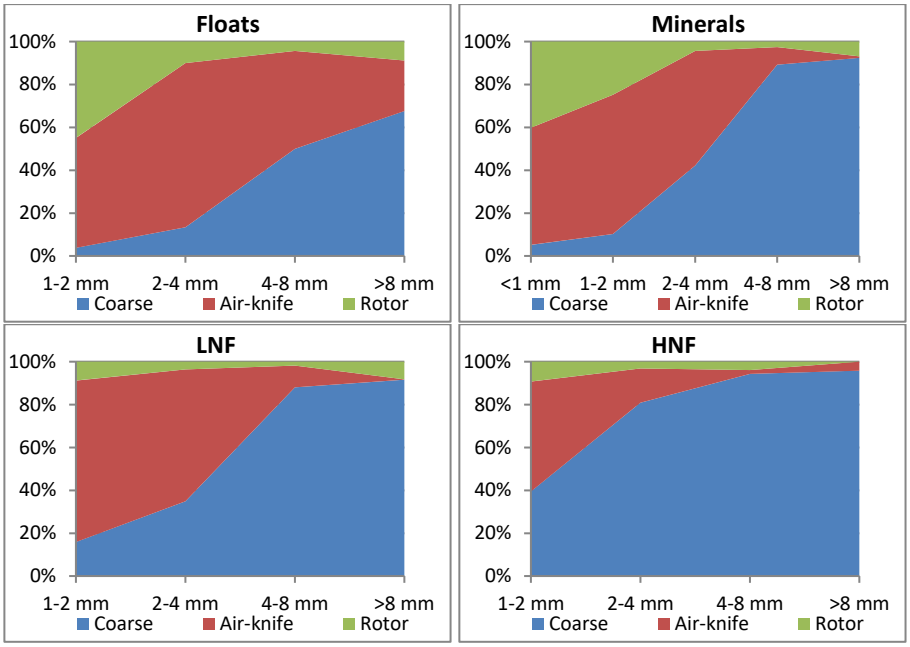

Figure 4.22: Recovery rates per size fraction for low throughput

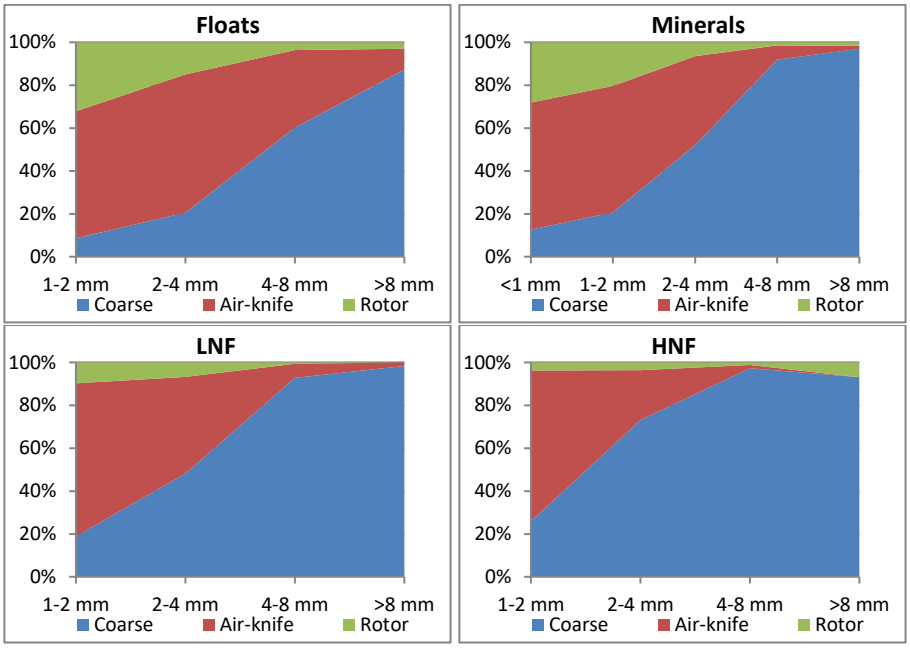

Figure 4.23: Recovery rates per size fraction for high throughput

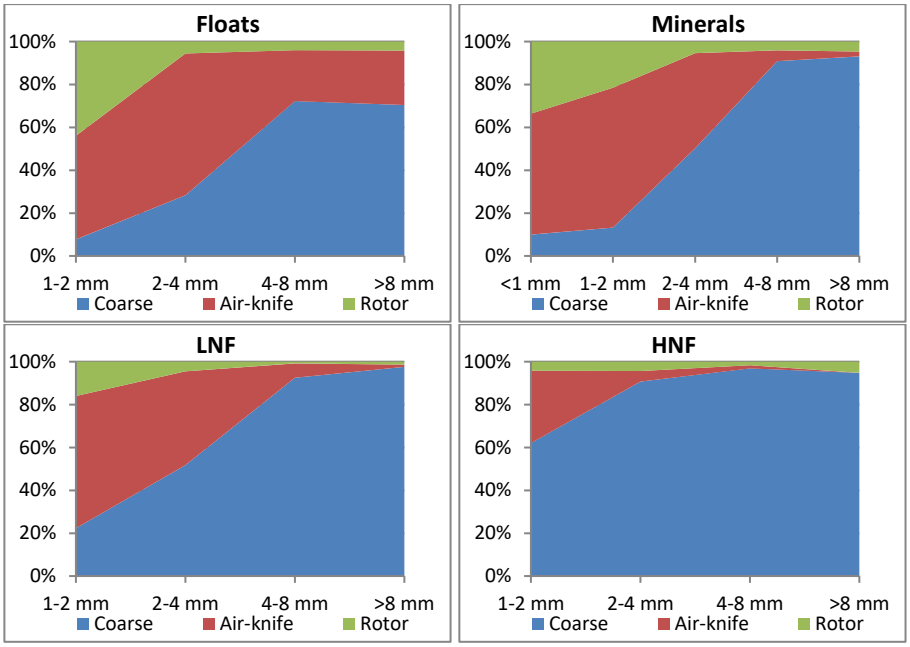

Figure 4.24: Recovery rates per size fraction for wet low throughput

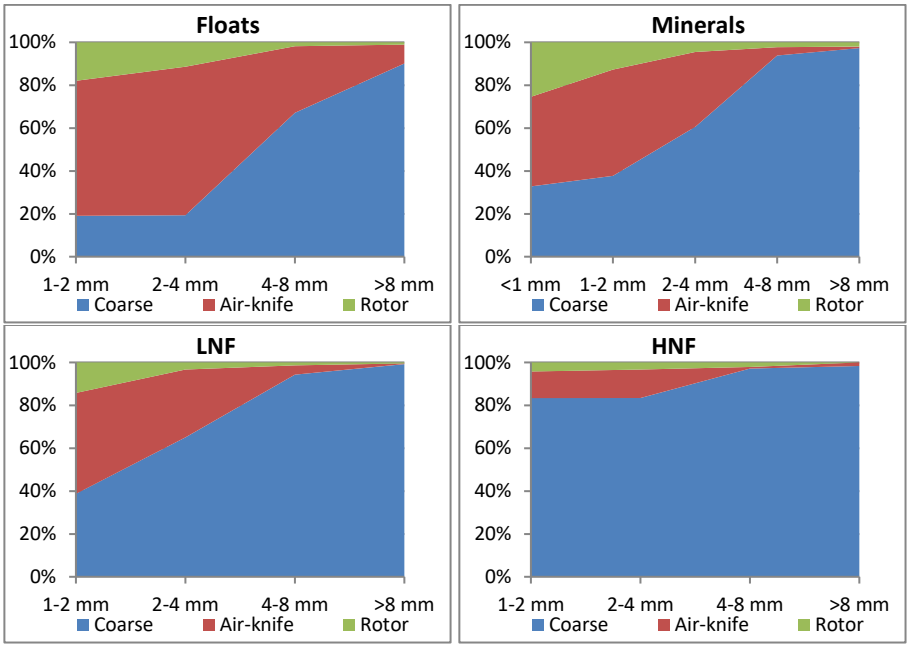

Figure 4.25: Recovery rates per size fraction for wet high throughput

The results show the influence of the material density on the classification. The cut-point of the recovery in the coarse product shifts with the density. Furthermore, the influence of throughput and moisture content can be seen. To better compare the results and see the influences of density, throughput and moisture content on the classification, the recovery into the coarse product is fitted with a sigmoid function.

$$R(D) = \frac{1}{1 + 3^{D_C - D}/\alpha}$$

Where R is the recovery of a size fraction, D_c is the 50% recovery diameter and α determines the width of the transition. Table 4.4 and Figure 4.26 show the results for the fits.

Table 4.4: Fitting parameters and RMSE of the four experiments

		Moist		**Wet**	
		Low throughput	High throughput	Low throughput	High throughput
D_c	Floats	5.7	5.0	4.3	4.6
	Mineral	3.2	2.8	2.9	2.2
	LNF	3.5	2.9	2.8	2.0
	HNF	1.7	2.1	1.0	0.4
α	Floats	1.6	1.7	1.5	1.8
	Mineral	1.1	1.2	1.0	1.5
	LNF	1.3	1.1	1.2	1.4
	HNF	0.9	0.8	0.9	1.7
RMSE	Floats	0.9%	0.4%	2.5%	5.2%
	Mineral	2.9%	1.3%	3.4%	1.6%
	LNF	4.3%	0.9%	1.3%	0.4%
	HNF	3.0%	1.2%	1.6%	0.9%

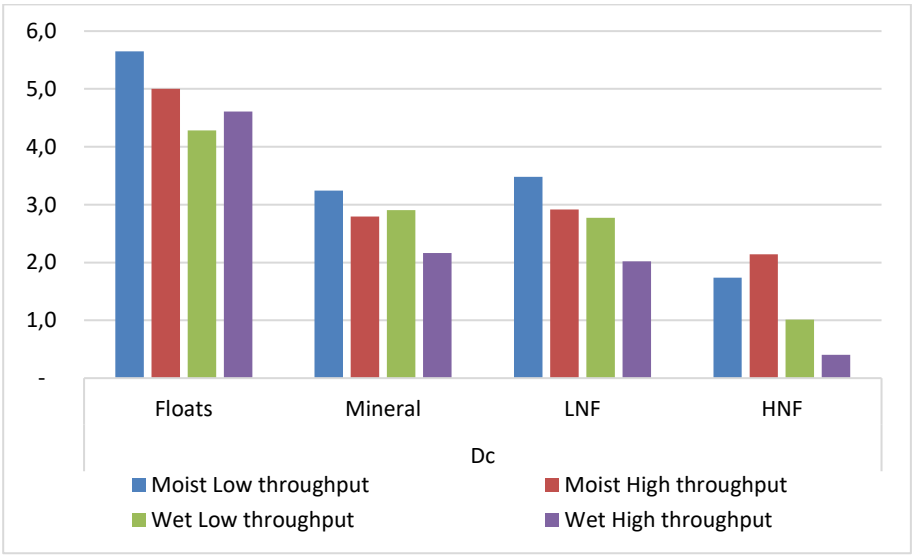

Figure 4.26: The 50% recovery diameters for four experiments for four constituent groups

The recovered size fraction in the coarse product for floats is roughly five times the diameter for HNF. This is directly related to the specific density of the materials. The beneficial effect of this for classification of bottom-ash is that a 2 mm cut size in minerals will result in a 0.5 mm cut size for HNF particles and therefore the overall HNF content in the coarse product increases.

Figure 4.27 shows a summary of the classification within the four experiments. The results show that the ADR removes 67% to 95% of the <1 mm minerals. Increasing the throughput and the moisture content reduces this removal. The recovery of NF particles is less sensitive to these operational parameters and shows a consistent value of over 85%.

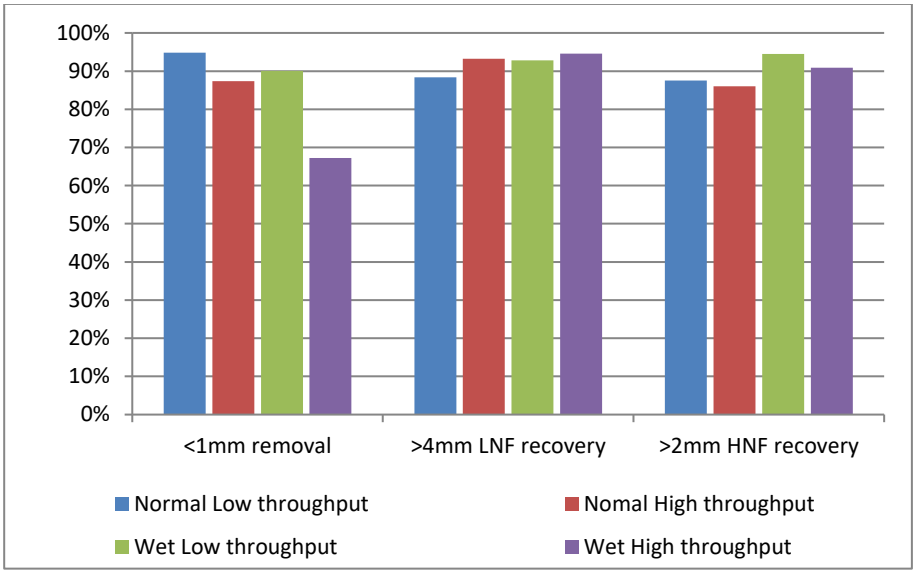

Figure 4.27: Recovery/removal rate into the coarse product

4.2.4 Post-processing

Images of the input, fine and coarse product of IBA are presented in Figure 4.28. The input mix of fine and coarse particles shows a surface coating of very fine particles on all grains because of the moisture that is present. After processing, the adhering fines are removed from the coarse product, resulting in a loose and processable mixture.

Figure 4.28: Bottom ash input, fine and coarse product

The coarse material produced by the ADR was further processed using industrial eddy current separators to concentrate the non-ferrous metals.

Results showed a high recovery of 89% of NF metals in the 1-8 mm product (twice the recovery of the state of art reference case). The amount of fines in the mineral reject of the ECS was strongly reduced, making it more suitable for road foundation. Furthermore, since more NF metal is recovered by ECS, the metal content in the mineral product, and with it the ultimate leaching potential, is reduced, improving its environmental properties when applying the material as a foundation layer. The fine fraction produced in the ADR (-1 mm), is an interesting material for the production of cement [40, 41].

4.3 Construction and demolition waste

4.3.1 Introduction

An early industrial prototype of the ADR was tested to process construction and demolition waste (CDW) streams, (Figure 4.29). The input was screened at 16 mm using conventional processes. Since the results of the prototype ADR showed insufficient recovery of the 0-1 mm fraction, the coarse product of the ADR was directly processed using an air-knife. In the industrial prototype this flow was directly combined with the rotor product, creating two outputs, which will be indicated as 'Coarse' and 'Fine'.

Figure 4.29: Early industrial ADR prototype

4.3.2 Methodology

The performance of the ADR on processing different construction and demolition waste (CDW) streams was assessed via three tests. The following three types of material were processed:

- Crushed concrete with a high level of floating contaminants (PCC)
- Relatively clean crushed concrete (CCC)
- Sifting sand (SS)

For every experiment, the input and two output streams were sampled (~100 kg) and analyzed. After drying the material, the material was classified down to a 250 µm mesh. For the material >4 mm the amount of floating contamination (i.e. wood) was measured according to the method of the Dutch NEN-EN 933-11.

4.3.3 Results

Input

An overview of the composition of the input materials is presented in Table 4.5. The particle size distributions (PSD) of the three input materials are shown in Figure 4.30.

Table 4.5: Main properties of CDW materials

CDW materials		**Moisture**	**0-1 mm**	**Floating (+4 mm)**
		(kg/kg wet)	(kg/kg)	(cm3/kg)
Polluted crushed concrete	(PCC)	11.7%	47.1%	12.3
Clean crushed concrete	(CCC)	8.4%	30.4%	1.38
Sifting sand	(SS)	20.5%	53.0%	215.5

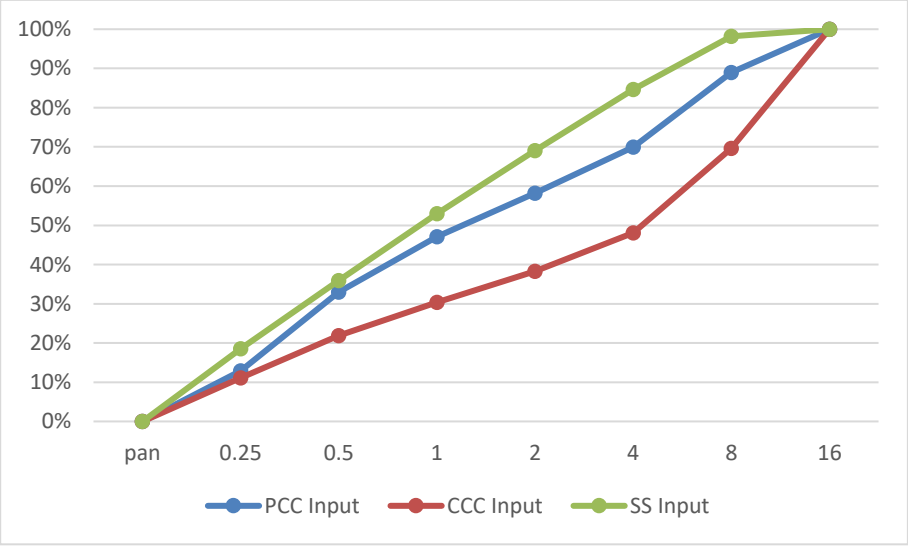

Figure 4.30: Sieve passing of three CDW-materials

Outputs

Three different types of CDW were processed using the same industrial ADR installation. Figure 4.31 to Figure 4.33 show the particle size distributions for heavily polluted crushed concrete, relatively clean crushed concrete and sifting sand, respectively.

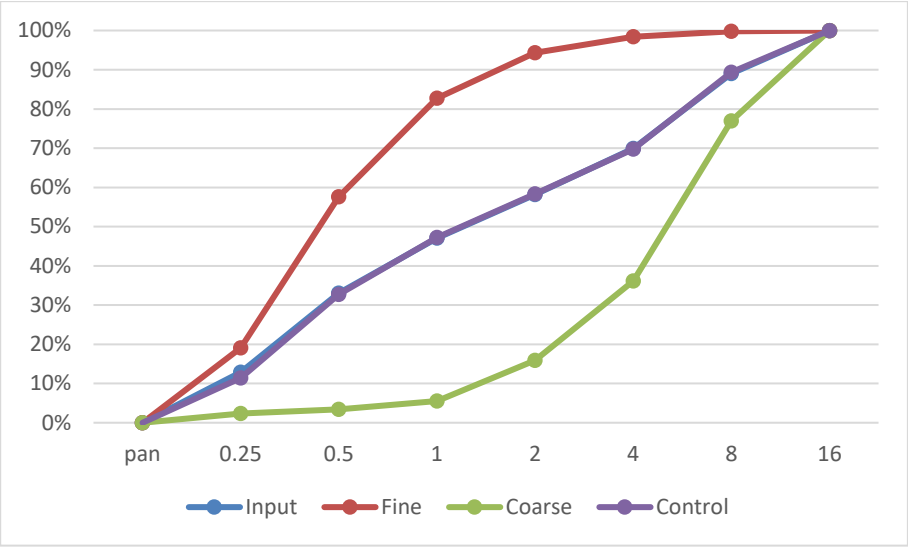

Figure 4.31: Sieve passing of processed Polluted crushed concrete

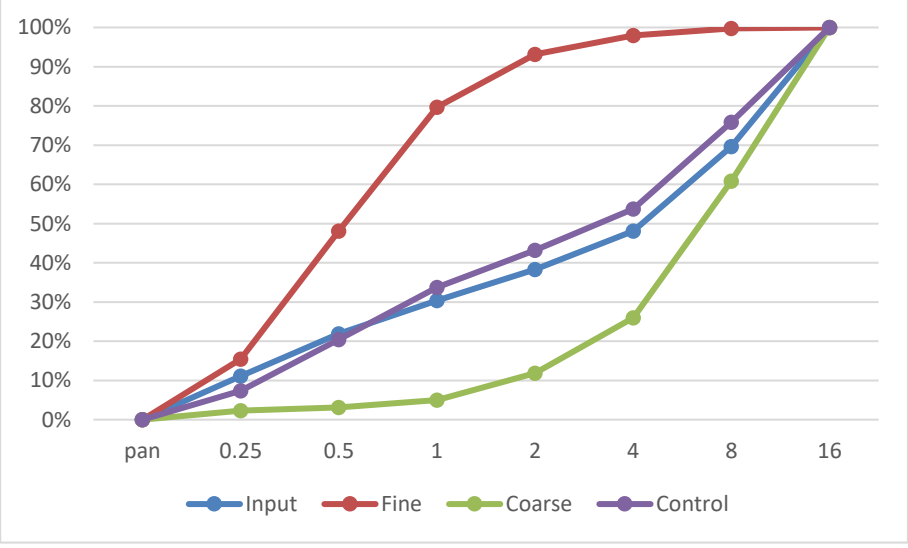

Figure 4.32: Sieve passing of processed Clean crushed concrete

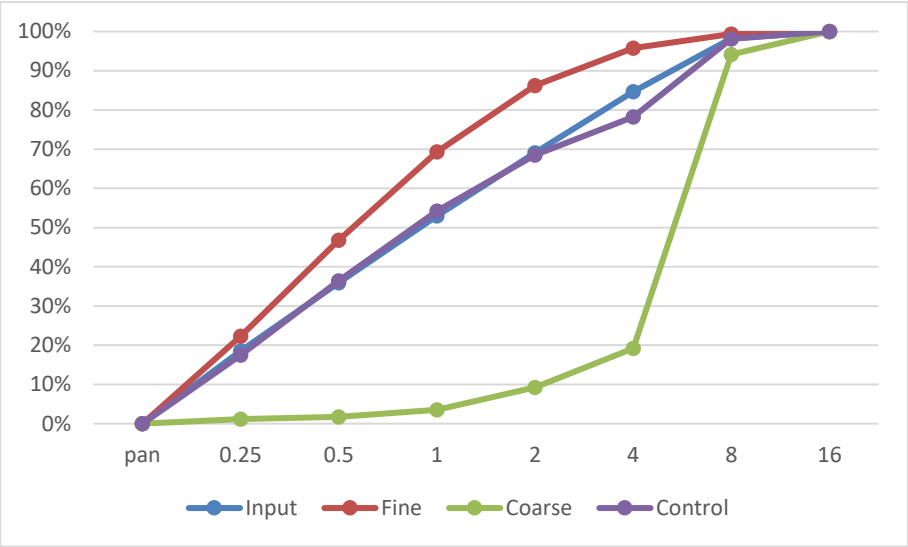

Figure 4.33: Sieve passing of processed sifting sand

For all three materials, the distinction between the coarse and fine product is very clear. The D_{10} of the coarse product increased by almost a factor eight with respect to the input. As can been seen in Table 4.6, this reduction in fine fraction is accompanied by a reduction in moisture content of about 25% with respect to the input.

Table 4.6: Moisture content of the input and two output products for all three tests

	PCC	**CCC**	**SS**
Input	11.7%	8.4%	20.5%
Fine	13.7%	11.2%	21.6%
Coarse	8.4%	6.7%	14.6%

The moisture present in the crushed concrete consists of absorbed and adsorbed moisture. The absorbed moisture is of no concern in processing the material since it plays no part in particle-particle interaction. Concrete contains pores created in the cement hydration process [42]. In moist crushed concrete these pores will be filled with absorbed moisture, which is typically in the range of 5%. If only the adsorbed moisture is considered, the reduction from input to coarse product is even more striking. This reduction makes the crushed concrete much more suitable for further processing.

Table 4.7 shows the mass distribution, grades and recoveries of the input, coarse and fine product for each of the three experiments.

Table 4.7: Summary of results and recovery rates

		PCC	CCC	SS
Mass distribution	Fine	54.1%	38.5%	77.0%
	Coarse	45.9%	61.5%	23.0%
0-1mm grade	Input	47.1%	30.4%	53.0%
	Fine	82.7%	79.7%	69.3%
	Coarse	5.5%	5.0%	3.6%
0-1mm recovery	Fine	94.6%	90.9%	98.5%
	Coarse	5.4%	9.1%	1.5%
>1mm recovery	Fine	17.7%	11.8%	51.6%
	Coarse	82.3%	88.2%	48.4%

Figure 4.34 shows the recovery of every size fraction in the coarse product for all three materials tested. It shows that the recovery per size fraction of CCC is very similar to PCC. There is only a difference in the recovery of the finest fractions. This is because of different interaction of the material at the rotor, causing a difference in the residual adhesion of particles. Furthermore, it shows that the recovery line for sifting sand is shifted almost two size fractions coarser. In these experimental series, the settings of the ADR were not adjusted, so the change in cut point is a result of the properties of the processed material. This difference in cut-size reflects the difference in specific density of the material.

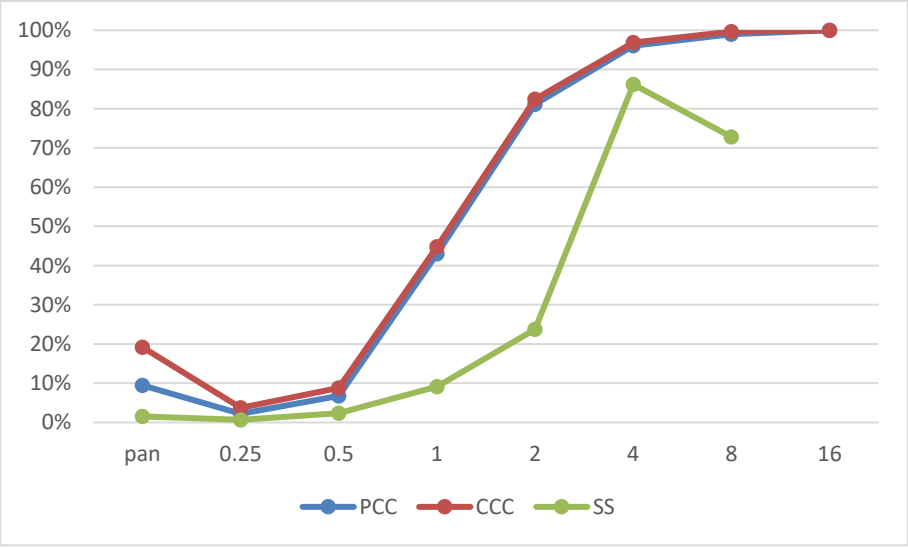

Figure 4.34: Recovery of every size fraction in the coarse product

Figure 4.35 and Figure 4.36 show images of crushed concrete and sifting sand that have been processed to form a fine and coarse product.

Figure 4.35: Concrete granulate input, fine and coarse product

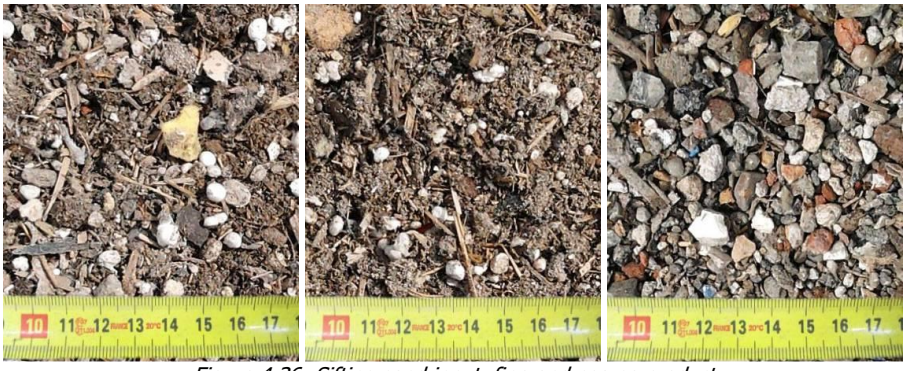

Figure 4.36: Sifting sand input, fine and coarse product

The images clearly show the cleaning effect of the ADR on the waste streams. To quantify this effect, the contamination levels of the products was determined.

Crushed concrete for use as aggregates in recycle concrete needs to meet a number of criteria. Of these criteria the workability and the contaminant concentrations are most critical. The workability of the bulk material (i.e. the ability to transport and store the material) sets boundaries to the amount of fines present. The contaminants mainly consist of floating material.

The ADR concentrates the light contaminants into the fine product. This effect was quantified following the method described in the Dutch NEN-EN933-11. The procedure entails the separation of light-weight material larger than 4 mm by means of floatation. The volume of floating material is then measured using a graduated cylinder. The results of this analysis are shown in Table 2.1.

Table 4.8: Amount of floating material in +4mm fraction

	PCC [cm^3/kg]	CCC [cm^3/kg]	SS [cm^3/kg]
Input	12.3	1.38	215.5
Fine	233.1	63.62	684.5
Coarse	4.0	0.04	71.3

The maximum levels for floating contaminants for various categories are given in Table 20 in the Dutch NEN-EN12620. Table 4.9 shows a copy.

Table 4.9: Pollution categories in the Dutch NEN-EN12620

Category	Content [cm^3/kg]
$FL_{0.2}$	≤0.2[a]
FL_2	≤2
FL_5	≤50
[a] The ≤ 0,2 category is intended only for special applications requiring high quality surface finish.	

The contaminant levels of the coarse products of both types of crushed concrete are well within prescribed categories for application of granulate as concrete aggregates. However, the value for the coarse product of the heavily contaminated crushed concrete is too high to satisfy the strictest categories. Further processing may therefore be desirable. One option for this is wind sifting, to remove all light particles in the size range of 1-16 mm. Because of their lower specific weight, light pollutants will be associated by 1-4 mm mineral material. This 1-4 mm mineral fraction (which then contains all contaminations) can be processed in a wet process (e.g. a screw classifier) to remove all floating material. Using this technique only 10 to 15% of the total 0-16 mm crushed concrete needs to be cleaned in a wet process. Since the amount of fines has already been significantly reduced, problematic amounts of sludge are avoided.

Clean coarse products of CDW can be used as aggregate in concrete. In this way it is possible to close the cycle of concrete aggregates, reducing the amount of unused waste material and depletion of natural resources. The fine material produced by the ADR is a promising material for the cement industry [44].

The contamination level of processed sifting sand does not fall within any category of the code. Therefore, this material will not be suitable for use in concrete. However, the reduction of contamination and fines do make it possible to use it as a granular mixture in various applications. Normally sifting sand is a very complex waste stream, which has no usable application. Therefore, it is preferred to reduce it as much as possible. Using the ADR, 23% of the input mass was classified into a coarse product, which does not need to be incinerated or landfilled.

4.4 Summary and conclusions

The working of the ADR was tested in various experiments. In these experiments the scale was increased from a laboratory setup to a full scale industrial installation. At the same time the scale of detail was tailored to the specific data required in the process of developing an industrial installation from a proof of concept.

Detailed experiments with a laboratory setup of the ADR showed the basic features of the classification. The overall results show the characteristics of a ballistic separator. For the very fine fractions (<1 mm) residual adhesion and the effect of air-movement within the ADR result in a deviation, where the fines recovery is wider distributed and further away from the rotor than might be expected on the basis of a purely ballistic separation. For the very coarse particles (>8 mm) the limited size of the ADR and the

size effect on the rotor-blades also cause a difference with ballistic separation but of a smaller magnitude.

Overall, the classification shows an optimum separation at a cut-point of 1-2 mm. At this cut-size the recovery of fine material in the coarse product is low enough to dramatically improve processability, while the recovery of coarse material is high enough for the process to be economically viable.

Processing with a lower throughput results in less residual adhesion of the ultra-fine fraction (<250 µm) because of the thinner layer thickness on the rotor. Since the momentum transfer in the air is decreased, the spread of the fine fraction (<1 mm) is reduced.

At a highly reduced moisture content, residual adhesion is eliminated. However, since more fines are free, more momentum is transferred to the air, increasing air movement. This increase in air-movement increases the spread of the recovery of fine particles.

When crushed concrete is processed instead of bottom ash the recovery of size fractions shows a bigger spread. This is due to the higher modulus of elasticity of crushed concrete, increasing the randomizing effect of particle shapes in collisions.

Results of an industrial ADR used to process municipal solid waste incinerator bottom ash showed that laboratory results had been translated successfully into a full scale installation. Furthermore, the results show the influence of specific density of a material in classification with the ADR. Lighter materials are recovered up to a bigger diameter into the fine product and heavier materials to a smaller diameter. This effect is very beneficial in processing bottom ash, since valuable constituents like heavy non-ferrous metals can be recovered in the coarse product, while light weight contaminants are recovered in the fine residue. Processing the coarse product of the ADR with conventional upgrading processes almost doubled the non-ferrous metal recovery for a state of the art reference case.

Industrial processing of construction and demolition waste resulted in a coarse product that had a strong reduction in moisture and fines. Because the ADR recovers light materials to higher diameter in the fine product, also the +4 mm floating contamination content was effectively reduced. For crushed concrete, this reduction enables the use of the material as recycled aggregates into new concrete. Analysis according to the Dutch NEN codes showed that for some input flows, the resulting coarse product met the quality demands of even the strictest category. Traditionally, sifting sand has no useful application. Processing sifting sand with the ADR transformed a significant part of the input flow into a product with a useful application, reducing the total volume to be landfilled.

5 Modeling

5.1 Introduction

Experimental results showed a good potential for the ADR concept. In this chapter the modeling of the ADR principles is presented. This modeling serves a number of objectives:

- Understand and verify the relevant physical principles
- Interpret and generalize experimental results
- Improve and tailor the design and settings of the ADR to a specific application

To serve each of these objectives, a basic and a comprehensive model is presented. The basic model incorporates the basic physical principles involved in classification with the ADR. It can be used to determine the dominant factors for the classification and to generalize experimental results.

For a deeper understanding of the relevant physics, a comprehensive model is introduced. In this model, more advanced methods of simulation are used to further refine the results of the basic model. This model will be more flexible to predict changes in design on classification results and provides more detailed insight on key aspects.

Both these models can be used to determine the recoveries of specific fractions in the fine and coarse product of the ADR. These recovery figures can be used in (economic) calculations to optimize the performance and profitability of an upgrading process.

Modeling considerations

In the ADR a large variety of physics has an influence on the classification results. Given the objective of modelling as given above, only the physics that has an impact in the practical application of the ADR concept is simulated. The complexity of modeling is weighed against the practical impact on separation results to obtain a balance between costs and benefits.

The primary component of both models is a description of the ballistic trajectory of the particles. This part is modelled accurately since it will provide the most relevant insight on the processes occurring inside the ADR. The comprehensive model includes a detailed description of collisions of particles with surfaces. This is needed because collisions will determine the initial conditions of trajectories (after impact by the rotor) and they are also critical to describe the interaction with the encasing of the ADR.

During flight, the particles have an interaction with the air. The air is not stationary as will be explained in the following chapter. Some knowledge of the air-flow is needed to take this influence into account. However, since this is a secondary order influence, its modeling does not require a high level of accuracy and simplifications are justified.

The probability and impact of particle-particle collisions in the air is discussed in an appendix to this chapter. Its impact is determined to be low, so this process is not taken into account in the general modelling. Theoretically, there can also be particle-particle collisions on a surface, i.e. when surfaces are polluted. Since the practical implementation of the ADR concept requires surfaces to remain clean, this does not need to be modelled.

Finally, it is recognized that crushing can have an influence on the trajectories of particles. When the outer layer of a particle is crushed by impact with the rotor, energy is absorbed, reducing the elasticity. This will be considered in the chapter below, but the phenomenon is not modelled, since this would be extremely complex and its influence is limited. The effect of particle size reduction can be taken into account by taking the particle size distribution (PSD) of the output of the ADR as input to the model. During experiments the PSD of the output can be easily compared to the input PSD to evaluate the impact of crushing.

5.2 Basic model

5.2.1 Modeling concepts

Introduction

In the ADR the final position of a particle and therefore the recovery rate of the corresponding material and size fraction over the outputs is determined by multiple influences. After a moist particle cluster is accelerated by the rotor blade, the fines are partially liberated from the coarse particles and the resulting sub-clusters of particles form a widening jet that interacts with the air. Depending on their size, some particles will be partially hit by the rotor and these particles will follow an aberrant trajectory. During the interaction with the air, momentum is conserved and therefore air movement is generated. Furthermore, a particle or sub-cluster can collide with the encasing, which alters its trajectory.

The basic model is set up to be a simple and fast model that gives a realistic indication of particle trajectories and recovery rates. First principle calculations are used wherever possible, striving for a minimum of empirical and fitting parameters. Since no fundamental influence of the width of the ADR is expected, the model is set up in 2D. The following sections describe the concepts of the basic model.

Definition of particles

The model defines a group of particles with similar properties as a *fraction*. The collection of fractions make up all particles simulated. Within a fraction, the particles are represented by spheres with the same diameter and particle mass.

Moist particle cluster breakup

The process of how moist particle clusters are liberated by impact with the rotor is extremely complex. The first steps into understanding this were given in Chapter 3. From this study it is understood that the degree of liberation shows a steep transition over particle size. The breakup of moist particle clusters into liberated and bonded

particles is therefore described by a sigmoid curve in the basic model. This function represents the probability that a particle, in function of its size, is liberated from *coarser* particles by the breakup of water bonds by the rotor. The function has two parameters defining the cut-size and the width of the transition zone from bonded to liberated.

The results on page 59 of chapter 3 suggest that the distribution of non-liberated fines over the coarse particles reflects the original kissing matrix of the clumpy waste. The Ergodic model then gives this distribution of the mass of fines M_i over the coarse M_j to be proportional to:

$$M_{ij} \sim M_i \, M_j \left(D_i + D_j\right)^2 / D_j^3$$

And since mostly $d_i \ll d_j$ this can be simplified to:

$$M_{ij} \sim M_i \, M_j \, D_j^{sp-3}$$

In which also a term sp is introduced to allow a correction for the surface properties of the particles. In the model the bonded fines will travel with their respective 'host' particles until they reach their final position.

Air velocity profile

During the ballistic phase of the particles, momentum is transferred from the particles to the air. This causes a movement of the air, which in turn, will affect the deceleration of particles. Therefore, an estimation of the air velocities is made before the ballistic trajectory of the liberated particles is determined. Since only an approximate air flow pattern is needed for the calculation of the ballistic trajectories, it is estimated on the basis of a simplified jet structure. For this the schematic as in Figure 5.1 is defined.

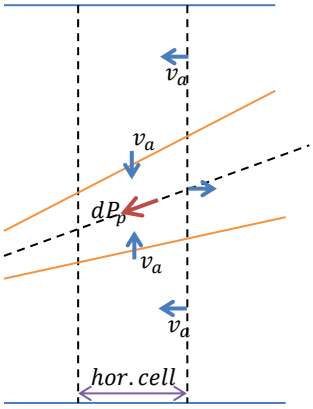

Figure 5.1: Schematic of a horizontal cell in the air-velocity profile

A simplification of the ballistic trajectory is used during the estimation of the air-profile. Gravity is neglected and all particles are assumed to be inside a particle jet that forms a cone that opens with a given angle and originates at the middle of the rotor-blade at its feed-position. The drag and deceleration of the particles are determined along the center-line of the cone. Horizontally, the air-profile is divided into a predefined number of cells. The calculation of the particle trajectories and air-profile is performed

from left to right, one cell at the time. The cone divides the horizontal cells into upper, lower and cone cells.

The lost momentum of particles (dP) in a cone cell is transferred to the air flowing into the same cone cell. The inflowing air is accelerated by this added momentum, increasing the velocity at which it flows outward. The air is regarded to be incompressible; therefore the total volume of air within a cell must be conserved. This determines the flows over the upper and lower boundaries, in which an equal inflow over the upper and lower boundary of the cone cell is assumed. The airflow over the vertical boundaries of the lower and upper cell are determined similarly. Once the velocities indicated in Figure 5.1 are obtained, a smoothing function is used to account for the transfer of momentum by turbulence at the edges of the jet [44]. This results in a continuous function and makes the profile more realistic.

The air-velocity in a cone cell is projected forward to better estimate the lost momentum of particles by drag in the next calculation step.

Ballistic trajectory with air drag and collisions

The ballistic trajectory of the particles is calculated via an explicit time-dependent numerical scheme that takes the estimated airflow profile into account for determining the air drag. The initial position and velocity of particles is most important. Variation of these initial conditions within a *fraction* accounts for the major part of the spread in landing positions. Therefore, for every fraction, different initial conditions are considered (typically 10), spread over the height of the rotor blade. To account for particles that are partially hit by the rotor, an additional 'aberrant' trajectory is calculated, starting from the tip of the rotor blade.

Collisions

During calculation of a ballistic trajectory, a crossing with the encasing will be detected. At this event the new velocity vector after collision is calculated using the graphical method of Wang and Mason [45]. Since particles are approximated as spheres, the graphical method reduces to a simple analytical solution.

Post processing

The calculation of a trajectory is stopped when a particle crosses a specified horizontal level (representing the floor or conveyor belt). With the basic model, only a limited number of trajectories per particle fraction is calculated. A normal distribution is therefore used to account for all the semi-random influences of collisions and initial conditions. The distributions are summed for all trajectories within one fraction. Hereafter, the effects of residual adhesion are taken into account to finally obtain the recovery curves of every fraction over the horizontal distance from the rotor.

5.2.2 Implementation of the basic model

Definitions

In the basic model, the feed is represented by n spheres within k size fractions. In each size fraction the spheres have a diameter D_j (with $j = 1{:}\,k$), and mass m_j, determined via the average particle density ρ_p. The total mass fraction within a size fraction D_j is given by M_j. The rotor is characterized by a rotational frequency f_r, a radius r_r and a blade height b_r. After impact by the rotor, the particles interact with the air, characterized by a specific density ρ_a and a dynamic viscosity μ_a. The interaction of particles with the surfaces of the encasing is characterized by a friction

coefficient μ_f and a coefficient of restitution e, for which the definition according to Poisson's hypothesis is used [46].

Moist particle cluster breakup

The liberated mass fraction (Lib_j) of each size fraction after impact by the rotor, is described by a sigmoid function, as in the equation below, in which the 50% point is defined by D_{lib} and the width of the transition is set via α_{lib}. Depending on the input material properties, the value of D_{lib} can range from 250 to 500 µm and α_{lib} ranges from 15 to 100 µm.

$$Lib_j = 1 - \frac{1}{1 + 3^{\frac{D_j - D_{lib}}{\alpha_{lib}}}}$$

The non-liberated mass fraction ($1 - Lib_j$) is distributed over the liberated particles, with a ratio according to ${D_j}^{sp}$, such that hosts carry only smaller particles. The ratios of redistribution are given by Red_j as in the equation below. Parameter sp accounts for the effect of the host particle diameter and can range from 1.5 to 3.

$$Red_j = Lib_j M_j {D_j}^{sp-3}$$

This redistribution results in a new mass distribution over the size fractions as given by the equation below.

$$Clus_j = Lib_j M_j + \sum\nolimits_{D_i < D_j} \left[\frac{Red_j}{\sum_{D_j > D_i} [Red_j]} (1 - Lib_i) M_i \right]$$

This is the modified mass fraction distribution of particles, representing the mass fractions of the clusters that move as individual particles of size D_j during the ballistic trajectory. This is also the mass distribution that is used in the calculation of the momentum transferred to the air. To obtain the masses of each fraction, as relevant for the momentum conservation calculation, all mass fractions are multiplied with the ADR's throughput T, which is expressed per unit width of the machine (so its unit is kg/s/m).

Air velocity profile

To determine an approximate air velocity profile, the 2D space of the ADR is discretized into a large number of cells (index i) in the horizontal direction and each cell is divided into three cells in the vertical direction. The boundaries of the vertical cells are given by the cone of the widening particle jet, which originates at the middle of the rotor-blade at feed-position and is represented by a principle direction α_0 ,an opening angle α_c. Particles are assumed to move along the center-line of the cone until they no longer convey momentum to the air or cross the x-coordinate of the backwall of the ADR (i.e. gravity is neglected). The initial conditions of the particle trajectories are given by a fully inelastic hit by the rotor blade at mid-height.

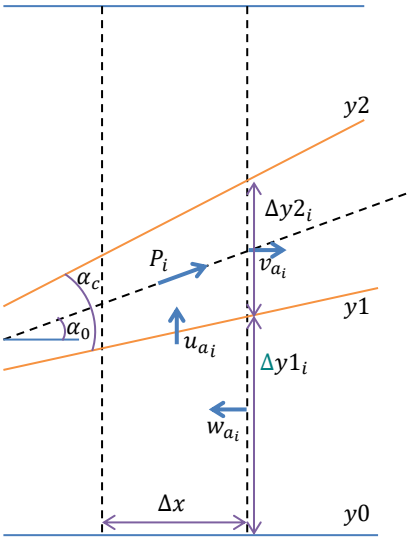

Figure 5.2: Schematic of parameters used to determine the air-velocity profile in cell i.

Within this framework, the air velocity profile is based on the incompressible Navier-Stokes equation:

$$\rho_a \left(\frac{\partial v_a}{\partial t} + v_a \cdot \nabla v_a \right) = -\nabla p_a + \mu_a \nabla^2 v_a + f$$

Here ρ_a is the density, μ_a the viscosity, v_a the velocity and p_a the pressure of the air. f represents the body force on the air resulting from the interaction with the flow of particles.

Since only the time independent behavior is of interest, the unsteady acceleration term $\left(\rho_a \frac{\partial v_a}{\partial t}\right)$ is neglected. The viscosity term $\mu \nabla^2 v$ is taken into account implicitly via the widening of the air cone. Flat turbulent jets widen with an opening angle α_c of about 20 degrees [44]. Since the particle jet widens with an angle which is at least this size, this mechanism of jet widening is more dominant than turbulent viscosity. This observation results in the simplified equations below.

$$\rho(v \cdot \nabla v) = -\nabla p + f$$

$$\nabla \cdot v = 0$$

The simplified equations are evaluated in 2D space and effectively reflect the conservation of horizontal and vertical momentum. Since the particle jet mostly conveys momentum in the horizontal direction, the vertical momentum conservation is neglected. With this the system of equations is reduced to two scalar equations for each cell i. By assuming the air influxes over the upper and lower boundary of the cone cell to be equal, a solution is obtained.

The deceleration of each fraction j is determined via its representing particle that moves along the center line of the cone. The drag-force on the particle is given by the

equations below, where C_d is the drag-coefficient of the particle, A_j is the cross-sectional area of particle j, v_{j_i} is the velocity of particle j in cone-cell i and v_{a_i} is the air velocity in that cone-cell.

$$F_{drag,j} = \frac{1}{2}\rho_a C_d A_j \left(v_{j_i} - v_{a_i}\right)^2$$
$$C_d \approx max\left(0.5; \frac{20.8}{Re^{0.6}}\right)$$
$$Re = \frac{D_j \rho_a \left(v_{j_i} - v_{a_i}\right)}{\mu_a}$$

The deceleration is used to determine the momentum lost by all particles of a fraction j in cell i and can be summed over all factions j to get P_i, which will be the total momentum gained by the air in cell i.

This momentum is transferred to the air flowing into the cell. The air velocity increases to v_{a_i}, and the total volume of air flowing out of the cell increases. The redistribution of air via the velocities over the boundaries can then be determined via the equations below.

$$v_{a_i} = \sqrt{\frac{{v_{a_{i-1}}}^2 \rho_a \Delta y2_{i-1} + cos(\alpha_0) P_i}{\rho_a \Delta y2_i}} \quad \textit{(momentum conservation)}$$
$$u_{a_i} = \frac{v_{a_i}\Delta y2_i - v_{a_{i-1}}\Delta y2_{i-1}}{2\,\Delta x} \quad \textit{(volume conservation)}$$
$$w_{a_i} = \frac{w_{a_{i-1}}\Delta y1_{i-1} - u_{a_i}\Delta x}{\Delta y1_i} \quad \textit{(volume conservation)}$$

The horizontal velocities $v_{a_i}$and w_{a_i} resulting from this calculation are smoothened over the vertical direction to obtain a continuous profile and prevent boundary problems over the edges of the cells. This is done via the sigmoid function as given below, in which the transition position is given by $y1$ (the lower boundary of the cone). The width of the turbulent layer is taken to be half the cone width as suggested by Gicquel et al [47].

$$v'_{a_i} = \frac{w_{a_i} - v_{a_i}}{1 + 3^{\frac{y-y1}{(y2-y1)/2}}} + v_{a_i}$$

The smoothed vertical air velocity u'_{a_i} is then given by the integral below, with its interval from the ground position $y0$ till evaluation position y.

$$u'_{a_i} = \int_{y0}^{y} \frac{v'_{a_i} - v'_{a_{i-1}}}{\Delta x} \mathrm{d}y$$

Ballistic trajectory with air drag

After the calculation of an approximate air-profile, the precise ballistic trajectories of the particles are determined. The position and velocity of the particles are represented by vectors with an x and y component.

The starting position of the particle on the rotor-blade has a big influence on its trajectory. Therefore, for each size fraction j, n different trajectories are determined (index $i = 1{:}n$), with their starting positions evenly divided over the height of the rotor blade. The angle of the center line of the particle jet, α_0, and the widening angle, α_c, are given as an input to the model, see Figure 5.3. The starting position and velocity of the particles are then given by:

$$p_{0_{x_i}} = \frac{\frac{1}{2}b_r}{\sin\left(\frac{1}{2}\alpha_c\right)}\cos\left(\alpha_1 + \frac{i-1}{n-1}\alpha_c\right)$$

$$p_{0_{y_i}} = \frac{\frac{1}{2}b_r}{\sin\left(\frac{1}{2}\alpha_c\right)}\sin\left(\alpha_1 + \frac{i-1}{n-1}\alpha_c\right)$$

$$v_{0_{x_i}} = 2\pi f_r\left(r_r + \frac{i-1}{n-1}b_r\right)\cos\left(\alpha_1 + \frac{i-1}{n-1}\alpha_c\right)$$

$$v_{0_{y_i}} = 2\pi f_r\left(r_r + \frac{i-1}{n-1}b_r\right)\sin\left(\alpha_1 + \frac{i-1}{n-1}\alpha_c\right)$$

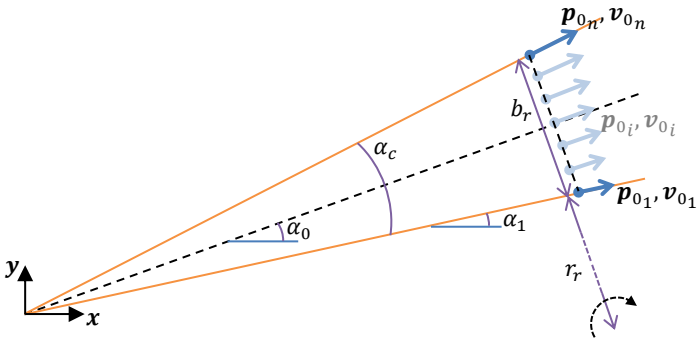

Figure 5.3: Schematic of starting conditions of n different trajectories.

Particles that are partially hit by the rotor are represented by a single extra 'aberrant' trajectory (subscript a), of which the initial speed is multiplied by a factor β (between 0 and 1) the initial direction rotated upwards by $\alpha_{partial\ hit}$ (between 0-45°) and the initial starting position is at the top of the rotor blade.

The fraction of the mass of size fraction j that is represented by the partially hit particle is estimated as the ratio of the particle's radius over the penetration depth into the height of the rotor blade (b_r).

$$M_{j_a} = \frac{D_j}{2b_r}$$

The ballistic trajectory with air drag is then calculated via an explicit time dependent numerical integration scheme with time-steps Δt, given by the set of equations below. These equations differ slightly from the ones given before, because particles now move along a 2D trajectory instead of along the centerline of the particle-cone. Both the position and the velocity of the particle are given by vectors. The position of the particle

in the air-profile is used to obtain the air velocity $\boldsymbol{v}_a$. The relative velocity of the particle to the air, $\boldsymbol{v}_r$, is used in the drag equation.

$$\begin{aligned}\Delta\boldsymbol{p}_t &= (\boldsymbol{v}_{t-1} + \Delta\boldsymbol{v}_t)\Delta t \\ \Delta\boldsymbol{v}_t &= \left(\frac{\boldsymbol{F}_{drag,t}}{m_j} + \boldsymbol{g}\right)\Delta t \\ \boldsymbol{F}_{drag,t} &= \frac{1}{2}\rho_a C_d A_p |\boldsymbol{v}_r| \cdot \boldsymbol{v}_r \\ \boldsymbol{v}_r &= \boldsymbol{v}_a - \boldsymbol{v}_t\end{aligned}$$

Here, $\boldsymbol{p}_t$ and $\boldsymbol{v}_t$ are the position and velocity of the i^{th} particle in the j^{th} fraction at time step t, $\boldsymbol{g}$ is the gravitational vector and ρ_a, C_d and A_p are as given before.

Collisions

Collisions result in a discontinuous change of the particle's velocity. If a collision with the encasing is detected during evaluation of the trajectory, the particle's new velocity is calculated via the method of Wang and Mason [45], which uses Routh's graphical method [48] to describe an impact process. For a spherical particle impacting on a flat unmovable surface, the method reduces to the equations given below. Evaluation is universal in the given axial system (ζ, η) with coordinate ζ running parallel and coordinate η perpendicular to the collision surface.

$$\Delta\boldsymbol{v}_{t_{\zeta,\eta}} = \boldsymbol{g}_{\zeta,\eta}\Delta t + \begin{cases} \begin{pmatrix} -\frac{2}{7}v_{i-1_\zeta} \\ (e-1)v_{i-1_\eta} \end{pmatrix} & , \quad v_{t-1_\zeta} \le \frac{7}{2}\mu_f(1+e)v_{t-1_\eta} \text{ (case of stick)} \\ \begin{pmatrix} (e-1)\mu_f v_{i-1_\eta} \\ (e-1)v_{i-1_\eta} \end{pmatrix} & , \quad v_{t-1_\zeta} > \frac{7}{2}\mu_f(1+e)v_{t-1_\eta} \text{ (case of slip)} \end{cases}$$

Upon detection of a collision, the particles properties are projected into the axial system (ζ, η), and the change in the velocity vector is determined. Hereafter the particle's properties are projected back into the global axis system (x, y).

Post processing

The numerical calculation of the ballistic trajectory with drag and collisions is stopped when particles hit the floor of the ADR. In the basic model only a limited number (n) of trajectories can be simulated and so representation of statistics is limited. The single discrete end position of each simulated trajectory is spread via a distribution function to account for the statistics. For the bonded fine particles, the landing position is that of their host particle. The two effects are accounted for by post-processing the results of the ballistic trajectory calculation.

The final position of every trajectory is spread via a normal distribution $(X \sim N(\mu, \sigma))$ with its mean at the final position $p_{end_{x_{i,j}}}$, with $i = 1{:}\,n$ for the simulated trajectories within one fraction and $j = 1{:}\,k$ for the size fractions. Parameter σ serves to translate the discrete particle positions into a smooth distribution. A value for σ of 2-4 m for normal particles (subscript n) and 4-8 m for the partially hit, aberrant, particles (subscript a) is found to create a smooth distribution that fits the experimental results well. The recovery of a size fraction (j) over the distance x from the rotor is given by:

$$R_j(x) = \left(1 - M_{j,a}\right)\sum\nolimits_{i=1..n} N\left(p_{end_{x_{i,j}}}, \sigma_j\right)/n + M_{j,a}N\left(p_{end_{x_{i,j}}}, \sigma_a\right)$$

This result is modified to account for the residual adhesion of fine particles over the coarser particles via the following equation:

$$R'_j(x) = Lib_j R_j + \left(1 - Lib_j\right) \frac{\sum_{i>j}[Red_i R_i]}{\sum_{i>j}[Red_i]}$$

5.2.3 Results of the basic model

Comparison with the experimental base case

The results of the basic model are compared with the Base Case of the experiments with the prototype ADR. All parameters used in the model are given in Table 4.1.

Table 5.1: Parameters used in simulation of the Base Case

Particle properties		
Fraction	D_p **[m]**	P_m **[-]**
11.2-16mm	13.4E-3	4.02%
8-11.2mm	9.47E-3	8.03%
4-8mm	5.66E-3	22.6%
2-4mm	2.83E-3	19.0%
1-2mm	1.41E-3	17.0%
0.5-1mm	707E-6	14.9%
0.25-0.5mm	354E-6	8.87%
0-0.25mm	177E-6	5.59%

Physical parameters		
Drag coefficient (C_w)	0.50	-
Density air	1.30	kg/m^3
Density particles	2400	kg/m^3
Viscosity air	18E-6	kg/m s
Gravity	-9.81	m/s^2
Restitution factor	0.01	-
Friction coefficient	0.80	-

ADR setup		
Throughput (T)	60	ton/h/m
Jet direction (α_0)	30	°
Jet opening (α_c)	20	°
Y-level roof	2.5	m
Y-level floor	-0.8	m
Rotor revolutions	1000	RPM
Rotor radius	0.2	m
Rotor blade height	0.08	m

Model and fit parameters		
Time step (Δt)	5E-3	sec
Distance step (Δx)	20.0E-3	m
Cut-size (D_{lib})	343E-6	m
Transition width (α_{lib})	18.7E-6	m
Redistribution (n)	2.32	-
Speed reduction (β_a)	0.50	-
α_a	20	-°
Smoothing factor (σ)	2.0	m

Figure 4.11 shows the fit for the Base Case. The figure presents the recovery curves as a function over the distance from the rotor and the particle size fractions are the different series. The experimental data is plotted as points, the result of the fit-model as the lines. The RMSE between the results of the experiment and the model is 2.72%, suggesting that the basic model addresses all the major phenomena of the process.

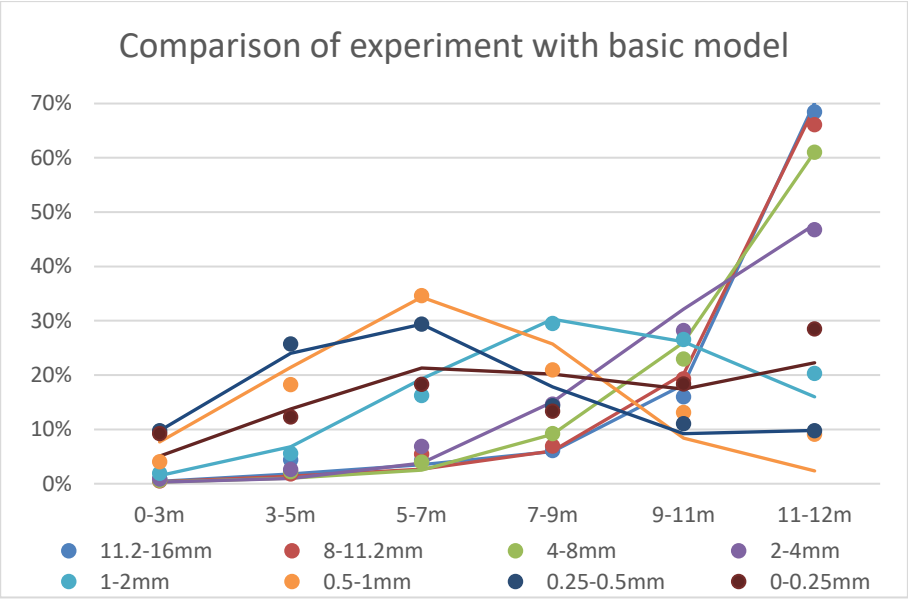

Figure 5.4: Comparison of experimental data (points) and the model (lines)

By essentially duplicating the experimental results with the model, details of the experiment can be investigated that could not be measured. Two items of interest are the trajectories of the particles and the profile of the air-velocity.

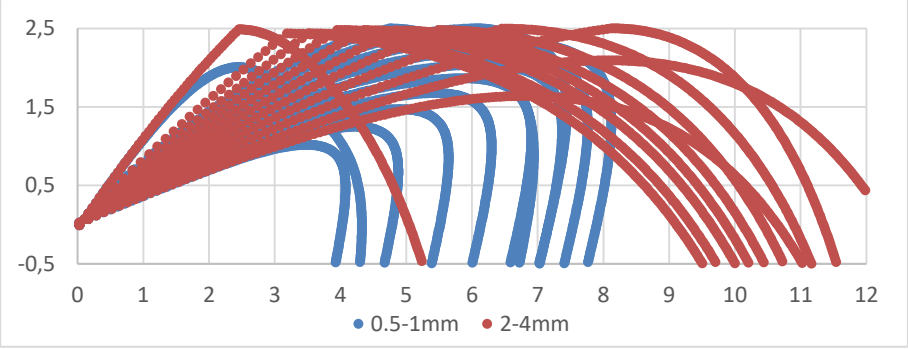

Figure 5.5: Trajectories for the 0.5-1 mm and the 2-4 mm fractions, as given by the model

Figure 5.5 shows the trajectories for the 0.5-1 mm and the 2-4 mm fractions. It can be seen that the trajectory of the fine fractions are influenced by the air-velocity. When the particles are still within the particle jet, they are transported further than if air movement would not have been taken into account. When the particles exit the particle jet, their trajectories are slightly bent backward, resulting in a rather wide spread of the particles upon landing. On the other hand, the air flow has only a minor effect on 2-4 mm particles.

Figure 5.6 shows the air-velocities over the length of the trajectory. It is clear that the horizontal velocity (v_a) quickly rises and then lowers to an asymptotic value. After impact with the rotor, all particles are projected away at high speed in a narrow cone. During this phase, differences between particle velocity and air-velocities are high and so a substantial amount of momentum is transferred. This results in a quick increase of the velocity of the air. As the jet widens and (finer) particles slow down, the momentum exchange decreases and the velocity profile stabilizes.

As the jet widens, the area for the return flow (w_a) reduces, generating a stronger air-flow in the backward direction. The vertical air-flow (u_a) compensates for the difference of the airflow over the left and right boundary, and therefore resembles the derivative of the horizontal airflow.

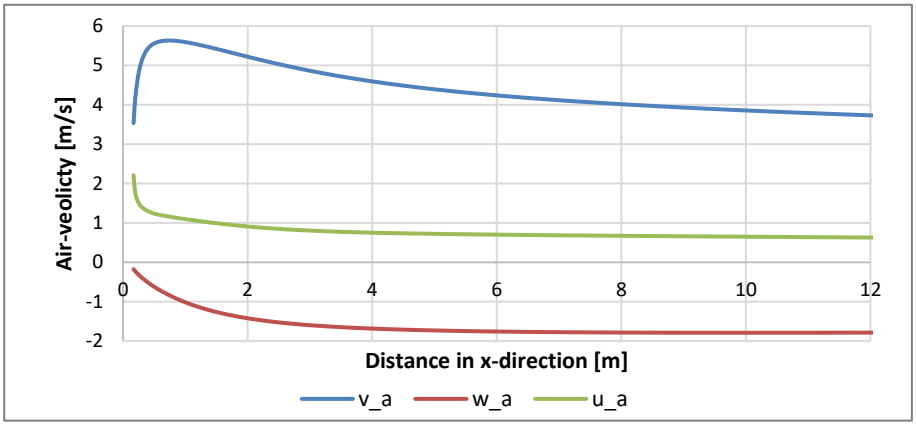

Figure 5.6: Air velocity profile, as given by the model

5.3 Comprehensive model

5.3.1 Introduction

The basic model offers a straightforward method to quickly assess the influences of the major parameters and phenomena on the classification of particles with the ADR. While the results show good agreement with experiments, the level of detail in the gained insight is limited. Furthermore, the implementation of the model limits the flexibility in varying the input geometry and feed characterization, calculation methods and presentation of results.

In addition to the basic model, a comprehensive model is therefore presented. The implementation of this model allows for a greater flexibility and more detail. The key enhancements upon the basic model are:

- Calculation methods
  - Simulation in 3D-space
  - Particle rotation is taken into account
  - Trajectory of each particle is simulated multiple times to account for random influences
  - Trajectory starts before collision with the rotor

- Particles
    - Flexibility in number of particles that is simulated
    - Particles described individually instead of as a group
    - Particles are represented by an ellipsoid with 3 spatial dimensions
- Collisions
    - Method of Keller is used to calculate 3D impact of collision with surfaces
    - Surfaces can be flat or cylindrical and can move in plane or rotate
    - Surfaces are defined by a set of vectors, instead of linear equations
    - Friction and restitution coefficient depend upon the two interacting materials
- Air-profile
    - Meshed with higher number of cells, adaptive to limit non-linear effects
    - Dispersion is taken into account explicitly
    - Momentum transfer of actual trajectories is used

The enhancements allow, e.g., the study of particles of different materials and shapes, the effect of the shape of the rotor blades and the action of the conveyors transporting the products out of the ADR. The section below elaborates on the general framework of the calculations used in the comprehensive model.

5.3.2 General framework

The general framework of the comprehensive model is similar to the basic model. However, some assumptions and methods used in the basic model restrict the applicability and are replaced by more generic descriptions. Below the framework of the comprehensive model is described.

Framework of calculations

Like in the basic model, there are four components in the calculation of the trajectory of the particle:

- residual adhesion of fine particles after impact from the rotor
- collisions of the particle with the rotor, the encasing and the conveyor belt
- ballistic trajectory of the particle, influenced by drag of the air-flow
- an air-flow profile, generated by momentum transferred via drag of the particles

The insight gained on the residual adhesion of fines after impact with the rotor, as given in Chapter 3, is not enough to arrive at a completely first principles description of this process. Therefore, the description of the residual adhesion of fines in the comprehensive model is the same as in the basic model.

The air-profile and ballistic trajectory have a mutual interaction via drag. In the basic model, this mutual interaction was estimated up-front. The calculation of the trajectory with air-drag and the influence of collisions is now integrated.

In the comprehensive model, all three components of drag, air-flow and collisions are integrated. As particles progress through the model, cells are added to the air-profile which are automatically re-sized to minimize non-linear effects of the mutual

interaction. The information from the detailed ballistic trajectory is used to obtain the body-force that acts on the air. This information is projected forward, to update the air-profile real-time as the particles run through them.

The calculation of the instantaneous influence of a collision can be isolated from the rest of the calculations. Therefore, the calculations in the comprehensive model are divided into:

- a numerical description of a collision of ellipsoidal particles with flat and cylindrical surfaces

and;

- a numerical description of the mutual interaction of an air flow and a body force resulting from the ballistic trajectory with drag of ellipsoidal particles

The following paragraphs will elaborate on the methods used.

5.4 Numerical description of a collision of ellipsoidal particles with flat and cylindrical surfaces

5.4.1 Introduction

The high velocities of particles within the ADR make an encasing necessary. Particles will collide with this encasing and a realistic description of this collision is essential for the accurate prediction of the landing position of the particles. This holds especially for the >2mm and heavy particles. The behavior of essentially smaller and lighter particles is dominated by their interaction with the air rather than by the interaction with the geometry of the ADR.

The interaction of a particle with the encasing introduces a quasi-randomness due to the influence of the random orientation of the particle relative to the surface at the moment of collision. In the basic model this influence was mainly accounted for by a statistical interpretation of the results. By explicitly taking the quasi random influence of the collisions into consideration, the statistical interpretation of the results can be reduced, thus creating a more detailed and first principles based description of the processes occurring in the ADR.

The comprehensive model considers collisions between particles and surfaces, but particle-particle interactions are neglected, since volumetric concentrations (for coarser particles) are relatively low. The effects of particle-particle interaction are described in detail in Appendix 0.

Overall, the description of collisions is mathematically complex. First a collision needs to be detected and then the discontinuous change of the particle's velocities needs to be determined. In the following sections, the main points of the used methods are described. The basis of the method is the model of Keller [49]. This model requires input data which follow trivially from the particle's and surface properties. Therefore, first the collision detection is discussed which also yields the proper inputs for the calculation method. Hereafter the method itself is introduced and finally results are discussed in section 5.4.4.

5.4.2 Concepts and definitions

Concept of calculations

The modeling problem of describing a collision is two-fold: detecting the collision and determining the discontinuous change of the velocity vector $\boldsymbol{v}$ and rotation vector $\boldsymbol{\Omega}$ due to the collision.

A collision is detected by a sign change of a particle's extreme coordinate normal to the relevant surface, see Figure 5.7. This check needs to be performed every time step, and is potentially very time-consuming. Therefore a detailed calculation of the distance is preceded by a simple check whether a collision may be excluded on the basis of a simple estimate. For this, the ellipsoidal particle is considered to be a sphere with a radius equal to the semi-major axis. When a collision cannot be excluded, a more precise analysis is performed, taking the ellipsoidal shape into consideration.

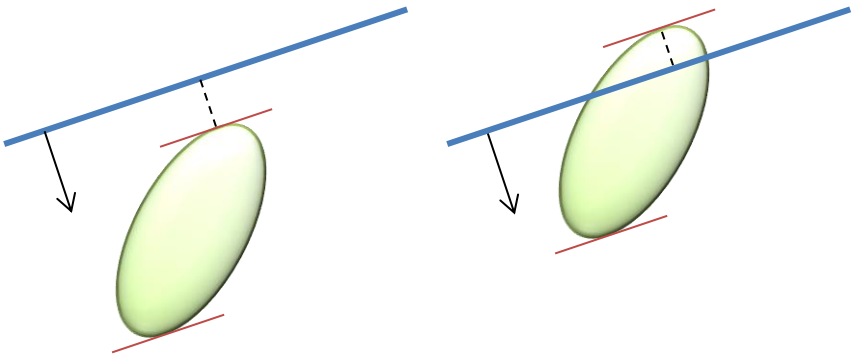

Figure 5.7: Detection of a collision of a particle with a surface

If a collision is detected, the relevant input properties for the calculation of the collision are determined and the discontinuous change of $\boldsymbol{v}$ and $\boldsymbol{\Omega}$ is determined via the method of Keller [49]. This method gives a general description of collisions with friction, taking into account that the slip direction can change during the collision.

The method of Keller is complex and deserves some further introduction. Instead of regarding the collision as instantaneous, Keller assumes it to have a duration t_c small compared to the typical timescale of the motion before and after the collision. The impact force at the point of contact is decomposed into its normal and tangential component. Then, instead of using t as the independent variable, the normal component of the collision impulse or momentum transfer, $\tau(t)$, up to time t is used, eliminating the normal force from the equations of motion. The point of zero relative normal velocity is determined (τ_0) and Poisson's hypothesis is adopted, stating that the collision terminates at $\tau_e = (1+e)\tau_0$. During the exchange of momentum, friction exerts a tangential force of which the magnitude is given by μF_n and the direction is determined via the equations of motion. It is checked whether the tangential velocity vanishes at some point. If so, the result is corrected, to finally obtain the change of $\boldsymbol{v}$ and $\boldsymbol{\Omega}$.

Definition of particles

The basic model does not account for the particle shape and its orientation with regard to a surface. This orientation is an important factor in the quasi randomness particles trajectories. Therefore, the comprehensive model uses an ellipsoid to describe the particles. This shape allows for a realistic description of a wide variety of particles shapes and the quasi random influence of this shape on the trajectory, while maintaining as much as possible an analytical description of the collision process.

All particles have radii along the three principle axes (a, b, c), a position $(\boldsymbol{p_p})$, a velocity $(\boldsymbol{v_p})$, an orientation of the two principal axes $(\boldsymbol{e_a}, \boldsymbol{e_b})$ and a rotational velocity $(\boldsymbol{\omega_p})$, all of which are represented by 3d vectors, see Figure 5.8. Each particle has an individual mass m_p and material type. For the calculations of momentum transfer to the air, each particle also represents a mass m_{p_r} of the feed. This is the fraction of the total throughput that consists of particles similar to the given particle. Furthermore, all particles have their own time variable to combine time-dependent and distance-dependent numerical calculations.

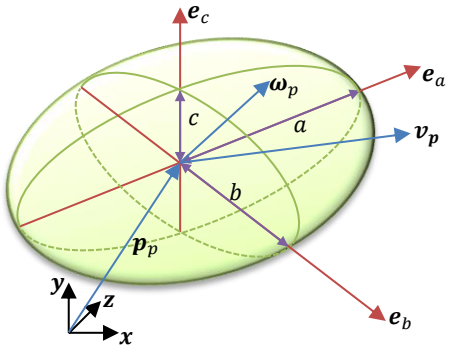

Figure 5.8: Definitions used to describe particles size, shape, orientation and motion

Definition of surfaces

In the basic model, all surfaces are described using 1D linear functions, limiting the configuration of the geometry of the ADR and the variety in types of surfaces. In the comprehensive model, the complete geometry of the ADR (including the rotor) is described using flat and cylindrical surfaces. All surfaces have a material type, just like particles. It is assumed that the combination of the two material types of particle and surface determines the friction and restitution coefficient needed in the collision calculation. This assumption is reasonable for the low coefficients of restitution that are observed between collisions of bottom ash particles with steel surfaces.

Flat surfaces are defined by an inward normal vector $\boldsymbol{n_s}$, distance of the surface from the point of origin d_s (parallel to the normal vector) and range in which they exist r_{max} , r_{min} (perpendicular to surface normal and the z-direction), see Figure 5.9. Flat surfaces can be stationary, rotate around the z-axis at the models point of origin $(\boldsymbol{\omega_s})$, or move in its planar direction (v_s) to represent e.g. a conveyor.

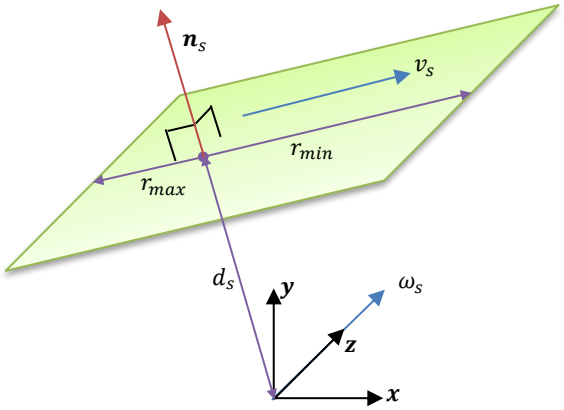

Figure 5.9: Definitions used to describe a flat surface

Cylindrical surfaces are defined by a pointing vector ($\boldsymbol{R}_s$), a direction vector of the cylinder ($\boldsymbol{l}_s$) and a radius (r_s), see Figure 5.10. Cylindrical surfaces can be stationary, rotate around the z-axis at the models point of origin, or rotate around their own axis (ω_s).

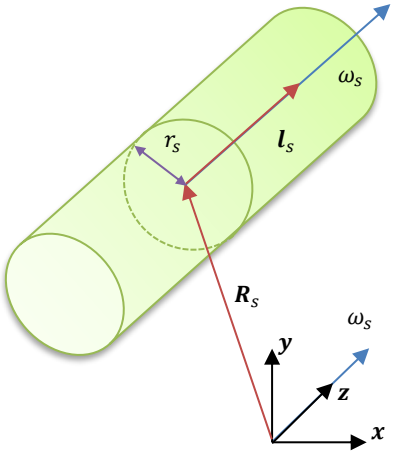

Figure 5.10: Definitions used to describe a cylindrical surface

5.4.3 Theoretical framework

Collision detection

For these two different types of surfaces, different methods of detecting the possibility of a collision are required. For a flat surface, the possibility of a collision can be ruled out by the condition in the equation below, in which r_p is the biggest radius of the ellipsoid representing the particle.

$$\boldsymbol{n}_s \cdot \boldsymbol{p}_p - d_s > r_p$$

For a cylindrical surface with radius r_s, the support ($\boldsymbol{R_s}$) and direction vector ($\boldsymbol{l}$) are first redefined in the particle's reference frame (indicated by single prime) and transformed such that $\boldsymbol{R}''$ and $\boldsymbol{l}''$ are perpendicular. For a cylindrical surface, the possibility of a collision can be ruled out if the condition in the equation below holds true

$$|\boldsymbol{R}''| - r_s > r_p$$

In which,

$$\begin{aligned}\boldsymbol{R}' &= \boldsymbol{E} \cdot (\boldsymbol{R}_s - \boldsymbol{p}_p)\\ \boldsymbol{l}' &= \boldsymbol{E} \cdot \boldsymbol{l}_s\\ \boldsymbol{l}'' &= \widehat{\boldsymbol{l}'}\\ \boldsymbol{R}'' &= \boldsymbol{R}' - (\boldsymbol{R}' \cdot \boldsymbol{l}'')\boldsymbol{l}''\end{aligned}$$

And

$$\boldsymbol{E} = \begin{bmatrix} e_{a_x} & e_{a_y} & e_{a_z} \\ e_{b_x} & e_{b_y} & e_{b_z} \\ e_{c_x} & e_{c_y} & e_{c_z} \end{bmatrix}$$

If a collision cannot be ruled out on the basis of the condition above, the exact distance between the particle and the surface is determined, taking the ellipsoidal shape into consideration. To obtain this distance, the closest point on the periphery of the ellipsoid to the surface, indicated by a vector originating at the center of mass: $\boldsymbol{r}_0$, must be found. The problems for a flat and cylindrical surface are illustrated in Figure 5.11.

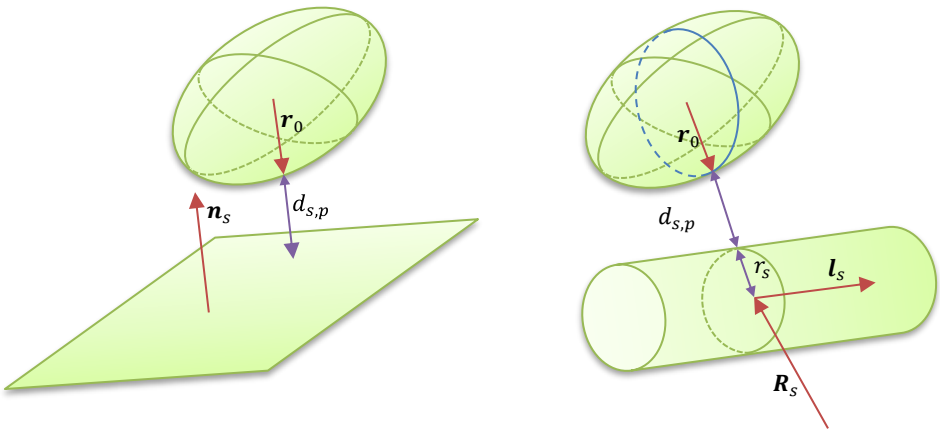

Figure 5.11: Determining closest distance for a flat surface (left) and cylindrical surface (right)

A solution is found via the notion that at the closest point of the ellipsoid to the surface ($\boldsymbol{r}_0$), the vector normal to the ellipsoid surface ($\boldsymbol{n}_p$) runs parallel to the vector normal

to the striking surface ($\boldsymbol{n_s}$). For an ellipsoid the vector normal to its surface can be determined analytically for every point on the surface. To obtain a general solution, the problem is analyzed in the particle's reference frame (indicated by single prime). For a flat surface the equations are given below.

$$\boldsymbol{r}'_0 = \boldsymbol{r}_0 \cdot \boldsymbol{E}$$
$$\boldsymbol{n}'_s = \boldsymbol{n}_s \cdot \boldsymbol{E}$$
$$\boldsymbol{r}'_0 = f \begin{bmatrix} a^2 \\ b^2 \\ c^2 \end{bmatrix} \cdot \boldsymbol{n}'_s$$
$$1 = \frac{r'^2_{0_a}}{a^2} + \frac{r'^2_{0_b}}{b^2} + \frac{r'^2_{0_c}}{c^2}$$
$$f = \pm \frac{1}{\sqrt{a^2 n'^2_{s_a} + b^2 n'^2_{s_b} + c^2 n'^2_{s_c}}}$$
$$\boldsymbol{r}_0 = \boldsymbol{r}'_0 \cdot \boldsymbol{E}^T$$
$$d_{s,p} = (\boldsymbol{p}_p + \boldsymbol{r}_0) \cdot \boldsymbol{n}_s - d_s$$

Here, a, b, c, are the principle radii of the ellipsoid.

For a cylindrical surface, the normal vector is only partially defined in its direction, however $\boldsymbol{n}_p$ will be perpendicular to $\boldsymbol{l}''$, which can be rewritten to define an ellipsoidal plane in which $\boldsymbol{r}_{0_E}$ must lie (indicated in blue in Figure 5.11). The parameters describing this ellipse are rotated to obtain its principle axes. The definition of this ellipse allows for an expression of the distance to $\boldsymbol{l}''$ by only one variable, the angle within the plane, ψ. The root of the derivative of the distance to $\boldsymbol{l}''$ that gives the closest distance to the center line of the cylinder yields the correct $\boldsymbol{r}'_0$, see definitions and equations below[1].

$$\boldsymbol{r}'_0 = \boldsymbol{r}_0 \cdot \boldsymbol{E}\boldsymbol{n}_p \perp \boldsymbol{l}'' \xrightarrow{yields} \boldsymbol{m} \perp \boldsymbol{r}'_0$$
$$\boldsymbol{f} \perp \boldsymbol{g} \perp \boldsymbol{m}$$
$$\boldsymbol{r}'_0 = \xi \boldsymbol{f} + \eta \boldsymbol{g}$$
$$1 = \frac{(\xi f_a + \eta g_a)^2}{a^2} + \frac{(\xi f_b + \eta g_b)^2}{b^2} + \frac{(\xi f_c + \eta g_c)^2}{c^2}$$
$$\xi = \xi' \cos\phi - \eta' \sin\phi$$
$$\eta = \xi' \sin\phi + \eta' \cos\phi$$
$$G = \left|\frac{\boldsymbol{f}}{\boldsymbol{r}_p}\right|^2, H = \frac{2(\boldsymbol{f} \otimes \boldsymbol{g})}{\boldsymbol{r}_p^2}, I = \left|\frac{\boldsymbol{g}}{\boldsymbol{r}_p}\right|^2$$

[1] The problem can also be formulated by defining a vector $\boldsymbol{m}$ as a linear combination of the vectors $\boldsymbol{R}''$ and $\boldsymbol{R}'' \times \boldsymbol{l}''$, which can also be expressed by only one angle ϕ. This results in a much simpler formulation of the problem, however, its (analytical) solution (finding the root of the derivative) is more complex and therefore not used.

$$\phi = tan^{-1}\frac{I - G + \sqrt{(I-H)^2 + H^2}}{H}$$

$$\boldsymbol{A} = \frac{(cos\,\phi\,\boldsymbol{f} + sin\,\phi\boldsymbol{g})}{\sqrt{G\,cos^2\,\phi + H\,sin\,\phi\,cos\,\phi + I\,sin^2\,\phi}}$$

$$\boldsymbol{B} = \frac{(cos\,\phi\,\boldsymbol{f} + sin\,\phi\boldsymbol{g})}{\sqrt{G\,cos^2\,\phi - H\,sin\,\phi\,cos\,\phi + I\,sin^2\,\phi}}$$

$$\begin{aligned}\boldsymbol{A}\cdot\boldsymbol{R}''\,sin\,\psi + \boldsymbol{B}\cdot\boldsymbol{R}''\,cos\,\psi \\ + (|\boldsymbol{B}|^2 - |\boldsymbol{A}|^2 + (\boldsymbol{A}\cdot\boldsymbol{l}'')^2 - (\boldsymbol{B}\cdot\boldsymbol{l}'')^2)\,sin\,\psi\,cos\,\psi \\ + \big((\boldsymbol{A}\cdot\boldsymbol{l}'')\big)(\boldsymbol{B}\cdot\boldsymbol{l}'')(sin^2\,\psi - cos^2\,\psi) = 0 \xrightarrow{yields} \psi\end{aligned}$$

$$\boldsymbol{r}_0' = \boldsymbol{A}\,cos\,\psi + \boldsymbol{B}\,sin\,\psi$$

$$d_{s,p} = |\boldsymbol{R}'' + \boldsymbol{r}_0'\cdot\ \boldsymbol{l}''\boldsymbol{l}'' - \boldsymbol{r}_0'| - r_s$$

The problem of finding the root is solved via a zero-in algorithm since the equation is quartic and an analytical solution would be too complex to implement [50].

When the exact collision distance d is determined, it can be evaluated whether a sign change has occurred. If so, a collision has occurred, and the impact on $\boldsymbol{v}_p$ and $\boldsymbol{\Omega}_p$ is determined.

Collision's influence on $\boldsymbol{v}$ and $\boldsymbol{\Omega}$

When a collision is detected, the vector pointing from the ellipsoid's center point to the contact point is defined as $\boldsymbol{r}_0$, the vector normal to the surface pointing into the ellipsoid at the contact point as $\boldsymbol{n}$ and the relative velocity of the contact point to the surface as $\boldsymbol{u}$. The discontinuous change in $\boldsymbol{v}_p$ and $\boldsymbol{\Omega}_p$ is determined by the method of Keller. For a detailed description reference is made to the publication [49], a summary of the method is given below.

As stated, in the method the timescale of the collision is considered to be short relative to the timescales of the rigid body movements $a/\boldsymbol{u}$ and $1/\boldsymbol{\Omega}_p$. Therefore, the rigid bodies can be assumed to be static, so $\boldsymbol{r}_0$ and the moment inertia $\boldsymbol{J}_0$ can be considered constant for the duration of the collision. Furthermore, the influences of external forces and torques can be neglected. Only the contact force $\boldsymbol{F}$ and the relative velocity $\boldsymbol{u}$ remain of relevance. The discontinuous change in $\boldsymbol{v}_p$ and $\boldsymbol{\Omega}_p$ is given by the impulse $\boldsymbol{I}$ and the equations of motion.

The contact force is decomposed into its normal and tangential part. The normal force $\boldsymbol{N}$ is eliminated by defining the impulse (exchange of normal momentum) up to time t as the independent variable τ. The tangential force is given to be proportional to $\boldsymbol{N}$, by the law of friction, as $f\boldsymbol{N} = -\mu\hat{u}_T\boldsymbol{N}$, which holds for $\boldsymbol{N} \geq 0$ and is defined if $|u_T| \neq 0$. Here μ is the coefficient of friction and u_T is the tangential part of $\boldsymbol{u}$. Now the total momentum exchange can be found by integrating over τ.

The direction of $\hat{u}_T$ is found by rewriting the equations of motion as differential equations over $d\tau$ and decomposing them into the normal u_N and tangential u_T direction. The tangential force f is set to $-\mu\hat{u}_T$, the differential equation of $du_T/d\tau$. This equation is solved by decomposing u_T into its length ρ and direction θ. The derivative of ρ is defined by $g(\theta)$, and that of θ by $h(\theta)/\rho$. By eliminating ρ from these

two equations, τ can be expressed in terms of θ by nested integrals that both integrate over θ.

In the model, this integral is solved numerically with an explicit scheme over $d\theta$. Every step over $d\theta$ results in a $d\rho$ (via the nested integral), a $d\tau$ (via the complete integral) and a du_N (via $du_N/d\tau$). By combining $d\theta$ and $d\rho$, du_T is found.

The integral cannot be solved numerically when $h(\theta_0) = 0$, since $d\theta/d\tau = 0$. However, then $\theta(\tau) = \theta(0)$, and ρ increases linearly in τ and the solution can be found analytically.

The numerical analysis holds as long as $|u_T| \neq 0$. The event $|u_T| = 0$ is denoted by τ^*. At τ^* the direction of u_T is no longer defined and it needs to be determined whether $|u_T|$ remains zero. For this, $du_T/d\tau$ is set to zero, and solved for f. If $|f| \leq \mu$ the collision is in stick mode. In this case $|u_T|$ will remain zero, and f will remain constant for $\tau \geq \tau^*$. If $|f| > \mu$, a new direction θ must be found with conditions $g(\theta) > 0, h(\theta) = 0$. There will always be a single solution that satisfies both, and it will always be different from θ^*, because $g(\theta^*) < 0$. The direction and derivative of u_T will remain constant for $\tau \geq \tau^*$, so that, again, the solution is found analytically.

The duration of the collision is determined by u_N. The event $u_N = 0$ is denoted by τ_0. For $\tau > \tau_0$ the interaction changes from compression to decompression and Poisson's hypothesis states that the collision terminates at $\tau_e = (1 + e)\tau_0$.

The relative position of $t = 0$ and τ^* to τ_0 and τ_e, and the evaluation of $|f|/\mu$ at τ^* determines the sequence of calculations.

Material constants μ and e

The method of Keller involves two material constants: the coefficient of restitution e and the coefficient of friction μ. Unlike μ, e can, strictly speaking, not be considered to be solely dependent on the two materials involved in the collision. The coefficient results from the specific way the compression wave travels through the particle during the compression and decompression phase of the collision. Therefore, it is a function of the materials, shape of the particle and orientation of the collision. [51] shows the dependency of e on the orientation of the collision for a strongly elongated shape (rod). It follows that the value of e can vary by a factor 0.3 to 1.5 depending on the orientation of the rod. This variation will have a significant effect on the manifestation of the collision. However, for relatively inelastic collisions and particle shapes with limited $a/b/c$ ratios, the influence of shape and orientation can be neglected.

In the model, the parameters μ and e are considered to be a property of the combination of the particle and surface material properties and must be given as input to the model for all relevant particle-surface interactions.

Painleve paradox

In the field of rigid body dynamics, a problem known as Painlevé's Paradox [52] exists. The most famous example of this paradox is the screeching of chalk on a blackboard. The problem is illustrated by Figure 5.12.

When μ is large and J/ml^2 is small, the parameters of the illustrated example can be such that a solution cannot be obtained via the method of Keller. For a detailed description of the problem, reference is made to the numerous publications on this problem [53, 54]. The essence of the problem is that the interactions at the collision

point result in a (counter clockwise) rotation of the rod into the surface, creating an inward motion that cannot be counteracted by finite force N. Solutions to this problem are proposed by Stewart [55]. However, Pfeiffer and C. Glocker [56] demonstrated that this problem can only appear when $\mu > 4/3$ for a rod with negligible thickness. For an ellipsoid, the limiting friction factor becomes $\mu > 4\sqrt{24}/20 \approx 0.98$.

In this thesis all particles are described using ellipsoids, and no material combinations with a friction coefficient larger than this constraint were analyzed, therefore the solution to the problem is not implemented. However, in future applications of the proposed model, caution must be taken that the constraint on the friction coefficient is satisfied to prevent inconsistent results.

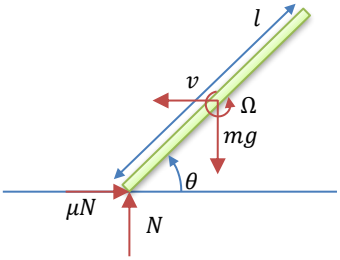

Figure 5.12: Illustration of Painlevé's Paradox

5.4.4 Results

In the ADR process, the material flow initially diverges from the rotor-blade into a cone shaped jet. When this cone hits the roof, it is converged and diverted towards a high velocity conveyor belt. On impact, material has to sync up with the belt-speed and the inclined angle. The model allows the study of these three specific moments in the particles trajectories in detail, resulting in understanding and improvement of the overall classification principle of the ADR. In all these cases the semi-random influence of the collision effect plays a role. This effect is also captured by the collision model. The following sections cover these four topics.

Randomization of particle velocities at the rotor

The randomization effect of the collision model is shown in isolation by simulating the collision of a single particle with a flat surface at 25 m/s (typical impact speed of the rotor blade). The properties of this single particle are taken to represent a typical particle in the ADR for which the collision behavior has an important effect on its classification. The major axis radius of the particle is taken to be 2 mm. Measurement data on bottom ash particles show a median for a/b ratio of 1.6 and b/c of 1.4. The specific density is 2200 kg/m^3. The friction coefficient is taken to be 0.2. The average coefficient of restitution (e) of bottom ash particles was measured to be 0.05. The simulation is also performed for e = 0.50. To obtain the statistics of the behavior, the particle is simulated 10^4 times with random orientations to the flat surface. Gravity and air drag are neglected in this simulation.

After the collision, the initial velocity $\boldsymbol{v}_p$ is transformed to $\boldsymbol{v}_p'$ and the particle will have an angular velocity of $\boldsymbol{\Omega}_p'$. To see the influence of the collision, the results are normalized by the particle dynamics before collision. Since particles start without rotation, the length of the angular velocity vector is normalized by the initial velocity

over the equivalent spherical radius of the ellipsoid: the radius of a sphere with equal volume as the ellipsoid ($R = a/\sqrt[3]{1.6^2 \cdot 1.4}$):

$$\text{Velocity: } \rho = \frac{\boldsymbol{v}_p'}{\boldsymbol{v}_p}$$

$$\text{Rotation: } \rho = \frac{\boldsymbol{\Omega}_p' a}{\boldsymbol{v}_p \sqrt[3]{1.6^2 \cdot 1.4}}$$

Figure 5.14 and Figure 5.15 show the normalized length ρ, azimuth ϕ and polar θ angle divided by π radians of the normalized returned $\boldsymbol{v}_p'$ and $\boldsymbol{\Omega}_p'$ vector for the two different restitution factors. The definition of ρ, ϕ and θ is given in Figure 5.13.

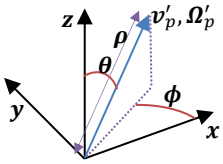

Figure 5.13: Definition of the normalized length ρ, azimuth ϕ and polar θ angle of the returned $\boldsymbol{v}_p'$ and $\boldsymbol{\Omega}_p'$.

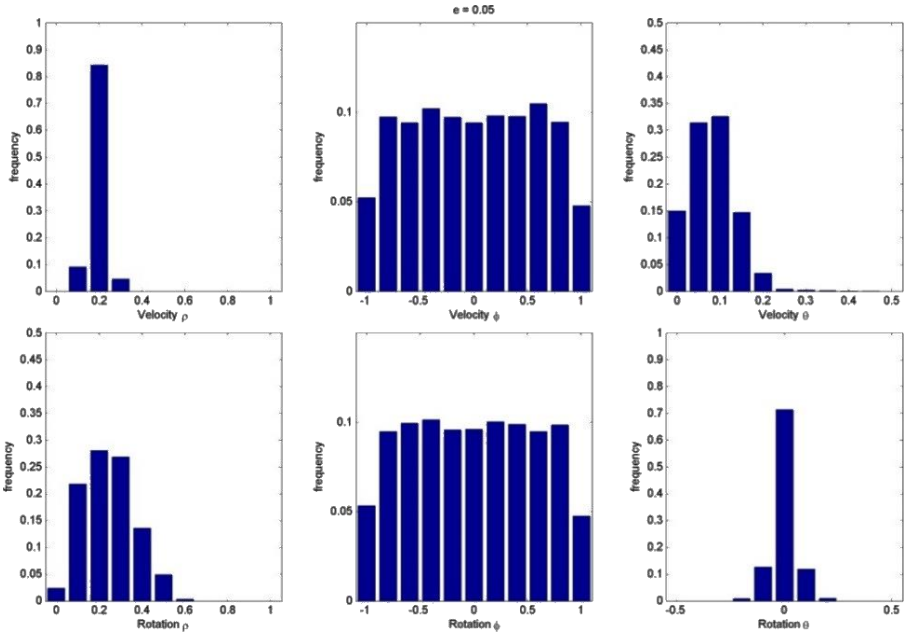

Figure 5.14: Distribution of the length, ρ (left), azimuth angle, ϕ (middle) and polar angle, θ (right) of the velocity (top) and angular velocity (bottom) vector at e = 0.05

For the typical restitution factor for bottom ash (e = 0.05), the impact velocity is returned to the particles velocity for about 20% and is transferred to angular velocity for about 30%. The orientation of the returned vector (for both the velocity as the

rotation) within the plane of the collision surface (ϕ) is fully random. The polar angle of the returned vector (for both the velocity as the rotation) is small.

It is noteworthy that the angular velocity of the particle can be considerable. The resulting centrifugal acceleration of $\Omega^2 r$ can be around[2] 4600g. This high rotation could result in the extra release of fine particles that were still adhered to the rotating particle.

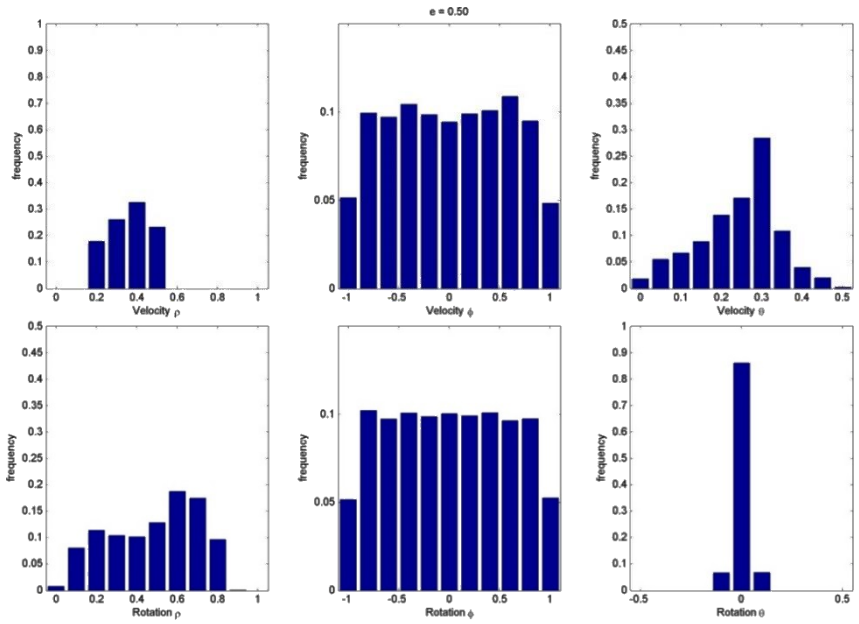

Figure 5.15: Distribution of the length, ρ (left), azimuth angle, ϕ (middle) and polar angle, θ (right) of the velocity (top) and angular velocity (bottom) vector at e = 0.50

At a higher restitution factor (Figure 5.15), the returned velocities are bigger. The distribution of the length of the velocity and rotation vector is wider. The distribution in the azimuth angle is not affected and still fully random. The polar angle of the velocity shows both an increase and a wider distribution. The spread in polar angle of the rotation velocity shows a decrease.

The overall effect is an increase in the randomization of the particle's behavior. This increase in the spread of particle behavior reduces the classification efficiency of the ADR. It is therefore expected that materials with different restitutions coefficients have different classification behavior in the ADR. Within the considered waste materials, the coefficient ranges from nearly zero (soft materials within sifting sand), to very small (bottom ash), to considerable (crushed concrete).

[2] $0.25^2 \cdot 25^2 \cdot (1.6^2 \cdot 1.4)^{\frac{2}{3}} / (2 \cdot 10^{-3}) / 9.81 \approx 4600$

Formation of particle jet by impact with the rotor

In the basic model of the ADR, the simulation starts with the initial velocity and direction of a number of trajectories per size fraction. The properties of this set of initial conditions are determined by the given opening angle and velocity of the particle jet. In the comprehensive model the collision model is used to generate the properties of the particle jet.

The properties of the particle jet are a result of a large number of influences:

- Quasi random behavior of a single ellipsoidal particle
- Material and geometrical properties of material and size fractions
- The position, direction and speed of the feed relative to the rotor position and RPM

By combining the collision model with a dynamical description of moving surfaces, the formation of the particle jet by the rotor can be simulated. The required input consists of data (e.g. geometry of the ADR, particle properties) that can be measured in the lab.

The formation of the particle jet is simulated by the release of a single size and material fraction (4-8mm, bottom ash minerals) at a single position ($x = -0.14$m, $y = 0.30$m, $z = 0.0$m). A set of 200 particles is simulated 20 times, to get a total of 4000 trajectories. The properties of this set of particles is generated by the following formulas to match the property distribution of 40 lab-analyzed bottom-ash particles.

$$b_{i=1..n} = \frac{1}{2}\left((8mm - 4mm)\cdot\frac{i}{n} + 4mm\right)R_{0.95-1.05}$$
$$a_i = b_i\left(\frac{1}{2.5}\cdot stt_{n=3} + 1\right)$$
$$c_i = b_i/\left(\frac{1}{2.5}\cdot stt_{n=3} + 1\right)$$
$$m_i = \frac{4}{3}\pi a_i b_i c_i R_{1500..2200}$$

In which R is a random number between the given boundaries, n is 200 and $stt_{n=3}$ is a random number from a student distribution with 3 degrees of freedom. The friction coefficient μ_p is estimated at 0.2, and the coefficient of restitution e was measured to be 0.05. The period of the rotor rotation is subdivided into 20 slots, and the timing of each simulation of 200 particles is random within that slot. Every particle is released with a random orientation. The release velocity is such that a blade will be almost completely filled.

Figure 5.16 shows the distributions of the particle jet from the rotor-blade from the side view (top figure) and top view (bottom figure). To the right the distribution of the y- and z-coordinates of particles at a distance of 1.2 m from the rotor is shown.

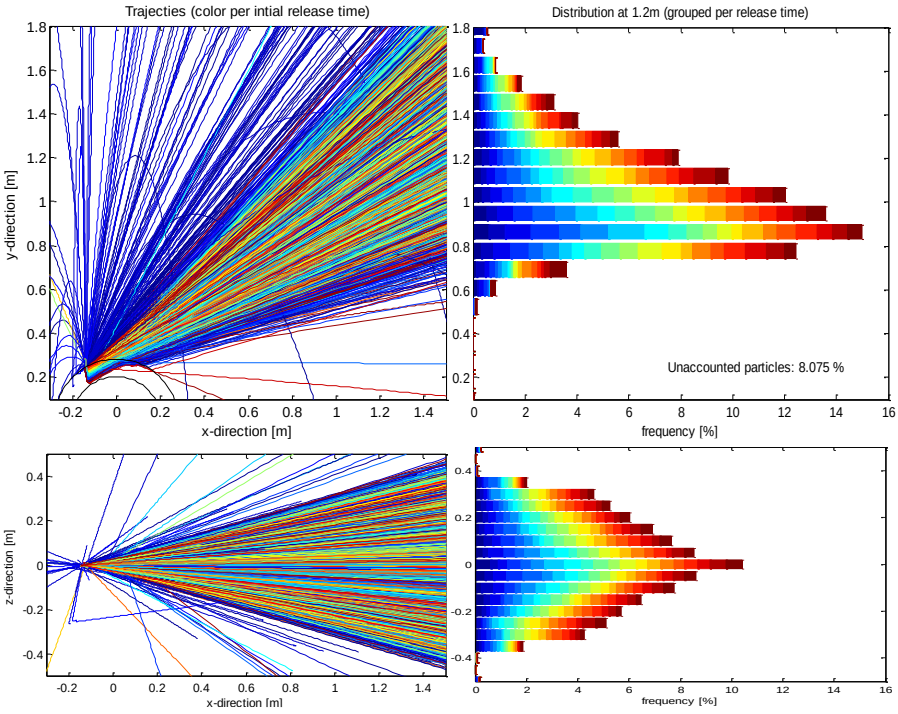

Figure 5.16: Distribution of the particle jet from the rotor-blade from the side view (top figure) and top view (bottom figure).

The trajectories show the formation of the cone. The histogram shows a peak at 0.9 m, the average angle of trajectories is 40°, and 90% of the material is propelled between 31° and 51°. From the top view it can be seen that 50% of the particles are propelled within a cone that opens with 13° and 90% within 28°.

The color of the trajectory and bar corresponds to the release time slot and so roughly to the position of impact on the rotor blade. It can be seen that there is little relation between the position on the blade and the trajectories mean angle and spread. The angle of the blade at impact is less dominant than previously thought.

About 8% of the particles have an aberrant trajectory and do not reach the 1.2m from the rotor. The graph of trajectories shows that these are primarily particles that are hit on the top of the rotor blade and are hit partially. The 8% corresponds with expectation based on geometrical considerations: the particle size relative to the rotor blade height ($6mm/75mm$)

Furthermore, it can be seen that there are trajectories propelled almost horizontally. These are particles that have penetrated the rotor-blade the deepest and did not get enough velocity to escape out of the rotor. They are hit repeatedly and stay within the rotor-zone, until they are finally swept out at a much lower angle than the bulk of the particles. This can be seen in detail in Figure 5.17.

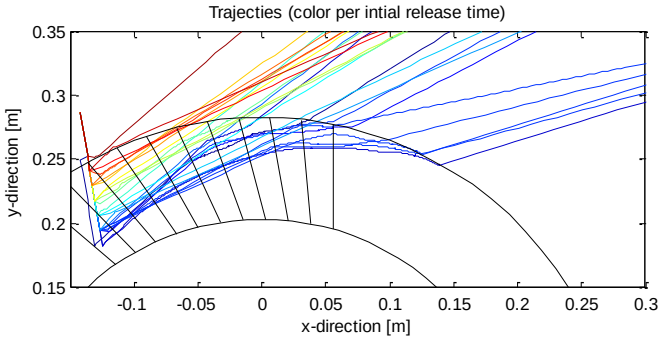

Figure 5.17: Detail of trajectories near the rotor

An experiment was performed to check the validity of this part of the model. The rotor was fed in the middle over 100 mm width with 4-8 mm bottom-ash minerals, 38 mm behind and 330 mm above the rotor axis. At 1 m away from the rotor, the jet was captured onto a sheet of thin paper. Figure 5.18 shows the results compared to a simulation with same input as the experiment (200 particles simulated 8 times). The simulation faithfully reproduces the center and elongated shape of the jet.

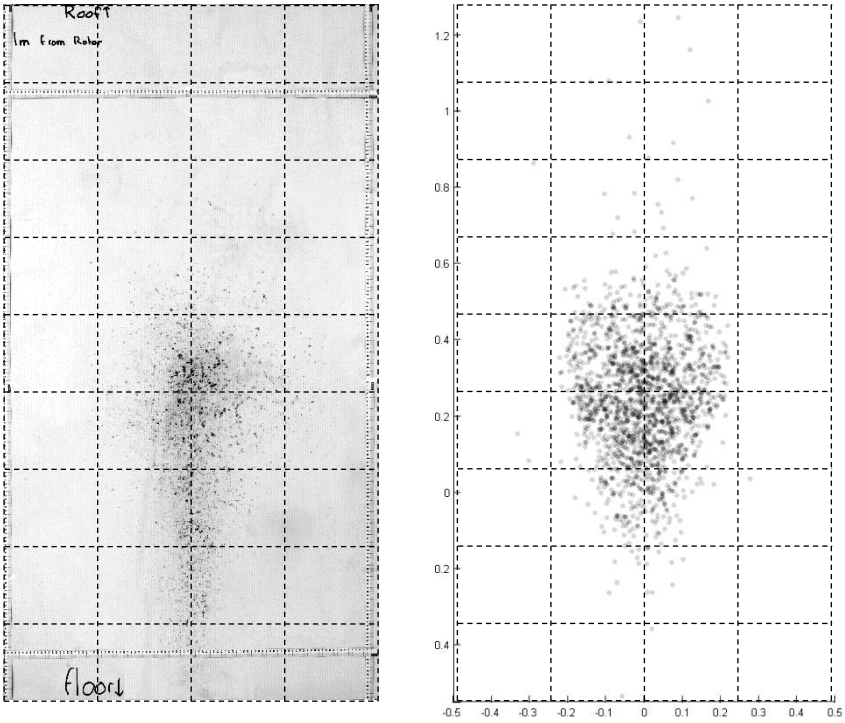

Figure 5.18: Comparison of experimental data (left) with simulation results (right)

In the experiment conditions are such that small fragments may break off from the particles as a result of impact by the rotor. This feature is not captured in the simulation

and will effectively reduce the restitution coefficient with respect to the value of 0.05 which was measured at low collision speeds. This may be the most important reason why the experimental pattern of particles is more compact than in the simulation.

Conversion of the jet by impact with the roof

The impact with the rotor causes a dispersion of the particles, creating a jet that opens at an angle of about 20°. Given the velocity of this jet, it will have an impact with the roof of the ADR enclosing. Upon this collision, the direction of the particles is altered and therefore the general direction and opening of the particle jet changes.

Figure 5.19 shows the continuation of the previously discussed simulation. The histograms show the distribution of the incoming and outgoing angle of the particles trajectories relative to the roof. It can be seen that the spread in the outgoing angle is significantly smaller than the incoming angle. This results in a converging effect, partly eliminating the diverging effect of the impact with the rotor.

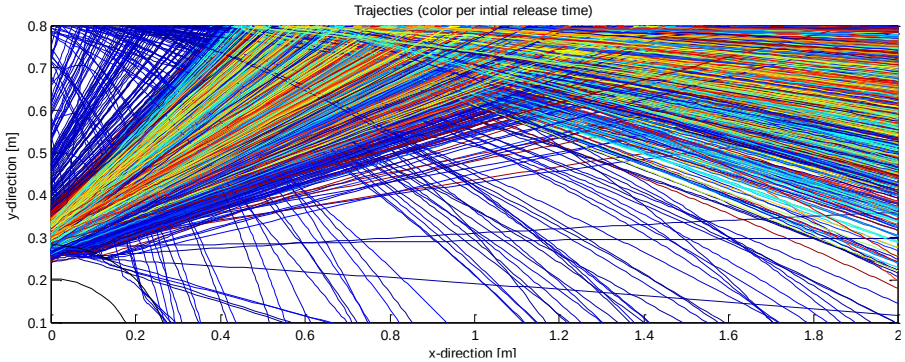

Figure 5.19: Trajectories of particles before and after collision with the roof

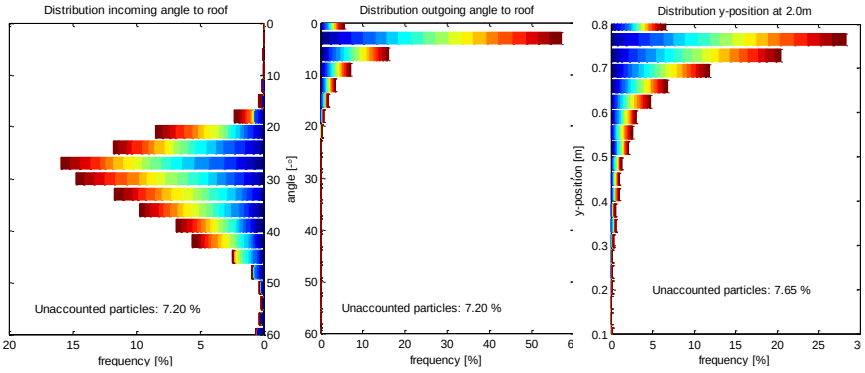

Figure 5.20: Incoming angle (left), outgoing angle (middle) and y-position at 2m (right)

The result of this effect can be seen more clearly in the bottom right figure, which shows the distribution of the y-position at 1.5 m from the rotor. It can be seen that more than 50% of the particles pass within 7 cm of the roof and 75% within 13 cm. This converging effect of the impact with the roof allows for a higher quality

classification, since the influence of the initial direction is reduced and classification is again dominated by the ratio of the particle's momentum to air-drag.

Figure 5.21 shows a close up of the impact with the roof with a random selection of all trajectories simulated. Here the converging effect can be seen more clearly.

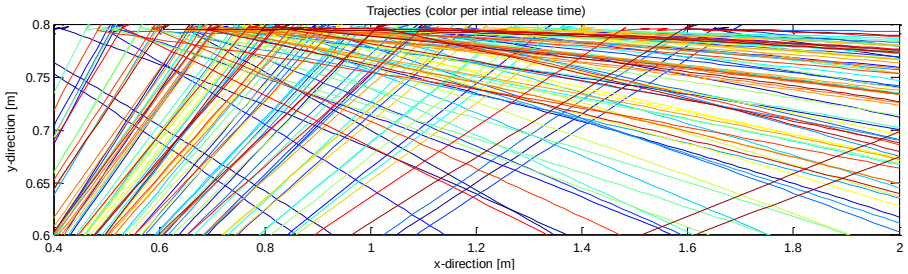

Figure 5.21: Close up of impact with the roof

Bouncing on conveyor belt

Upon impact of a particle with the high velocity conveyor belt, the particle will bounce up due to the non-zero coefficient of restitution. If the surface would be flat and stationary, the resulting bouncing would quickly diminish. If the surface is moving and especially when it is inclined, the kinetic energy of the belt is partly absorbed by the particle, causing more bouncing. In some situations, a particle can keep bouncing on an inclined moving belt forever. In reality, the effect of bouncing particles on the moving inclining conveyor belt is also influenced by the total amount of material on the belt. Material on the belt, especially fine particles, absorb energy from the bouncing particle and reduce the length to a stable position significantly. This effect cannot be simulated since particle-particle interaction is not taken into account in the model.

To show the influence of the inclination angle on the residual height of a particle, simulations were performed for a moving conveyor belt at 4 m/s at an inclination of 0, 10, 20 and 30°. The a/b ratio was varied from 1.2 to 3.8, with steps of 0.2 to show the influence of the geometrical properties of the particle. Each of these 16 particles were simulated 300 times. The particles were released at x-position = 4m and 1m above the belt, with no initial velocity.

Figure 5.22 shows the trajectories of the 16x300 particles for all 4 inclinations of the belt. The coloring corresponds with the a/b ratio (blue = 1.2, red = 3.8). The images are rotated to compensate for the inclination of the belt.

Figure 5.23 shows the residual potential plus kinetic energy in the vertical direction normalized by the initial potential: $\left(\frac{1}{2}mv^2 + mgh\right)/mgh_{initial}$, averaged over all particles within the x-range in each a/b ratio category (color blue to red). Figure 5.24 shows the same but averaged only for the particles still moving relative to the belt.

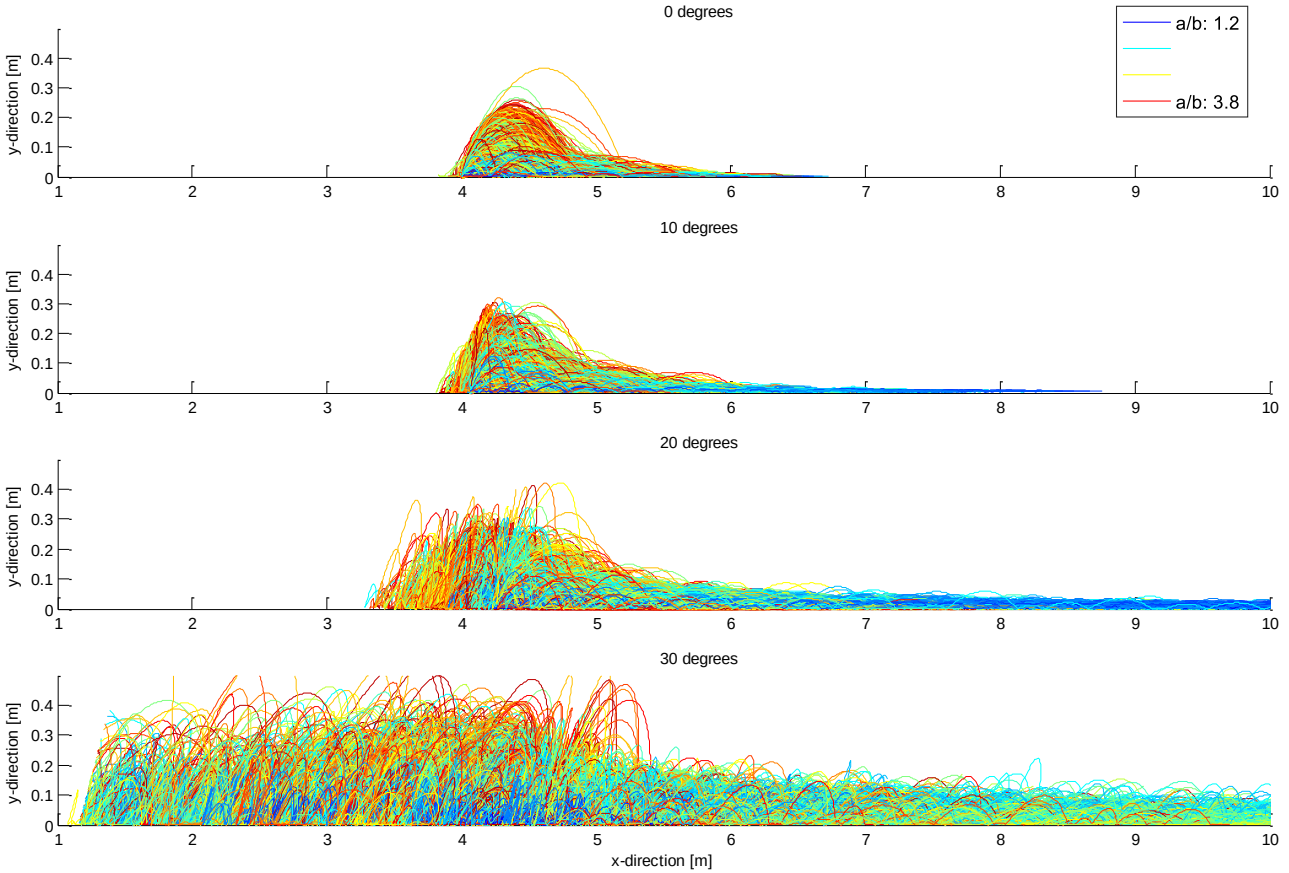

Figure 5.22: Trajectories of particles with different a/b ratios, bouncing on inclined belt

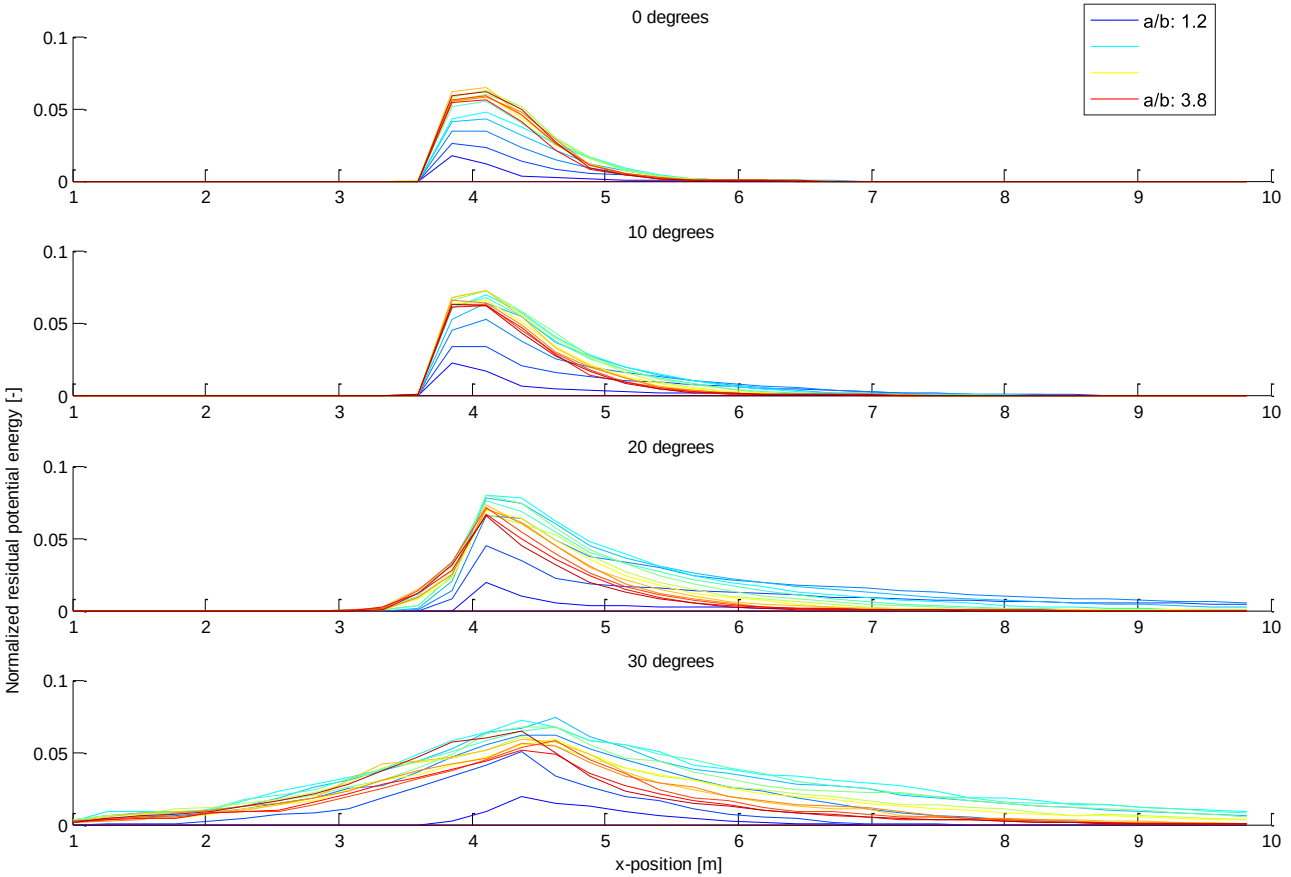

Figure 5.23: Average of normalized residual potential plus kinetic energy in the vertical direction

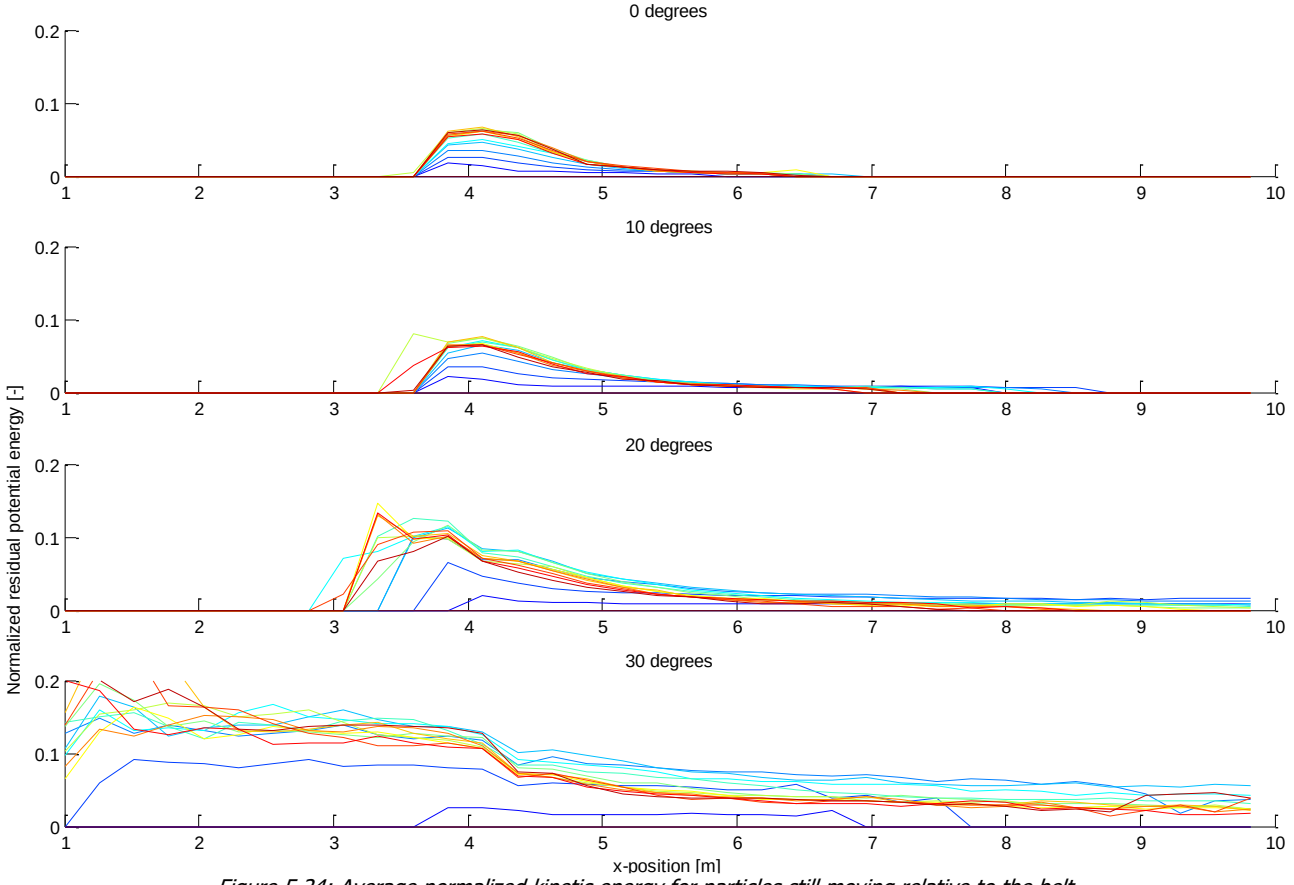

Figure 5.24: Average normalized kinetic energy for particles still moving relative to the belt

If the surface would be stationary, particles bouncing up would only get maximum upward velocity $e \cdot v_y$. Therefore, one would expect a rapid decrease of the bouncing height in the trend of $\sqrt{2gh} \cdot e^n$, in which n is the number of collisions on the belt. Since the coefficient of restitution, e, for mineral and rubber is in the order of 0.1, one would expect the height of the particle to diminish quickly (an order of magnitude with every bounce). The figure for a belt inclination of 0° shows this result. However, at an inclination of 30°, there is a range of values of a/b for which the residual height does not diminish. A certain percentage of the particles keeps bouncing and does not seem to lose energy. Particles moving in the opposite direction of the belt velocity can even gain energy with bouncing. This is caused by the inclination and movement of the belt. Upward energy of the belt is conveyed into the particle.

The results show that for inclinations exceeding 20°, particles can stay bouncing on the belt for a long time, causing operational problems and reducing classification efficiency at the air-knife downstream of the conveyor for the coarse fraction. For an air-knife to classify particles according to their size and mass, the particles should all have the same initial trajectory. Particles that are bouncing on the conveyor have different initial velocities and will not be classified correctly. This phenomenon has, in fact, been observed in practice.

5.5 The mutual interaction of air-flow and particle jet

5.5.1 Introduction

The ADR classifies granular material with a size range of 0-16mm at a cut size around 1mm. After the particles within a moist cluster are liberated by the rotor, they are propelled into a ballistic trajectory during which they will interact with the air inside the encasing. With the drag-induced deceleration of the particles, momentum is transferred onto the air, creating an airflow inside the casing of the ADR. This airflow can be of paramount influence on the trajectory of the <2mm particles and is therefore of importance on the classification results.

Influence of exchange of momentum

In order to estimate the exchange of momentum to the air, and the effect of the resulting air-flow on the particles deceleration, a straightforward calculation is performed.

In the ADR, material is slowed down by air-drag. The total momentum lost by particles of diameter D_i, is calculated by multiplying the mass flow rate times the reduction in velocity for each fraction i, as in the equation below. This momentum drives the air-flow within the ADR.

$$\Delta P = \sum_i T_i \cdot \Delta v_i$$

The ADR will typically operate at throughputs of around 60 t/h/m_{width}. Roughly 50% of the material will be 1mm or smaller material. These fine particles will have lost most of their velocity, and therefore most of their momentum, within the first couple of meters. The particles will start at 25 m/s. It may be assumed, for a rough calculation, that within 5 m the particles will lose 50% of their initial velocity. This momentum is transferred to the air within the cone of particles. The cone expands with an opening

angle of roughly 20°. To conserve the total momentum, the momentum of the air flowing out the end of the cone must be equal to the momentum lost by the particles.

With these assumptions the velocity of the air is estimated to be:

$$v_{air_x} = \sqrt{\frac{16.67\frac{kg}{s \cdot m_{width}} \cdot 50\% \cdot 25\frac{m}{s} \cdot 50\%}{5m \cdot 2 \cdot tan(10°) \cdot 1.2\frac{kg}{m^3}}} \cong 7\ m/s$$

At these velocities, there is a strong interaction between the air flow and particles with a size near the cut-point of the ADR, so that a realistic estimation of the airflow is needed. The airflow driven by a body force is described by the Navier Stokes equations. Current solvers often use Computational Fluid Dynamics (CFD). However, these calculations are computationally intensive and contain levels of detail that are not strictly necessary. Therefore, simplifications will be used to speed up calculations for the model derived here. Below the concept of calculations is given, followed by the implementation and the results.

5.5.2 Concepts and definitions

Concept of calculations

The Navier Stokes equations generally do not have an analytical solution; therefore, numerical approximations are used to obtain a solution. The air-profile is discretized into horizontal cells, which are subsequently divided into vertical cells. Per cell, the components of the Navier Stokes equation are treated separately to obtain an approximate result for the air-profile. The calculation of the air-profile and the ballistic trajectory are then integrated in the following step by step sequence:

- Determine the appropriate width of the next horizontal cell downstream
- Determine the ballistic trajectory of particles to the end of this cell
- Calculate the air-velocities in all vertical cells and project them into the next air-profile cells

The spacing of cells in the vertical direction is predetermined but flexible to capture different geometries of the encasing. The maximum spacing of horizontal cells is also predetermined, but the actual size will adjust to the momentum transferred in the cell to minimize discretization errors due to non-linear effects in the interaction of the flow and the motion of particles.

The flow of air in the cells is calculated from left to right (main direction of the particles and the flow) in line with conditions for numerical stability. With the particles decelerating from drag, the air is accelerated by the conservation of momentum. An increase in air-velocity will reduce the amount of momentum transferred. Therefore, if a cell is chosen to be very large, this non-linear effect of mutual interaction results in a large discretization error, or even instability. To avoid this, the size of the horizontal cell is reduced until this effect is small. This is done in the following way.

The size of the horizontal cell is determined by trying one iteration loop of the mutual influence process. First the air in the cell is assumed to have the velocity of the left boundary. The momentum loss of the passing particles is estimated by letting the particles pass the cell in a single numerical integration step. Based on the lost momentum of the particles, the air-velocities of the right boundary are estimated. The velocities on the right boundary are copied to the left boundary and the calculation is

repeated. When the differences between calculated air velocities of the first and second calculation are large, the cell size is reduced. This process is repeated until the differences in air velocity are small enough with respect to a pre-defined criterion.

Once the correct size of the horizontal air profile cell is determined, the precise ballistic trajectory of all particles is determined. During this process, the time-steps of the numerical integration of the trajectory calculation are adjusted to the particles velocity. The total momentum lost by the particle is added to the total influx of momentum of the air in the appropriate cell.

When all particles have cleared the right boundary of the air-cell, the calculation of the ballistic trajectories is interrupted and the air profile is updated. The air velocity profile resulting from the body force imposed by the momentum exchange of the ballistic trajectory and the air is given by the incompressible Navier Stokes equation:

$$\rho\left(\frac{\partial \boldsymbol{v}}{\partial t} + \boldsymbol{v} \cdot \nabla \boldsymbol{v}\right) = \mu \nabla^2 \boldsymbol{v} + \boldsymbol{f} - \nabla \boldsymbol{p}$$

An approximate solution is obtained by isolating and approximating the separate components of the equation. Since only the steady state average flow profile is of interest, the unsteady acceleration term $\rho \frac{\partial \boldsymbol{v}}{\partial t}$ is fully neglected. The components describing the effects of dispersion, the imposed body force and pressure gradients are solved consecutively in a numerical way, as described later on. Finally, the three components are combined, and the remaining component of volume conservation is used to evaluate the air-velocity in the vertical direction. The obtained air-velocity of the right boundary is copied to the left boundary of the next air-profiles cells and the full calculation process is repeated.

Definitions of air-profile

In the basic model, the air-profile was defined by a fixed number of cells in the horizontal direction, and three cells in the vertical direction. For the comprehensive model a more detailed and flexible meshing is used. More cells in the vertical direction can be used and the size in the horizontal direction will be dynamic to minimize the non-linear effect caused by the mutual interaction of particles and air-flow.

The air-profile is divided into horizontal x-cells that each span an interval dx along the x-axis and the complete height of the installation along the y-axis, see Figure 5.25. The total height is defined by the closest floor and roof on the left (y_l) and right (y_r) boundary. Within the x-cell the air-profile is divided into n equidistant vertical y-cells. Within a single y-cell, the calculation of the air velocities on the right side $\boldsymbol{v}_{a_r}$ will be calculated based on the air-velocity on the left side $\boldsymbol{v}_{a_l}$ and the influx of momentum $\boldsymbol{P}_p$. The calculation of $\boldsymbol{v}_{a_r}$ is subdivided into the isolated effects of dispersion $\boldsymbol{v}_{a_{disp}}$, added momentum $\Delta \boldsymbol{v}_{a_p}$ and pressure gradients $\Delta \boldsymbol{v}_{a_{press}}$, as will be explained later.

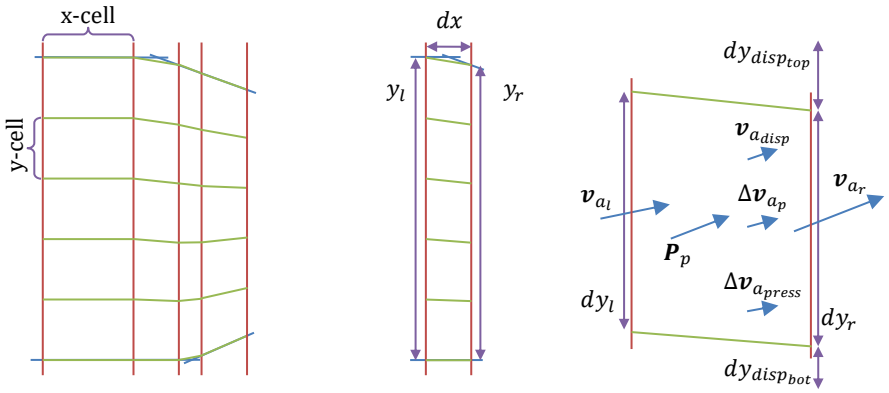

Figure 5.25: Definitions used in the comprehensive model to describe the air-profile

5.5.3 Theoretical framework

The separate steps of calculation are elaborated in the following sections. The overall order of calculations is as follows:

- The width of downstream air-profile cell is determined such that discretization errors are negligible.
- The ballistic trajectory of particles to the end of this cell is determined via an explicit numerical integration. The air-velocity of the left border of the cell is used during calculation. The momentum lost by particles as they advance through the cell is summed.
- When all particles reach the end of the cell, the air-velocities in the cell are calculated from conditions at the left side and the transferred momentum. The air-velocities on the right side of the cell are projected forward to the left-side of the next cell

Width of air-profile cell

The initial width of an x-cell is set to twice the size of the previous cell, subject to a predefined maximum. The air-velocity within the y-cells is set equal to the right boundary air-velocity of the corresponding previous y-cell. The ballistic trajectory of all particles still in the model is projected forward over the complete length of the x-cell in a single time-step. The momentum lost by the particles is summed for each y-cell. These are used to calculate the air-velocities on the right side boundaries.

The calculation results in an estimation of the air-velocities on the right side of the x-cell. Using this estimated air-velocity, the calculation is repeated and the differences between the first calculation and the second are averaged for all y-cells. When the difference is larger than a pre-defined maximum, the width of the cell is reduced by a factor two and the calculation is repeated.

Ballistic trajectory with drag

The ballistic trajectory of the particle is calculated via a time-dependent numerical method that takes the airflow profile into account for the air drag. This is done similar

to the method used in the basic model. However, now also the orientation and rotation of the particle is taken into account. At every time step the change in the particle's velocity and rotation over time is calculated, see equations below. With these, the position and orientation are updated.

$$d\boldsymbol{v}_p = d\boldsymbol{v}_{p_{drag}} + \boldsymbol{g} \cdot dt$$
$$d\boldsymbol{\omega_p} = \boldsymbol{I}^{-1}\boldsymbol{T}_{drag} \cdot dt$$

The change in velocity is determined via aerodynamic drag and gravity. The formula describing aerodynamic drag is the same in the basic model and given by:

$$d\boldsymbol{v}_{p_{drag}} = \frac{\boldsymbol{F}_{drag}}{m_p} \cdot dt = -\frac{\frac{1}{2}\rho_a C_d A_p |\boldsymbol{v}_r| \boldsymbol{v}_r}{m_p} \cdot dt$$

To determine the drag-force, the relative velocity between particle and air, $\boldsymbol{v}_r$, is used. The position of the particle is used to find the correct x- and y-cell and the air-velocity of the left boundary of that cell is used in the calculation of the drag-force.

To increase stability and better describe a zero-crossing of the relative velocity a partially implicit scheme is used that evaluates the drag equation partially on $\boldsymbol{v}(t)$ and partially on $\boldsymbol{v}(t + dt)$, see below.

$$d\boldsymbol{v}_{p_{drag}} = \frac{\beta}{1-\beta}\ \boldsymbol{v}_r$$
$$\beta = \frac{-\frac{1}{2}\rho_a C_d A_p}{m_p} |\boldsymbol{v}_r| dt$$

In which β is the parameter accounting for the influence of drag. This method of evaluating the influence of drag allows for the particle's velocity to slowly adjust to the air velocity, without overshoot. This is especially important for smaller particles.

In the comprehensive model, all particles are represented by ellipsoids, see section *Definition of particles* on page 116. To describe the drag coefficients (C_d) of ellipsoidal particles over large ranges of Reynolds number has proven to be a challenge [57]. Chhabra et al. have a done an intensive evaluation on the available methods and found: '*The best method appears to be that of Ganser which uses the equal volume sphere diameter and the sphericity of a particle. The resulting overall mean error is about 16%. In general, the lower the sphericity, the poorer is the prediction.*' The method of Ganser [58] uses a low number of parameters to accurately describe the drag coefficient over large ranges of Reynolds numbers and is implemented in the comprehensive model presented here. Effects of particle rotation on lift and drag are not taken into account.

The projected area (A_p) of an ellipsoid is not as trivial as it is for a sphere, but an analytical solution is provided by Vickers [59]. In this method, the projected area is given from the three principal radii and the angle of attack (given by the orientation of the relative velocity vector in the coordinate system of the ellipsoid).

The momentum lost by the particle due to air-drag is given by:

$$\boldsymbol{P}_p = \frac{-d\boldsymbol{v}_{p_{drag}} \cdot m_{p_r}}{n_p}$$

Here, m_{p_r} is the mass the particle represents (differing to the mass of the single particle m_p). This mass also takes the effects of residual adhesion into account. The particle multiplier n_p gives the number of simulated trajectories per single particle. The momentum is added to an air-profile cell based on the particle's position.

The rotation of the particle $\boldsymbol{\omega}_p$ is only of minor interest. The orientation and rotation of a particle plays a role in the quasi-random influence of collisions with the confinement. Also a collision can transform linear kinetic energy into rotational energy and vice versa. To control an increase in rotation, a rough estimation of a rotational drag $\boldsymbol{T}_{drag}$ is required. A precise description of this drag is overly complicated [61, 62] and not needed for the purpose it serves in the model. Therefore, a useful estimation for $\boldsymbol{T}_{drag}$ is derived via dimensional analysis:

$$\boldsymbol{T}_{drag} = -\frac{\frac{1}{4}\rho_a A_p \sum_{i=a,b,c}\left(i^2 \cdot \left|\boldsymbol{\omega}_p \times \boldsymbol{e}_i\right|^2\right)^{3/2}}{\left|\boldsymbol{\omega}_p\right|^2}\boldsymbol{\omega}_p$$

The momentum exchange in this rotational interaction with the air will not influence the air velocity since it is only of an angular nature. The influence on the air velocity profile is therefore not taken into account.

All particles progress according to this scheme until they cross the boundary of the air profile cell, at which point the air velocities are updated according to the exchanged momentum.

Calculation of the air profile

As soon as the ballistic trajectory is complete to the end of the x-cell, the air velocities in the y-cells are evaluated. The air velocities are described by a steady state form of the Navier Stokes equation:

$$\rho(\boldsymbol{v} \cdot \nabla \boldsymbol{v}) = \mu \nabla^2 \boldsymbol{v} + \boldsymbol{f} - \nabla \boldsymbol{p}$$

As a result of the geometry of the encasing and the main direction of the particles, variation in the horizontal direction will be dominant for all air-flows and the pressure gradient. The pressure gradient in the vertical direction is therefore conveniently neglected.

$$\frac{d\boldsymbol{p}}{dy} = 0$$

To obtain a workable calculation scheme, the calculation is subdivided into a dispersion part $\mu \nabla^2 \boldsymbol{v}$, a momentum transfer part $\boldsymbol{f}$, and a pressure driven part $-\nabla \boldsymbol{p}$, which are combined at the end of the evaluation.

The dispersion term accounts for the momentum dispersed via the turbulent zone of the air-jet. The formation and opening angle of the jet is described by several authors [44, 62]. These sources describe the opening angle of the velocity profile and of the turbulence profile. In the comprehensive model, the angle of the momentum exchange profile is of interest. Based on the referenced analysis on velocity and turbulence, the angle of the momentum exchange profile is taken to open at an angle of 7°. For every y-cell the momentum of the air flowing into the left boundary of the cell is conserved but exchanged with the cells above and below, along the right boundary according to

the angle of 7°. This spreading and redistribution of the air flowing in at the left results in a dispersed airflow $\boldsymbol{v}_{a_{disp}}$, at the right boundary of all y-cells.

The momentum lost by the particles is transferred to the air via the body force $\boldsymbol{f}$. The increase of the air velocity is determined by adding the total momentum lost by the particles that have traveled through the cell, $\sum \boldsymbol{P}_p$, to the dispersed airflow via a separate term $\Delta \boldsymbol{v}_{a_p}$:

$$\left(\boldsymbol{v}_{a_{disp}} + \Delta \boldsymbol{v}_{a_p}\right)^2 - {\boldsymbol{v}_{a_{disp}}}^2 = \frac{\sum \boldsymbol{P}_p}{\rho_a \cdot dy_r \cdot dz}$$

$$\Delta \boldsymbol{v}_{a_p} \cong \frac{\sum \boldsymbol{P}_p}{\rho_a \cdot dy_r \cdot dz \cdot \boldsymbol{v}_{a_{disp}}}$$

As the velocity of the air is increased by the influx of momentum, the total volume of air flowing towards the right end of the ADR increases. This is counteracted by a pressure gradient over the width of the x-cell. Since $\frac{d\boldsymbol{p}}{dy}$ is assumed to be zero, the pressure gradient will be a constant over all y-cells within the x-cell. The pressure build-up will result in a return flow in the x-direction, and is added in all y-cells. The return flow effectively accounts for the conservation of the total air volume within an x-cell and is determined via the formula's below. Since all velocities are small with respect to the speed of sound, the air-density can be considered a constant.

$$dp_x = \frac{\sum_{y-cells}\left[\boldsymbol{v}_{a_{disp_x}} + \boldsymbol{v}_{a_{p_x}}\right]}{\sum_{y-cells}\left[\frac{1}{\rho \cdot v_{a_{disp_x}}}\right]}$$

$$\Delta \boldsymbol{v}_{a_{press}} = \frac{-dp_x}{\rho \cdot v_{a_{disp_x}}}$$

Hereafter the resulting air velocity at the right boundary of all y-cells is determined by combining the effects of dispersion, momentum transfer and the pressure gradient.

$$\boldsymbol{v}_{a_r} = \boldsymbol{v}_{a_{disp}} + \Delta \boldsymbol{v}_{a_p} + \Delta \boldsymbol{v}_{a_{press}}$$

As a final step, the vertical component of $\boldsymbol{v}_{a_r}$ is evaluated for the conservation of the total air volume in all cells. Starting with the bottom cell, the difference in air flowing into the cell at the left and the air flowing out of the cell on the right is balanced by correcting $\boldsymbol{v}_{a_{r_y}}$.

To get a smooth transition of the air-velocity from (close to) zero to non-zero, the x-cell can be subdivided into a predefined number of n sub-cells. When the initial air-velocity on the left boundary is lower than a predefined minimum air-velocity and the calculated velocity at the right is more than twice the minimum air-velocity, the air velocity at the cells right boundary is calculated via an interpolation via the n sub-cells.

Entrainment

The ballistic trajectory of very small particles could be dominated by an effect known as entrainment. The wake of a coarse particle can trap and shed fine particles, altering their trajectory to that of the coarse particle for some period of time. The impact of this effect is estimated below.

The concentration of particles in the air is the highest just after impact with the rotor. To assess this concentration, a certain volume must be regarded. The total amount of particles within this volume is determined by the throughput and the residence time. The residence time is determined by the particle velocity and the length of the regarded volume. The concentration can then be estimated with the equation below.

$$C = \frac{T/\rho \cdot w \cdot l/v}{w \cdot l \cdot h} = \frac{T}{\rho \cdot v \cdot h}$$

In which C is the particle concentration (volume/volume), T is the throughput (in kg/s/m_{width}), ρ the average density of the particles, v the average velocity of the particle and h the height span of the trajectory of particles.

When the concentration is evaluated just after impact with the rotor, the height span of the particles can be regarded to be the height of the blade (80 mm), and the velocity can be estimated by the speed of the blade (25 m/s). At 60 t/h/m and a particle density of 2000 kg/m^3, the particle concentration in the air is 4‰.

It is assumed that coarse particles induce a wake, and fines are able to be entrained in a wake. The amount of wake inducing particles is indicated by p_w. For Reynolds numbers bigger than 10^5, the wake following a particle can be estimated to be roughly five times the volume of the particle [63]. This volume will contain a concentration of particles as determined before. Of this concentration $(1 - p_w)$ is susceptible to entrainment. The total percentage of fine particles which at any given time is being entrained in a wake can then be estimated to be:

$$C_{f_t} = C \cdot p_w \cdot 5$$

Since p_w will always be smaller than 1, the maximum fraction of fine particles which can be influenced by this effect is ≪2%. Therefore, this effect can be neglected for particles of sizes moving at speeds essentially higher than 2% of the coarse particle velocity. Since all fine particles move at a speed of several m/s due to the air flow, and coarse particles move at speeds of ca 25 m/s, entrainment is a negligible effect for the overall transport of fines.

5.5.4 Results

By modeling the mutual interaction of ballistic trajectory with drag and the induced airflow, interesting aspects can be studied in more detail. The general properties of the air-profile and effect on particles trajectories for the base case are discussed below. Effects of changing the total throughput, the size of the encasing and changing the particle size distribution (PSD) of the particles are investigated.

Base case

In the base case, the ADR is simulated with a feed of 60 t/h/m. The particle size distribution and other physical parameters are as given in Table 4.1. The bottom ash input is represented in six size fractions, with 20 particles per size fraction and every particle is simulated 10 times, so in total 1200 trajectories are calculated. The properties of the particles are set via the formulas in section *Formation of particle jet by impact with the rotor* on page 125.

A random selection of 30% of the particles trajectories can be seen at the top of Figure 5.26, followed by the air-profile and the recovery curve per 3 m intervals (ticks are positioned at center of bin).

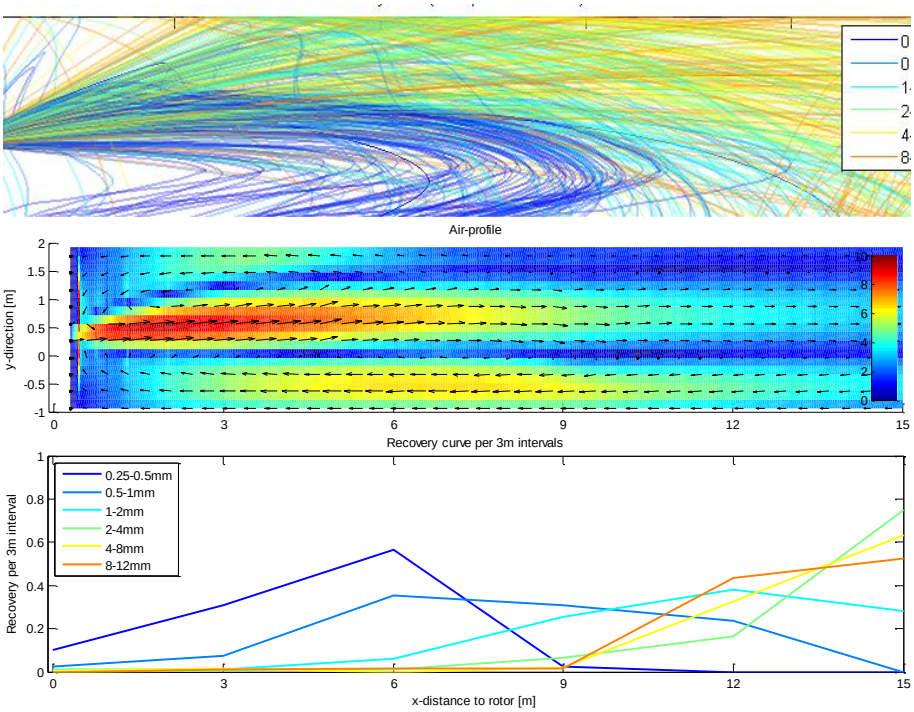

Figure 5.26: Trajectories, air profile and recovery curves of the air-profile base case simulation

It can be seen that an air-jet forms in the general direction of the particle jet. The air propelled to the right inside the jet is compensated by a return flow at the top and bottom. The generated airflow has a maximum around 10 m/s and averages around 3-4 m/s. The airflow in the jet and the return flow has a significant effect on the landing position of the particles, and therefore of the recovery curve.

This can be seen in Figure 5.27, which shows the result of the same simulation without air movement. The effect of the airflow is most notable in the 0.25-0.5 mm size fraction, which is mainly recovered in the bin centered at 6 m if the conservation of momentum is taken into account instead of the bin around 3 m if the air is static.

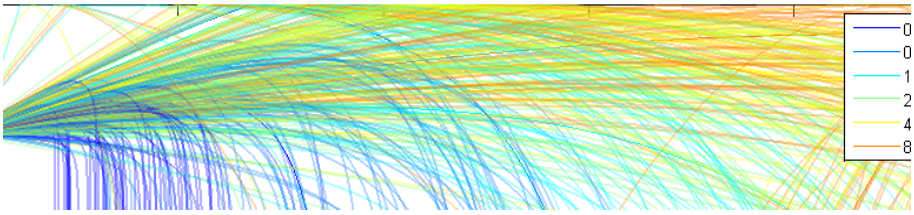

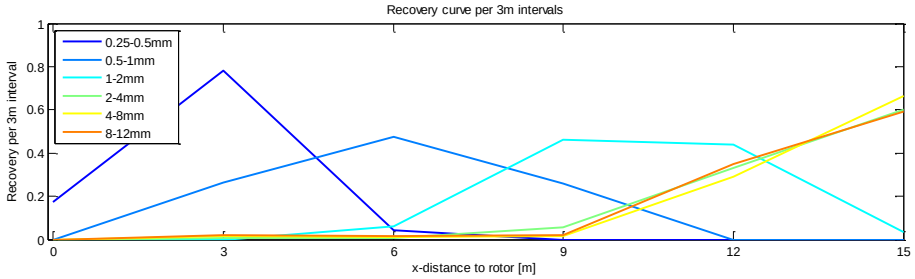

Figure 5.27: Trajectories and recovery curves of the base case simulation without air-movement

Change in throughput

The total momentum transfer to the air is a function of the throughput. When less particle mass is interacting with the air, air-velocities will be lower. This can be seen in Figure 5.28, which shows the result of the same simulation at a throughput of 15 t/h/m.

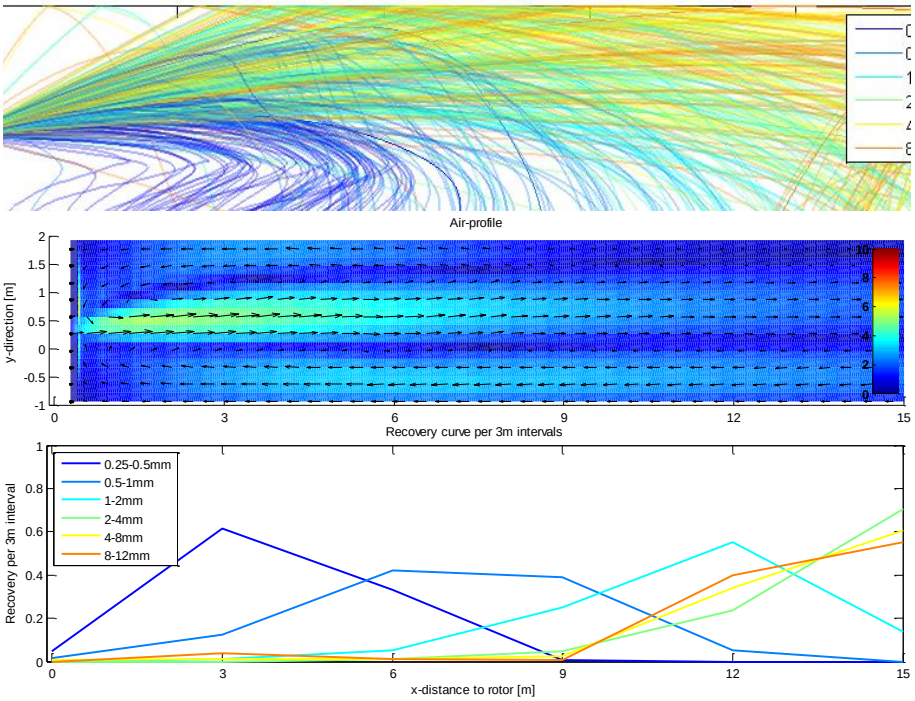

Figure 5.28: Trajectories, air profile and recovery curves for low throughput (15 t/h)

The maximum air-velocity reduces to around 5 m/s. It can be seen that the recovery curves converge to the result of the simulation in which the air is static.

Change in particle size distribution

Most momentum is transferred to the air via the finest particles, because fines represent a considerable part of the input mass flow and air-drag decelerates fine

particles the most. Therefore, changing the particle size distribution will change the air-profile. Figure 5.29 show the results of a simulation in which the amount of finest material is reduced from 14.5% to 5% and the difference is redistributed over the coarser particle in ratio of their specific surface area.

The results show a subtle decrease of the maximum air velocity. This results in a higher peak at 3 m in the recovery curve of 0.25-0.5 mm.

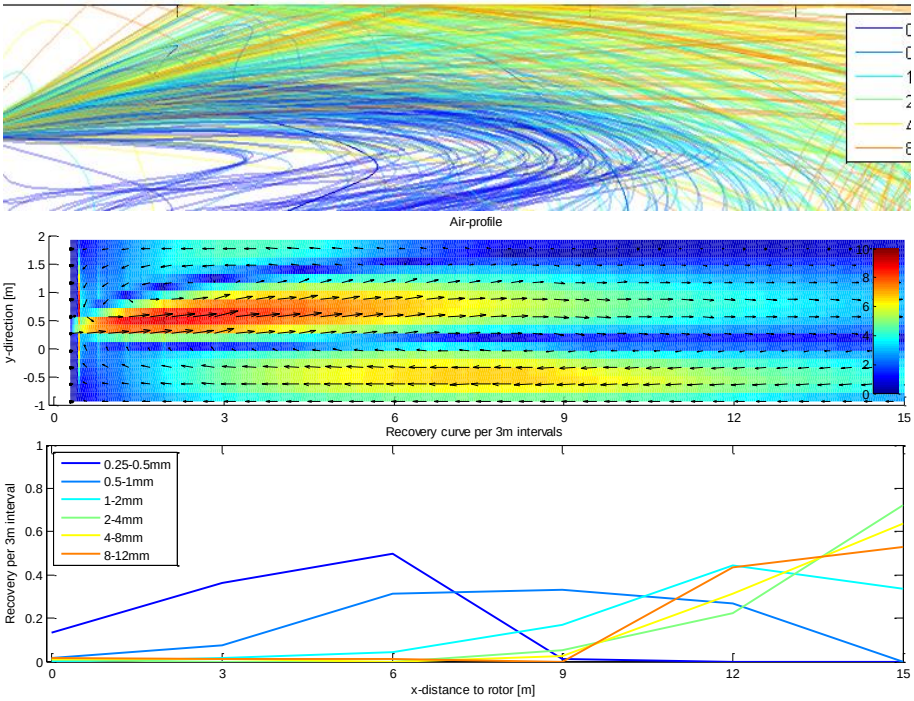

Figure 5.29: Trajectories, air profile and recovery curves of the changed PSD simulation

By redistributing the fines mass over the coarse particles via surface area, basically the effect of more residual adhesion after impact by the rotor is simulated. When the feed material has a stronger internal adhesion, or impact by the rotor is less effective, the results are twofold. On the one hand fine particles would remain attached to coarse particles, decreasing the classification sharpness. On the other hand, less momentum will be transferred, resulting in a sharper classification of the fines that are liberated.

Change in encasing

The ADR is surrounded by an encasing, first to contain the particles that are accelerated to high velocities. However, the encasing also has an effect on the air-profile, which in its turn affects the particles trajectories. The Base Case results showed that a large return flow is generated because of the compensation of the air accelerated within the jet. By reducing the height, the velocity of this return flow becomes quite substantial and therewith the effect on the particle trajectories. Figure

5.30 show the results of a simulation in which the upper and lower boundaries are extended.

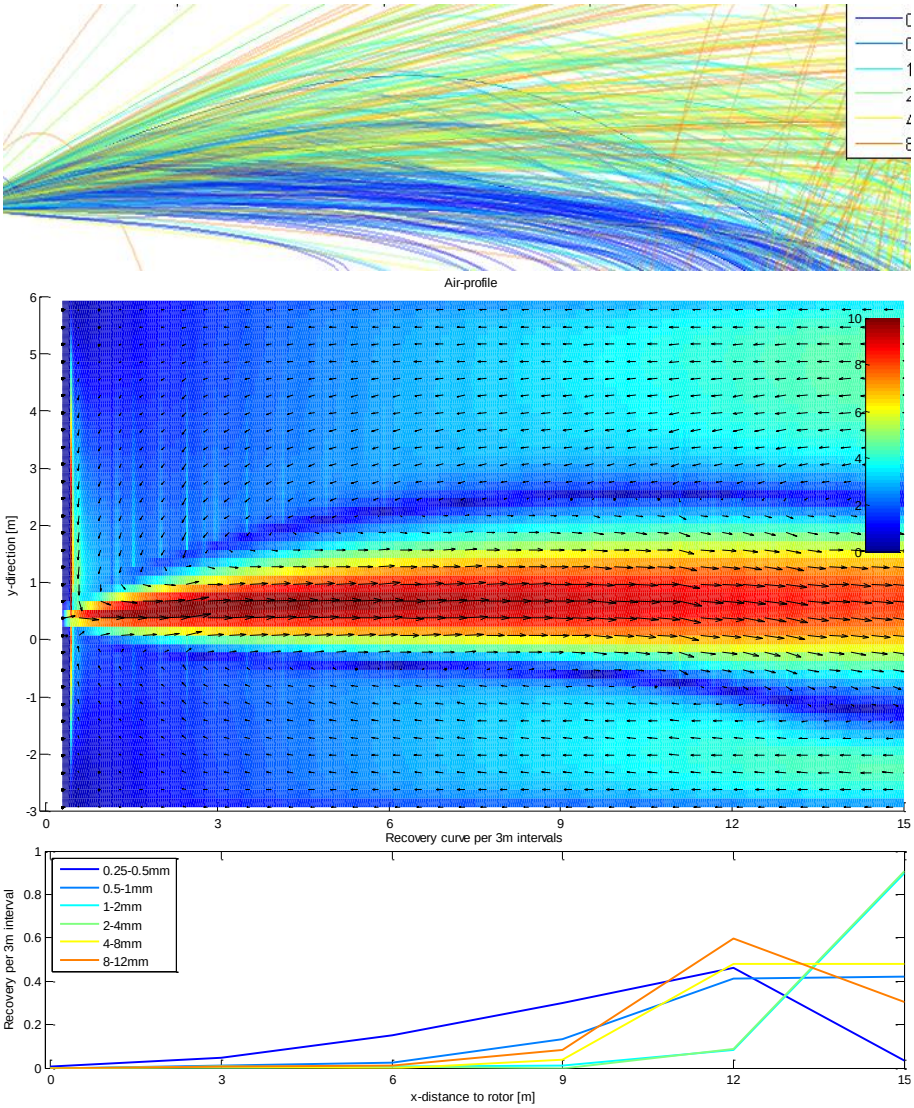

Figure 5.30: Trajectories, air profile and recovery curves for a high encasing.

It shows that the high air-velocities of the jet are sustained longer. Therefore, the finer fractions are transported further. Furthermore, the return flow is substantially slower, so fine particles that have fallen down to below the main jet are not transported back to the rotor.

5.6 Simulation using the comprehensive model

The model describing the mutual interaction of a ballistic trajectory with drag and an induced air-flow and the numerical description of a collision of ellipsoidal particles with flat and cylindrical surfaces are combined into one simulation. This simulation will be referred to as the comprehensive model. The results of this model are compared with the base case of the experiments with the prototype ADR.

The parameters used in the model are the following:

- Experiment parameters
  - Throughput, $T = 16.6\ kg/s/m_{width}$
  - Particle release position, $\boldsymbol{p}_{x,y,z} = [-0.2 \quad 0.28 \quad 0.0]$
  - Particle release velocity, $\boldsymbol{v}_{x,y,z} = [0.93 \quad -5.25 \quad 0.0]$
  - Particles description: three principal radii of ellipsoid, particle mass, representative mass, material type. These are set via formula's given in section *Formation of particle jet by impact with the rotor* on page 125, with a mass over size distribution as in the basic model.
  - Surfaces described by set of vectors and distances. Geometry of encasing like in the basic model. Rotor design described by flat and cylindrical surfaces.
- Model parameters
  - Time step (0.001 s), particle multiplier (4), number of y-cells (20), minimum air velocity (0.01 m/s).
  - Randomization in particle orientation and release time.
- Physics parameters
  - Gravity, air density, air viscosity, friction coefficients and restitution coefficients of material combinations, all like in the basic model.

Figure 5.31 shows the experimental and simulation results for the base case. The figure presents the recovery curves as a function over the distance from the rotor and the particle size fractions are the different series. The RMSE between the results of the experiment and the model is 6.59%.

It can be seen that the results of the model are comparable to the experimental model.

By using the comprehensive model, geometries of the encasing can be optimized freely, while critical assumptions from the basic model are no longer required to be estimated or fitted:

- Formation and opening of the cone
- Initial speed and angle of each trajectory
- Stochastic interpretation of the final position of the limited number of trajectories.

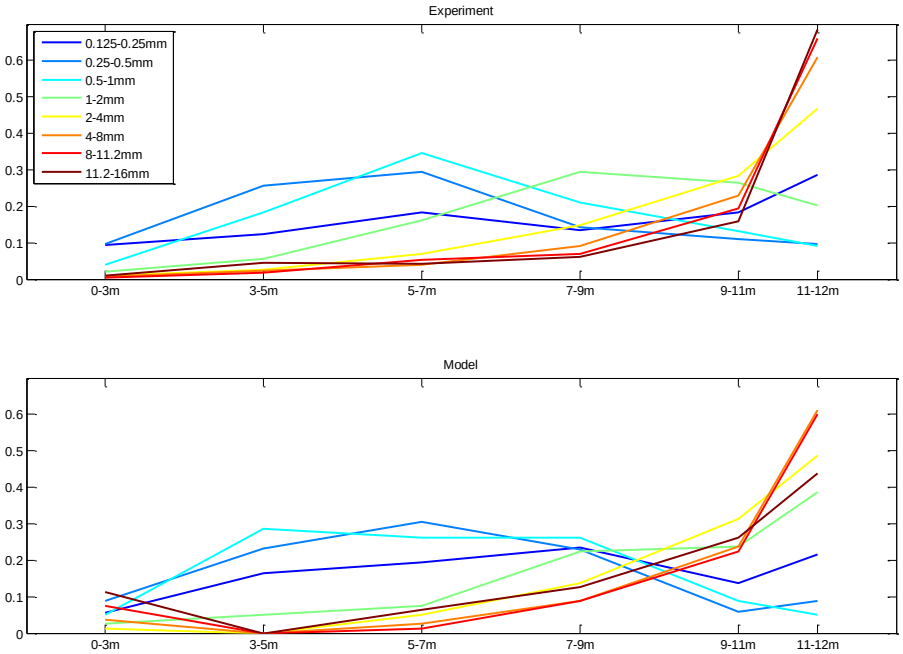

Figure 5.31: Recoveries per size fraction over distance: experimental (top), model (bottom)

5.6.1 Conclusion

Despite the complex interaction between particles, air flow and moving and static solid surfaces, the classification of particles in the ADR process can be predicted fairly accurately from first principles. This is done with a model that takes into account the overall behavior of the air flow and the detailed effects of drag and particle-wall collisions on the trajectories of the particles.

The main phenomena that are not described by this model from first principles are the de-agglomeration and breaking of particles during collisions and particle-particle interactions in flight as well as at solid surfaces of the rotor blades, the wall and the conveyor belt. Of these, the first two phenomena could be modeled without involving essentially new theory. The breaking of particles may be captured by introducing experimental data from lab experiments to account for changes in the particle size distribution and collision parameters at higher collision speeds. The interaction of particles during flight is described separately in an appendix. However, these effects are not important enough to stand in the way of an adequate prediction of the model of the classification performance of the ADR, as a function of the input material and particle size distribution, the throughput, the geometry of the encasing and the separation point for the coarse and fine products.

Appendix
Particle-particle interaction in the ADR

A.1 Introduction

During the ballistic trajectory of particles within the ADR encasing, it is possible that a particle interacts with another particle through a collision. In this appendix, the influence of particle-particle interactions will be investigated. The probability of a particle-particle collision in mid-air is estimated. Hereafter it is assessed what the impact of this probability on the overall classification result will be.

A.2 Concepts and definitions

The input of the ADR is characterized by a set of particles, $p = 1, \ldots, N_p$. Each particle has a particle mass m_p as well a volume and shape that is approximated by an ellipsoid with main axes a_p, b_p, c_p. Numerical analysis requires that N_p must be a small number; so each of the N_p particles will represent a large number of similar particles with a combined mass flow rate per meter width of the ADR, T_p [kg/ms]. During the simulation of the trajectory of the particles of type p, stochastic effects occur that affect the trajectory of some of them. Such effects are addressed by launching n_p particles of the same type, allowing each of the n_p representations to follow a different path according to stochastic rules. The combined flow of n_p particles may then give a realistic picture of the influence of a great many stochastic influences. In particular, particles may start their trajectory through the ADR with different initial conditions $c = 1, .., n_p$, defining their initial position and velocity. The result of the simulation then, is a set of trajectories, each of which has an identifying index pc.

A.3 Theoretical framework

The trajectory of a given particle of type p with initial conditions c proceeds in steps, by integrating its motion from the left boundary x_{left} of a cell with size $V = \Delta x \Delta y$ (per meter width of the ADR along the z-axis) to its right boundary x_{right}. In the following, we will assume that the particle takes a time τ_{pc} to move from x_{left} to x_{right}, and that the major part of its trajectory during this time can be assigned to one particular cell (in reality a particle may also move to the cells below or above). Since the given trajectory represents a group of similar particles, there will be a number

$$\frac{T_p \tau_{pc}}{m_p n_p}$$

of particles of the similar type p and with the same initial conditions c in the cell at any time. In other words, the volumetric density of such particles (their number per unit volume) will be

$$\frac{T_p \tau_{pc}}{m_p n_p V}$$

Suppose now that another trajectory $p'c'$ also crosses the same cell. This trajectory represents

$$\frac{T_{p'}\tau_{p'c'}}{m_{p'}n_{p'}}$$

similar particles. This second group of particles travels with a relative speed of $\Delta v = \left|\vec{v}_{p'c'} - \vec{v}_{pc}\right|$ through the cloud of particles represented by trajectory pc. Each of the particles of this second group carves out a cylindrical volume per unit of time of this cloud, in the sense that particles of type p would be hit if they have their center in this volume (see Figure A.6). Together, the particles of the second group carve out a volume of the cloud of

$$\frac{T_{p'}\tau_{p'c'}}{m_{p'}n_{p'}}\Delta v\Delta t\left(A_{pc} + A_{p'c'} + \frac{P_{pc}P_{p'c'}}{2\pi}\right)$$

in a time interval Δt, if A_{pc} is the area of the ellipse formed by the projection of particle p along $\overrightarrow{\Delta v}$ and P_{pc} is the perimeter of this same ellipse.

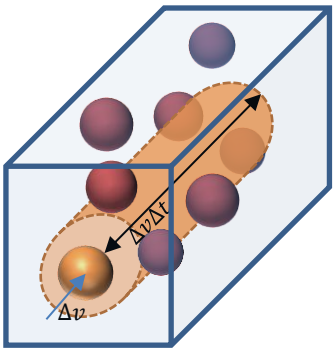

Figure A.6: Particle of type p' (orange) moving with relative speed Δv with respect to a cloud of particles of type p (red). In a time interval Δt, the trajectory of p' carves out a cylindrical volume (light orange) of this cloud such that any particle of type p that has its center inside this volume will be hit. The cylinder has a length $\Delta v\Delta t$ and a cross-sectional area $A_{pc} + A_{p'c'} + \frac{P_{pc}P_{p'c'}}{2\pi}$, where A_{pc} is the area of the ellipse formed by the projection of particle p along $\overrightarrow{\Delta v}$. P_{pc} is the perimeter of this ellipse.

It is possible to calculate the ellipse projection of an ellipsoid along any direction analytically, but since the relative orientation of the ellipsoids is random, a nice option is to approximate A_{pc} and P_{pc} by taking values A_p and P_p averaged for the projections along three main axes (e.g. $A_p = \pi(a_p b_p + b_p c_p + a_p c_p)/3$). By multiplying the carved out volume with the density of particles p, we obtain the number of collisions in the cell in time-interval Δt:

$$Number\ of\ collisions\ [pc, p'c', \Delta t] = \frac{T_p\tau_{pc}}{m_p n_p}\frac{T_{p'}\tau_{p'c'}}{m_{p'}n_{p'}}\frac{\Delta v\Delta t}{V}\left(A_p + A_{p'} + \frac{P_p P_{p'}}{2\pi}\right)$$

Of course, this number is symmetric with respect to the parameters of the two trajectories.

For any given particle of type p, the probability that it will collide with a particle of type p' during its passage through the cell is therefore equal to:

$$Probability\ of\ collision_{pc}\ [p'c'] = \frac{T_{p'}\tau_{p'c'}}{m_{p'}n_{p'}}\frac{\Delta v\tau_{pc}}{V}\left(A_p + A_{p'} + \frac{P_pP_{p'}}{2\pi}\right)$$

A.4 Results

One option to simulate collisions is to evaluate the given probability for each trajectory pc and for collisions with all other trajectories $p'c'$ in a cell and then change the velocity of trajectory pc according to a collision with a trajectory $p'c'$ with this probability. However, each of the individual probabilities is expected to be vanishingly small, so that this can be completely ignored.

To verify this assumption, the probabilities of collisions are assessed. For the Base Case simulation, the total volume is divided into cells with Δx and Δy of 0.1 m. For all particles passing a cell, the full collision probability matrix is determined. To assess the impact of a collision on the particles trajectories, the collisions are grouped per particle size fraction, and the distribution of the order of collision probabilities ($log_{10} P$) is determined.

The distributions per size-fraction pair are given for cell (x, y = 0.85, 0.95 m) in Figure A.7. The distributions approximate a normal distribution and the means of the distributions are given in Table A.3.

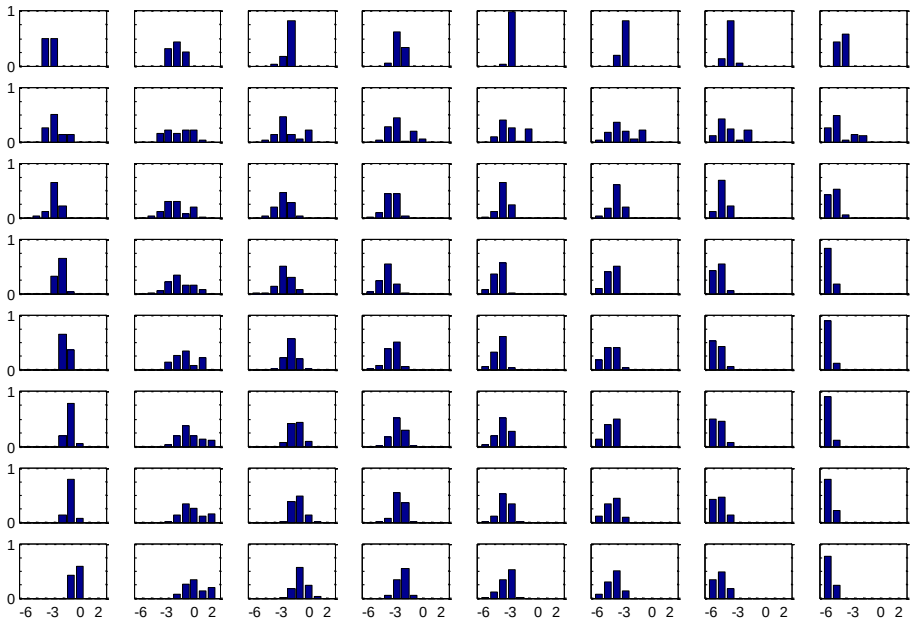

Figure A.7: Distribution of the order of collision probability of each size fraction pair

Table A.3: Mean of order of collision probability per size fraction pair

Hit part.	Hit by:	0.063	0.125	0.25	0.5	1	2	4	8
		0.125	0.25	0.5	1	2	4	8	11.2
0.063	0.125	-3.5	-2.1	-2.3	-2.7	-3.0	-3.2	-4.1	-4.5
0.125	0.25	-2.9	-1.8	-2.4	-2.8	-3.1	-3.3	-4.2	-4.6
0.25	0.5	-2.8	-2.1	-2.9	-3.6	-3.9	-4.1	-4.9	-5.4
0.5	1	-2.4	-1.7	-2.7	-4.1	-4.5	-4.6	-5.4	-6.0
1	2	-1.7	-1.0	-2.0	-3.6	-4.4	-4.7	-5.6	-6.3
2	4	-1.2	-0.5	-1.5	-2.9	-4.0	-4.7	-5.5	-6.2
4	8	-1.0	-0.3	-1.3	-2.7	-3.8	-4.5	-5.4	-6.1
8	11.2	-0.5	0.1	-0.9	-2.4	-3.6	-4.3	-5.2	-6.1
d_{min}	d_{max}								

It can be seen that small particles are only rarely hit by a big particle (probability <1‰), therefore these can be neglected (shaded green). The chance that a big particle is hit by a small particle is substantial. However, the impact of this is very small, as can be seen in the following assessment.

All particles generally move in the same direction, therefore Δv between particles is maximally the speed of the bigger particle, v_D. During the collision momentum is exchanged and the relative velocity change of the big particle can be maximally: $\frac{\Delta v}{v_D}\frac{m_d}{m_D} \approx \left(\frac{d}{D}\right)^3$. When $\frac{D}{d} > 2.2$, the maximum velocity change is <10% (shaded orange) so the effect of the collision will be relatively small. If the ratio is $\frac{D}{d}$>4, the effect can be fully neglected (shaded red).

It can be seen that only the collisions between particles <1mm could be of relevance. Between these particles the speed difference is small and so the influence of a collision is relatively small. These are also the particles strongly influenced by air-movements and residual adhesion. The effect of collisions can therefore be regarded to be of a secondary order and does not need to be taken into account in the comprehensive model.

To see how the situation in this particular cell compares to the rest of the volume, the mean of all orders of probability per cell is given in Figure A.8. The mean of the mean of all orders of probabilities given in Table A.3 is *-3.4*, (the appointed cell).

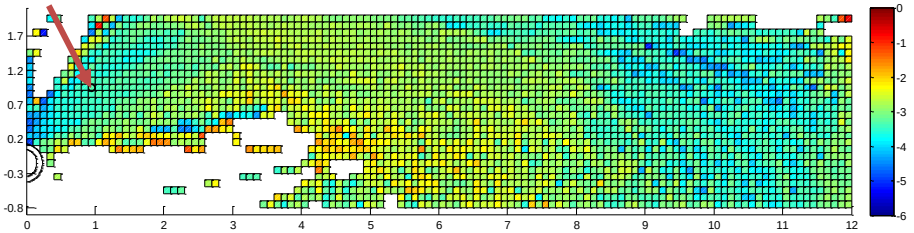

Figure A.8: Mean of the order of collision probability in each cell

Note that the analysis above assumes approximately granular particle shapes. If a substantial part of the input consists of light (thin) particles of sizes of > 4 mm, the impact of collisions may become relevant.

6 Comprehensive summary

Introduction

Recycling originated from societies' twofold desire to reduce volumes of waste and reduce dependency on primary raw materials. By looking at today's recycling objectives it is concluded that it is much better to look at recycling in terms of value recovered than mass recycled.

When optimizing the recycling of value, externalities should also be considered. The externalities of a recycling process can be accounted for via taxes or subsidies. When these taxes and subsidies are assigned, societal costs and benefits should be carefully optimized via an integral approach to prevent a waste of resources. For this, durable legislation, which considers the long term, is required.

Recycling value out of a waste flow is achieved by separating the valuable constituents. This is typically done via liberation, classification and separation of the material at various levels of complexity, using different techniques at each level.

A recycling technique can be optimized by taking into account the grade-recovery performance of the process and then optimize for the total value generation of the process as a whole.

Bottom ash is the residue of municipal solid waste incineration. This waste flow has a high potential for value recovery because it contains large amounts of ferrous and non-ferrous metals. To recover this value, recycling techniques are needed that require efficient classification according to size. For the fine 0-16 mm fraction of bottom-ash, this classification is difficult because of the moisture present which turns the flow of ash particles into agglomerates.

Recycling construction and demolitions waste has a high potential to reduce the carbon footprint of the industry. Crushed concrete could be reused as a replacement of primary aggregate in concrete, but fines and contaminations should then be removed.

The problems and objectives associated with bottom ash and crushed concrete require a novel classification technique. This technique should reduce the material's

compositional complexity, remove contaminations and enable the recovery of valuable metals so effective and economic recycling, beyond the state of art, can be achieved.

The ADR concept

The fundamental problem in the classification of materials that are rich in fines is the binding force of moisture at the millimeter level. Dimensional analysis shows that accelerations beyond the level of conventional technology are required to liberate these moisture bonds. In an ADR, a rotating rotor provides such acceleration with perpendicular blades impacting the material at 25 m/s. The efficiency of classification at 2mm is dominated by the layer thickness of the feed, the specific feeding position relative to the rotating rotor, and the shape of the encasing.

Moist particle clusters

Classification begins with breaking the water bonds between particles. To arrive at a model for the structure of unsaturated poly-disperse particle mixtures, a sample of a randomly deposited particle mixture is scanned using X-ray tomography. The images are interpreted to obtain a description of every particles center position, radius and kisses with other particles. From this, the coordination (or kiss) matrix can be determined.

A new model is constructed based on the observation that each pair of spheres has a so-called kissing surface on which a track is formed when particles come into contact and move along each other. By assuming that the number of kisses, or the length of kissing track per unit area of the kissing surface, will be uniform over the total of all kissing surfaces, a kiss matrix can be derived. For the one-dimensional case, this ergodicity argument can be fully deduced and proven. The experimental results for the 3D case compare well with the ergodic model and the results can be used to further study a partially saturated particle system.

A description of moist particle systems is obtained by assuming a liquid bridge at every kiss position described by the Laplace equation and assuming thermodynamic equilibrium of all moisture in the kisses (i.e. uniform Δp). The pressure difference over the liquid surface can then be expressed as a function of the moisture content, the PSD of the mixture and the model giving the kiss-matrix. With the mathematical description of all liquid bridges, the binding forces between particles can be determined.
This analysis shows that the acceleration required to liberate particles depends more on particles size than on moisture content. Also, it follows that liberation is dominated by the size of the smaller particle much more than the size of the larger particle to which it is attached and so the degree of liberation will increase sharply with this smaller particle size.

The validity and conclusions of this model are confirmed by an experiment in which the residual adhesion after impact with the rotor is studied in isolation. The data of this experiment further suggest that liberation will be complete in the limit of zero throughput, supporting the theory that moist particle clusters are transformed into pancakes at the rotor blade.

Experiments

To further develop the ADR as a prototype and to enable modelling, experiments were performed with a pilot installation. The results of the 'base case' show the classification achieved over distance from the rotor. By studying the recovery curves, special

features of certain size fractions become clear. Basic ballistic classification dominates in the size fractions between 1 mm and 8 mm, where the recovery over distance shows a clear distribution with an increasing mean over particle size. Secondary effects like residual adhesion and air movements in the ADR affect the finer particles. For coarser fractions the means do no longer increase with size because relative impact of air drag is similar for these sizes. The coarse fractions are also affected by a boundary effect of rotor blades, which causes a part of the trajectories to start at a very different angle and velocity. Despite the deviations of the smallest and biggest particles, a very effective separation can be achieved for a classification at 1 or 2 mm.

Influences of important operational parameters like throughput, moisture content and material type are shown by experimental variations on the base case. The analysis shows that classification sharpness increases at lower throughput. At very low moisture content, the airflow becomes stronger and the fine fractions are dispersed more, but the distance between the means of size fractions increases. Processing coarser and more elastic crushed concrete causes the randomizing effect of collisions to become more dominant. Comparing the performance for all experiments shows that despite these differences, the overall classification result is very robust.

The use of the ADR concept in processing MSWI bottom-ash was tested with an industrial pilot. The results illustrate the ballistic classification between different material types. The behavior of light materials (floats) and heavy materials (heavy non-ferrous metals: HNF) in bottom-ash show the effect of specific density on the classification. For a classification in which the minerals of bottom ash are recovered for >2 mm, floats are only recovered in the size fraction >4 mm while HNF will be recovered down to 0.5 mm. This combination results in a very effective use of eddy current separators and other metal separation techniques to concentrate the non-ferrous metals. Using the ADR, an overall NF-metals recovery rate of 89% was achieved, doubling the state of art value.

For different types of construction and demolition waste, the ADR concept was tested with an early prototype. Results show a very clear classification on both size and density. The ADR can be used to significantly increase the quality of crushed concrete. It therefore becomes suitable to replace natural aggregates in the production of concrete. By using the ADR on sifting sand, almost a quarter of the very complex waste stream is saved from landfilling and can be applied as a useful aggregate.

Modeling

The ballistic classification of the ADR is modelled in a two-step process by starting with a basic model and expanding it into a comprehensive model. The basic model describes the ballistic trajectory of particle groups, in which the effects of residual adhesion, air-drag, air-movement and collisions are taken into account using elementary models and some assumptions. A statistical function is used to expand the results of a limited number of simulated trajectories. This model can be used to quickly quantify impacts, visualize the classification process and give more general insight.

In the comprehensive model, using more complex descriptions of physics reduces the dependency on assumptions on starting conditions and statistical interpretation. The collisions of particles with (moving) surfaces are described using a numerical implementation of the collision model of Keller, and the mutual interaction of airflow and a ballistic trajectory with drag is described in more detail.

The refinements allow a detailed study of the statistics of collisions, showing that the shape of the particle jet is determined mainly by the randomizing effect of the collisions instead of the geometry of the feed and rotor. The diverging jet is converged upon collision with the roof because of the limited restitution coefficient. And the bouncing of a particle on an inclined high velocity conveyor belt can be sustained for long times because of the constant influx of energy into a rotating ellipsoidal particle.

The detailed air-profile description, combined with the calculation of a high number of ballistic trajectories can be used to see the effects of a change in throughput, particle size distribution (PSD) and size of the encasing. By reducing the throughput, the total momentum influx to the air is reduced and air-velocities are lower, resulting in a sharper classification. Changing the PSD will affect the amount of momentum transferred from particles to the air, and less fines result in less air movement. This explains the twofold effect of an increase of residual adhesion. Because more fines remain attached to coarse particles the classification efficiency reduces, but since less momentum is transferred, the 'free' trajectories classify more efficiently. Finally, the size of the encasing determines the effect of a return airflow and the sustainment of the airflow in the particle jet. A larger encasing will have a reduced return flow and air movement in the particle jet is sustained longer, resulting in an overall reduction of classification performance.

Despite the complex interaction between particles, air flow and moving and static solid surfaces, the classification of particles in the ADR process can be predicted fairly accurately from first principles

Summary
Recycling is improved by optimizing the recovery of value from our waste streams. To enable this value recovery for municipal solid waste incineration bottom ash and construction and demolition wastes, a classification at 1 or 2 mm is required which cannot be achieved by conventional dry classification techniques. The ADR uses high accelerations to break the moisture bonds between fine particles, which is the fundamental cause of classification problems for fine moist materials. An ergodic model can be used to describe the structure of the moist particle clusters so they can be better understood. Experiments show the robustness of the ADR concept in the classification of waste streams by size and density. Case studies show that the ADR enables high recovery of valuable NF-metals from incinerated household waste and that it enables the reuse of crushed concrete into concrete. Modeling the physics of the ADR shows how the different influences on the ballistic particle trajectories result in the observed classification performance.

7
Conclusions

Introduction into recycling

- Society should use the unit of 'value recovered' including integral costs, benefits and externalities to objectively assess recycling processes and to optimize use of scarce resources.
- To professionalize recycling, materials and recycling processes should be analysed quantitatively for value and risks, performance (recoveries) and in relation to each other to optimize for total added value.
- Within solid waste, municipal solid waste incineration ash, crushed concrete and sifting sand are substantial flows due to their positive potential, large volumes or negative impact. To enable effective recycling, it is required to classify these moist materials according to size and density.

The ADR concept

- Classifying moist material is problematic due to liquid bonds between the finest particle creating clusters, which are only liberated at high accelerations.
- The ADR concept of a rotor with impact blades can be used to impose high accelerations under well-defined and controlled circumstances, enabling effective classification.

Structure and break up of unsaturated poly-disperse particle mixtures

- The structure of poly-dispersed particle mixtures is complex, but forms the first step in understanding and modelling the liberation of moist particle clusters.
- X-ray tomography combined with an advanced image analysis algorithm can determine the particle structure of a real-life random dry particle mixture, to obtain an experimental kissing matrix.
- The kiss-matrix of mixtures can be estimated by an ergodic assumption that the total number of kisses ($C \cdot N$) is uniformly distributed over the total surface of kissing spheres (with diameter $D_i + D_j$) of all particles pairs.
- In one dimension the exact number of microstates resulting in a given kiss-matrix can be determined and the most likely kiss-matrix can be calculated. Likewise, the Ergodic solution can be derived rigorously and compared to the model, showing that the errors from the simplifications used in the Ergodic model are negligible.
- The results of the Ergodic model for 3D compare well with measured data. The order of errors agrees with expectation from statistical effects of the limited size of the measured sample.

- By combining the Young-Laplace description of a liquid bridge between two spheres and the kiss-matrix as given by the Ergodic model, the liquid bond properties and macroscopic properties of the mixture can be given as a function of the moisture content and the particle size distribution of the mixture.
- Accelerations needed to liberate an adhered particle from the accelerated particle are dominated by the size of the adhered particle. Liberation of a particle of a size fraction will therefore be relatively independent of the size of particle originally connected to.
- The required acceleration increases one order of magnitude with every halving of the size of the adhered particle. The degree of liberation will therefore sharply decrease with smaller sizes.
- The results of a residual adhesion experiment in which the liberation effect of the rotor was carefully isolated, confirm the conclusions from modelling.
- The experimentally found distribution of non-liberated fines over coarse particles is in line with the predictions of the Ergodic model.
- Experimental results suggest full liberation as throughput goes to zero, supporting the idea that clumps of particles are compressed into pancakes at the rotor before liberation.

Experiments

- The 60 t/h bottom-ash base-case experiment shows the classification effect of the ADR in that fine <1 mm particle are liberated and collected close to the rotor and large particles far away.
- Particles between 1 and 8 mm show a ballistic separation in which the mean of the landing position distribution increases with particle diameter. The spread among the mean is caused by differences in starting position, collisions with the encasing and differences of particle properties within a size fraction.
- The smallest particles are also influenced by residual adhesion and air-movements in the ADR, causing the differences between means to be smaller and distributions to be wider.
- The distribution of the coarsest particles become similar due to reduced relative influence of air-drag and the limited size of the ADR. The limited size of the rotor-blade causes the biggest particles to be hit partially resulting in aberrant trajectories and recovery closer to the rotor.
- The recovery-recovery curve shows the optimum size-cut of the ADR to be at around 1 mm. In the coarse product, >50% of the <1mm is removed at a 90% >1 mm recovery, resulting in a dramatic yet efficient improvement of processability.
- Reducing throughput reduces residual adhesion and air-movement, improving classification.
- Reducing moisture reduces residual adhesion, but air-movement increases due to conservation of momentum. In the extreme of no moisture, distributions of the finest fractions become much wider reducing classification effectiveness.
- Changing the input material to coarser, more elastic crushed concrete make the distribution of a size fraction wider, but there is more distinction between the means.
- The small overall differences in the recovery-recovery curves of the variations on the base case show the robustness of the ADR concept as a classification technique.

- An industrial pilot ADR equipped with an air-knife at the coarse fraction processing municipal solid waste incinerator ash shows a 90% <1mm removal at a 90% >4mm LNF and 90% >2mm HNF recovery. Subsequent processing of the loose coarse material using ECS's shows a doubling of 1-8 mm NF-recovery compared to the state of art case.
- By processing crushed concrete with an industrial pilot ADR, the amount of fines, moisture and floating contamination is greatly reduced, allowing the use of crushed concrete as a high-grade primary aggregate replacement.
- The industrial pilot ADR can extract >20% of the complex sifting sand waste stream into a coarse product that does not need to be incinerated or landfilled.

Modeling

- Modelling the physics of the ADR process results in a deeper understanding and will support break-through improvements of the concept.
- The basic model shows that the combination of relatively simple modelling concepts can help interpret experimental results and isolate the impact of different physical phenomena.
- Detailing the physics in crucial aspects of the model reduces the dependence on assumptions, so these aspects can be studied in more detail.
- The collision model of Keller, together with an ellipsoidal description of particles and a description of moving surfaces can properly simulate the formation of a particle jet by impact with a rotor.
- The convergence of the particle jet at impact with the roof and the bouncing behaviour on an inclined fast belt can be understood via the collision model, enabling effective design improvements.
- Knowledge of the details of the particle jet allow for a quantitative evaluation of the probability of collisions. Collisions of small particles by big particles can be completely neglected. Collisions of a big particle being hit by a small particle is fairly common, but the impact is negligible. Collisions between particles <1 mm could be of relevance but other influences like residual adhesion and air-movement are more dominant.
- The effect of air-movement in the ADR is complex. Particles liberated and accelerated by the rotor, transfer momentum to the air via drag, causing the air to accelerate. This air-movement can have a relevant influence on the <2 mm particles movement, creating a mutual influence.
- The components of the Navier-stokes equation are isolated, solved and effects are combined to obtain a workable description of the air-movement, integrated with the numerical calculation of the particle trajectories to solve the mutual influence and see the effects of changing throughput, PSD and the shape of encasing.
- The comprehensive model can be used to simulate the experimental results with less dependence on assumptions and statistical interpretation of the results.

References

[1] European Parliament, "Waste statistics," September 2015. [Online]. Available: http://ec.europa.eu/eurostat/statistics-explained/index.php/Waste_statistics.

[2] European Parliament, "Directive 2008/98/EC of the European Parliament and of the Council of 19 November 2008 on waste and repealing certain Directives," *Official Journal of the European Union,* vol. L 312, p. 3–30, 2008.

[3] M. Hüther, "Volkswirtschaftliche Bedeutung der Entsorgungs-und Rohstoffwirtschaft.," in *BDE Bundesverband der Deutschen Entsorgungs-, Wasser-und Rohstoffwirtschaft e. V.*, Berlin, 2010.

[4] W. Kuilman, P. C. Rem and R. B. Leeftink, "Operations management for solid waste treatment," in *Turning waste into ideas*, Lisbon, 2009.

[5] S. P. M. Berkhout, B. P. M. Oudenhoven and P. C. Rem, "Optimizing non-ferrous metal value from MSWI bottom ashes," *Journal of Environmental Protection,* vol. 2, no. 5, p. 564, 2011.

[6] European Parliament, "Key Waste Streams - Eurostat," [Online]. Available: http://ec.europa.eu/eurostat/web/waste/key-waste-streams.

[7] European Parliament, "Construction and Demolition Waste," European Commission, 25 11 2015. [Online]. Available: http://ec.europa.eu/environment/waste/construction_demolition.htm.

[8] C. S. Psomopoulos, A. Bourka and N. J. Themelis, "Waste-to-energy: A review of the status and benefits in USA," *Waste Management,* vol. 29, no. 5, pp. 1718-1724, 2009.

[9] O. Eriksson, G. Finnveden, T. Ekvall and A. Björklund, "Life cycle assessment of fuels for district heating: A comparison of waste incineration, biomass- and natural gas combustion," *Energy Policy,* vol. 35, no. 2, pp. 1346-1362, 2007.

[10] C. Riber, G. S. Bhander and T. H. Christensen, "Environmental assessment of waste incineration in a life-cycle-perspective (EASEWASTE)," *Waste Management & Research,* vol. 26, no. 1, pp. 96-103, 2008.

[11] L. A. Ruth, "Energy from municipal solid waste: A comparison with coal combustion technology," *Progress in Energy and Combustion Science,* vol. 24, no. 6, pp. 545-564, 1998.

[12] M. J. Clarke, "Burning garbage in the US: Practise vs. State of the Art," in *INFORM*, New York, 1991.

[13] J. A. S. Green, "Recycling of Aluminum (7)," in *Aluminum Recycling and Processing for Energy Conservation and Sustainability*, ASM International, 2007, pp. 109-113.

[14] A. Damgaard, A. W. Larsen and T. H. Christensen, "Recycling of metals: accounting of greenhouse gases and global warming contributions," *Waste Management & Research ,* vol. 27, no. 8, pp. 773-780, 2009.

[15] J. Dijkstra, H. A. van der Sloot and R. N. J. Cormans, "The leaching of major and trace elements from MSWI bottom ash as a function of pH and time," *Applied Geochemistry,* vol. 21, no. 2, pp. 335-351, 2006.

[16] C. A. Johnson, et al., "Leaching behaviour and solubility - Controlling solid phases of heavy metals in municipal solid waste incinerator ash," *Waste Management,* vol. 16, no. 1, pp. 129-134, 1996.

[17] O. Hjelmar, "Disposal strategies for municipal solid waste incineration residues.," *Journal of Hazardous Materials,* vol. 47, no. 1, pp. 345-368, 1996.

[18] H. A. Rijnsburger, "Gebruik van secundaire grondstoffen bij de Rijkswaterstaat," Dienst Weg- en Waterbouwkunde , Den Haag, 2003.

[19] R. K. Pachauri and A. Reisinger, "Climate Change 2007: Synthesis Report," IPCC, Geneva, 2007.

[20] F. Pacheco-Torgal, V. W. Y. Tam, J. A. Labrincha, Y. Ding and J. de Brito, Handbook of Recycled Concrete and Demolition Waste, Elsevier, 2013.

[21] E. K. Lauritzen, "Recycling concrete-an overview of challenges and opportunities," *ACI Special Publication,* vol. 219, pp. 1-10, 2004.

[22] W. L. Huang, D. H. Lin, N. B. Chang and K. C. Lin, "Recycling of construction and demolition waste via a mechanical sorting process," *Resources, Conservation and Recycling,* vol. 37, no. 1, pp. 23-37, 2002.

[23] E. Mulder, T. P. R. de Jong and L. Feenstra, "Closed Cycle Construction: An integrated process for the separation and reuse of C&D waste," *Waste Management,* vol. 27, no. 10, pp. 1408-1414, 2007.

[24] S. Lotfi, C2CA Concrete Recycling Process: From Development To Demonstration (Ph.D. thesis), Delft, 2016.

[25] N. L. Weiss, SME Mineral Processing Handbook, Society of Mining Engineers of the American Institute of Mining, Metallurgical, and Petroleum Engineers, 1985.

[26] N. Ouchiyama and T. Tanaka, "Estimation of the average number of contacts between randomly mixed solid particles," *Ind. Eng. Chem. Fundam.,* pp. 338-340, 1980.

[27] M. Suzuki and T. Oshima, "Estimation of the co-ordination number in a multi-component mixture of spheres," *Powder Technology,* vol. 35, pp. 159-166, 1983.

[28] M. Suzuki and T. Oshima, "Co-ordination number of a multi-component randomly packed bed of spheres with size distribution," *Powder Technology,* vol. 44, pp. 213-218, 1985.

[29] J. Goodling and M. Khader, "Co-ordination number distribution of spherical particles in a packed cylindrical bed," *Powder Technology,* vol. 44, pp. 53-55, 1985.

[30] R. Zou, X. Bian, D. Pinson, R. Yang, A. Yu and P. Zulli, "Coordination number of ternary mixtures of spheres," *Part. Part. Syst. Charact,* vol. 20, pp. 335-341, 2003.

[31] M. Song, K. Chuang and K. Nandakumar, "A theoretical correction of the Ouchiyama and Tanaka Formula for predicting average porosity of packed beds consisting of nonuniform spheres," *Ind. Eng. Chem. Res.,* vol. 37, pp. 3490-3496, 1998.

[32] W. de Vries and P. Rem, "ADR, a classifier for fine moist materials," in *Separating Pro-Environment*, Eds. V. Gente and F. La Marca, 2012, pp. 43-58.

[33] M. Arakawa and M. Nishino, *J. Soc. Mat. Sci. Japan,* vol. 22, p. 658, 1973.

[34] K. de Lange Kristiansen, A. Wouterse and A. Philipse, "Simulation of random packing of binary sphere mixtures by mechanical contraction," *Physica A,* vol. 358, pp. 249-262, 2005.

[35] R. Al-Raoush and M. Alsaleh, "Simulation of random packing of polydisperse particles," *Powder Technology,* vol. 176, pp. 47-55, 2007.

[36] A. Marmottant, L. Salvo, C. Martin and A. Mortensen, "Coordination measurements in compacted NaCl irregular powders using X-ray microtomography," *Journal of the European Ceramic Society,* vol. 28, pp. 2441-2449, 2008.

[37] Y. Gan, M. Kamiah and J. Reimann, "Computer simulation of packing structure in pebble beds," *Fusion Engineering and Design,* vol. 85, pp. 1782-1787, 2010.

[38] G. Seidler, G. Martinez, L. Seeley, K. Kim, E. Behne, S. Zaranek, B. Chapman, S. Heald and D. Brewe, "Granule-by-granule reconstruction of a sandpile from X-ray microtomography data," *Phys. Rev. E,* vol. 62, pp. 8175-8181, 2000.

[39] X. Fu, M. Dutt, A. Bentham, B. Hancock, R. Cameron and J. Elliott, "Investigation of particle packing in model pharmaceutical powders using X-ray microtomography and discrete element method," *Powder Technology,* vol. 167, pp. 134-140, 2006.

[40] L. D. Landau and E. M. Lifshitz, "Fluid Mechanics," 2 ed., vol. 6, Oxford, Pergamon Press, 1987, p. 238.

[41] L. Muchová, Wet physical separation of MSWI bottom ash, Delft: Ponsen & Looijen, 2010.

[42] J. R. Pan, C. Huang, J. Kuo and S. Lin, "Recycling MSWI bottom and fly ash as raw materials for Portland cement," *Waste Management,* vol. 28, no. 7, pp. 1113-1118, 2008.

[43] J. E. Aubert, B. Husson and N. Sarramone, "Utilization of municipal solid waste incineration (MSWI) fly ash in blended cement," *Journal of Hazardous Materials,* vol. 136, no. 3, pp. 624-631, 2006.

[44] A. M. Neville, Properties of concrete, 1997.

[45] S. Lotfi, J. Deja, P. C. Rem, R. Mróz, E. van Roekel and H. van der Stelt, "Mechanical recycling of EOL concrete into high-grade aggregates," *Resources, Conservation and Recycling,* vol. 87, pp. 117-125, 2014.

[46] L. Landau and E. Lifshitz, Fluid Mechanics, Pergamon Press, 1978.

[47] Y. Wang and M. T. Mason, "Two-Dimensional Rigid-Body Collisions With Friction," *Journal of Applied Mechanics,* vol. 59, no. 3, pp. 635-642, 1992.

[48] F. P. Beer, E. R. Johnston and D. F. Muzarek, Vector mechanics for engineers, 1984.

[49] L. Y. M. Gicquel, P. Givi, F. A. Jaberi and S. B. Pope, "Velocity filtered density function for large eddy simulation of turbulent flows," *Physics of Fluids,* vol. 14, no. 3, p. 1196, 2002.

[50] E. J. Routh, Dynamics of a System of Rigid Bodies: Elementary Part, New York: Dover Publications, 1905, pp. 126-162.

[51] J. B. Keller, "Impact With Friction," *Journal of Applied Mechanics,* vol. 53, no. 1, 1986.

[52] S. L. Shmakov, "A Universal Method Of Solving Quartic Equations," *International Journal of Pure and Applied Mathematics,* vol. 71, no. 2, pp. 251-259, 2011.

[53] D. Stoianovici and Y. Hurmuzlu, "A critical study of the applicability of rigid-body collision theory," *Journal of Applied Mechanics,* vol. 63, no. 2, pp. 307-316, 1996.

[54] P. Painlevé, "Sur les lois du frottement de glissement," *Comptes Rendu des Séances de l'Academie des Sciences,* vol. 141, pp. 401-405 and 546-552, 1905.

[55] F. Génot and B. Brogliato, "New results on Painlevé paradoxes," 1998.

[56] R. I. Leine, B. Brogliato and H. Nijmeijer, "Multibody Dynamics with Unilateral Contacts," *European Journal of Mechanics,* vol. 21, no. 5, pp. 869-896, 2002.

[57] D. E. Steward, "Rigid-body dynamics with friction and impact," *SIAM review,* vol. 21, no. 1, pp. 3-39, 2000.

[58] F. Pfeiffer and C. Glocker, Multibody dynamics with unilateral contacs, New York: Springer, 1996.

[59] R. P. Chhabra, L. Agarwal and N. K. Sinha, "Drag on non-spherical particles: an evaluation of available methods," *Powder technology,* vol. 101, pp. 288-295, 1999.

[60] G. H. Ganser, "A rational approach to drag prediction of spherical and nonspherical particles," *Powder Technology,* vol. 77, pp. 143-152, 1993.

[61] G. T. Vickers, "The projected areas of ellipsoids and cylinders," *Powder Technology,* vol. 86, no. 2, pp. 195-200, 1996.

[62] M. Zastawny, G. Mallouppas, F. Zhao and B. van Wachem, "Derivation of drag and lift force and torque coefficients for non-spherical particles in flows," *International Journal of Multiphase Flow,* vol. 39, pp. 227-239, 2012.

[63] M. Mandø and L. Rosendahl, "On the motion of non-spherical particles at high Reynolds number," *Powder Technology,* vol. 202, no. 1-3, pp. 1-13, 2010.

[64] S. B. Pope, "Calculations of a plane turbulent jet," *AIAA journal,* vol. 22, no. 7, pp. 896-904, 1984.

[65] J. Richmond-Bryant, A. D. Eisner and M. R. Flynn, "Considerations for Modeling Particle Entrainment," *Aerosol Science and Technology,* vol. 40, pp. 17-26, 2006.

[66] T. van Gerven, et al., "Carbonation of MSWI-bottom ash to decrease heavy metal leaching, in view of recycling.," *Waste Management,* vol. 25, no. 3, pp. 291-300, 2005.